

**The Development
of
The MIC Detector
for
Space Applications**

A Thesis Submitted for the Degree
of
Doctor of Philosophy of the University of London
by
Jonathan Gareth Bellis



Department of Physics & Astronomy
University College London
University of London

1992

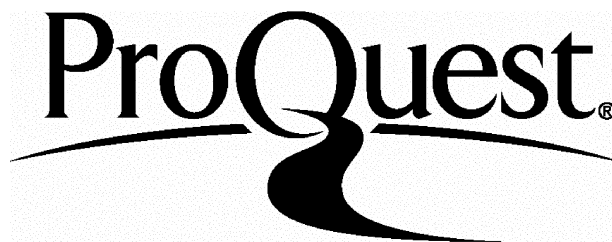
ProQuest Number: 10044263

All rights reserved

INFORMATION TO ALL USERS

The quality of this reproduction is dependent upon the quality of the copy submitted.

In the unlikely event that the author did not send a complete manuscript and there are missing pages, these will be noted. Also, if material had to be removed, a note will indicate the deletion.



ProQuest 10044263

Published by ProQuest LLC(2016). Copyright of the Dissertation is held by the Author.

All rights reserved.

This work is protected against unauthorized copying under Title 17, United States Code.
Microform Edition © ProQuest LLC.

ProQuest LLC
789 East Eisenhower Parkway
P.O. Box 1346
Ann Arbor, MI 48106-1346

Abstract

Since the development of the original Boksenberg IPCS at UCL several innovations have led to a highly compact, lightweight detector, the MIC-IPCS. A version specially designed for space applications is described here. The design has been based around the special requirements of a space based system.

The design and operation of each component of the detector is described. The detector incorporates a microchannel plate intensifier specifically designed for photon counting. The properties of the intensifier that limit the detector performance are considered. The output of the intensifier is coupled to a CCD via a fibre optic taper. The characteristics of fibre coupling are discussed and the effects the fibre taper introduces via pin cushion distortion are considered in detail. A fast scanning CCD is used as a readout device and the operation and design of the camera is described. The CCD data is presented to the image processing electronics that perform various important functions on the data. The design of each component circuit is considered in detail, in particular, a new interpolative centroiding technique has been developed.

Tests were carried out to assess the performance of the detector. The results are discussed and the performance characteristics of the detector evaluated.

I have been personally responsible for the design and testing of the processing electronics, the analysis of the phosphor decay characteristics of the image intensifier and for analysis of fibre taper distortion and efficiency. Additionally, when construction of the detector was complete, I took part in all the subsequent system tests and data reduction together with the other members of the group.

Acknowledgements

I would like to thank my supervisor, John Fordham, for all his help and advice over the past three years and for generally sorting things out. I would also like to thank Dave Bone for knowing all the answers; Tim Norton for all his information and Dave Rooks for his speedy photographic work.

On the non-academic side I would like to thank my parents for their support. Moldy deserves thanks for being a good laugh and for keeping me sane. Finally, I must thank the other people who have kept me amused or relieved the boredom – Helen, Helen M., Stuey, Big Al, the UCL squash club and the rest of my friends.

Contents

Title Page	1
Abstract	2
Acknowledgements	3
1 Introduction	13
1.1 Present Day Electronic Detectors for Astronomy	15
1.1.1 The CCD	15
1.1.2 Photon Counting Detectors	16
1.2 The History of the Development of MIC	19
1.2.1 The IPCS	19
1.2.2 The CCD-IPCS	21
1.2.3 The Microchannel Plate Intensified CCD Image Photon Counting Detector (MIC-IPCS)	24
2 The Space Based MIC	26
2.1 The Application of a Space Based System	27
2.2 Scientific Requirements of the XMM Optical Monitor	28
2.2.1 Overview of the XMM-MIC	30
3 The Image Intensifier	34
3.1 Introduction	34
3.2 The Design and Operation of the Intensifier	37
3.2.1 The Input Window	38
3.2.2 The Photocathode	40

3.2.3	The Channel Plates	42
3.2.4	The Phosphor Screen	46
3.2.5	Intensifier Housing	48
3.2.6	The Intensifier Power Supply	48
3.3	Limitations on the Performance of the Intensifier	49
3.3.1	Resolution	49
3.3.2	Detective Quantum Efficiency	51
3.3.3	Lifetime	52
3.3.4	Dynamic Range	57
3.3.5	Other Intensifier Properties Affecting Detector Performance	67
4	Fibre Optics	70
4.1	Introduction	70
4.2	The Fibre Optic Output of the Intensifier	71
4.3	The Fibre Optic Taper	72
4.3.1	A Comparison of Lens and Fibre Optic Coupling	74
4.3.2	Analysis of Pin-cushion Distortion for the Correction of Guide Star Positions	77
4.4	The Fibre Optic Block on the CCD	92
4.5	The Effect of Radiation on Fibre Optic Glass	93
5	The CCD Camera	96
5.1	Introduction	96
5.1.1	The Operation of CCDs	97
5.2	CCD Performance	101
5.3	The CCD Camera	102
5.3.1	The Signal Processing and Digitizing Section	103
5.3.2	The CCD Support Section	108
5.4	The Effect of Radiation on the CCD	112
5.4.1	A Summary of Radiation Effects	112
5.4.2	Radiation Effects for the MIC CCD	114
5.4.3	The XMM Radiation Environment	115

6	The Image Processing Electronics	117
6.1	Introduction	117
6.2	The Command Interface	122
6.2.1	Circuit Description	122
6.3	Data Analysis Array	126
6.3.1	Circuit Description	128
6.4	Event Validate	135
6.4.1	Criteria for event determination	135
6.4.2	Circuit Description	137
6.5	Multiple Event Discriminate	140
6.5.1	Introduction	140
6.5.2	Principle of Operation of the Multiple Event Discriminator	141
6.5.3	Circuit Description	144
6.6	Centroid	146
6.6.1	Introduction	146
6.6.2	The Problem of Pattern Noise and its Removal	148
6.6.3	The Centroiding Technique Used with MIC	151
6.7	Address Generator	167
6.7.1	Circuit Description	169
6.8	The Frame Store	177
6.8.1	Circuit Description	178
6.9	The Memory Interface	181
6.9.1	Introduction	181
6.9.2	The Read-Modify-Write Cycle	182
6.9.3	Operation of the Memory Interface as a Slave	194
7	System Performance	197
7.1	Introduction	197
7.2	Photocathode Sensitivity	201
7.3	Dynamic Range	202
7.3.1	The lower limit	203
7.3.2	The Bright Limit	203
7.4	Detector Resolution	213

7.5	System Detective Quantum Efficiency	218
7.6	Detector Uniformity	218
7.6.1	Fixed Pattern Noise	220
7.6.2	The Effect of Fibre Optic Multifibre Junction Defects	222
7.6.3	The Effect of low quantum efficiency CCD pixels	223
7.6.4	Other Detector Non-Uniformities	223
7.6.5	Variation of Pattern Noise with Count Rate	224
7.7	Observing Trials	226
7.7.1	The Observing Programme	226
7.7.2	Observing	227
7.7.3	Data Analysis	230
8	Conclusions	235
8.1	Summary	235
8.2	Future Developments	238
	References	243
	List of publications	246

List of Tables

2.1	Primary scientific requirements of the photon counting detector for XMM .	29
2.2	Required characteristics of the XMM-MIC	29
4.1	Coefficients of a straight line fit to fibre taper grid lines	81
4.2	Errors introduced by the fibre taper in a 300 μ m straight line	85
4.3	Deviations from the data of the polynomial fits to pin cushion distortion . .	86
4.4	Coefficients of a 3rd order polynomial fit to horizontal errors introduced by pin cushion distortion	87
6.1	Commands used to communicate with the image processing chassis	123
6.2	Boundary positions and centroid positions for equal channels	153
6.3	Boundary positions and counts per channel for four iteratively corrected flat fields	161
6.4	Sequencer states for the memory interface	188
7.1	Observing log for the XMM-MIC detector	228

List of Figures

1.1	Block diagram of the original IPCS	19
1.2	Cross section through the EMI four stage image intensifier	22
1.3	Block diagram of the CCD-IPCS	23
2.1	The XMM spacecraft	28
2.2	An example of the use of the windowing facility	30
2.3	Block diagram of the XMM-MIC	31
2.4	The prototype MIC system	32
3.1	Schematic of the various stages of the MCP intensifier	34
3.2	The 25mm microchannel plate image intensifier	37
3.3	Schematic of a cross section of the intensifier incorporated into the detector head	38
3.4	Transmission of MgF_2 and Sapphire windows	39
3.5	Hexagonal close packed structure of the MCP pores	43
3.6	Cross section through a typical microchannel	44
3.7	Typical MCP intensifier pulse height distribution	46
3.8	Typical EMI intensifier pulse height distribution	47
3.9	Measured phosphor decay curve	58
3.10	Relationship between times required to evaluate the phosphor decay	60
3.11	Fit to the phosphor decay	62
3.12	Energy emitted by the phosphor as a function of time	63
3.13	Ratio of the height of the residual to the height of the real event	64
4.1	The way in which light propagates down a fibre by total internal reflection .	71
4.2	Two fibre optic tapers	73

4.3	Propagation of light down a tapered fibre	74
4.4	Spot diagram for the CCD-IPCS relay lens	75
4.5	Grid lines as seen through the fibre optic taper.	79
4.6	Exaggeration of the distortion introduced on a grid by the fibre taper	80
4.7	Errors of a fibre optic image grid from a straight line grid	82
4.7	(<i>contd.</i>)	83
4.7	(<i>contd.</i>)	84
4.8	Greyscale plot of the horizontal pin cushion distortion	88
4.9	Greyscale plot of the vertical pin cushion distortion	89
4.10	Absolute error introduced by pin cushion distortion	90
5.1	Generalised structure of a charge storage site of a buried channel CCD	97
5.2	Clocking voltages and potential well structures that give rise to charge transfer	98
5.3	The frame transfer CCD	99
5.4	The camera electronics	104
5.5	Block diagram of the CCD camera electronics	105
5.6	Block diagram of the video processor section of the CCD camera electronics	105
5.7	Timing for the signal processing and digitizing section of the CCD camera .	106
5.8	The Flash Analog-to-Digital Converter	107
5.9	A simple example of CCD windowing	110
6.1	Block diagram of the image processing electronics	118
6.2	The image processing chassis	121
6.3	The command interface	124
6.4	Typical timing for the write cycle of the command interface	125
6.5	The way in which a photon event might appear on the CCD	126
6.6	Schematic showing the idea behind the operation of the Data Analysis Array	127
6.7	Data analysis array root diagram	129
6.8	The array of the data analysis array	130
6.9	Data analysis timing circuitry	131
6.10	Timing of the various components of the data analysis array	133
6.11	Cross hair used by Event Validate and a possible profile of the data	135
6.12	Profile of an event that has landed on the boundary between two pixels . .	136

6.13	Root diagram of event validate and centroid	138
6.14	The event validate circuit	139
6.15	Dynamic range curve illustrating the non-linearity seen at higher count rates	141
6.16	Two events not exactly coincident	142
6.17	Possible pulse energy for single and double events	143
6.18	The pulse energy discriminator circuit	145
6.19	A pixelated event profile	147
6.20	Pattern noise introduced into a flat field as a result of centroiding errors . .	148
6.21	Profile of a real event seen with MIC	149
6.22	Asymmetry of photon events	150
6.23	An illustration of how the size of memory needed for a look-up table is greatly reduced by partially calculating the centroid in hardware	153
6.24	Flow diagram depicting the procedure for correcting the pattern noise . . .	155
6.25	Centroid look-up tables circuitry	156
6.26	Circuitry for calculating M and N of the centroiding algorithm	157
6.27	Four flat fields showing the gradual removal of the fixed pattern noise with each successive iteration	160
6.28	Fourier transform power spectra of corrected and uncorrected flat fields . .	162
6.29	Eight spectra associated with the same pixel	164
6.30	Ideal form in which to have a memory address	168
6.31	Memory allocation with a window length of 256	168
6.32	Waste of memory encountered when the window length is not 256	168
6.33	Block diagram of the address generator	170
6.34	Root diagram of the address generator	171
6.35	Address generator circuitry	172
6.36	Control circuitry for the transfer of data to the memory	173
6.37	FIFO write cycle timing	175
6.38	FIFO read cycle timing	176
6.39	The frame store circuit	179
6.40	Schematic of the memory interface in master mode	183
6.41	Root diagram of the memory interface	187
6.42	Memory interface control circuitry	189

6.43	Address handling section of the memory interface	190
6.44	Data handling section of the memory interface	191
6.45	Timing diagram for read-modify-write	192
6.46	The timer of the memory interface	196
7.1	Signal induced background seen with ITL image intensifiers	199
7.2	RQE of ITL photocathode	201
7.3	RQE of DEP photocathode	202
7.4	Flat field dynamic range curve on full format	204
7.5	Point source dynamic range curve on full format	204
7.6	Theoretical point source dynamic range curves for two frame rates	206
7.7	Point source dynamic range curve on a format of 256×2048	207
7.8	Flat field dynamic range curves for three multiple counting thresholds on a format of 2048×2048	208
7.9	Point source dynamic range curve for three multiple counting thresholds on a format of 2048×2048	209
7.10	Point source dynamic range curve for three multiple counting thresholds on a format of 2048×2048	210
7.11	Real and simulated dynamic range curves showing the effect of phosphor persistence	212
7.12	Cross section of a 5 μ m pin-hole acquired with the 25mm intensifier	214
7.13	The effect of channel plate pore structure on detector resolution	215
7.14	Worst case resolution of 5 μ m pin-hole	216
7.15	Input point source position giving rise to worst case resolution	216
7.16	High signal to noise flat field	219
7.17	Magnified portion of the high signal to noise flat field	220
7.18	Profile through the stitching resulting from multifibre junction defects	222
7.19	Point source profile at various count rates	225
7.20	Four star fields observed at the University of London Observatory using the prototype XMM-MIC	229
7.21	Dynamic range curve derived from astronomical trials	232

Chapter 1

Introduction

Essential to astronomy is the ability to make a permanent record of the object being observed, for example, a star field or the spectrum of a star. This allows the astronomer to take the data away and perform a detailed scientific analysis. To make a permanent record it is necessary to have some form of detector attached to the back of the telescope. A detector must be able to respond to the energy of the incoming photons but, unlike the human eye, it also must keep a permanent record of the scene that is being viewed.

Eccles et al. (1983) outline the properties of an ideal detector. It should have the following characteristics.

- It should be efficient at detecting photons, that is, it should have a high *quantum efficiency*. It also should respond to a wide range of wavelengths, or photon energies.
- It should accurately retain the spatial position of each incoming photon and it should also have *high resolution*, that is, it should be able to resolve two closely spaced objects or features.
- It should be able to record the true brightness of any feature in an image, that is, it should have *photometric accuracy*. It should be able to do this over a wide range of brightnesses, that is, it should have a high *dynamic range*. A detector is said to be *linear* over a wide range if it has this property.
- It should have temporal resolution and be able to resolve time varying features in an image on any timescale
- The spatial position registered for photons should be stable with time.

- The photometric accuracy should be uniform over the detector area.
- It should have a large area so that as much information as possible can be recorded in one image.
- It should have a simple and reliable design.

No real detector is ideal in any of these respects. However, depending on the application, some of the above characteristics are less important than the others so that it is possible to choose a detector that best suits the application.

Photographic emulsions were introduced to astronomy in the 19th Century. They have a number of undesirable properties compared to the electronic based detectors that have now replaced them for most applications. They have a low quantum efficiency, are non-linear at low and high count rates and they suffer from adjacency effects whereby grains are activated by the presence of a photon nearby. They are uniform to around 2% but any non-uniformities cannot be removed as is the case for most modern electronic detectors. The processing of photographic emulsions is inherently untidy as it involves liquids, so that considerable expertise is needed for good processing. Data reduction is most easily accomplished with the aid of computers which, for photographic emulsions, means that complex measuring and digitizing machines need to be employed. Despite all their shortcomings, photographic emulsions are still superior for applications that require a very large field of view and high resolution.

McLean (1989) describes how the 1960s saw a minor revolution in astronomy, with new observatories, observations at new wavelengths and, moreover, the introduction of electronic based and computer controlled detectors. These new detectors used sophisticated devices such as photocells, photomultiplier tubes, night vision devices and TV cameras. Each detector offered superior performance to the photographic emulsion in one or more aspect. In particular, the quantum efficiency of these detectors was far superior to that of photographic emulsions. A lot of these detectors still used photographic emulsions to record an intensified image so that they retained many of the deficiencies of emulsions. Of those that did not, most were subject to increased noise introduced by the various components of the detector. In addition to noise introduced by undetected photons and sky background, sources of noise may have resulted from

- uneven gain processes in the detector,

- image spreading and halation,
- the dark current that is present in any electronic detector even when there is no source of photons,
- the readout noise present in detectors that employ electronic sensing devices.

1.1 Present Day Electronic Detectors for Astronomy

Today, the use of detectors in astronomy is dominated by two types of detector,

- the integrating charge coupled device (CCD),
- photon counting detectors.

1.1.1 The CCD

CCDs are slices of silicon, typically $2\text{-}3\text{ cm} \times 2\text{-}3\text{ cm}$, that convert the energy of incoming photons into charge. A CCD consists of a large array, for example, 1024×1024 , of picture elements, or pixels. When the energy of the incoming photon is converted into charge, the charge is stored in the pixel nearest to the position of impact of the photon. An image of a scene is built up in charge, the amount of charge in a given pixel being proportional to the flux of photons on it. The charge image may be read out of the device into appropriate processing electronics and the data may be stored directly in computer memory. Data reduction may then be carried out.

CCDs used as integrating devices, much as photographic plates are used, are now the most commonly used detectors in astronomy, mainly due to the advantages they have in performance over other detectors:

- They have very high quantum efficiency. Some specially treated CCDs may have quantum efficiencies up to 80–90% at some wavelengths.
- They are highly linear. The charge stored in a pixel will be proportional to the flux incident on it at any count rate until the signal becomes too high for the charge storage capability of a pixel and saturation takes place.
- They are responsive over a broad range of wavelengths and so may be used for a wide range of applications.

- They have low noise, particularly when cooled to cryogenic temperatures.
- Data are easily read into a computer for immediate data reduction
- They are compact and have a low power consumption
- Sensitivity variations across the CCD are constant and so may be removed by the use of a uniform illumination, or ‘flat’ field that reveals the variations.

These properties make the CCD the most suitable detector for most applications in astronomy. However, for some applications, photon counting detectors give superior performance.

1.1.2 Photon Counting Detectors

Photon counters amplify the incoming photons. A photon strikes a photosensitive surface, the *photocathode*, which forms the input to an image *intensifier*. The electron emitted by the photocathode undergoes electron multiplication in the intensifier and the resulting electron cloud, or photon *event*, may then be directly detected or converted back into light by a *phosphor* and then detected. Some form of *readout* device is needed in either case. The principle behind photon counting is to amplify the signal produced by an incoming photon to a sufficient level that it is clearly discernible above the system noise so that the noise may be rejected. The process of detection is then a matter of counting photons and the data become photon noise limited as opposed to system noise limited.

In applications where there is low signal to noise, such as high dispersion spectroscopy, the dark noise and readout noise of a CCD may be comparable to the signal noise and this makes their performance inferior to that of photon counters for these applications. Photon counters also have other characteristics that make them more suitable than CCDs for some applications.

- Photon counters possess high temporal resolution whereas a CCD used as an integrating detector does not. This allows time resolved applications such as speckle interferometry.
- The spectral response of photon counters may be tailored to the application by selecting an appropriate photocathode. Although CCDs have a large wavelength response and may be used in numerous wavelength regions by using an appropriate

filter, they have had a poor UV response up to now. For this reason photon counters have been the best detectors to use in the UV.

- CCD images, particularly those obtained after long exposures, show large spikes formed by the impact of cosmic rays. For CCDs used in photon counters, cosmic rays have a much smaller effect since they merely contribute a little to the readout noise.
- Photon counters allow the observer to monitor the progress of the exposure because they show the build up of the data. With CCDs, the correct integration time has to be estimated and even then it is assumed that data are being accumulated on the correct object.
- Integrating CCDs need to be operated at cryogenic temperatures in order to minimize dark count, whereas photon counters do not.

Two major disadvantages of photon counters compared to CCDs are their low quantum efficiency and low dynamic range.

Timothy (1991) gives a review of development in photon counting detectors. Essentially, present day photon counting detectors may be split into three categories.

- Those that use television type readout devices. In these photon counters the electron cloud is converted back into light by a phosphor. The phosphor is scanned many times per second by the readout device and photon events are registered in computer memory. In these types of photon counting detector the size of the event on the phosphor covers several picture elements of the readout device and so a technique of centroiding needs to be employed to regain resolution.

The first and most successful of these types of photon counters was the original IPCS developed by Boksenberg (e.g. Boksenberg, 1971; Boksenberg and Burgess, 1972) which used a Philips Plumbicon TV camera. Nowadays, readout devices tend to be fast scanning CCDs, for example, the 2D-Frutti (Schectman, 1981), the PCA (Hobbs et al., 1983) and the CCD-IPCS (Fordham et al., 1986). Photon counters of this type are highly versatile as CCDs are available in a wide range of configurations. They are also of simple construction, are geometrically stable and may be large format. Their

main disadvantage compared to photon counters of different design is the lower time resolution.

- Those that use direct electronic readout systems. Here, the readout forms the intensifier output. The charge cloud is incident directly onto some form of anode, or group of anodes, and the current delivered at various electrodes is used to determine the position of arrival of the event.

Examples of types of readout devices are the resistive anode (Lampton and Carlson, 1979) which is a sheet of resistive material with electrodes at its four corners – the position of the event is deduced from the magnitudes of the signals at the four electrodes. More recent variations on the resistive anode are the wedge and strip (Martin et al., 1981), the multianode microchannel array (MAMA) (Timothy, 1986) and the double delay line array (DADA) (Siegmund et al., 1989). These types of array have the advantage of a very fast response time, so that the dynamic range is generally not limited by the readout device. Their main disadvantages are that misregistration of events can occur and that some degree of image distortion is also present, particularly with resistive anode type readouts. Also, up to now, the largest detector diameter has been limited to 25mm. More recent readout constructions have necessarily required more complex electronics.

- Coded aperture systems. There is only one type of photon counting detector of this construction, the Precision analog photon address (PAPA) system (Papaliolios and Mertz, 1981) which uses an array of coded masks and photomultiplier tubes behind a conventional image intensifier to give a format of 512×512 .

The remaining sections describe the construction and performance of a photon counting detector that is classified in the first of the above categories. The detector is a descendant of the original Image Photon Counting System (IPCS) developed by Boksenberg which became an important detector at major UK telescopes.

1.2 The History of the Development of MIC

1.2.1 The IPCS

The IPCS uses an EMI magnetically focussed 4-stage cascade image intensifier lens coupled to a Philips Plumbicon TV camera. Each photon event is recorded with equal weight and its position of arrival is stored in computer memory. An image is formed by an accumulation of the stored data. A block diagram of the IPCS (taken from Boksenberg, 1978) is shown in figure 1.1. At the time of its development at University College

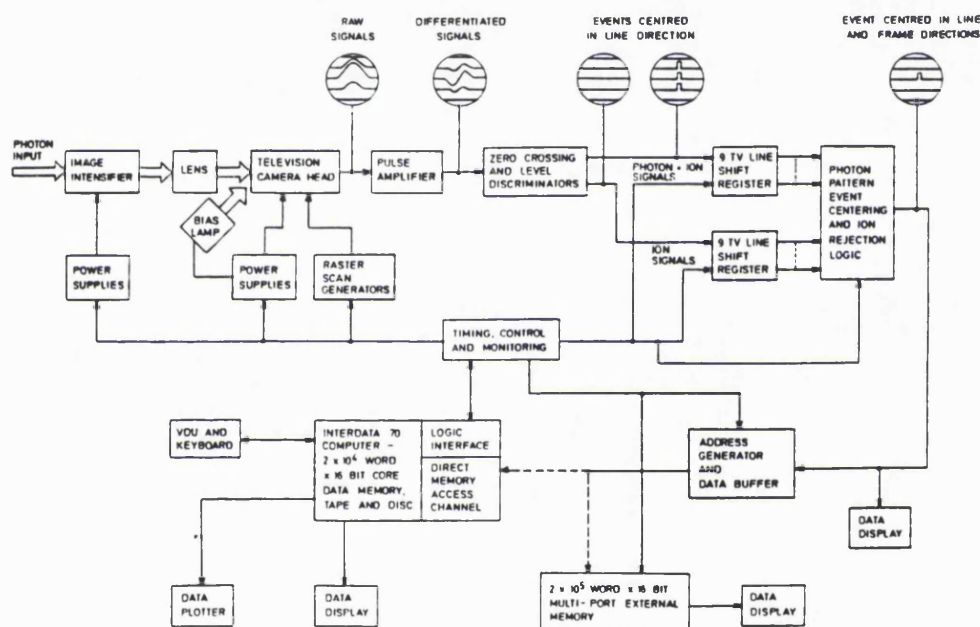


Figure 1.1: Block diagram of the original IPCS

London (UCL) by Boksenberg (Boksenberg, 1971) it had the following advantages over conventional methods of detection.

- All photons were recorded with equal weight. Hardware discriminator thresholds were set such that amplifier noise and large ion events that originate from the image intensifier were rejected. Every photon event detected incremented by one the memory location corresponding to its position. By cooling the photocathode the thermionic emission of electrons was reduced to such a level that the dark count originating from the intensifier was very low. With all other forms of detector noise rejected, the IPCS was essentially photon noise limited.

- It had improved resolution. Conventionally, image intensifiers were used to create an intensified image of a scene, this being an accumulation of many overlapping photon event scintillations. When photon counting, it is only the presence of an event that represents real information and so it is valid to record only the position of the centre of an event. The technique of ‘centroiding’ was used with the IPCS to find the centre of the events and it led to greatly improved resolution.
- The storage capacity of the IPCS was determined by the size of the computer memory but, in practical terms, it was unlimited. Photographic emulsions often became saturated for bright objects.
- It was possible to observe time varying effects with the IPCS by appropriately phasing several memory locations.
- The handling of the data was simple and convenient. Furthermore, it was possible to view accumulated data as the integration progressed so that astronomers were able decide when to stop an integration.
- The IPCS had exposure linearity which allowed accurate photometric calibration.
- The acceptance format was completely flexible, that is, a data acquisition window of almost any size could be used and placed anywhere in the detector’s area.

The IPCS had the following important performance characteristics.

- Resolution. This may be measured as the full width at half maximum (FWHM) of the image of a point source of light. When subtended back to the input of the photocathode this was $\sim 25\mu\text{m}$ for the IPCS.
- Detective quantum efficiency (DQE) – this was $\sim 14\%$, that is, 14% of incoming photons were detected by the IPCS. The DQE was primarily limited by the responsive quantum efficiency (RQE) of the first photocathode.
- Dynamic range. At the low count rate end this was determined by the dark count of the image intensifier which was $\sim 50 \text{ events cm}^{-2} \text{ s}^{-1}$. At the high count rate end the achieved count rates for point sources were $\sim 0.05 \text{ counts pix}^{-1} \text{ s}^{-1}$ on full format, 2048×512 pixels, and between 1 and 2 counts $\text{pix}^{-1} \text{ s}^{-1}$ on a smaller spectroscopic format, 2048×32 .

- Time Resolution. The IPCS could record a frame of data on a 2048×32 format every ~ 15 ms.

Common user versions of the IPCS were built for the Anglo-Australian Telescope (AAT) and the Isaac Newton Telescope (INT). Although the IPCS had significant advantages over conventional detectors it did have limitations.

1.2.2 The CCD-IPCS

The IPCS had a number of disadvantages.

- The maximum achievable count rate was low due to the slow frame rate of the Plumbicon – with slow frame rates the chance of spatial coincidence between events in the same frame is higher than with fast frame rates. When events are coincident it is difficult to distinguish them from a single event and so the two are counted as one and losses result.
- There were small drifts in the Plumbicon camera scan waveforms over a long period of time which meant that there was misregistration of events between integrations taken hours apart.
- The IPCS was physically large, heavy and power consumptive.

In order to overcome most of these deficiencies a new system was designed that still used an EMI intensifier but replaced the Plumbicon with a fast scanning CCD. The resulting photon counting detector was called the CCD-IPCS (Fordham et al., 1986), or IPCS-II. This innovation was anticipated to introduce the following improvements.

- High frame rates were possible with the CCD, which meant that the dynamic range could be increased by decreasing the number of coincidences within a frame. For example, on a spectroscopic format the IPCS had 2048×32 pixels with a frame time of 15ms whereas the CCD-IPCS would have a format of 3072×32 with a frame time of 1.6ms.
- The CCD would have electronic stability since the CCD pixels were physically fixed and thus stable with time.
- The CCD camera was physically smaller than the TV camera and required simple drive electronics which meant that it was less power consumptive.

Although the second and third of these advantages were seen, the anticipated increase in dynamic range was not. This was not due to the frame speed of the CCD but to the phosphor decay of the EMI image intensifier being used. A cross section of this intensifier (taken from Boksenberg and Burgess, 1972) is shown in figure 1.2. There were four

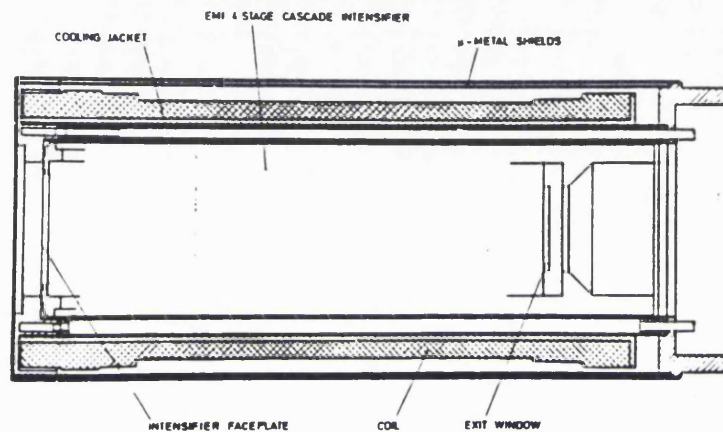


Figure 1.2: Cross section through the EMI four stage image intensifier

phosphors altogether in the intensifier and this meant that the final output phosphor decay was much longer than that of a single phosphor, being 3ms to 10%. On fast frame rates the phosphor decay was causing problems. Double counting was being seen with some events due to the same event being detected in contiguous frames. Although the event discriminator threshold could be raised to minimise the double counting, it meant that data was being lost due to the rejection of smaller events. Nevertheless, the detector was successfully developed and an engineered system was built for the 4.2m William Herschel Telescope (WHT).

The incorporation of a CCD in place of the TV camera required a substantially different system. A block diagram of the system is shown in figure 1.3. In particular, there were a number of important features built into the system.

- Because the CCD physically had a small number of pixels, the system would only have had a very small format unless the technique of interpolative centroiding had

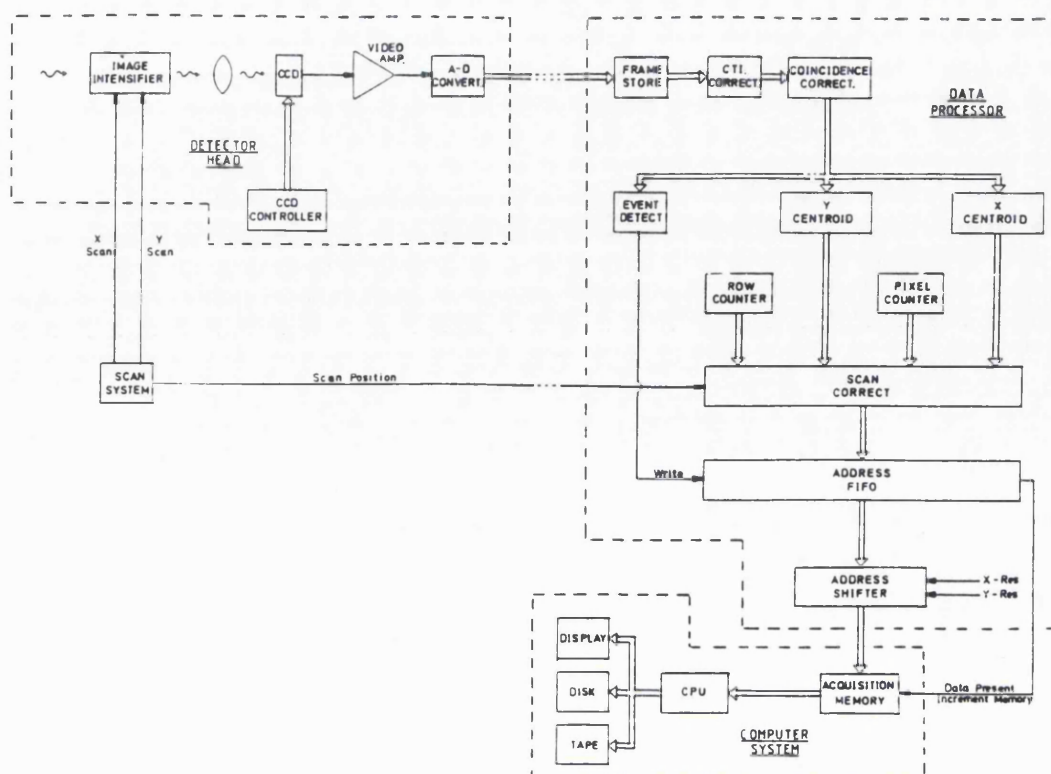


Figure 1.3: Block diagram of the CCD-IPCS

been employed. This technique, which is described in section 6.6.3, finds the position of the centre of an event by looking at the shape of the profile of photon events as they appear on the output phosphor. In the CCD-IPCS, electronics were incorporated into the system to centroid in both the X direction and the Y direction giving a format of 3072×2304.

- There were two sources of noise present in the system that required the incorporation of two sets of scan coils surrounding the EMI intensifier. By moving the primary photoelectrons in a controlled manner across the detector and then correcting for the movement within the processing electronics, a technique known as 'dithering', the two noises could be minimized. The two noise sources were
 - the granularity associated with the grains of the first of the four phosphors,
 - the fixed pattern noise that resulted from errors in the implementation of the interpolative centroiding technique.
- It was necessary to incorporate a frame subtraction circuit into the system. This process subtracted the previous frame's data away from the present frame's and this

required a frame store circuit. Frame subtraction was performed for two reasons,

- to remove the double counting caused by the phosphor decay,
- to remove the CCD dark current which provided a pedestal upon which the event data sat. This DC bias was variable across the CCD due to the inherent time differences associated with reading out different areas of the CCD.

Frame subtraction did limit the dynamic range, however, since losses occurred when two events arrived in contiguous frames in the same location.

- It was necessary to correct for the charge transfer inefficiency of the CCD. Small amounts of charge are left behind when CCD pixels are read out of the device by charge transfer, which is described in section 5.1. This changes the shape of the photon event as seen by the processing electronics and results in errors in the centroiding. By incorporating a charge transfer inefficiency (CTI) correction circuit this effect could be accounted for.
- A ‘partial scan’ facility was incorporated into the CCD camera electronics in order to achieve spectroscopic formats and reduce the frame time, thus increasing the dynamic range.

Important performance characteristics of the CCD-IPCS are

Resolution	25 μ m averaged over the field	
Quantum efficiency	14%	
Dynamic range	Spectroscopic format	7 counts pix ⁻¹ s ⁻¹
	Full format	1 count pix ⁻¹ s ⁻¹
Time resolution	1.6ms on a format of 3072 \times 32	

1.2.3 The Microchannel Plate Intensified CCD Image Photon Counting Detector (MIC-IPCS)

The MIC-IPCS (MIC) (e.g. Fordham et al., 1990, Fordham et al., 1991) was the next update in the UCL development of photon counting systems.

The deficiencies of the CCD-IPCS were associated with the EMI intensifier but, at about the time of the commissioning of the CCD-IPCS on the WHT, Imperial College

of Science, Technology and Medicine (ICSTM) were collaborating with the Royal Greenwich Observatory (RGO) and Instrument Technology Limited (ITL) in order to develop a microchannel plate (MCP) intensifier specifically designed for photon counting applications. Compared to the EMI intensifier, the MCP would provide higher dynamic range, be more compact and would have a lower power consumption. These advantages are discussed in detail in chapter 3. Essentially, the processing electronics developed for the CCD-IPCS were used with the new MCP intensifier and this system became the ground based MIC-IPCS (MIC).

There was another important innovation that distinguished MIC from the CCD-IPCS and that was the incorporation of fibre optic coupling from the intensifier to the CCD in place of lens coupling. The fibre optic taper provides a high transfer efficiency and compact optical coupling without the optical aberrations associated with lenses. This innovation is discussed in detail in chapter 4.

With the two new components discussed above the prototype MIC photon counting detector had become a very compact, lightweight system having the following performance characteristics,

Resolution	27 μ m
Quantum efficiency	14%
Dynamic range	Spectroscopic format 20–40 counts pix ⁻¹ s ⁻¹ Full format 2 counts pix ⁻¹ s ⁻¹
Time resolution	1.6ms on a format of 3072 \times 32

The following chapters describe the design, operation and performance of a version of MIC specifically designed for space applications.

Chapter 2

The Space Based MIC

The previous chapter described how 20 years of development in photon counting detectors at UCL led to the development of the ground based MIC system. Successive changes to the original IPCS have led to the development of a highly compact, lightweight system suitable not only for large telescope applications, but also for small telescopes and, in particular, space applications.

However, the ground based and space based environments are sufficiently different that it is not possible simply to use the ground based MIC for space applications. For example, there are very strict power and space constraints placed upon any space based system so that only the essential features of the ground based system can be included in a space version. Also, the performance characteristics required of a space system are not necessarily the same as those of a ground based system. In this respect new features may need to be included into a space system or some features of the ground based system may not be needed. Although the main features of the ground and space based systems are essentially the same, the number of differences between the two make them very distinct.

In particular, some differences between the ground based MIC and the space based MIC are:

- The ground based MIC uses data about an event contained in 5 pixels in order to perform centroiding. For the purposes of lowering power consumption, the space version of MIC uses 3 pixels of data.
- Also for the purposes of reducing power consumption, the processor uses high speed CMOS logic instead of the TTL used with the ground based MIC.

- The frame subtraction circuit is no longer needed because the CCD dark current, or DC bias, is removed in the CCD camera before it reaches the processing electronics.
- The charge transfer inefficiency correction circuit is no longer needed because the transfer efficiency of modern CCDs has become so high. Again, removing it lowers power consumption.

In addition to these changes outlined above, which are mainly associated with a reduction in power consumption, there are changes associated with the intended application which is described shortly. For example, only a portion of the CCD is used and, furthermore, a facility has been included for reading out only selected areas of the CCD. Other changes to the space system compared to the ground based system will become apparent when a description of the space system is given.

2.1 The Application of a Space Based System

The development of a space version of MIC was funded from two sources.

- The European Space Agency (ESA) provided funding for the development as part of the Boresight Faint Star Detector (BFSD) project. Here, the intended application of the system would be as an optical monitor (OM) operating at visible and UV wavelengths on a spacecraft where the primary telescopes operate at non-visible wavelengths. This would allow the same objects to be viewed simultaneously at different wavelengths.
- The Science and Engineering Research Council (SERC) provided funding for the development of a space version of MIC as the optical monitor on the X-ray Multi-mirror Mission (XMM) which is an ESA 'Horizon 2000' space observatory due for launch in 1998. Here, the primary telescopes operate at X-ray wavelengths. Figure 2.1 shows how the XMM satellite might look with the three primary X-ray telescopes clearly visible and the optical monitor as indicated.

The system described in the remaining chapters was designed to meet the requirements of the XMM project, although a system designed for the BFSD project would be very similar.

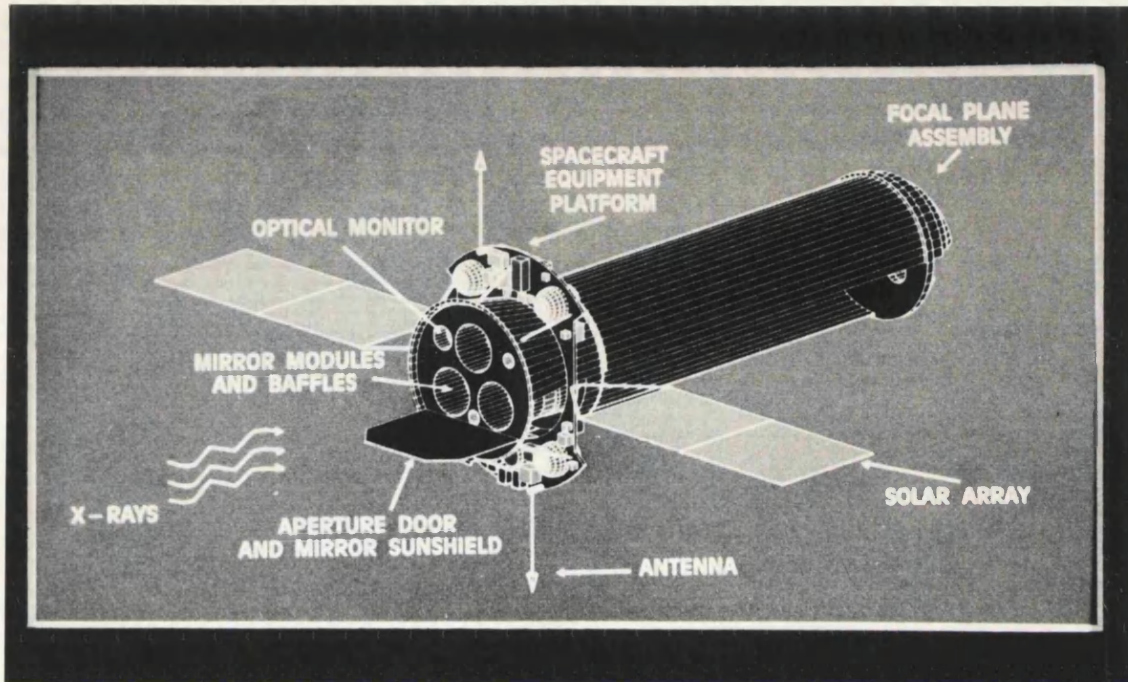


Figure 2.1: The XMM spacecraft showing the location of the optical monitor

2.2 Scientific Requirements of the XMM Optical Monitor

The XMM-OM will have two detectors, the red camera which is a CCD camera operating in the range 6500–10000Å and the blue camera which will be the photon counting detector operating in the range 1500–6500Å. The primary scientific requirements of the photon counting detector upon which the development of the XMM-MIC has been based (Mason, 1989) are summarised in table 2.1.

The *Zodiacal light background* will be $0.2 \text{ counts s}^{-1} \text{ arcsec}^{-2}$ and the detector must be able to detect the target objects in the presence of this background. The *3 σ detection limit* means that the detector must be able to detect a 24 magnitude star to 3σ above the background in 1000 seconds. This magnitude is equivalent to a flux of $0.04 \text{ counts s}^{-1} \text{ arcsec}^{-2}$ and represents the faint limit of the detector's performance. The *brightest star observable* should have a magnitude of 13.2 for white light – this is equivalent to $1000 \text{ counts s}^{-1} \text{ arcsec}^{-2}$ and represents the bright limit of the detector's performance. The *detector dark noise* should be no greater than $4 \times 10^{-4} \text{ counts s}^{-1} \text{ arcsec}^{-2}$. This requirement is not so important for a space version of MIC because the Zodiacal light

Table 2.1: Primary scientific requirements of the photon counting detector for XMM

	White Light (1500–6500Å)	B-band
Zodiacal light background ($\text{s}^{-1} \text{ arcsec}^{-2}$)	0.2	0.04
3σ detection limit in 1000 s (equiv. B mag.)	24.0	23.0
Brightest star observable (Mag.)	13.2	12.0
Detector dark count ($\text{s}^{-1} \text{ arcsec}^{-2}$)	4×10^{-4}	
Detector lifetime	10 years	

background will dominate the background signal in the detector. The *detector lifetime* should be ten years which means that it should still be operating after this period.

In addition to these requirements the detector should have a 16 arcmin field of view with a resolution of 1 arcsec. If one allows two pixels per resolution element then the detector characteristics shown in table 2.2 can be derived. Another requirement of

Table 2.2: Required characteristics of the XMM–MIC

Detector resolution	$< 20 \mu\text{m}$ FWHM
Pixel scale	1 pixel = 0.5 arcsec
Diameter of active area	25mm
Active detector area	18.94mm \times 18.94mm
No. of pixels in detector format	2048 \times 2048
Pixel size	9.24 μm

the XMM-MIC is a hardware ‘windowing’ facility whereby up to 16 user definable data acquisition windows can be placed within the 2048 \times 2048 detector format. This facility is required for two reasons.

- Memory limitations prevent data acquisition on the full 2048 \times 2048 format.
- To enable data acquisition on a number of ‘guide stars’ within the detector full format. These will be used for measurement of telescope tracking and roll errors which are inherent in the input image. For each integration with the detector the

data associated with the guide stars will be time sliced into 10–50 second exposures. The image of each guide star in each time slice is then software centroided and its position compared against a datum defined at the start of the integration thus giving a measure of image movement. These data are then fed to correction mechanisms in the red camera to maintain imaging resolution on that camera. This tracking facility is required as the imaging resolution of the XMM-OM will be higher than that of the X-ray telescope and hence of the spacecraft guidance system.

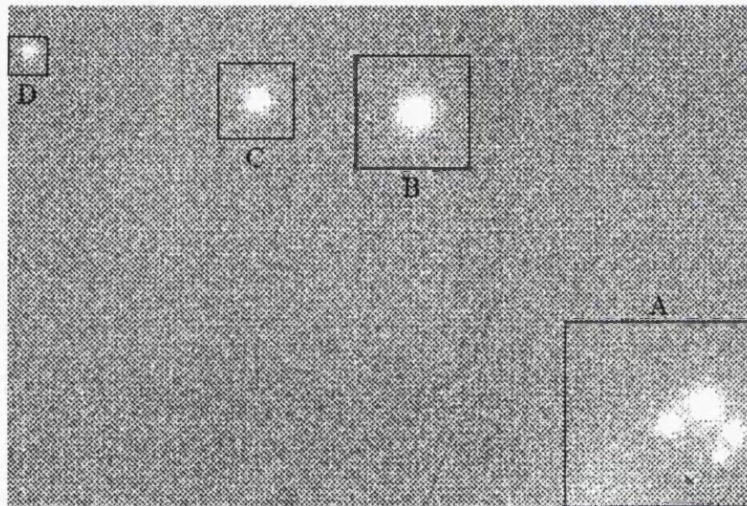


Figure 2.2: An example of the use of the windowing facility. Data are only acquired in the four windows A–D. Window A might be used to acquire scientific data while windows B–D would be used for star tracking

Up to 10 of the 16 windows will be used for guide star data acquisition leaving 6 free for scientific purposes. An example of the use of the windowing facility is shown in figure 2.2. Apart from being a requirement of the XMM-OM MIC, the windowing facility also provides a means of increasing the dynamic range of the detector. The way in which this is achieved will be discussed in section 5.3.2.

2.2.1 Overview of the XMM-MIC

To best meet the requirements and characteristics described in the previous section, the XMM-MIC was designed. A block diagram of this system is shown in figure 2.3 and a

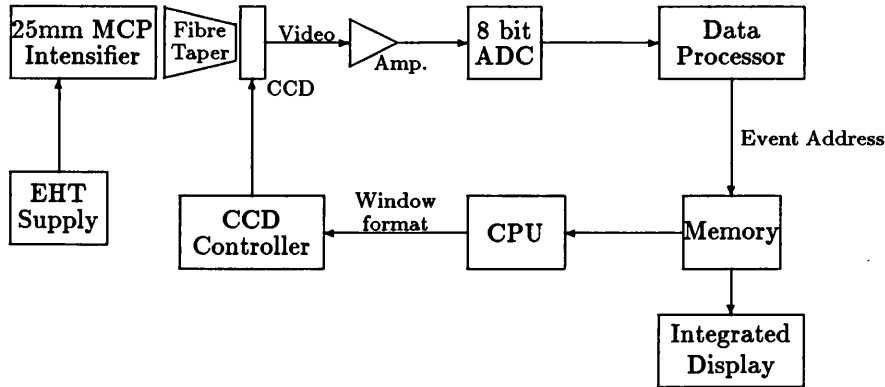


Figure 2.3: Block diagram of the XMM-MIC

photograph of the system is shown in figure 2.4. The photograph shows various components of the system depicted in figure 2.3, the detector head, comprising intensifier, fibre taper and the CCD with its associated electronics is mounted on the optical bench on the left with a real time display beneath it. To the right of that is the computer, comprising CPU and memory, with the image processing chassis, or data processor, on top of that. On the far right is the monitor that allows real time viewing of the integrated image.

The most crucial element of the system is a 25mm diameter microchannel plate (MCP) image intensifier. The intensifier converts an incoming photon to an electron, produces electron multiplication and then converts the resulting electron pulse into a light pulse, or photon event containing $\sim 10^7$ photons. An EHT power supply provides the potential differences within the tube necessary to produce the electron multiplication. The spatial position of the incoming photon is preserved during the intensification process so that the output is essentially an amplified image of the input.

The light output from the intensifier is coupled via a 3.06:1 reduction fibre optic taper to a fast scanning CCD. The CCD has a usable area of 256×256 pixels within its total array of 384×288 pixels. Photon events that are output from the image intensifier are captured within the imaging area of the CCD.

The raw video signal from the CCD is amplified, processed and digitized by an 8-bit 'flash' analog to digital converter (ADC) before being passed onto the image processing electronics. These processing electronics recognise photon events, centroid them to within 1/8th of a CCD pixel and define their address for storage in the detector memory. The

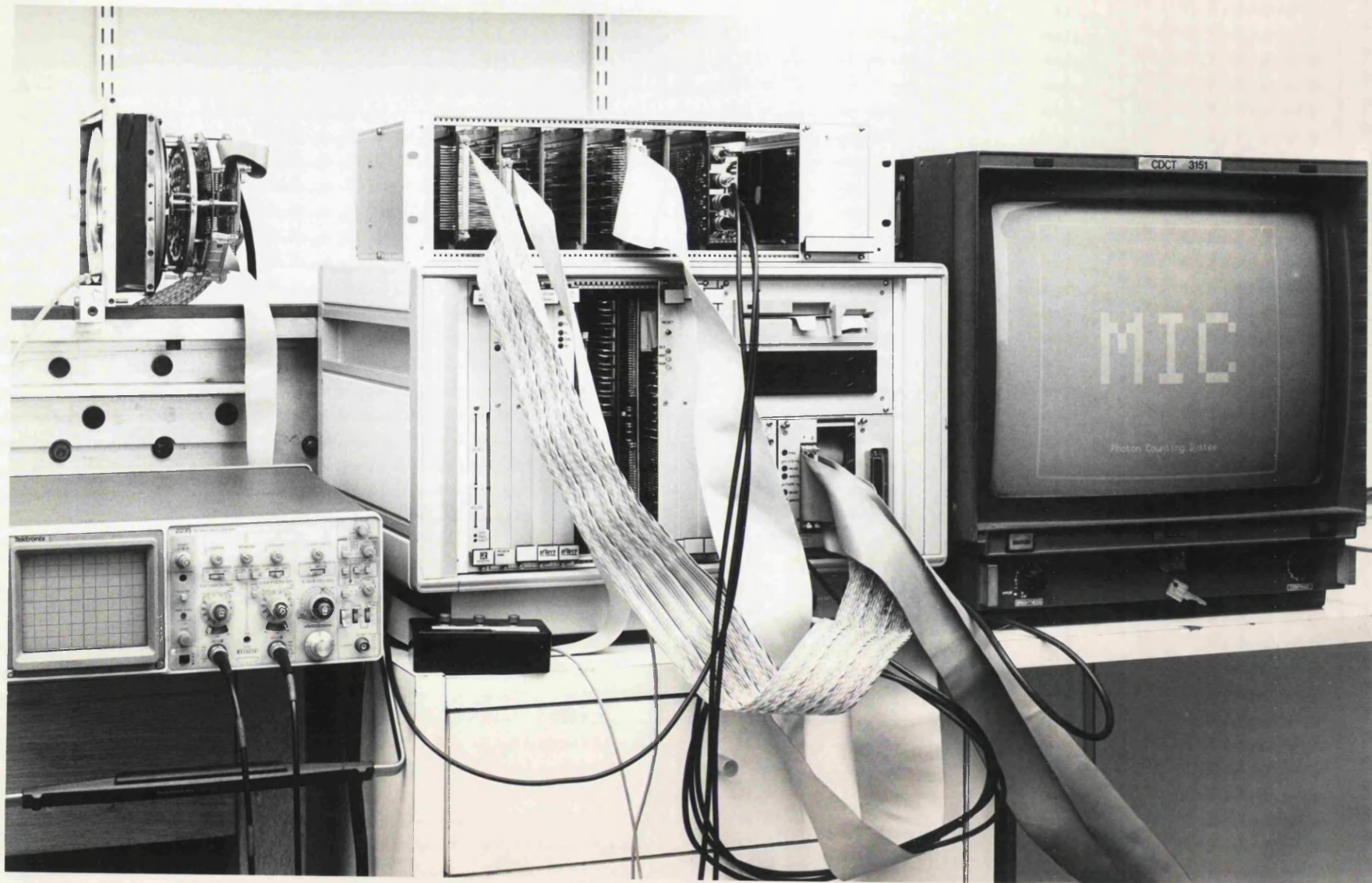


Figure 2.4: Photograph of the prototype MIC system

data contained in the memory are shown as an integrated display on a monitor so that the data may be viewed as they are coming in.

Software control of the system is provided by the CPU. In particular, the CPU calculates the window format to be used for a particular integration and loads the information into the CCD controller which controls the reading out of the CCD.

Two features of the system described above which are unique to the XMM-MIC are:

- The hardware windowing facility described in the previous section that is incorporated into the CCD controller to allow up to 16 user definable data acquisition windows to be placed within the 2048×2048 detector format
- A multiple event discriminator circuit incorporated into the processing electronics. This recognises when there is more than one event present at the same place on the CCD. This facility helps to increase the dynamic range of the detector by increasing the maximum detectable count rate. A full description of the circuit is given in section 6.5.

Also, in common with the ground based MIC, the XMM-MIC has a resolution select circuit that enables the maximum format to be 2048×2048 with $9\mu\text{m}$ pixels or 1024×1024 with $18\mu\text{m}$ pixels.

The following chapters describe the design and operation of the various components of the XMM-MIC. The overall performance characteristics of the detector to date are described in chapter 7.

Chapter 3

The Image Intensifier

3.1 Introduction

The image intensifier is the most crucial component of the system. It detects individual photons and intensifies them, producing a splash of photons at the output that is visible even to the naked eye. It retains the spatial position of the detected photons so that the output is essentially an intensified image of the input. Each splash of photons, or photon event, at the output is conveniently detected by a CCD reading out many frames per second.

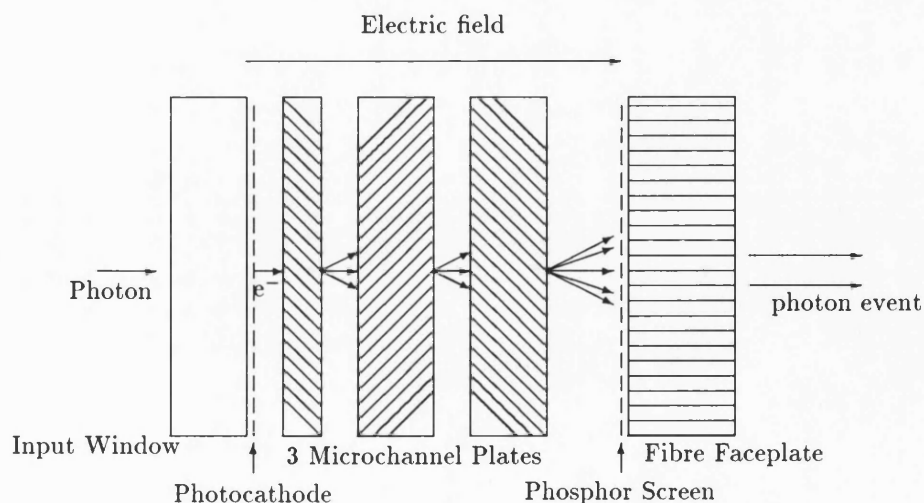


Figure 3.1: Schematic of the various stages of the MCP intensifier

The image intensifier used in MIC is a 25mm diameter microchannel plate (MCP) intensifier. A schematic of the various stages of the intensifier is shown in figure 3.1. Photons enter the intensifier via an input window and strike the photocathode. The photocathode emits an electron which is accelerated under the influence of an applied potential and enters a pore of the first of three microchannel plates arranged in a Z-configuration. Each microchannel plate is a wafer of semiconducting lead glass with $>10^6$ microscopic pores extending from the input face to the output face. These pores are capable of electron multiplication when a potential is applied across them. A cloud of $\sim 10^5$ electrons emerges from the last channel plate and is again accelerated by an applied potential to strike a phosphor screen. The phosphor emits around 10^7 photons, which constitute a photon event, and these emerge at the intensifier output via a fibre optic faceplate.

Previous UCL photon counting detectors, the IPCS (e.g. Boksenberg and Burgess, 1972) and the CCD-IPCS (Fordham et al., 1986), used an EMI magnetically focussed four stage image intensifier. These intensifiers had high gain and high resolution, as is ideally required of photon counters, but they also had a number of undesirable characteristics. However, towards the end of the CCD-IPCS development, Imperial College of Science, Technology and Medicine (ICSTM), The Royal Greenwich Observatory (RGO) and Instrument Technology Limited (ITL) had been developing an MCP intensifier specifically designed for photon counting applications. This intensifier offered the following advantages over the EMI intensifier.

- The EMI intensifier was limiting the system's dynamic range. The four stages within the intensifier, each with a phosphor screen, were resulting in a very long output phosphor persistence of around 3ms to 10%. On fast frame rates this was causing two problems. Firstly, with the CCD-IPCS, not enough charge was being accumulated on the CCD in single frames which meant that not many events were being detected. Secondly, on slower frame rates, a high percentage of detected events were being counted twice. This second effect required the implementation of a frame subtraction circuit to remove the second event but this then resulted in an additional source of coincidence loss whereby the second of two real events that arrived in the same place in contiguous frames was being lost.

The MCP intensifier had only one phosphor and its decay, $2\mu\text{s}$ to 10%, would elimi-

nate lost events and double counting since all the photons emitted by the phosphor would arrive at the CCD in the same frame. A gain in dynamic range would then be possible with the use of the MCP intensifier in place of the EMI.

- The EMI required an external magnetic focussing field which was provided by a coil surrounding the intensifier body. The coil consumed a lot of power, made the intensifier very bulky and heavy and dissipated a lot of heat which required a large portable cooler to be incorporated into the system. These factors effectively limited the detector's applications to large telescopes.

The MCP intensifier is physically very compact and requires no external magnetic fields which considerably reduces its size, power consumption and heat dissipation. This enables the detector to be used for applications where there are space and power constraints such as on small telescopes and in space.

- The magnetic focussing of the EMI intensifier introduced a characteristic distortion known as S-distortion which had to be removed by software during data reduction. The absence of a magnetic field in the MCP intensifier meant that there was no distortion in the image.
- The EMI intensifier, which was a commercially available product, was not standardly available with a choice of photocathode or input window which restricted its use to one wavelength range. The MCP intensifier is available with a choice of photocathodes, for example, S-20, bi-alkali or gallium arsenide, and a choice of input window, for example, magnesium fluoride, sapphire, Suprasil and ZKN7. With a suitable choice of photocathode and input window any number of wavelength ranges becomes possible.

In addition, the MCP intensifier has a desirable pulse height distribution which makes it superior to the EMI for photon counting.

UCL collaborated with ICSTM and ITL on the development of MIC, incorporating the MCP into the CCD camera system developed for the CCD-IPCS. The XMM-MIC is a compact, low power version of that original MIC. The intensifier has certain features that make it ideal for photon counting and for use in a space environment. The design and operation of the intensifier is discussed in the next section.

3.2 The Design and Operation of the Intensifier

The image intensifiers for the prototype XMM-MIC have been supplied by two sources. ITL have manufactured two and a third is in production at Delft Electronische Producten (DEP). The intensifiers have been designed as far as possible to meet the requirements for XMM shown in table 2.1 in terms of resolution, detective quantum efficiency (DQE), dark count and maximum count rate. Figure 3.2 shows a photograph of the intensifier;



Figure 3.2: The 25mm microchannel plate image intensifier

the small size of the intensifier is indicated by the centimetre scale. A schematic of a cross section of the intensifier incorporated into the detector head is shown in figure 3.3.

The various components of the intensifier shown in the figure and their functioning are described in the following sections.

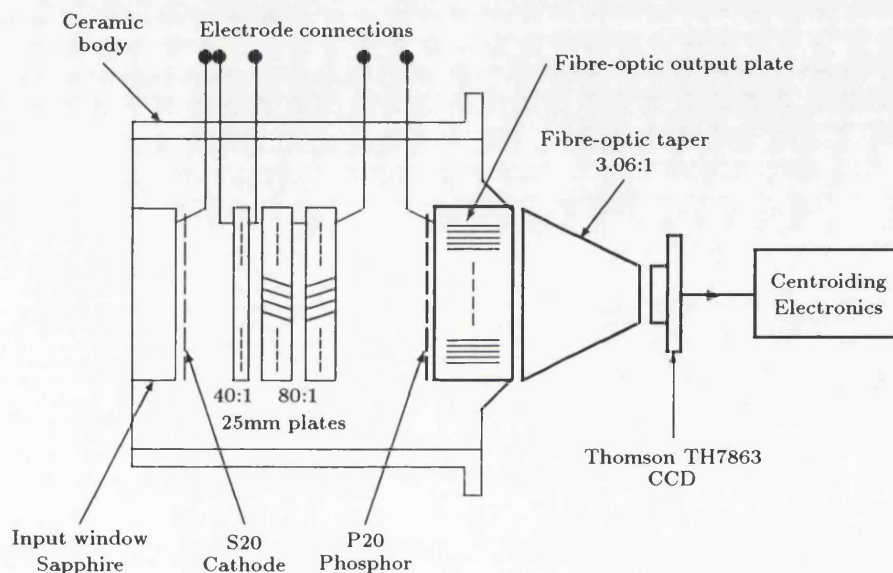


Figure 3.3: Schematic of a cross section of the intensifier incorporated into the detector head

3.2.1 The Input Window

The input window serves two purposes:

- Its inner surface has the photocathode deposited directly onto it.
- It is used to form a vacuum seal with the intensifier body.

Together with the photocathode the input window determines the spectral response of the intensifier. The choice of window material determines the transmission of the window to various wavelengths.

The required wavelength coverage of the detector, 1500–6500Å, limits the choice of materials to either sapphire or MgF_2 . The transmission of these two materials in this range is shown in figure 3.4. Although MgF_2 has higher transmission, both ITL and DEP report that the deposition of a photocathode onto this material presents problems. In particular, photocathodes deposited onto MgF_2 tend to have a spatially non-uniform

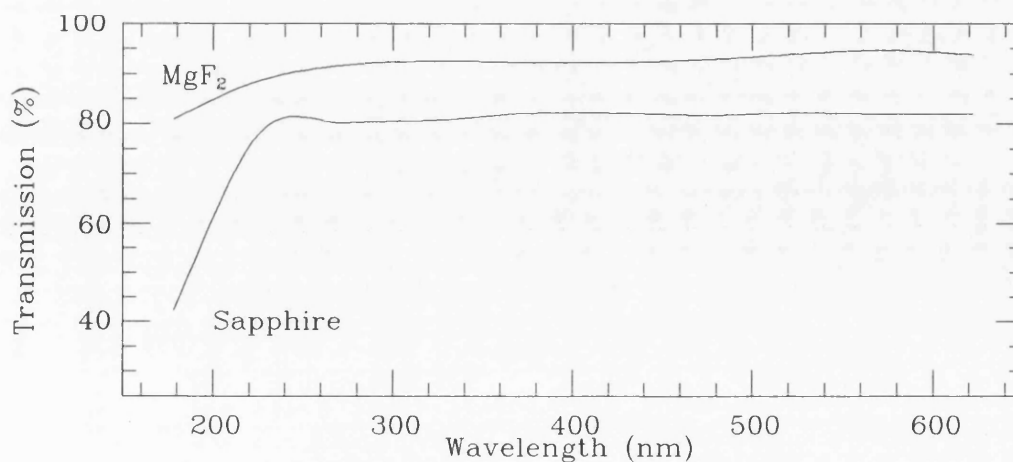


Figure 3.4: Transmission of MgF₂ and Sapphire windows

responsive quantum efficiency (RQE). The RQE of a photocathode is the percentage of incident photons that give rise to an emitted electron. A consequence of the difficulty of depositing photocathodes onto MgF₂ is that photocathodes deposited onto sapphire have consistently shown higher RQE, typically by 30%, compared to the same photocathode on MgF₂.

The two intensifiers supplied by ITL were manufactured with sapphire windows because they wished to widen their experience to include knowledge of deposition onto sapphire as well as on MgF₂. This also allows a comparison of photocathode response using two window types since data already exist for MgF₂. The ‘hot seal’ technique used by ITL initially was not useful for sapphire windows because the high thermal conductivity of sapphire resulted in a dry joint using an indium-tin solder. An indium-bismuth solder, which has a higher melting point, was used to solve the problem.

The sapphire windows have the undesirable characteristic that they fluoresce when bombarded by radiation, as discussed by Oldfield (1991). The contribution from radioactive isotopes within the window material and from cosmic rays leads to frequent ‘flashes’ seen at the intensifier output.

As yet, the choice of input window has not been decided and more data are needed before a final choice is made.

3.2.2 The Photocathode

The photocathode is an important component of the detector that determines the spectral response, quantum efficiency and, to some extent, the resolution of the detector. A photon incident on the photocathode causes it to emit an electron. The efficiency of the photocathode in converting photons into electrons is known as the responsive quantum efficiency (RQE) and is a measure of the percentage of photons giving rise to an emitted electron. The RQE of a photocathode is different for different photon energies, that is, for different wavelengths. The variation of RQE with wavelength determines the photocathode spectral response. The resolution of the system depends, amongst other things, upon the velocity and direction of the emitted electrons which in turn depends upon the photocathode material and incident photon energy.

Theory of Photocathode Operation

The theory of photocathode operation is essentially photoemission and may be understood by considering the band theory of solids. Csorba (1985) describes how photoemission may be considered to be a three stage process.

- In the first stage the incident photon raises the energy of an electron in the valence band by an amount E_{gap} , the forbidden gap energy, to the conduction band. The electron is then free to move about in the photocathode.
- The electron must then move through the lattice to the photocathode-vacuum interface.
- The electron has to overcome the surface potential barrier, or electron affinity, E_{aff} , to be able to escape into the vacuum.

The energy, E_{pho} , of a photon must be at least as large as the sum of the band gap and electron affinity, that is

$$E_{pho} \geq E_{gap} + E_{aff} \quad (3.1)$$

for photoemission to take place. After escape from the photocathode any excess energy the electron possesses becomes the kinetic energy of the electron.

Each of the three processes above has a loss mechanism associated with it which contributes to the lowering of the RQE at a given wavelength.

- If the photocathode is too thin then photons are not absorbed in the photocathode and light transmission leads to a loss of response, especially at longer wavelengths – a thicker photocathode will improve the red response.
- Electrons lose energy via collisions with lattice atoms as they move through the photocathode towards the vacuum. Very energetic electrons may give rise to electron-hole production. Electrons may lose so much energy that they are unable to overcome the electron affinity. It is transport losses that determine the cutoff of the spectral response in the blue – blue photons generate mobile electrons at a greater distance from the photocathode–vacuum interface and are thus more susceptible to transport losses.
- Electrons with insufficient energy cannot overcome the surface potential. This means that there is a cutoff at the long wavelength end of the photocathode response which is determined by

$$\frac{hc}{\lambda} = E_{aff} + E_{gap} \quad (3.2)$$

but even this assumes that there are no transport losses.

The photocathode spectral response, that is the RQE at different wavelengths, is determined by the three loss mechanisms described above.

For the XMM MIC the spectral response must stretch from 1500Å to 6500Å. The S-20 photocathode is the primary choice. This has good red response and can be made with > 20% RQE in the region 2000Å–4000Å. Real spectral response curves of S-20 photocathodes are given in section 7.2. The S-20 is a multialkali photocathode having the general composition (Na₂KSb)Cs. The cesium layer serves to lower the electron affinity of the photocathode and is responsible for the S-20 red response. It also means that the photocathode is able to emit an increased number of thermally generated electrons giving rise to a dark count which, for the MIC S-20, is typically 50 cm⁻²s⁻¹. This noise level is negligible compared to the Zodiacal light background contribution expected for XMM-OM.

The photocathode is very susceptible to surface contamination. Tubes are often found to have photocathode dead spots or field emission points. Every precaution must be taken in the manufacturing process to ensure that the photocathode is clean and the tube contains a minimum of contaminating gases and ions. The gradual degradation of the

photocathode due to the bombardment from ions in the tube is thought to be the primary limit to the lifetime of the tube. This is discussed more fully in section 3.3.3.

3.2.3 The Channel Plates

In the XMM MIC intensifier there are three channel plates arranged in a Z configuration and these produce the electron multiplication. There are numerous aspects of the design and operation of the channel plates which affect many performance characteristics of the system and these are discussed in the following sections.

The Front Gap and Proximity Focussing

Electrons leaving the photocathode have a range of emission energies both perpendicular and parallel to the surface of the photocathode. They are kept in the vicinity of the point at which they left the photocathode by the electric field across the front gap between the photocathode and the first channel plate. The electrons are quickly accelerated in a direction perpendicular to the surface of the photocathode so that they strike the first channel plate. The technique of spatial confinement by the application of an electric field is called proximity focussing.

It is the transverse emission energies of the emitted electrons that determines the extent to which they spread out from their point of emission. In addition, the field strength and size of the front gap also determine the transverse distance between the point of emission and the point of impact. As will be seen, these three factors contribute to limiting the resolution of the detector.

The Open Area Ratio and Detective Quantum Efficiency

The individual channels of each channel plate are arranged in a hexagonal close packed structure as shown in figure 3.5. The ratio of the area occupied by the open pores to the total area of the surface of the plate is known as the open area ratio (OAR). The OAR determines what proportion of the electrons emitted by the photocathode go down a channel and initiate an electron cascade. Thus, assuming that every single electron that enters a channel is detected, the OAR is equal to the proportion of electrons that are detected. Together with the RQE of the photocathode and the detection efficiency of

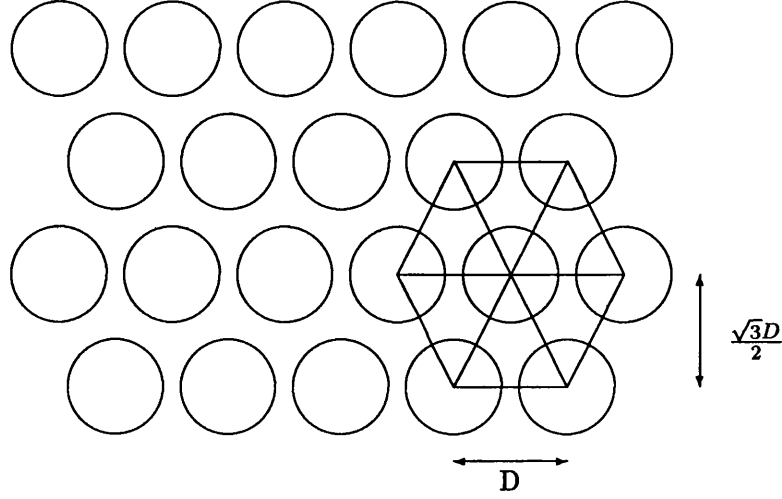


Figure 3.5: Hexagonal close packed structure of the MCP pores. The hexagon shown may be used to derive the open area ratio of the channel plates

the camera, which could be unity, the open area ratio determines the detective quantum efficiency (DQE) of the detector.

It is easy to derive an expression for the open area ratio by considering a hexagon as shown in figure 3.5. Within the hexagon the area occupied by the pores is

$$A_{pores} = \pi r^2 + 6\left(\frac{1}{3}\pi r^2\right) = 3\pi r^2 \quad (3.3)$$

whereas the total area can be found by considering the hexagon to be composed of six identical triangles each of base D and height $\sqrt{3}D/2$, where D is the channel centre to centre spacing and r is the channel radius. The open area ratio is then given by

$$\text{OAR} = \frac{2\pi}{\sqrt{3}}\left(\frac{r}{D}\right)^2 \quad (3.4)$$

Typical dimensions for the hexagonal structure might be $10\mu\text{m}$ diameter pores on $12\mu\text{m}$ centres which would give an open area ratio of 0.63. If the inputs to the channels are made to be funnel shaped then the open area ratio may be effectively increased to 0.75.

In previous MCP intensifier designs there were two plates arranged so that the bias angle of the channels was reversed in the second and the two formed a chevron. An ion barrier film was deposited on the front of the first channel plate to prevent the feedback of ions to the photocathode. This was found (Airy et al., 1990) to affect the energies of the electrons entering the pores which resulted in some of them not initiating a cascade so that

the DQE was reduced. In more recent designs the ion barrier film has been replaced by an extra channel plate that has been highly scrubbed to remove all impurities adsorbed on its surface. This acts as a barrier to ions desorbed from the surface of the other two channel plates and has been shown to be effective (Norton et al., 1991). The Z configuration of the channels also serves to prevent direct streaming of ions from the rest of the tube.

Electron Multiplication

The electron multiplication process is analogous to photoemission except that it is incident electrons, not photons, that increase the energy of the electrons in the bulk material sufficiently to produce secondary electron emission. Microchannel plates are fabricated from lead glass and the channel surfaces are treated in such a way as to make them semiconducting. Figure 3.6 shows a cross section through a typical channel of a MCP. At

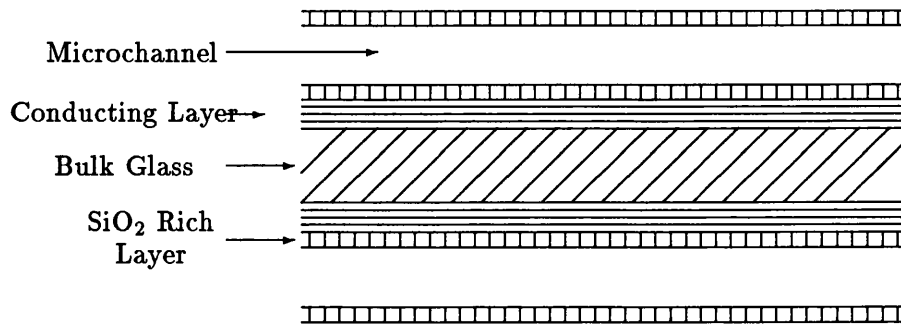


Figure 3.6: Cross section through a typical microchannel showing the various layers that make up the whole

the channel surface is a thin layer which is SiO_2 rich and provides the electrons necessary for secondary electron emission. Behind that is a layer of glass $\sim 600\text{\AA}$ thick which has been reduced in such a way as to precipitate lead ‘islands’. This conductive layer carries current via electron hopping between the islands and this replenishes the charge lost from secondary electron emission. The next layer is untreated glass which separates one channel from the next.

Electrons entering a pore need not necessarily initiate an electron cascade. The secondary electron emission coefficient, δ , is the average number of electrons emitted per

primary electron and it depends, amongst other things, upon the energy of the primary electrons. As the energy of an incident electron increases it is able to impart energy to more electrons in the solid and δ initially increases with energy. As the energy increases further more secondary electrons are generated further away from the surface. These electrons suffer more collisions and tend to lose their energy before they reach the surface so that δ decreases at higher energies. As long as δ is greater than one then, once the electron multiplication process is underway, it ought to be self sustaining. Also, the higher the δ the greater the probability that the primary electron entering the first plate will initiate electron multiplication. The photocathode to first channel plate voltage is such that δ is high for this primary electron and nearly all give rise to a cascade. The probability of the primary initiating a cascade is also increased by the 8° bias angle of the channels with respect to the electric field. This increases the velocity of the electron perpendicular to the channel wall and thereby increases the chance of emission.

Saturated Gain and the Pulse Height Distribution

MCPs may be operated in either d.c. mode or saturated mode. MIC MCPs are operated in a saturated gain mode which, as will be seen, is ideal for photon counting. In this mode of operation the voltages across the plates are such that the electron gain of each channel is high. As the size of the electron cloud increases down the channel, space charge effects induce positive wall charging which reduces the accelerating field and lowers the energy of the electrons. Eventually, as the size of the cloud increases, the energies of the electron collisions with the wall are reduced to such an extent that the secondary electron emission coefficient, δ , becomes one and the charge cloud no longer increases in size. At this point the gain is said to be saturated.

Operating the intensifier in this mode leads to a characteristic distribution of output pulse heights as seen on the CCD. An example of a saturated pulse height distribution is shown in figure 3.7. This distribution is ideal for photon counting because it separates noise from real photon events incident on the photocathode. This means that in the processing electronics a threshold can be set in the valley such that everything above it is counted as real and everything below it is discarded as noise. The EMI tube used in previous UCL photon counting detectors had a pulse height distribution far less suitable for photon counting. An example of this distribution is shown in figure 3.8 and one can

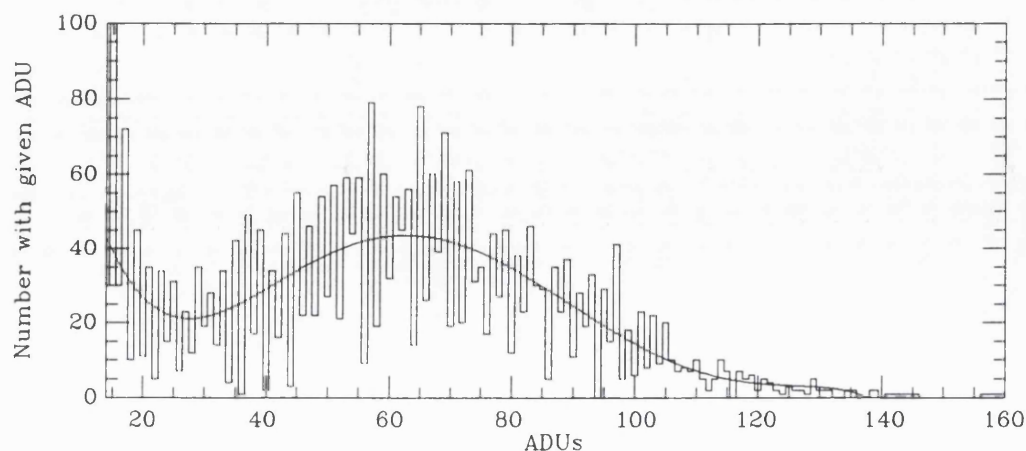


Figure 3.7: A typical saturated pulse height distribution obtained with the system; the arrival time of events within a CCD frame has broadened the distribution. The modulation in the data is due to A/D conversion errors introducing a bias to odd numbers.

see that the real events are indistinguishable from the noise. The pulse height distribution of the MCP in saturated mode constitutes another advantage of the MIC intensifier over the EMI.

The two rear channel plates in the MIC intensifier both have a length to diameter ratio of 80:1 and are operated with a high voltage across them to provide a high saturated gain. On the other hand, the front channel plate, which is not designed to give appreciable gain, has length to diameter ratio of 40:1 and acts primarily as an ion barrier.

At the end of the cascade process a large electron cloud emerges from the back of the rear channel plate.

3.2.4 The Phosphor Screen

The electron cloud emerging from the rear channel plate is proximity focussed by an accelerating electric field onto a phosphor screen which is deposited directly onto a fibre-optic output faceplate. The phosphor emits a large number of photons which are transmitted via the faceplate and fibre taper to the CCD.

The back gap and the voltage applied across it are important parameters. The centroiding technique described in section 6.6.3 requires that the output light pulse event on the CCD should have a particular width. The back gap is set such that when a convenient

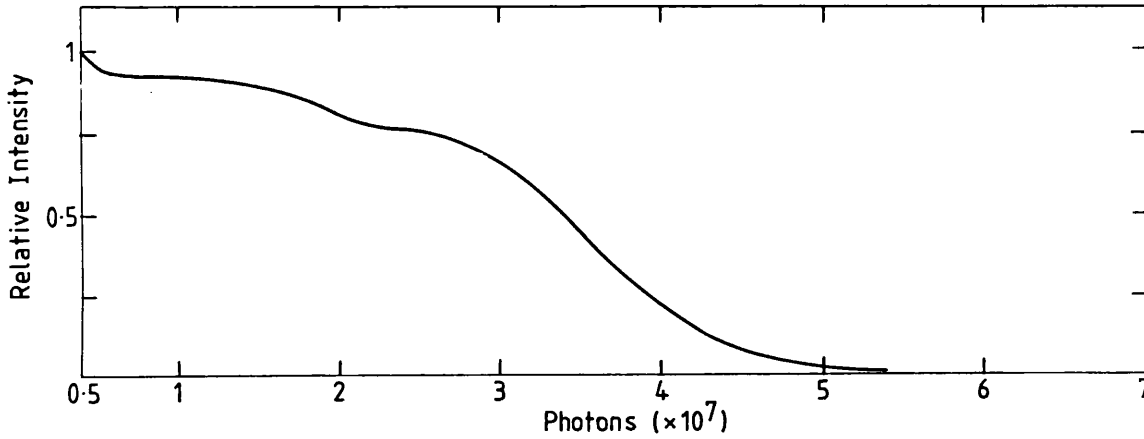


Figure 3.8: Typical EMI intensifier pulse height distribution showing that its shape is undesirable for photon counting. The units of the horizontal axis have been converted into photons at the output phosphor, that is, gain.

potential difference is applied across it the event width is optimized. The width can be altered by appropriately setting the voltage.

The basic process by which the phosphor converts the electron energy into photons is this: The incident electrons impart their energy to form localised excited states within the phosphor material. These excited states, or luminescent centres, are occupied by electrons in their ground state and unoccupied in their excited state. These excited states are unstable and are quickly occupied again by an electron whereupon energy is released in the form of a photon of characteristic energy. The energy of the P20 phosphor photons gives rise to a green light centred around 490nm which is well matched to the spectral sensitivity of the CCD. The spectral sensitivity of the CCD is discussed in section 5.3.

A thin layer of Aluminium about 1000\AA thick is deposited on the inside face of the phosphor. This provides a uniform potential across the phosphor, prevents light feedback and acts as a reflector for the screen, thus improving its efficiency.

Because there is only one phosphor in the MCP intensifier, the decay is fast, being $2\mu\text{s}$ to 10%, which eliminates the double counting problem experienced with the EMI intensifier. However, there are long, low level secondary components to the P-20 decay and these are discussed in section 3.3.4

3.2.5 Intensifier Housing

The MCPs are housed in a ceramic body and made vacuum tight using the ‘hot seal’ technique which allows the most compact geometry; when potted, the diameter of the intensifier is 52.7mm and the length is 26.2mm.

Electrode layers are deposited onto the surfaces of the channel plates and these extend to the mounting where metal rings are used to make connections with leads extending out of the intensifier. These leads are used to establish the potential differences across the various gaps.

Included in the intensifier mounting is a ring of material known as the getter which acts to absorb any residual gas atoms within the intensifier that are incident on it.

3.2.6 The Intensifier Power Supply

The potential differences required to operate the intensifier are provided by an EHT power supply via leads which extend into the intensifier housing to make contact with the appropriate electrodes.

Typical working voltages for the intensifier are

Across front gap:	300V
Across 1st plate:	1.2kV
Across 2nd and 3rd plates combined:	2.4kV
Across back gap:	4.5kV

Thus, 8.4kV is typically required across the intensifier. This is supplied by a Wallace HiVolt 30kV supply (VCS303-1), the various voltages being generated via a divider chain. These voltages can drift from their initial setting and the consequence of this is discussed in section 7.6.1.

For a space qualifiable version of MIC the primary requirement of the supply would be minimal drift of the various voltages. Additionally, two other facilities would need to be incorporated:

- Remote programming of the separate electrode voltages. This would allow alteration of various characteristics of the output pulses.
- An automatic cutout on the photocathode to MCP voltage if the input is too bright.

3.3 Limitations on the Performance of the Intensifier

The performance of the intensifier determines many aspects of the system performance, both wholly and in combination with other components of the detector. For example, the fundamental limiting resolution and DQE of the detector are determined almost entirely by parameters associated with the intensifier whereas the dynamic range is determined mainly by properties of the CCD but also to some extent by intensifier characteristics.

The required performance characteristics of the intensifier are derived from the performance requirements of the detector as a whole. The XMM-OM requirements of the blue detector that are affected by the properties of the intensifier were listed in table 2.1. The intensifier affects all the requirements of the detector to some extent.

In addition to the performance requirements of the detector, there are other constraints which affect the design of the detector. These and the limitations on the performance with respect to the requirements of table 2.1 will be discussed in the following sections.

3.3.1 Resolution

The resolution of the system may be measured in two ways. A commonly used unit for resolution measurements is line pairs per millimetre (lp/mm), that is, the number of pairs of black and white lines per millimetre that may be resolved by the detector. The more lines there are per millimetre, the less well resolved the lines become – the maximum number that may be resolved is the limiting resolution. Alternatively, one may quote the full width at half maximum (FWHM) of the profile of a point source as seen by the system. Although the input is a delta function, the output is spread out into a characteristic distribution about the position of the input. The FWHM of this distribution is a measure of the resolution of the the detector. The reciprocal of the resolution in lp/mm is the FWHM in mm of the image of a point.

A number of factors determine the resolution of the system:

1. The spread across the front gap of the primary electrons emanating from the photocathode,
2. The centre to centre spacing of the pores of the front channel plate,
3. The resolution of the centroiding electronics,

4. If the input source is of finite size then the FWHM of the source will contribute to the FWHM of the image.

The combined effect is simply the square root of the sum of the squares of each of the above contributions, that is

$$\text{FWHM} = \sqrt{\text{Gap}^2 + \text{Pores}^2 + \text{Electronics}^2 + \text{Source}^2} \quad (3.5)$$

If the intensifier has been manufactured correctly then accurate centroiding will be possible and the contribution from the resolution of the centroiding electronics will be small compared to the contribution from the first two. The last factor is merely a property of the source. Therefore, the intensifier may be considered as the source of the fundamental limiting resolution of the detector.

Of the two contributions to the resolution from the intensifier, the spread of the primary electrons has the greater effect. The spread of the primary electrons depends upon three parameters.

- The transverse emission energy, ϵ , of the primary electrons. This is the kinetic energy they possess due to the component of their velocity parallel to the photocathode.
- The potential difference, V , that exists between the photocathode and the front channel plate. The higher the potential the faster the electrons will be accelerated in a direction perpendicular to the photocathode and the less they will spread out from their point of emission.
- The size, L , of the gap between the photocathode and the front plate. The larger the gap the more the electrons will be able to spread out from their point of emission.

The limiting resolution associated with proximity focussing is usually defined as the spatial frequency at which the modulation transfer function (MTF) is 3%. The MTF is a special function used for measuring the resolution of an image tube and is the ratio of the contrast in the image to that in the object. Eberhardt (1977) derives a formula for the limiting resolution using this definition and by assuming that the primary electrons have a Maxwellian emission energy distribution. He finds that the limiting resolution, R , is given by

$$R = \sqrt{\frac{\ln 0.03}{4\pi^2}} \frac{1}{L} \left(\frac{V}{\epsilon}\right)^{\frac{1}{2}} \quad (3.6)$$

Alternatively, the FWHM of a point source would be given by

$$FWHM = 3.35L\left(\frac{\epsilon}{V}\right)^{\frac{1}{2}} \quad (3.7)$$

Eberhardt also gives a table of measured radial emission energies of photoelectrons from a multialkali photocathode. Here, ϵ ranges from 0.3eV in the UV to 0.05eV in the red, although the actual value depends on the composition of the photocathode. At a mid-spectrum 500nm the value of ϵ is ~ 0.1 eV. With the present MIC intensifiers the front gap is $300\mu\text{m}$ and typically 300V are applied across it. Using these values in equation 3.7 and inserting the result into equation 3.5 gives

$$\text{Theoretical Limiting Resolution} = 21.1\mu\text{m} \quad (3.8)$$

where the electronic centroiding resolution has been assumed to be $4\mu\text{m}$ (see section 7.4) and the centre to centre spacing in the present intensifiers is $12\mu\text{m}$. With red light the limiting resolution is $14.9\mu\text{m}$ and in the UV it is $36.5\mu\text{m}$.

Tests were carried out to find out the actual, as opposed to theoretical, resolution of the detector and the results are discussed in section 7.4.

3.3.2 Detective Quantum Efficiency

Properties of the intensifier almost entirely determine the detective quantum efficiency (DQE) of the detector. The DQE is a measure of the overall efficiency of the detector in detecting photon events. DQE is usually quoted as a percentage and may be considered as the percentage of incident photons that are detected by the system and stored in the memory.

The XMM MIC must be able to detect a 24.5 magnitude star at the 3σ level in 1000 seconds and this requires a DQE of $>20\%$ in the blue. The DQE depends on three factors:

- The RQE of the photocathode. This is the percentage of incident photons that give rise to an electron. It is wavelength and photocathode composition dependent. The choice of photocathode for XMM is an S-20 which will enable detection up to the required 6500\AA . These have been manufactured with $> 25\%$ RQE in the blue.
- The open area ratio of the front channel plate as given by equation 3.4. For the XMM MIC tube the pores have a diameter of $10\mu\text{m}$ and their centres are separated by $12\mu\text{m}$ which gives an open area ratio of 63% .

- The efficiency of the camera. This depends upon the quality of the pulse height distribution and the setting of the photon counting threshold. If the pulse height distribution clearly separates the events from the noise then the photon counting threshold is easily set and the efficiency of the electronics becomes 100%.

The expression for the DQE is

$$\text{DQE} = \text{RQE} \times \text{Open area ratio} \times \text{Camera Efficiency} \quad (3.9)$$

which for an RQE of 25%, an open area ratio of 63% and a camera efficiency of 100% could be as high as 15–16%, rising to 18–19% with funneled inputs to the pores of the front channel plate. The above result assumes that every electron that enters a pore of the front plate gives rise to an event on the output phosphor. The validity of this was discussed in section 3.2.3.

The results of DQE measurements are discussed in section 7.5.

3.3.3 Lifetime

The intensifier is believed to be the main lifetime limiting component of the detector. It is more susceptible to contamination and subsequent performance degradation than any other component of the detector.

During operation of the tube a large number of atoms are desorbed from the surfaces of the MCPs. It is the rise in the number of gas atoms within the tube that gives rise to a number of life limiting processes. There are three processes that are most likely to limit the useful lifetime of the tube:

- A reduction in the gain of the MCPs,
- A reduction in the quantum efficiency of the photocathode,
- A rise in pressure leading to an increased number of ion events.

Of these processes, the second is thought to be the most serious. The projected XMM mission lifetime is ten years and the intensifier should still be usefully operating after this period. All the above processes depend on the outgassing from the MCP surfaces so, with respect to the projected ten year lifetime of the tube, this is an important process to understand.

Scrubbing

Before the photocathode can be sealed to the rest of the intensifier, the MCPs must undergo a scrubbing procedure to remove most of the gas atoms adsorbed to the surface of the glass. If this were not done then during tube operation a large number of gas atoms would be released and may react with the photocathode. The quantum efficiency of the photocathode would quickly degrade and the tube lifetime would be short.

Scrubbing involves bombarding the MCPs under operation with either electrons or UV. Electron collisions with the walls of the MCP release ions, atoms and radicals adhering to the surface. Scrubbing is terminated after typically ~ 2 coulombs of charge have passed through the plates. This is a value that is found by observing when the rate of generation of gas from the MCP has reached a very small value.

Norton et al. (1988) describe the scrubbing process used when developing a 40mm intensifier for the ground based MIC system. They note that the principal gases evolved during the scrub are, in descending order of partial pressure, hydrogen, methane, carbon monoxide, water and carbon dioxide. Now, although most of the above species are removed during the scrubbing process, this cannot continue indefinitely in order to remove 100% of the atoms and ions. Excessive scrubbing begins to remove significant amounts of other materials from the glass and this leads to a rapid and unrecoverable fall in gain. Therefore, since not all the adsorbed species are removed it can be expected that further outgassing will take place during normal tube operation. It is this further outgassing that gives rise to the life limiting processes outlined previously and it is this that needs to be evaluated when considering the lifetime of the tube.

Life Limiting Processes

Gain Degradation. It is a well known phenomenon that the gain of MCP stacks is decreased during operation due to the gradual desorption of gas atoms from the surface of the MCP glass. The process is modelled by assuming that an 'electron source population' (Sandel et al., 1977) is gradually removed from the active layers of the glass. Authinarayanan and Dudding (1976) propose that an electropositive material adsorbed at the MCP surface reduces the secondary electron escape probability by reducing the surface barrier potential. Thus, removing these materials would increase this potential and reduce the secondary electron yield resulting in a drop in gain.

The amount of gain degradation depends on the history of the tube, that is, on the amount of charge that has already been extracted from the tube. Norton et al. (1988) describe how the gain of their tubes decreases during the scrubbing procedure of tube processing. They report how the initial drop in gain is rapid but that after a total charge of $\sim 1000\text{mC}$ has been extracted from the plates the gain drops only very slowly. It is in this slow gain drop 'plateau' region that the tube is sealed off. They note that the gain is still appreciable and that the pulse height distribution is still good. They go on also to say that at some much larger value of extracted charge the gain drops irreversibly due to the migration of positive alkali metal ions into the bulk of the MCP glass.

Fraser (1987) points out that the lifetime of MCPs, in terms of retaining the initial gain, can be extended by several orders of magnitude if the voltage across the plates is incremented at intervals. Thus, so long as the tube is sealed off in the plateau region of the gain curve, the gain degradation should not be a problem as the voltages across the plates can be incremented in order to restore the gain.

Degradation of the Photocathode Quantum Efficiency. By its nature the photocathode is a very reactive surface. It is susceptible to contamination from atoms and ions that exist in the intensifier tube and this results in a loss of sensitivity. Atoms may exist in the tube and migrate to the photocathode where they may make a chemical reaction. Ions backstream and may be readsorbed or they may reach the photocathode where their reaction is more severe due to the acceleration they receive in the proximity focus field that exists between the photocathode and first channel plate.

Csorba (1985) showed that the S-20 photocathode consists primarily of a bialkali photoemissive surface with an additional cesium monolayer that extends the long wavelength range of the photocathode. Any contamination of this layer will reduce the red sensitivity of the S-20

Decker (1969) investigated relative reactivity of the S-20 photocathode to various atomic species. He found that the photocathode could be exposed to high partial pressures of $1\text{--}5 \times 10^{-4}$ torr of hydrogen, nitrogen, methane and oxygen before significant decay of sensitivity was noted and that the sensitivity returned. However, exposure to carbon dioxide, carbon monoxide, chlorine and water vapour at much lower partial pressures from 2×10^{-6} to 5×10^{-8} resulted in an unrecoverable loss in sensitivity. Decker attributes

water's considerable effect as being due to the reactivity of the OH radical.

Norton et al (1988) report the partial pressure of various atoms in scrubbed tubes. After a period of scrubbing the principal gas species evolved were largely hydrogen, but also methane, carbon dioxide and water vapour. The partial pressure of hydrogen was an order of magnitude higher than that of any other atomic species. It is expected that the same gases would be released during normal operation of the tube. Since the MIC tubes are made by the same company as is used by Norton it can also be expected that these would be the main gases desorbed from the MIC MCPs during operational life of the tube. The extent of photocathode degradation depends upon the species reacting with it and on their outgassing rate from the channel plates. Norton (1988) states that at the end of the scrub process, the outgassing rates of species such as water, methane and carbon monoxide are reduced to $\sim 7.5 \times 10^{-19}$ torr cm⁻³ s⁻¹. At that rate, even if the illumination during normal operation was as intense as that during scrub, the pressure of these gases at the end of the mission lifetime would be 6×10^{-11} torr. This is three orders of magnitude lower than the pressure reported by Decker that resulted in loss in sensitivity.

Rise in Pressure. As ions are desorbed from the surface of the plates, some may be neutralised and thus contribute to a general rise in pressure within the tube. The rate of rise in pressure depends also on the pumping speed of the getter – this is discussed again shortly. If the pressure reaches $\sim 10^{-5}$ torr then the presence of such a large number of atoms in the tubes leads to a lot of ion events; atoms within the tube are ionised by the accelerated electrons and they backstream directly to the photocathode where they may chemically sputter its surface. An increase in ion events may lead to failure of the tube.

Lifetests

The processes that limit the lifetime of a tube are complicated. For each process there are numerous factors to take into account when estimating the likely performance degradation. Moreover, the processes are, as yet, not fully understood. In order to evaluate the lifetime of the tubes reliably it is necessary to carry out tests. The purpose of the tests would not only be to obtain life expectancies for the tubes but to identify and understand the important processes so that modifications to tube design could be made. These tests will be carried out on the MIC tubes when the design has been finalised and the tubes have

been manufactured.

Boskma (1990) describes accelerated lifetests done on single stack intensifiers. The photocathode generally showed only a 2–25% wavelength dependent decrease in sensitivity during the tests. He makes the important point that when the light intensity was increased by an order of magnitude and the tests carried out for 1/10th of the time, the photocathodes showed exactly the same response, that is, increasing the light level and speeding up the test led to the same performance degradation. This suggests that an accelerated life test is a valid test for evaluating the tube lifetime.

Norton et al., (1991) report the result of accelerated lifetests done on 40mm tubes of a very similar design to the 25mm XMM MIC tubes. They note that the photocathode sensitivity at peak response was reduced by approximately 5%. They also note that the red sensitivity showed significant decay up to 50%. This is expected as the cesium layer, which is responsible for the red response, is very susceptible to contamination.

The effects of other features of the tube design could be evaluated during the tests. For example, the composition and partial pressure of the various constituents of the desorbed gas in the tube will determine the loss in sensitivity. The pressures will depend on the outgassing rate of the channel plates compared to the pumping speed of the getter. The getter is a ring of activated titanium in the tube that absorbs active species. Without the getter the pressure in the tube would rise more quickly. The influence of the getter on tube lifetime could be evaluated during lifetests. Also, Boskma mentions that tubes with an ion barrier film showed no degradation of photocathode sensitivity over the entire life test. He goes on to suggest that the use of a highly scrubbed extra plate, such as with the MIC tubes, may have the same effect as an ion barrier film. The validity of this approach to protecting the photocathode could be assessed during an accelerated life test. The results of Norton et al., (1991) already give some insight into the efficiency of the extra plate in stopping ion backstreaming. Another way of improving the lifetime of the tube, suggests Boskma, is to gate the tube off when it is not operating. This would temporarily halt the outgassing process and also the ion backstreaming process which directly affects the photocathode. An assessment could be made during life tests of the validity of this approach.

3.3.4 Dynamic Range

The dynamic range of the system is the range of input count rates over which the detector is able to accurately record the number of incident photons. For a linear detector the dynamic range curve, that is, a curve of counts in versus counts out, is a straight line of gradient one. With MIC, the dynamic range curve becomes non-linear at high count rates – the detector records fewer counts than are actually input. However, it does not matter that the dynamic range curve is non-linear so long as it is possible to calibrate an input source brightness using the curve.

Three intensifier properties affect the characteristics of the dynamic range curve

- **Dark count.** The dark count of the intensifier effectively sets the lower limit to the count rate that can be detected with MIC. With the present intensifiers this is around $50 \text{ counts cm}^{-2} \text{ s}^{-1}$.
- **Phosphor decay.** This affects the whole of the dynamic range curve. Although the primary decay of the phosphor is $2\mu\text{s}$ to 10%, longer residual phosphorescence causes some double counting. This effectively increases the linearity of the dynamic range curve.
- **Channel recovery.** When a pore of the MCP is fired it takes a finite time for the pore to recover ready for another event. Events arriving in this time may not be recorded. The result is that at high count rates the effects of channel recovery lead to further departure from a linear dynamic range curve.

Of the above, the channel recovery effects are the most serious and difficult to quantify.

Dark Count

The dark count entirely determines the lower limit of the detector's dynamic range characteristics since the noise due to the electronics is negligible. The dark noise of the S-20 photocathode at the expected operating temperature is $\sim 50 \text{ counts cm}^{-2} \text{ s}^{-1}$. However this is dominated by noise generated by scintillations in the sapphire input window. It is expected that any dark noise will be negligible compared to the contribution from the Zodiacal light background which is expected to be $\sim 60\text{k counts s}^{-1} \text{ cm}^{-2}$ in white light.

Phosphor Decay

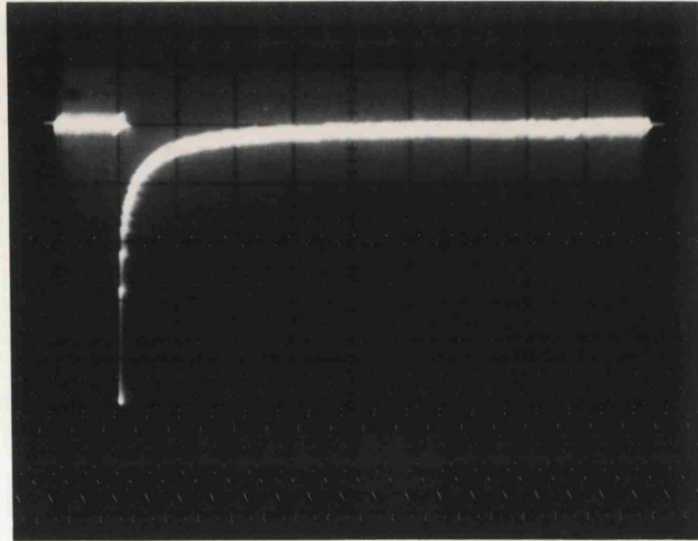


Figure 3.9: Oscilloscope trace of the phosphor decay characteristics of the P-20 phosphor of the intensifier. Each division is along the horizontal axis is $2\mu\text{s}$.

As discussed in section 3.1, one of the advantages of the MCP intensifier over the EMI intensifier is the much shorter decay of the MCP intensifier output phosphor. This was measured by T. Norton of ICSTM as being $2\mu\text{s}$ to 10% as shown in figure 3.9, which shows an oscilloscope trace of the decay. This decay time is far too short for any double counting to occur. Even for events occurring right at the end of a CCD frame, the short time between the end of one frame and the start of the next, which is about 0.1ms, ensures that the phosphor output has completely decayed. However, the decay of the phosphor has been found to be more complex.

A computer simulation was made (Oldfield and Fordham, 1991) on the effect of CCD frame rate on the dynamic range curve of the detector for point sources. These simulations predicted that with a full CCD frame read out there was a 10% loss in linearity at an input count rate of $\sim 15\text{Hz}$ and that when 32 rows were read out the 10% loss occurred at about 40Hz. However, dynamic range tests on the detector showed that the 10% point for the respective count rates occurred at 25Hz and 200Hz which was far greater than predicted.

This discrepancy between the predicted and actual count rate can be explained if one

assumes that some events are being counted twice, that is, that there is double counting, and that events occurring in the CCD frame transfer period are being counted. One can discount events being counted twice in the same frame as the processing hardware will not allow this. Therefore, the additional events must be counted in frames where there are actually no real data. This implies a storage mechanism for which there are only two possibilities:

- The CCD could leave a large amount of charge behind during readout. However, this would require a very large charge transfer inefficiency that would have manifested itself quite obviously in previous detector trials.
- The phosphor. The hypothesis is that, in addition to the primary decay of $2\mu\text{s}$ to 10%, there are longer low level secondary components to the decay that would not have been picked up in the oscilloscope trace of figure 3.9. When integrated over a frame period these longer components would accumulate enough charge on the CCD to appear to the processing electronics as an event.

The hypothesis was tested by an experiment designed to measure the phosphor decay characteristics of the ground based MIC detector.

Modelling the MCP Phosphor Decay. The ground based MIC system was set up so that a light emitting diode (LED) was flashed for a short duration of $40\mu\text{s}$ in every other frame. In the flash frame, A, photon events were recorded in the form of charge on the CCD. In the dark frame, B, in which there were no photon events, smaller amounts of charge were seen to have accumulated in the same place as real photon events in frame A. These residual ‘events’ are those that lead to double counting and are caused by the longer secondary decay components of the P20 phosphor. A series of two consecutive frames were analysed by the computer to find correlations between real events in frame A and residual events in frame B. Having found a correlation the computer used a 3×3 array of pixels around the event and calculated the energy, E_b , in frame B as a fraction of the energy in both frames. Assuming that the energy in each frame is entirely due to the phosphor emissions then the calculated ratio, E , is the ratio of the energy of the residual event to the energy of both, that is

$$E = \frac{E_b}{E_a + E_b} \quad (3.10)$$

where E_a is the energy of the real event in frame A. An average of this ratio was found for 200 correlations.

The energy of the residual depends on the time of arrival, t , of the photon event with respect to the end of frame A since the extent to which the secondary components will have decayed before the start of frame B will be different for different t . Photon events were simultaneous with the LED flash so, by performing the correlations with N different known flash times, it was possible to obtain a real curve of E versus t

After the end of frame A there is a frame transfer period t_t during which the entire frame is transferred to the storage area. Any photon events arriving in this period will not be counted and nor will their residuals contribute to the mean residual energy since they will not be correlated with events in frame A. Frame B begins a time t_t after the end of frame A and ends one frame period, t_f , after it. The relationship between t , t_t and t_f is shown schematically in figure 3.10. In order to deduce the decay constants

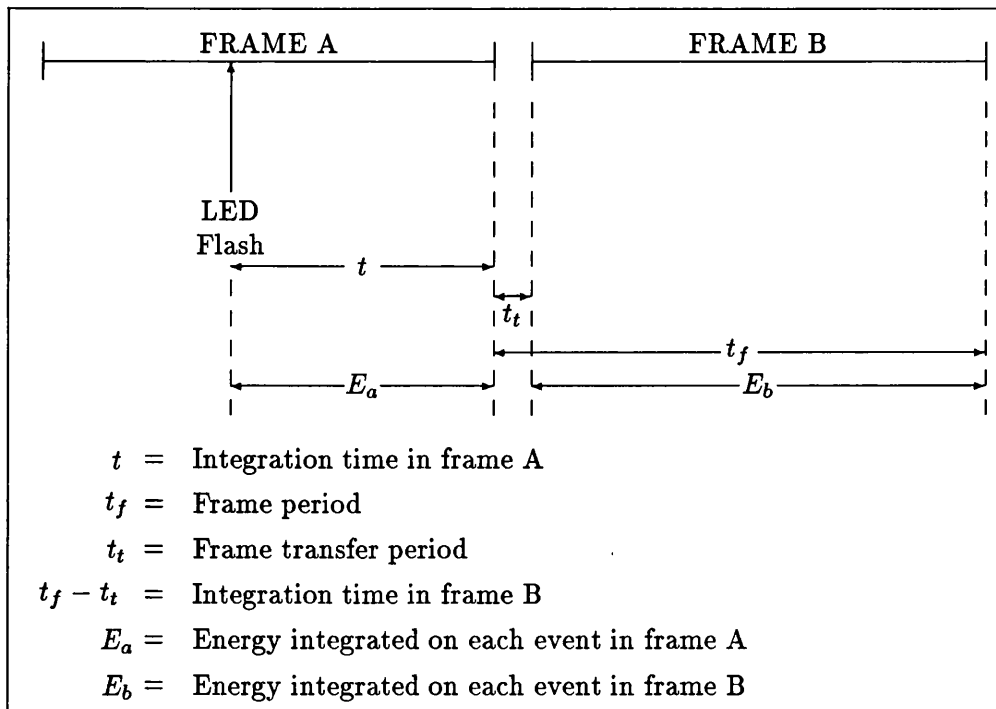


Figure 3.10: The relationship between t , t_t and t_f and between E_a and E_b .

and relative intensities of the secondary components it is necessary to consider the area under the decay curves. Williams and Eyring (1947) describe how the rate of emission

of photons, that is, the rate of change of the number of excited states, depends on the concentration of luminescent centres, that is

$$\frac{dN}{dt} = (\text{const})N = \frac{N}{\tau} \quad (3.11)$$

Solving this equation for N gives an exponential variation with time of the number of centres. Therefore, the rate of emission of photons and thus, the intensity, takes the form

$$I(t) = ke^{-\frac{t}{\tau}} \quad (3.12)$$

where I(t) is the time dependent intensity of the phosphor output, k is the initial intensity and τ is the characteristic time constant of the decay. The use of exponential functions to model phosphor decay is well known as in, for example, Smith and Lowrance (1972) and Flam (1969). For simplicity it is assumed that all components have an exponential form.

Imagine that there are n different components to the decay and that each component, $i(i = 1, n)$ has a characteristic decay constant τ_i and intensity k_i at $t = 0$. The energy emitted by the phosphor in frame A may be written

$$E_a = \sum_{i=1}^n \int_0^t I_i(t) dt = \sum_{i=1}^n \int_0^t k_i e^{-\frac{t}{\tau_i}} dt \quad (3.13)$$

The frame transfer period is always sufficiently long that the primary component of $2\mu\text{s}$ to 10% has completely decayed before the start of frame B. The energy emitted by the phosphor in frame B can then be written

$$E_b = \sum_{i=2}^n \int_{t+t_i}^{t+t_f} k_i e^{-\frac{t}{\tau_i}} dt \quad (3.14)$$

It is possible to derive a theoretical equivalent, $\varepsilon(t)$, for the ratio E of equation 3.10. Integrating both equation 3.13 and equation 3.14, inserting the result into equation 3.10 and letting $k_i/k_1 = R_i$ gives

$$\varepsilon(t) = \frac{\sum_{i=2}^n \tau_i R_i (e^{-\frac{(t+t_i)}{\tau_i}} - e^{-\frac{(t+t_f)}{\tau_i}})}{\tau_1 (1 - e^{-\frac{t}{\tau_1}}) + \sum_{i=2}^n \tau_i R_i (1 - e^{-\frac{t}{\tau_i}} + e^{-\frac{(t+t_i)}{\tau_i}} - e^{-\frac{(t+t_f)}{\tau_i}})} \quad (3.15)$$

Now, each of the N different flash times, t_j , gives rise to a real value of E denoted by E_j . Each E_j has an uncertainty σ_j given by the spread of the 200 values of E_j about their mean. The values of τ_i and R_i are found as follows. Firstly, the number of decay components is chosen, that is, n is assigned a particular value. Then the values of all τ_i and R_i are varied until

$$\chi^2 = \sum_{j=1}^N \frac{(E_j - \varepsilon(t_j))^2}{\sigma_j^2} \quad (3.16)$$

is a minimum. When this condition is satisfied the τ_i and R_i are those that best describe the complete phosphor decay.

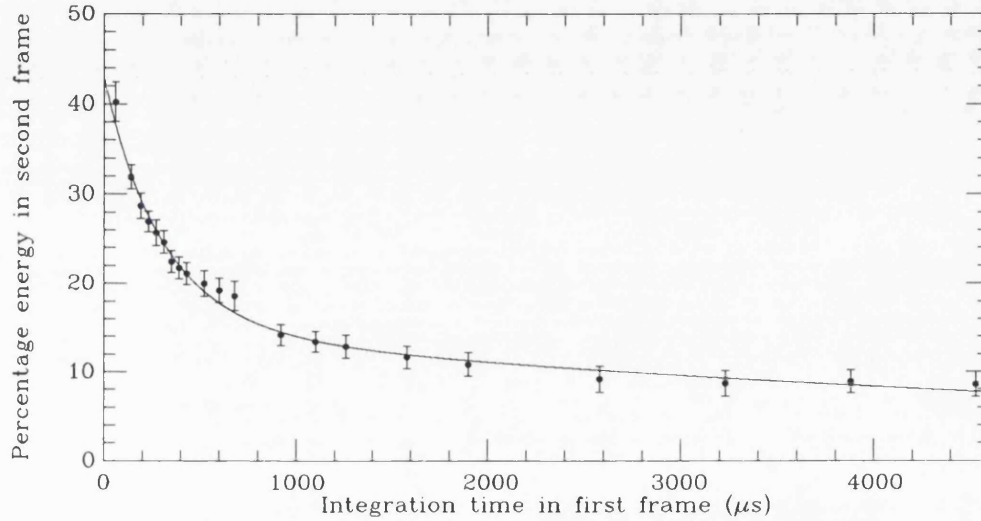


Figure 3.11: Fit to the phosphor decay using $n=3$. Transfer and frame times were $136\mu\text{s}$ and $12100\mu\text{s}$ respectively. Error bars extend σ above and below each point.

Results of Modelling the Phosphor Decay The data were poorly fitted by a $\varepsilon(t)$ with $n=2$. A much better fit was obtained with $n=3$ giving a r.m.s. deviation of the fit from the data of 5.18%. The fit is shown in figure 3.11. The values of τ_i and R_i derived from the fit are

τ_1	$0.8686\mu\text{s}$ (primary component)
τ_2	$340\mu\text{s}$
τ_3	$7300\mu\text{s}$
R_1	1 (primary component)
R_2	570
R_3	23000

The fit was sufficiently good that it was not necessary to fit the data with larger values of n . These values enable the calculation of the energy emitted by the phosphor as a function of time. This is shown in figure 3.12.

Now, given the values above it is a simple matter to determine whether an event of a particular height in frame A will give rise to a residual event in frame B whose height is

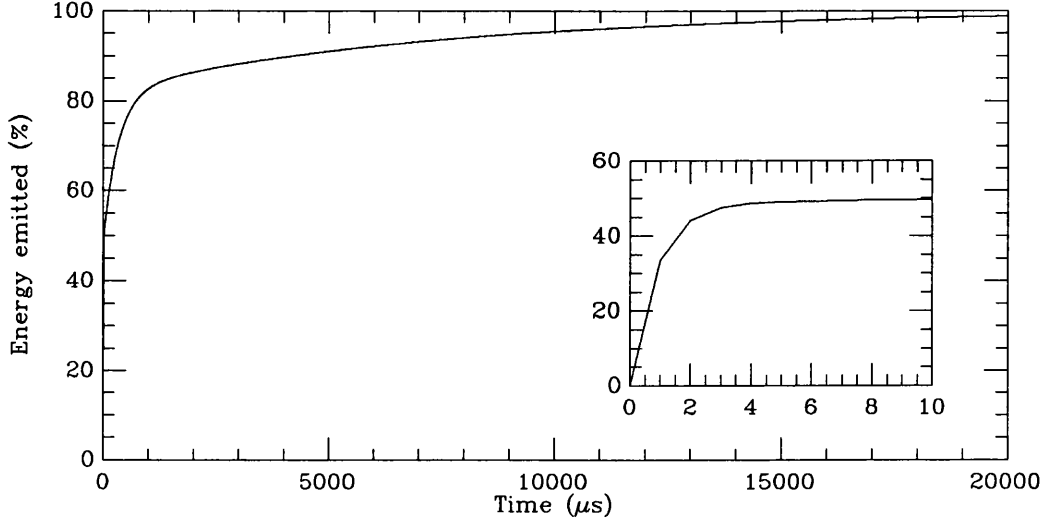


Figure 3.12: Energy emitted by the phosphor as a function of time

above the hardware threshold set for noise discrimination. If the height of the residual is above this photon counting threshold then it will be counted as a real event and a double count will result.

One can derive an expression which is useful for determining whether a residual is above the photon counting threshold. One may say that the energy emitted by the phosphor in frame A is equal to that contained under the real event as seen on the CCD. Now, if one assumes that on the CCD the primary event appears as a Gaussian of height H_a and width parameter σ_a then one can say

$$E_a = \int_0^\pi d\theta \int_{-\infty}^{\infty} H_a e^{-x^2/2\sigma_a^2} dx = (const)\sigma_a H_a \quad (3.17)$$

where x is the radial displacement from the centre of the event. Similarly for the residual event one can say

$$E_b = (const)\sigma_b H_b \quad (3.18)$$

If one assumes that the decay characteristics are the same at every point of the spot on the phosphor then $\sigma_a = \sigma_b$ and, replacing E in equation 3.10 by $\varepsilon(t)$ one finds

$$H_b = \frac{\varepsilon(t)H_a}{1 - \varepsilon(t)} \quad (3.19)$$

A curve of H_b/H_a is shown in figure 3.13. For events not arriving during frame transfer, then, this curve can be used to determine whether the height of the residual is above

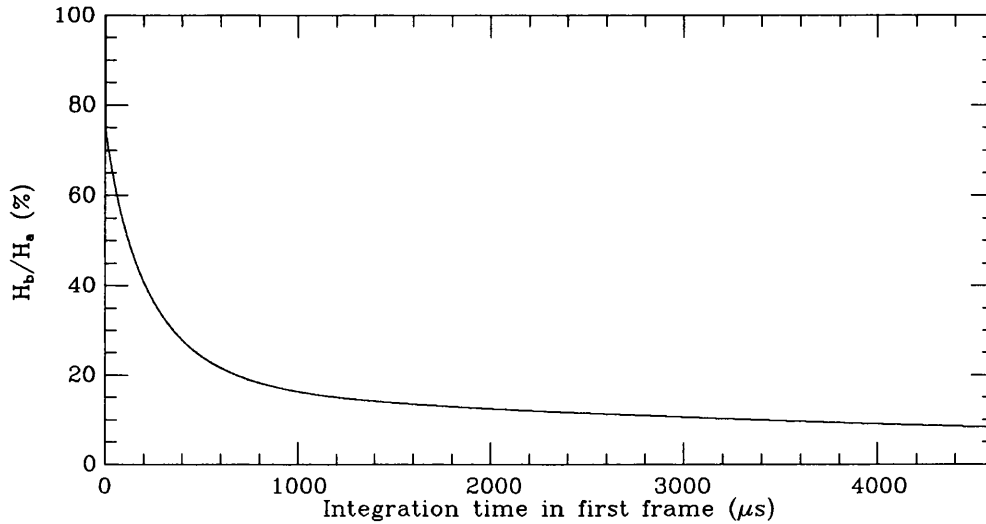


Figure 3.13: Ratio of the height of the residual to the height of the real event

the photon counting threshold. For example, imagine that the photon counting threshold is set at 20 analog-to-digital-units (ADU), and that the condition for an event, real or residual, to be counted is that its height is above the threshold. Take an event with a height of 110 ADUs – if it occurs 600 μs before the end of the first frame then the residual will have a height which is 22% of the primary height, that is, its height would be 24ADUs which is above the photon counting threshold and so a double count would result. On the other hand, if it occurred 1000 μs before the end of the frame then its height would be 17% of 110ADUs, that is, 19 ADUs and so it would not be counted.

Since events have a distribution of heights and also have a random temporal distribution, the easiest way to assess the effect of the secondary phosphor decay on the dynamic range curve of the detector is to use computer simulations. The results of these simulations are discussed in section 7.3.2.

MCP Channel Recovery

When an electron enters a pore and electron multiplication results, the pore is left depleted of electrons. Electrons are replenished via the current flowing in the conducting layer but, because of the high resistivity of MCP glass, this takes a finite time. During the time between the electron cloud leaving the pore and the pore being completely replenished the pore is said to be recharging. At any given time during recharging, the pore has regained

some charge but does not have the largest amount possible for electron multiplication. Therefore, if another electron arrives in the same pore during recharge, it will not undergo multiplication to the same extent as if the pore was fully charged.

At low input count rates there is only a small chance of an event arriving spatially coincident with a pore before it has fully recharged. However, at higher count rates this could be a frequent occurrence. Since electrons that arrive during recharge undergo a smaller multiplication, the resulting electron cloud is smaller and, therefore, the pulse height as seen by the processing electronics is smaller. If a lot of events arrive early during recharge then there will be a lot of very small pulse heights. If these are below the hardware photon counting threshold then they will be lost. At high count rates then, the linearity of the dynamic range curve is affected by the finite channel recovery time of the MCP pores.

The way in which channels recharge is not well understood – there are numerous factors that complicate the understanding of the process. Yet it is important to quantify the process since it affects the linearity of the detector.

The State of Current Knowledge of MCP Channel Recovery There have been numerous theories and models to predict the recharge process in MCP pores.

Eberhardt (1981) considers the MCP pore to act as fixed number of discrete electron multipliers, or dynodes. With this model and because of the exponential nature of the electron multiplication process, most of the charge depletion occurs in the last dynode. In a low gain, or d.c., mode Eberhardt says, the charge is replenished by the strip current that flows between the two faces of the MCP. However, in saturated mode the charge delivered in the output charge cloud far exceeds the charge available in d.c. operation. Eberhardt attributes the extra charge as being supplied by the *lateral capacitance* that exists between the active channel and its quiescent neighbours. Wiza (1979) treats the MCP pore as a simple RC circuit and estimates the recharge time from this to be 10^{-2} s, that is, linearity will result if the channel is not fired more than once every 0.01s.

Gatti et al (1983) suggest an alternative approach to finding the channel recharge time and apply Maxwell's equations directly to the MCP structure. By treating the channels as distributed impedances they conclude that the recharge time is much larger. They go on to point out that the recharge time would be much shorter if there was conductivity

not just down the pores but also due to the bulk glass through to other pores.

Measurements (e.g. Pearson et al., 1988; Nartallo Garcia, 1990; Cho and Morris, 1988; Fraser et al., 1991) have shown that the larger the active area of the MCP, the longer the recharge time constant. That is, the maximum achievable count rate is smaller for larger areas of illumination. This is thought to be strong evidence for the existence of capacitive coupling between adjacent channels, as proposed by Eberhardt. Generally, the recharge time constant, or dead time, depends upon the spatial distribution and intensity of the input image and therefore, because of ‘adjacency’ (Sharma and Walker, 1989), the dead time of a channel must be considered the local dead time (Cho and Morris, 1988; Sharma and Walker, (1989).

Fraser et al (1991) show that the behaviour of single plates is different from that of multistage detectors. They also report that for multistage MCP stacks, the recovery time depends on the illuminated area. They attribute their findings to the interchannel coupling and to local changes in the conduction current during plate operation. Conversely, Edgar et al. (1992) also report the dependence of recharge time on illuminated area but they attribute the effect as being due to the influence on the radial electric field that results from a discharged channel as discussed by Gatti. The field is thought to affect the electron trajectories in neighbouring channels and thereby reduce their gain.

MCPs have been modelled as paralyzable (Cho and Morris, 1988) and non-paralyzable (Sharma and Walker, 1989) counters. Paralyzable counters are those that remain unresponsive during the dead time but if an event arrives during this time the dead period is extended. Thus, if the count rate is high, these counters could remain indefinitely unresponsive and therefore paralyzable. Non-paralyzable counters, on the other hand, do not have their dead period extended. MCP pores clearly fall into neither of these categories. Instead, MCPs are non-ideal paralyzable counters – the recharge period is extended by the arrival of an event but, instead of being unresponsive, the pore responds but not with the full signal. Moreover, each channel is not independent; its dead time depends on upon the state of depletion of its nearest neighbours.

The phenomenon of pore paralysis is evidently a complicated one and is still not well understood. What is clear is that the dead time for point sources is shorter than that for extended sources. The XMM MIC will be detecting star images, that is point sources, on a background of Zodiacal light, or extended source. The consequence of this in terms of pore

paralysis is difficult to estimate because the lack of understanding about the phenomenon and also, as yet, the lack of a successful model to predict its effects. It is likely that the dead time for the star images will be reduced to that for the Zodiacal light background since this is an extended source that covers the entire area of the detector input. Whether or not the frame rate of the CCD will dominate the reduction in dynamic range due to coincidence losses is again difficult to estimate. Pore paralysis is discussed again in sections 7.3.2 and 7.7.

3.3.5 Other Intensifier Properties Affecting Detector Performance

A number of other factors concerning the operation of the intensifier affect the performance of the final space version of MIC.

Signal Induced Background

Intensifiers used with MIC can exhibit background that arises from the presence of the signal

- Charge cloud fragmentation – As will be discussed in section 7.6, the presence of too many gas atoms in the intensifier leads to the fragmentation of a developing charge cloud in the gaps between plates. This leads to smaller, irregular, randomly placed splashes of photons in the immediate vicinity of the main photon event. The presence of these ‘strawberries’ means that the pulse profile becomes random in shape and this affects the centroiding procedure described in section 6.6.3. Excessive amounts of gas are caused by incomplete scrubbing of the plates prior to seal off. Desorption of gas that should have been removed during scrubbing leads to a rise in pressure in the tube.
- Ion feedback – the passage of an electron cloud down a channel may desorb positive ions from the surface of the glass which can stream back to the photocathode and give rise to ion event flashes. These are very noticeable and give rise to a large number of phosphor event scintillations but because they occur randomly in position they contribute to the general background.

- Halation. This exhibits itself , for example, as wings at the base of strong emission lines and may be attributed to two sources
 - specular reflection from the front channel plate may result if light is transmitted through the photocathode. This gives rise to events around the region of the true position.
 - electron scatter from the front channel plate may result from electrons that are incident on the region between pores and that then enter a nearby channel. Again, this results in events around the true position

Cosmetic Quality

There may be various blemishes or defects associated with components of the intensifier

- The photocathode – defects on the photocathode can give rise to
 - field emission points produce a constant signal. These are caused by asperities on the photocathode surface which result from contamination during manufacture. The field strength is higher at these points and this leads to the emission of electrons. These points are unstable and so do not flat field out
 - Photocathode non-uniformity resulting in a spatial variation in quantum efficiency. The cause of this is also contamination giving rise to asperities and variations in the photocathode quality.
- Channel plates.
 - Occasionally, a turned on channel is seen which results in a constant signal incident on the phosphor. The defect results from defects in the channel wall that give rise to field enhanced emission of electrons which are then subsequently multiplied.
 - Channel plate dead spots may be seen. These are channels or groups of channels that do not produce electron multiplication and so are dead. They are caused by the fusing together of channels during the manufacturing process.

Power Supply Stability

The power supply is very susceptible to changes in temperature and time since switch on. The voltages indicated on the power supply may gradually drift in time up to 16 hours after switch on. Any tests should be done after the supply has stabilized for at least this time. This affects the properties of the pulse profile which in turn affects the accuracy of the centroiding technique described in section 6.6.3.

The effect of all the above is discussed more fully in section 7.6.

Chapter 4

Fibre Optics

4.1 Introduction

Fibre optics are used to couple the phosphor output to the CCD. There are three sections to these fibre optics,

- the faceplate which forms the output of the image intensifier,
- the taper which collects light output from the intensifier,
- the faceplate bonded to the CCD which collects light from the narrow end of the fibre taper.

These faceplates or taper consist of tiny light transmitting fibres tightly packed together to form a vacuum tight plate. Each fibre consists of a core glass surrounded by a cladding glass of lower refractive index. Figure 4.1 shows how light propagates down a fibre by total internal reflection at the core cladding interface. Light will only be reflected at this interface if its angle of incidence, θ , is greater than the critical angle, θ_c . The critical angle determines the maximum angle, α_c , with respect to the fibre axis, at which light may be incident on the fibre and still be able to propagate along the fibre by total internal reflection. This angle is a measure of the light gathering power, or numerical aperture, NA, of the fibre and is defined as

$$\text{NA} = n_0 \sin \alpha_c = \sqrt{n_1^2 - n_2^2} \quad (4.1)$$

where n_0 , n_1 and n_2 are the refractive indices of the outside medium ($\simeq 1$ for air), the core and cladding respectively. Any light arriving at an angle greater than α_c will not be

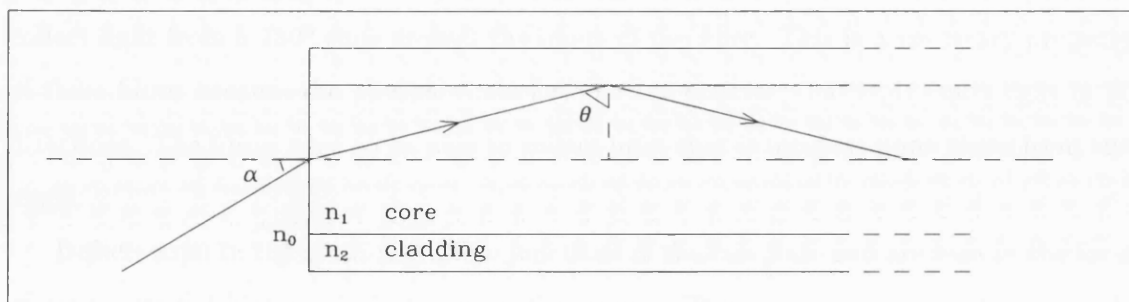


Figure 4.1: The way in which light propagates down a fibre by total internal reflection

propagated by the fibre and will pass through the fibre wall.

Fibre faceplates and tapers are made by a repetitive assemble and draw process. Individual fibres are stacked and drawn to form a 'multifibre' which is stacked, heated and drawn again to form a 'multi-multifibre.' A stacked, fused collection of these constitutes a fibre optic 'boule' which can be cut, ground and polished to form a vacuum tight faceplate or heated and stretched around the middle to form an hourglass shape from which two identical tapers may be made. With the fibre optics used with MIC, extra, light absorbing black glass fibres are interspersed with the light transmitting fibres to prevent optical crosstalk. This extra mural absorption (EMA) helps to ensure that the spatial information in an image is retained and to prevent degradation of the image contrast.

Whereas the two faceplates transfer the image on their inputs to one of the same size on their outputs, the taper demagnifies the image by the ratio of the two end diameters which for XMM-MIC is 3.06.

Associated with each of the three sections above are various defects and distortions which arise from the manufacturing process and these are the subject of most of the rest of this chapter. In addition, the performance of the taper may be affected by exposure to radiation as will be the case for the fibre optics here.

4.2 The Fibre Optic Output of the Intensifier

The P-20 phosphor of the image intensifier is deposited directly onto a 1:1, output fibre optic faceplate with fibre diameters of $\sim 6\mu\text{m}$. The faceplate is around 14mm thick which is convenient for placing the phosphor at the correct distance from the back channel plate.

The fibres in the faceplate have a numerical aperture of 1 – this means that they can collect light from a 180° cone around the input of the fibre. This is a necessary property of these fibres because the phosphor is a Lambertian emitter, that is, it emits light in all directions. The fibres need to be able to collect light that is incident upon them from any angle.

Defects exist in the multi-multifibre junctions of the faceplate and are seen in the form of a hexagonal ‘chicken wire’ pattern in the image. This is usually only just discernible since the defect does not cause any loss of data but just alters slightly the position of events occurring along the multi-multifibre junctions. The patterning does not present a problem since it is at such a low level and is completely fixed and so may be removed by flat fielding.

Shear distortions are likely to be present in this faceplate but their effect has not been noticed in any image.

4.3 The Fibre Optic Taper

This 3.06:1 reduction fibre taper is 2.5cm long and couples the output of the fibre block in the image intensifier to the fibre block on the CCD. The taper reduces the size of the image in order to make it compatible with the size of the CCD imaging area. Figure 4.2 shows two of these tapers and illustrates their use both as a magnifier and as a minifier. The size of the fibres in the taper is $5.8\mu\text{m}$.

The transmission efficiency of the taper is around 6% and is low compared to that of the 1:1 blocks. This is understood when one considers the numerical aperture of the taper. The transmission efficiency of tapered fibres is discussed by Siegmund (1991). Figure 4.3 shows how light behaves in a tapered fibre. At each reflection the angle of the light ray with respect to the fibre axis is increased by 2ϕ , ϕ being the cone angle of the taper. Rays entering the fibre with too large an angle, α , will eventually be incident on the core cladding interface with an angle less than the critical angle and will pass through the wall of the fibre to be absorbed by the EMA. What this means in terms of numerical aperture (NA) is that the NA is not constant along the fibre but is effectively smaller at the wide end. If D_1 and D_2 are the diameters of the wide and narrow ends respectively and NA_2 is the numerical aperture of the narrow end then one can use geometry to show that the

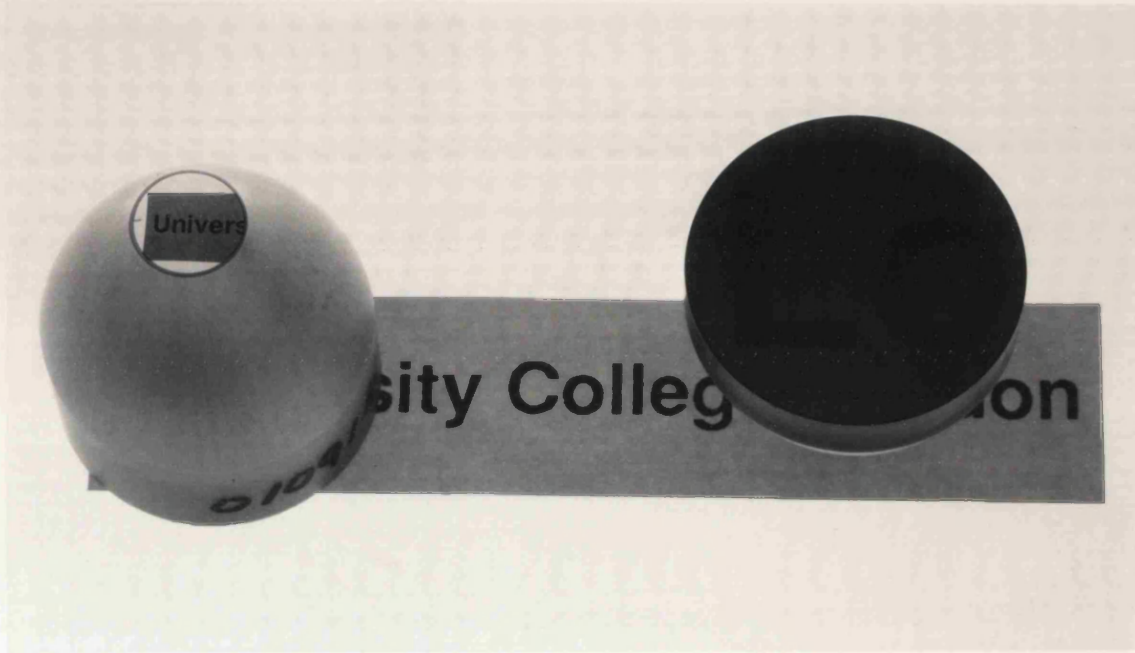


Figure 4.2: Two fibre optic tapers, one being used as a minifier and the other as a magnifier. The MIC fibre optic is used to demagnify the image.

numerical aperture, NA_1 , of the wide end is given by

$$NA_1 = NA_2 \frac{D_2}{D_1} \quad (4.2)$$

The numerical aperture at the narrow end is given by Schott Fiber Optics Inc. (Schott) as 1.0 and the ratio of the diameters is 3.06 which gives

$$NA_1 = 0.327 \quad (4.3)$$

This means that the wide end of the taper can only gather light from a cone which has an angle of $\sin^{-1}(0.327) = 19^\circ$

The transmission efficiency of the taper as a whole depends on three other factors

- The wavelength dependent transmittance, $T(\lambda)$, of the core glass which for the green light of the P20 phosphor is about 0.95 (95%).
- The core area ratio, C_A , which is quoted by Schott as being 0.75.

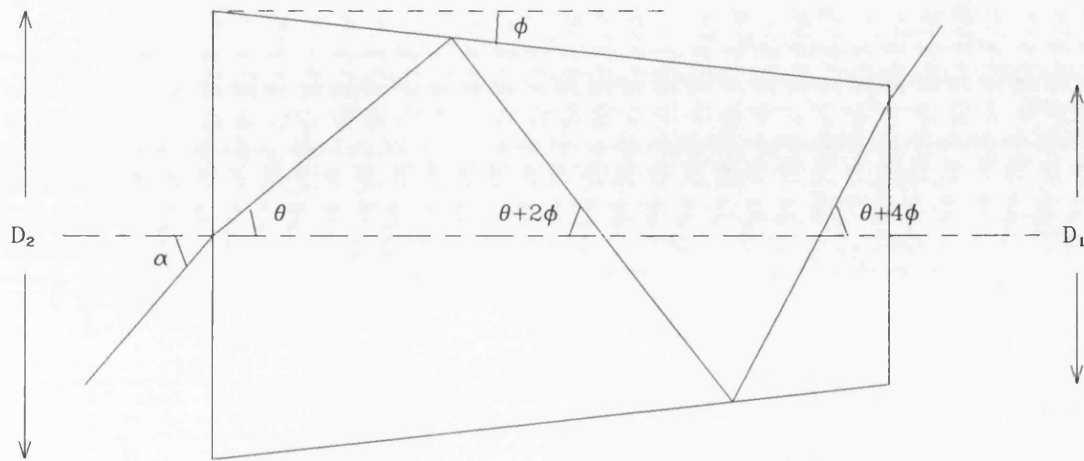


Figure 4.3: Propagation of light down a tapered fibre

- The effect of Fresnel reflections at each end of the taper. This is when light which is incident on the fibre within α_c is reflected at the air core interface. This introduces a factor, R , at each end face.

The expression given by Siegmund (1991) for the transmission efficiency, T , of the taper is

$$T = T(\lambda) \cdot C_A \cdot (1 - R^2) \cdot (NA_1)^2 \quad (4.4)$$

Inserting the values for these quantities gives

$$T = 6.4\% \quad (4.5)$$

NA_1 appears squared in this expression due to the $\sin^2 \alpha$ nature of Lambertian emitters such as the phosphor or the output side of the intensifier faceplate. The efficiency may be improved somewhat when the system is in operation because optical coupling oil is used between the intensifier and the wide end of the taper which helps to reduce Fresnel reflections. The 6% efficiency is sufficient that 3×10^5 photons are still incident on the CCD.

4.3.1 A Comparison of Lens and Fibre Optic Coupling

In the CCD-IPCS (Fordham et al., 1986), which used a four stage, magnetically focused EMI intensifier, a relay lens (Worswick and Wynne, 1985) was used to couple the image

of the phosphor to the CCD and to provide a 3.8:1 reduction. The lens suffered from aberrations of a different sort to those found in the fibre optic taper. Figure 4.4 is a

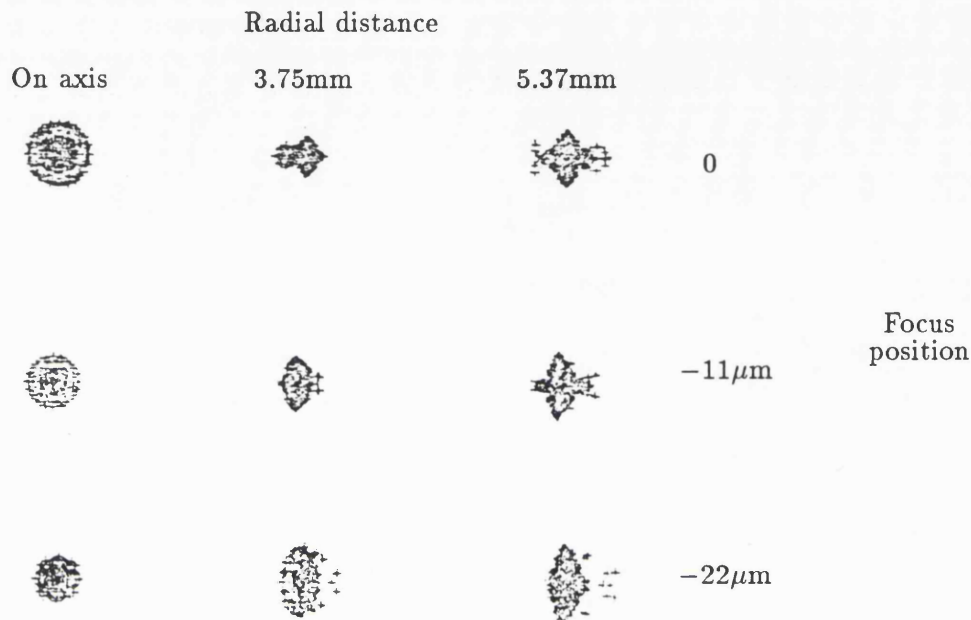


Figure 4.4: Spot diagram for the CCD-IPCS relay lens

spot diagram showing the image of a point source seen through the lens for different focus positions and different radial distances from the optical axis of the lens. One can see that the best focus position is different for each of the three radial distances given above. Moreover, the coma and astigmatism exhibited by the lens give rise to different spot profiles for each radial distance, whatever focus position is chosen. Asymmetrical profiles such as these give rise to centroiding errors and thus pattern noise in the accumulated data as described in section 6.6.2.

In the CCD-IPCS the coils of the EMI intensifier were used to 'dither' (Shectman, 1981; Jorden and Fordham, 1986) the image and this enabled the pattern noise to be removed. However, with an MCP intensifier dithering presents much more of a problem since there are no scan coils. It is possible to remove the pattern noise without dithering, as described in section 6.6.3, but this procedure requires the spot profile to be constant across the entire image which would not be the case with lens coupling. Dithering is discussed again in section 6.6.2.

The fibre optic taper does not exhibit aberrations of the type seen with the lens. However, tapered fibre optics are subject to distortions. The manufacture of tapers, although it is designed to minimise distortion, does involve the flow of glass in the softened region of the hourglass structure and this is not always uniform. Consequently, fibre tapers exhibit a higher level of distortion relative to faceplates. No multifibre junction defects have been seen with the fibre taper but two other forms of distortion are present:

- Shear distortion. This is a localized distortion arising from discontinuities in the fibre packing structure.
- Pin cushion distortion. This is a global distortion which is a consequence of the fibre drawing process.

The pin cushion distortion varies slowly across the image and so has only a very small effect on the pulse profile. Therefore, shears may be considered as the only source of distortion arising from the fibre taper that affects the pulse profile. Schott quote a maximum shear distortion of $64\mu\text{m}$ but no shears have been apparent so far in any image although shears have been seen with the 3.85:1 taper used with the ground based MIC. Any shears that are present must be small enough to have an invisible effect on the recorded image. This means that the pulse profile has a constant shape across the entire image and so the pattern noise can be removed by the procedure described in section 6.6.3. A fibre optic taper is much preferred to a lens with regard to the pulse profile and also has the advantages of being much more compact and having a light gathering power an order of magnitude higher than that of a lens.

The lens does not exhibit a spatial distortion such as the pin cushion effect seen with the fibre optic. This distortion is visible by eye and is by far the major source of spatial distortion associated with MIC. It is particularly important that the pin-cushion distortion should be quantified in view of the star tracking function of the blue camera which was described in section 2.2. It will be necessary to correct for the pin-cushion distortion before analysing the shift in the guide star positions caused by telescope drift and roll.

Schott have manufactured a new, low distortion fibre optic glass, type 32AS. Four tapers were purchased from Schott and, after a brief analysis, one was selected as having the lowest distortion. This taper, number 916-1, was then analysed in order to quantify the errors it would introduce via pin-cushion distortion.

4.3.2 Analysis of Pin-cushion Distortion for the Correction of Guide Star Positions

A 1.5mm square grid was placed at the narrow end of the fibre taper and a photograph was taken of the image seen at the wide end. This photograph showed a grid of 17 horizontal lines and 17 vertical lines. The photograph was digitized using the microdensitometer at the Royal Greenwich Observatory and two $5400 \times 5 \mu\text{m}$ by $100 \times 270 \mu\text{m}$ images were obtained, one of which contained information about the 17 vertical lines, the second of which contained information about the 17 horizontal lines.

The analysis of the distortion introduced by the taper was done with two objectives

- To obtain a figure for the likely maximum error in the position of a guide star due to fibre taper distortion.
- To obtain a more general qualitative description of the distortion over the whole taper.

The Maximum Error in the Position of a Guide Star

When considering the maximum likely error in the position of a guide star due to fibre taper distortion the following specification for telescope tracking errors is useful

- **The maximum tracking error due to spacecraft drift will be 30 arc seconds in 10 hours.** The pixel size will be 0.5 arc seconds and at the detector input there will be 2048 pixels spanning an 18mm diameter. This means that at the input window 1 arc second is equivalent to $18 \mu\text{m}$. Now, assuming a maximum exposure time with MIC of 10000 seconds this gives a *maximum tracking error due to spacecraft drift of $150 \mu\text{m}$ at the input window.*
- **The maximum angular error per 1000 seconds due to spacecraft roll will be 6 arc minutes with respect to the centre of the detector input window.** With a detector diameter of 18mm this means 6 arc seconds gives rise to an error due to roll of $15 \mu\text{m}$ at the edge of the detector. Again, given a maximum exposure time with MIC of 10000 seconds this gives a *maximum tracking error due to spacecraft roll of $150 \mu\text{m}$.*

In the worst case these two errors would add in the same direction to give

$$\text{Maximum tracking error} = 300\mu\text{m}$$

That is, at worst the position of a star will travel $300\mu\text{m}$ across the input window of the detector and thus also across the front face of the fibre taper. In practice the maximum tracking error will almost certainly be smaller than this and the exposure times will typically be 2000 seconds. Also, since the tracking errors arise from gradual thermal drift, it can be assumed that there will be no oscillations between larger limits. However, in order to give an upper limit to the distortion introduced by the taper, it is important that the maximum tracking error should be considered.

For each grid line in the digitized photograph the location of the line centre at each bin was determined. The DIPSO package on Starlink was then used to fit curves with a bin size of $300\mu\text{m}$, the maximum tracking error, to each grid line. These curves are shown as a grid in Figure 4.5 and as a ten-fold exaggeration of the taper distortion in Figure 4.6. The distortion appears barrel shaped since it was viewed in the opposite sense to that in which it will be used in the detector. Pin-cushion distortion is the reverse of this and would be seen if the grid was placed at the wide end and viewed from the narrow end.

From manufacturer's measurements it is known that the grid lines in each orientation are parallel to an accuracy of less than $1\mu\text{m}$. Therefore, by fitting a grid of parallel straight lines to the grid of image curves one is effectively reproducing the square input grid. The distortion introduced by the taper can be found by comparing the image curves to these fitted straight lines. Straight lines were fitted simultaneously to the horizontal and vertical curves with two conditions imposed:

- That the fitted straight lines in each orientation must be an equal distance apart
- That all the horizontal straight lines should have the same gradient and that all the vertical straight lines should similarly have the same gradient.

It was not assumed that the horizontal lines of the input grid were perpendicular to the vertical lines and later this is seen to be justified.

With these conditions imposed on the fits it was necessary to fit straight lines of the form

$$y = ax + b + (m - 1)c \quad (4.6)$$

where a is the gradient of the lines; b is the intercept of line 1 on the y -axis ; m is the number of the line as in Figure 4.5 and c is the gap between each line. The same equation

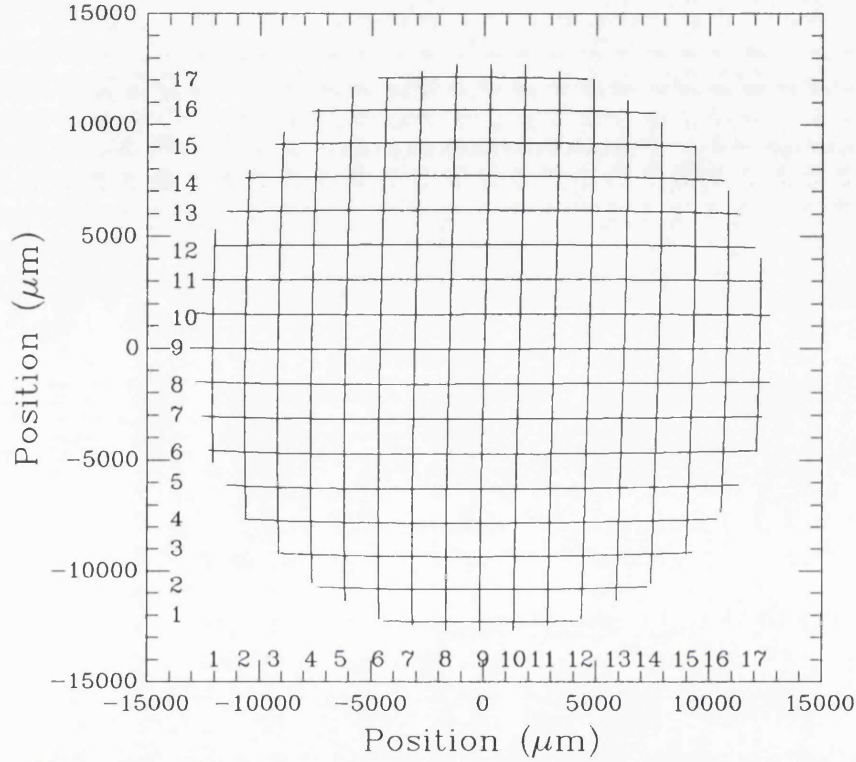


Figure 4.5: Grid lines as seen through the fibre optic taper.

was used for the vertical straight lines but with x replaced by y and vice versa. The quickest way of fitting the lines was to vary a , b and c until

$$\chi^2 = \sum_{k=1}^N [y_k - ax_k - b - (m-1)c]^2 \quad (4.7)$$

was a minimum for a set of lines. χ^2 is a measure of the goodness of fit and N is the number of datum points which was 1176 for the horizontal lines and 1180 for the vertical lines.

If y is one coordinate of a point on a fitted straight line and Y is that corresponding point on the image curve then $\Delta y = y - Y$ gives the vertical error introduced by the fibre taper with the sign appropriate to pin cushion distortion, *i.e.* as if the curved grid was the input at the wide end of the taper and the straight line grid was the resulting image at the narrow end. For every line in the grid the deviation, Δy or Δx , of the curve from the fitted straight line was found at every bin; this deviation is the same as the positional error caused by the fibre taper distortion at that point on the taper. The difference, $\epsilon_{300} = \Delta y_n - \Delta y_{n-1}$, between the deviations of adjacent bins on the horizontal lines is then

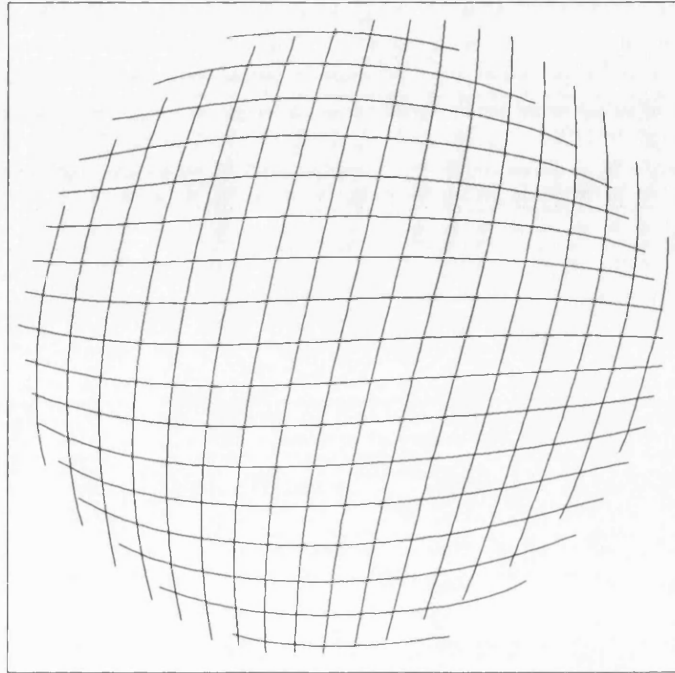


Figure 4.6: Ten-fold exaggeration of the distortion introduced on the grid lines by the fibre taper.

the positional error associated with moving in a straight line for $300\mu\text{m}$ at that particular part of the line and similarly for the vertical lines. The largest ϵ_{300} is then an indication of the likely maximum error in the position of a guide star during an integration.

Results. The intensity profile of each grid line in the two images was Gaussian in shape. The Gaussian peaks were treated as the line centres and the errors in these line centres were derived from the full width at half maximum (FWHM) of the Gaussians. The FWHM was found everywhere to be 11 pixels or $55\mu\text{m}$ giving a standard deviation in the determination of the line centres of $\sigma = \text{FWHM}/2.354 = 23.4\mu\text{m}$. The curves fitted to these lines using Starlink software had r.m.s deviations with respect to the data of between $1.5\mu\text{m}$ and $3.5\mu\text{m}$. This error is sufficiently small that the error in the coordinates of each point of these curves is dominated by the uncertainty in the position of the line centres.

The straight line fits of equation 4.6 were made separately for horizontal and vertical lines. The coefficients of these fits are shown in Table 4.1 for both orientations.

Table 4.1: Coefficients of the straight line fit to the grid curves

Coefficient	Horizontal lines	Vertical lines
a	-1.85×10^{-4}	1.8433×10^{-2}
b	$-12345 \mu\text{m}$	$-12186 \mu\text{m}$
c	$1537.3 \mu\text{m}$	$1528.2 \mu\text{m}$

Figure 4.7 shows plots of Δy against x and Δx against y for each of the horizontal (H) and vertical (V) lines respectively. Intuitively one expects that the shapes of the curves and the way the shapes change should be similar for both sets of curves. Previously it was assumed that the horizontal lines were perpendicular to the vertical lines but this was found to give different shaped curves for the two orientations. Here, this assumption was dropped and was shown to be invalid in view of the similarity of the two sets of curves shown in figure 4.7. Table 4.2 shows the maximum ϵ_{300} and r.m.s. ϵ_{300} of each line for both orientations. The maximum ϵ_{300} is large in both orientations, but for every line the maximum occurs at the end of the line and ϵ_{300} drops off quickly towards the centre.

A General Quantitative Description of the Pin-cushion Distortion

It is important to have a quantitative description of the pin cushion distortion, both for the correction of guide star positions and for the removal of the distortion from scientific data during data reduction. The analysis of the preceding section provides two large arrays of points $(x, y, \Delta x)$ and $(x, y, \Delta y)$. It is possible to find two expressions for Δx and Δy in terms of the coordinates (x, y) . Convenient functions for fitting Δx and Δy are polynomials and in two dimensions these take the form

$$\Delta x = \sum_{j=1}^{n+1} \sum_{i=1}^j A_{i,j} y^{i-1} x^{j-i} \quad (4.8)$$

$$\Delta y = \sum_{j=1}^{n+1} \sum_{i=1}^j B_{i,j} x^{i-1} y^{j-i} \quad (4.9)$$

where $A_{i,j}$ and $B_{i,j}$ are the polynomial coefficients and n is the order of the polynomial. For example, a second order polynomial would be

$$\Delta y = B_{1,1} + B_{1,2}y + B_{2,2}x + B_{1,3}y^2 + B_{2,3}xy + B_{3,3}x^2 \quad (4.10)$$

Figure 4.7: Plots of Δy against x and Δx against y for the horizontal (H) and vertical (V) lines respectively.

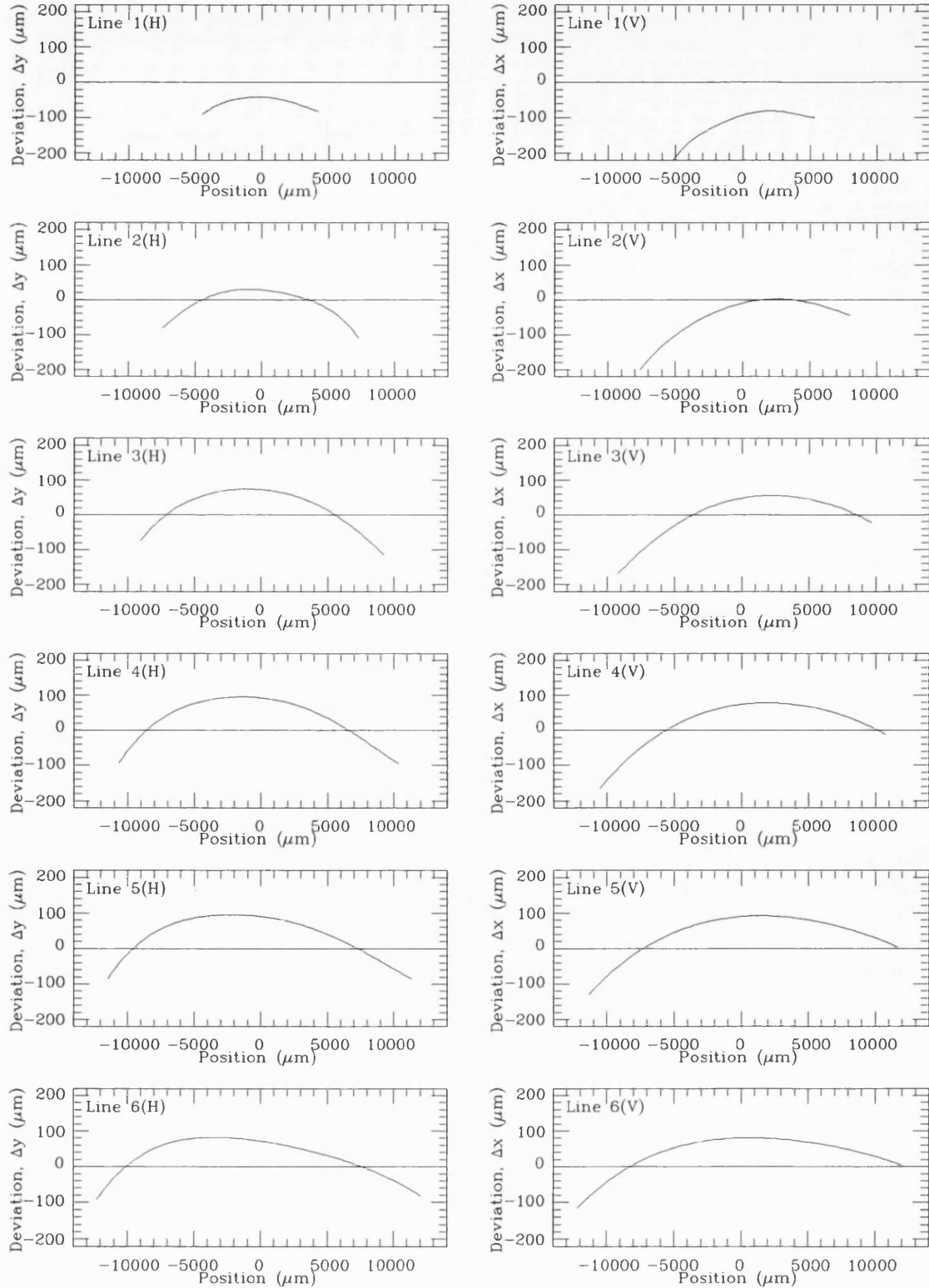


Figure 4.7: (contd.)

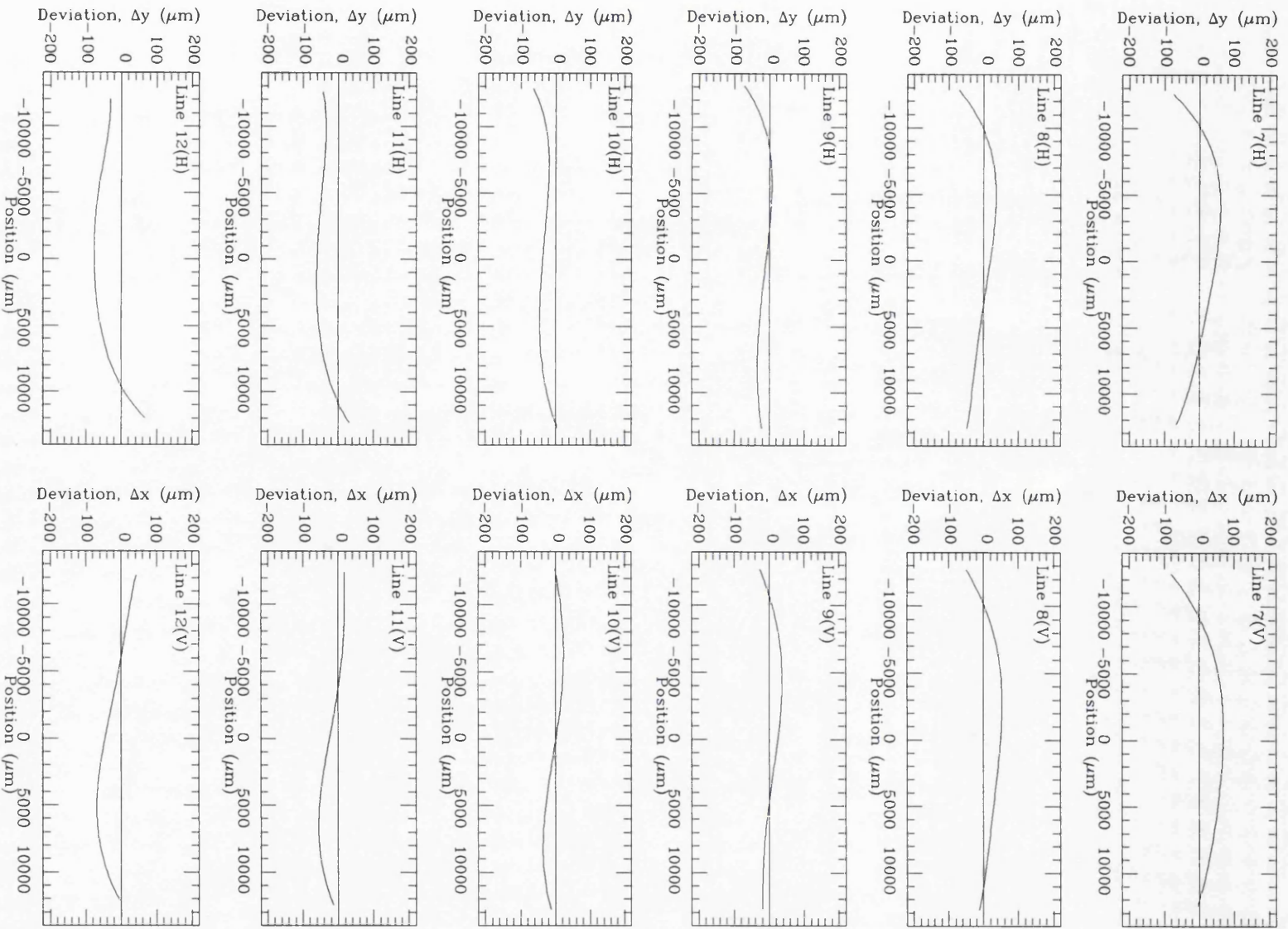


Figure 4.7: (contd.)

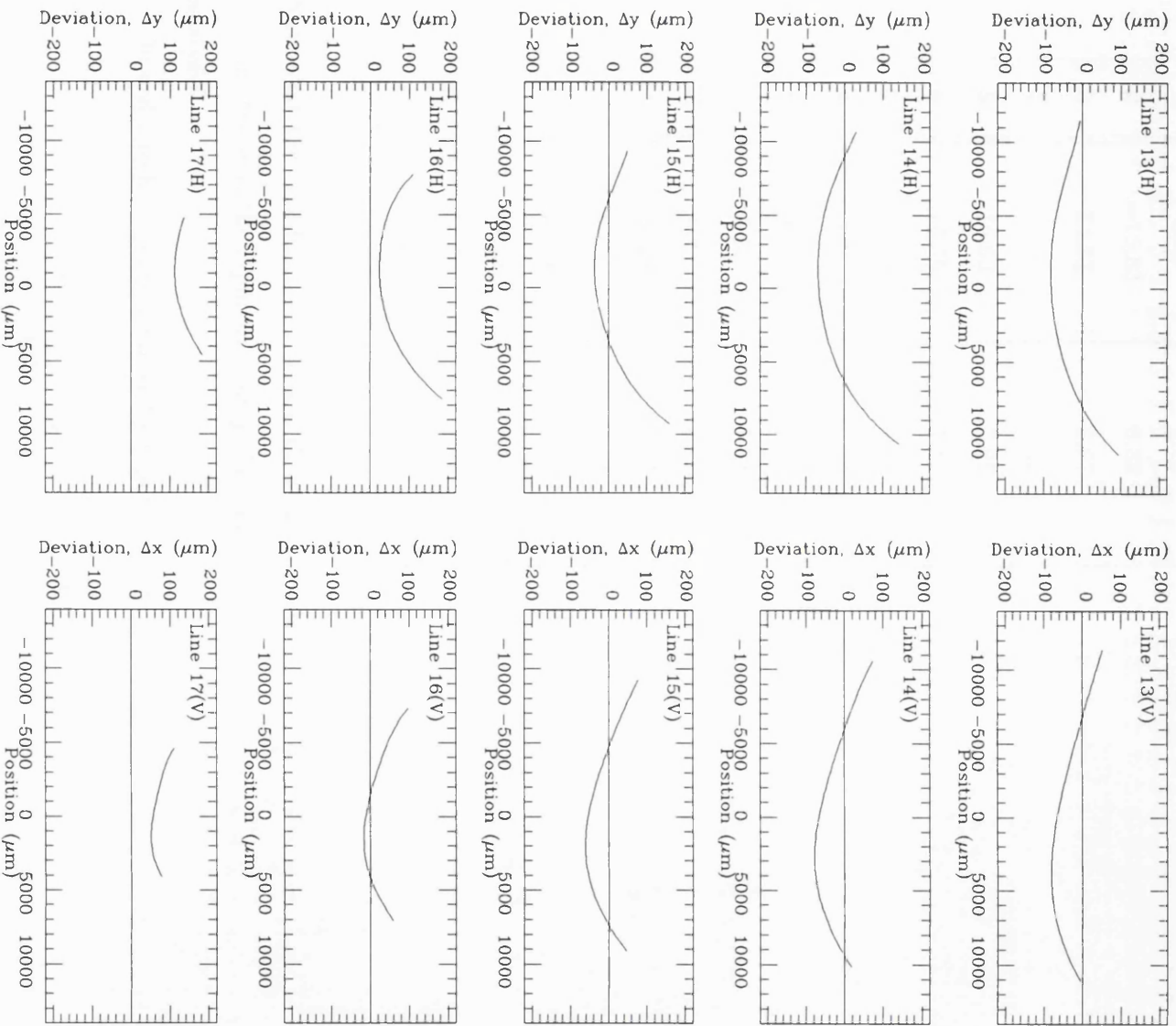


Table 4.2: Maximum and r.m.s. error in a 300 μ m straight line.

Line	Horizontal lines		Vertical lines	
	max ϵ_{300} (μ m)	r.m.s. ϵ_{300} (μ m)	max ϵ_{300} (μ m)	r.m.s. ϵ_{300} (μ m)
1	8.83	3.73	14.90	5.77
2	-15.53	6.38	14.10	5.98
3	14.31	6.67	11.74	5.87
4	17.00	6.62	13.44	5.90
5	16.63	5.96	12.24	5.10
6	15.65	5.41	11.22	4.43
7	11.58	4.01	9.11	3.52
8	9.35	2.98	6.81	2.56
9	7.60	2.24	4.51	1.81
10	5.58	1.94	3.08	1.44
11	6.89	2.21	4.29	1.70
12	10.58	3.37	5.87	2.42
13	11.30	4.17	6.38	3.11
14	14.54	5.48	7.09	3.97
15	14.38	5.58	8.94	4.54
16	11.95	5.89	-8.98	4.49
17	7.47	3.71	-7.12	3.40

Note that the coordinates (x, y) are those at the narrow output end of the fibre optic and not those at the input since only the coordinates at the output will be available for analysis.

In order to fit a polynomial to Δy it is necessary to make

$$\chi^2 = \sum_{k=1}^N \left[\Delta y_k - \sum_{j=1}^{n+1} \sum_{i=1}^j A_{i,j} x_k^{i-1} y_k^{j-i} \right]^2 \quad (4.11)$$

a minimum. Again, χ^2 is a measure of the goodness of fit and N is the number of datum points. One can find the minimum of χ^2 with respect to any of the coefficients by finding the derivative of χ^2 with respect to the coefficient and setting the resulting

expression equal to zero. It is necessary that χ^2 should be a minimum with respect to all of the coefficients simultaneously. Therefore, by setting the derivative with respect to every coefficient equal to zero, one has a set of simultaneous equations which when solved will yield the coefficients for a minimum χ^2 . The equations can be solved using matrix methods and they yield the polynomial coefficients directly.

Polynomials up to order seven were fitted using the above procedure.

Results. Polynomial fits of Δx and Δy were successful for orders 3 and higher. Table 4.3 shows the maximum and r.m.s. deviation from the data of polynomial fits of order 3 to 7. Although the fit is better for higher order, the complexity of the polynomial is increased,

Table 4.3: Maximum and r.m.s. deviation from the data of polynomial fits of orders 3-7.

Order	Horizontal lines		Vertical lines	
	max error (μm)	r.m.s. error (μm)	max error (μm)	r.m.s. error (μm)
3	-26.5	4.84	-21.54	4.86
4	18.3	3.36	14.69	3.63
5	12.08	1.98	-9.47	2.19
6	9.83	1.90	-8.60	2.05
7	-10.9	1.48	8.77	1.88

for example, with 10 coefficients for 3rd order and 36 for 7th. An illustration of the complexity of the polynomials is provided in Table 4.4 which gives the coefficients of the 3rd order fit to Δy , with Δy having been in millimetres. A polynomial of order 5 gives the best compromise between complexity and goodness of fit. Figure 4.8 and Figure 4.9 show greyscale plots of the two 5th order polynomial fits of Δy and Δx respectively. In this figure the background represents zero deviation; anything darker represents an error due to distortion in the negative x or y direction and anything lighter represents an error due to distortion in the positive x or y direction. With this in mind it is easy to see that the pattern of shading would produce pin-cushion distortion. Figure 4.10 is a greyscale plot of the absolute error, $(\Delta x^2 + \Delta y^2)^{\frac{1}{2}}$, where white represents zero deviation. This shows that the greatest distortion occurs at the very edge of the taper and that there is an approximately circular area within which the errors are restricted to relatively small

Table 4.4: Coefficients of the 3rd order polynomial fit to Δy .

Coefficient	Value	Order in x, y
$B_{1,1}$	$-7.28 \times 10^{-3} \mu\text{m}$	
$B_{1,2}$	-2.11×10^{-2}	y
$B_{2,2}$	-4.16×10^{-3}	x
$B_{1,3}$	$3.33 \times 10^{-4} \mu\text{m}^{-1}$	y^2
$B_{2,3}$	$4.21 \times 10^{-4} \mu\text{m}^{-1}$	xy
$B_{3,3}$	$-1.69 \times 10^{-4} \mu\text{m}^{-1}$	x^2
$B_{1,4}$	$1.81 \times 10^{-4} \mu\text{m}^{-2}$	y^3
$B_{2,4}$	$3.94 \times 10^{-5} \mu\text{m}^{-2}$	xy^2
$B_{3,4}$	$1.86 \times 10^{-4} \mu\text{m}^{-2}$	x^2y
$B_{4,4}$	$3.47 \times 10^{-5} \mu\text{m}^{-2}$	x^3

values.

Figure 4.8: Greyscale plot of the 5th order polynomial fitted to Δy .

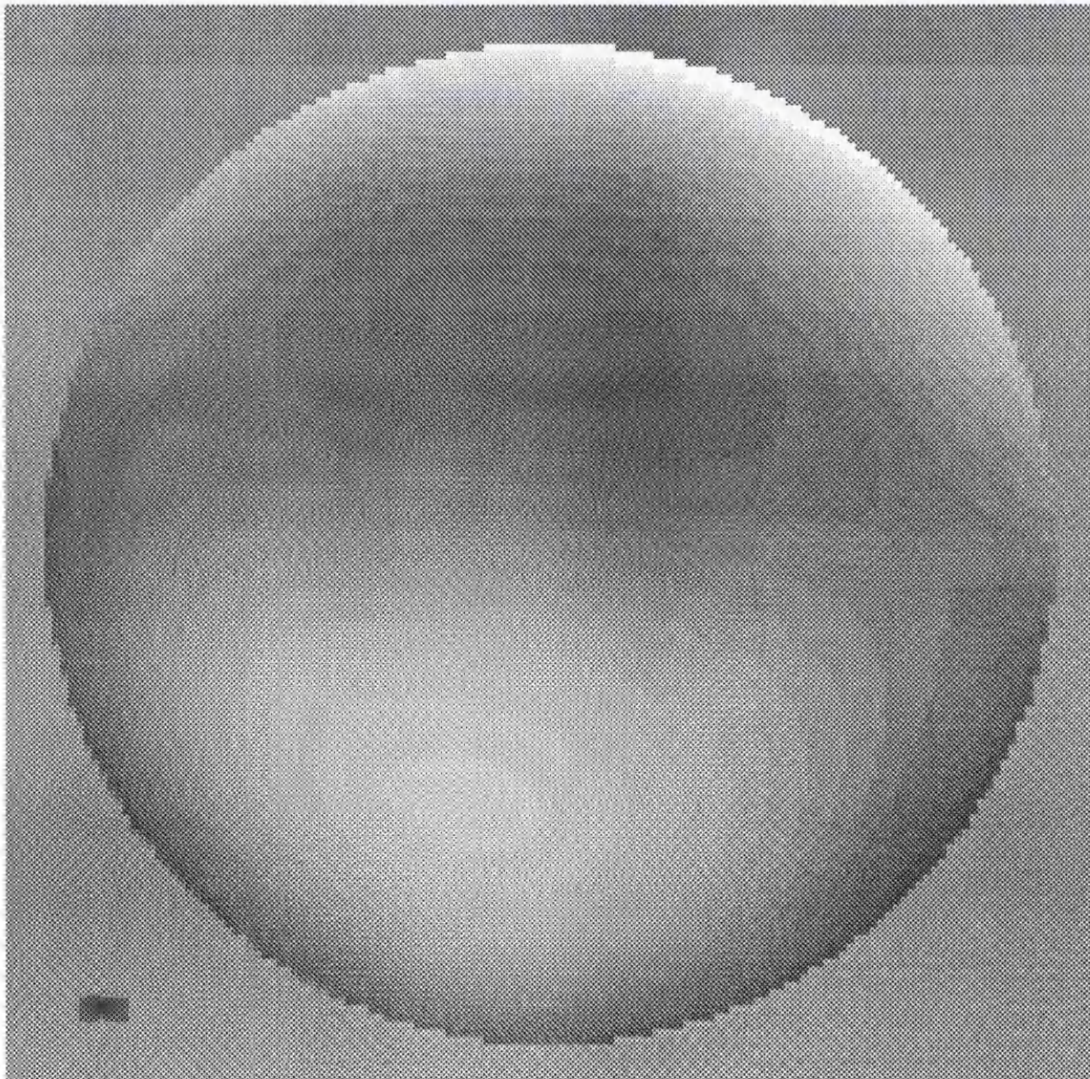


Figure 4.9: Greyscale plot of the 5th order polynomial fitted to Δx .

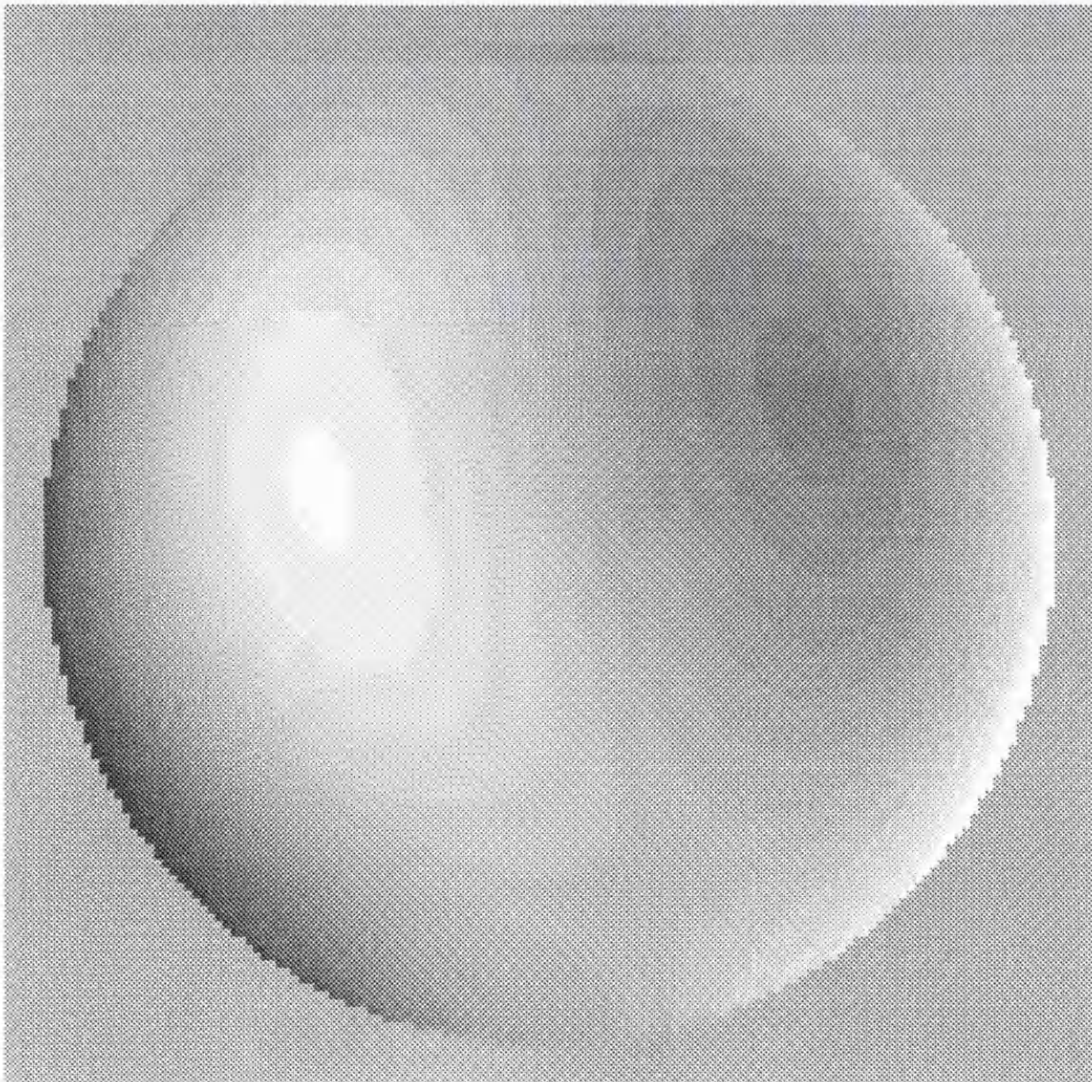
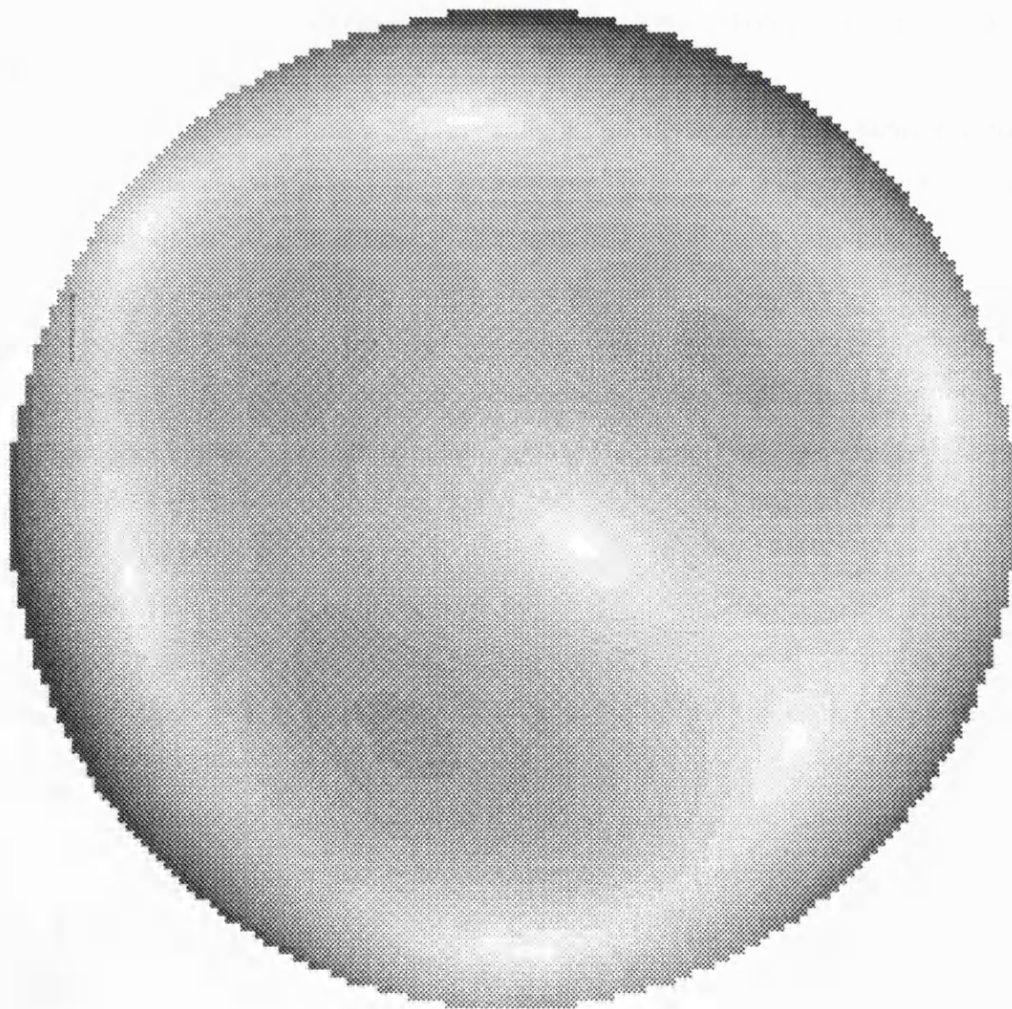


Figure 4.10: Greyscale plot of the absolute error, $(\Delta x^2 + \Delta y^2)^{1/2}$.



Conclusions

A straight line grid was placed at one end of the fibre optic taper and the distorted image grid seen at the other end was recorded and digitized. The object grid was effectively reconstructed by fitting straight lines to the image curves and, by comparing the curves with the straight lines, it was possible to map the distortions introduced by the taper. This map was used both to obtain a figure for the likely maximum error in the position of a guide star due to taper distortion and to characterize the distortion globally in terms of two dimensional polynomials that could be used both to correct guide star positions and in data reduction.

The largest deviation from a $300\mu\text{m}$ straight line anywhere on the taper was found to be $17\mu\text{m}$ and this was at the very edge of the taper. This value is likely to be representative of the largest distortion over $300\mu\text{m}$ of the taper as a whole since pin-cushion distortion is a slowly varying global distortion. Given this property of pin-cushion distortion it is likely that the polynomial fits are a true representation of the errors over the whole taper. These fits can be used to find the error introduced when moving any distance in any direction and at any part of the taper. This is exactly what is required for the purposes of correcting the positions of guide stars which are affected by tracking and roll errors and subsequently correcting scientific data.

The uncertainty in the evaluation of the fibre taper distortion is dominated by the uncertainty in the position of the line centres as seen on the two images. The finite width of the grid lines would have contributed to the FWHM of the intensity profiles and so the actual uncertainty in the line centres is probably smaller than was indicated by these FWHM, especially in view of the small spread of points about the curves fitted by the Starlink software. Without the uncertainty in the position of the line centres the r.m.s. error of the predicted distortion from the true distortion is at most $5\mu\text{m}$ for a 5th order polynomial.

The distortion is greatest at the very edge of the taper and it is also this region where the polynomial fits deviate most from the data. However, only the four corners of the field will be affected by the edge of the taper. This arises from placing an 18mm square into a circle of diameter 25mm – only the four corners of the 18mm field are coincident with the edge of the circle, that is, with the edge of the fibre optic where the distortion is greatest. It should be possible to orientate the taper such that the four corners coincide

with regions of the edge that have low distortion. Therefore, it is unlikely either that the maximum error will be encountered.

A careful examination of the 17 horizontal and 17 vertical lines obtained from the digitized photograph revealed no sign of shear distortions. Within the $5\mu\text{m}$ resolution available in the images there were no discontinuities visible in any of the lines. Thus, one may say that, for the parts of the taper covered by the grid lines, there were no shear distortions greater than $5\mu\text{m}$. This does not mean to say that there are no shears on the rest of the taper – only a small proportion of the taper was covered by the grid lines and so any shears between these lines would not have been visible in the data. It would be necessary to do a similar analysis for every part of the taper in order to say conclusively whether there were shears present. However, one would expect that the effect of shears in the fibre taper would be quite obvious in flat field data but, since no such effect has been seen, it is reasonable to say that any shears that are present have a negligible effect on the data.

4.4 The Fibre Optic Block on the CCD

This 1:1 faceplate is 7mm thick, has $6\mu\text{m}$ fibres and is bonded to the surface of the CCD. The fibres need to have a numerical aperture of 1 to collect light from the narrow end of the fibre taper which emits light in all directions.

Since the block is not tapered, the global distortions are minimal. There are likely to be shears but they must be small and have not introduced any noticeable features into any image.

Effects arising from multi-multifibre junction defects have been observed. In the image they take the form of straight lines of a lower count level which are caused when events are placed in the wrong position. These features are discussed more fully in section 7.6.

In the space qualifiable version of the detector it is intended that the fibre taper will be bonded directly to the CCD and that this will also form the intensifier output faceplate. This will serve two purposes: It will eliminate a source of junction defects and it will also improve the optical coupling by removing the Fresnel reflections which must occur at the two fibre-air boundaries between the taper and the faceplate. In the prototype MIC it is often necessary to raise and lower the CCD with respect to the taper and it is convenient

to have a separate faceplate to protect the CCD.

4.5 The Effect of Radiation on Fibre Optic Glass

It is known (e.g., Friebele, 1979; Manara et al., 1984; Friebele et al., 1984) that glass is affected by high levels of radiation. In particular, Friebele (1979) reports the effect of radiation on optical fibres. There are two effects that could degrade the amplitude of the photon event reaching the CCD

- Colour centre formation. Ionizing radiation may produce electron-hole pairs in the bulk glass which give rise to localised colour centres. These colour centres produce two effects
 - they cause attenuation of light passing down a fibre and thus reduce the transmission of the fibres
 - when the electron hole pairs recombine they may cause luminescence. The luminescence is most intense for shorter wavelengths where the radiation induced attenuation is generally greater. This means that these wavelengths are self-absorbed and so luminescence should not be a problem. In any case, it would be at a very low level compared to the intensity of an event.
- Density changes give rise to a change in the index of refraction of the fibre glass. This can degrade the bandwidth of the fibres. However, since the MIC fibres must transmit only the green light of the phosphor, it is anticipated that this will not be a problem.

Of the above processes the attenuation due to colour centres is likely to be the main cause for concern.

Friebele measured the attenuation in various optical fibres as a function of radiation dose in rads(Si). He notes that the amount of damage incurred by the fibres depends upon

- properties of the radiation – total dose; time since irradiation; dose rate; nature of radiation, that is protons, neutrons etc. and on the energy of the radiation
- operating conditions, notably the fibre composition; the wavelength of transmitted light; the ambient temperature; the intensity of the transmitted light and the radiation history of the fibres.

The damage in a particular fibre depends on all these parameters and so the attenuation in a fibre is very specific to the fibre, the operating conditions and the radiation environment. Now, although Friebele's experimental setup did not resemble the operating conditions or environment expected with XMM, it is possible to infer the likely effect of the XMM radiation environment on the transmission of the fibre optics incorporated in MIC.

The total radiation dose over the ten year XMM mission is not expected to exceed 50 krad. It is necessary from Friebele's data to estimate the likely effect of 50krad on the attenuation in the MIC fibre optics. Friebele tested several different fibre types using light of wavelength 820nm and with a steady state ^{60}Co irradiation. Only one fibre type, the lead silicate fibre, showed severe attenuation at this dosage. Extrapolating the data for this fibre to a dosage of 50 krad gives a total loss of 3×10^5 decibels per kilometre for this fibre. Now, there are ~ 4 cm of fibre optics in MIC so that the attenuation over this distance can be expected to be 12 decibels. This corresponds a ratio of the input to output intensity of 16, that is, the photon pulse output from the fibre optics would be attenuated by a factor 16 compared to the output pulse from the phosphor. There are two points to make here.

- The dose rate for the above experiment was 1.8×10^4 rads per minute which is much higher than that in the space environment. When the source of irradiation is removed all types of fibre show a recovery, the attenuation decreasing with time. Thus, with a high dose rate the level of attenuation reached with a given total dose will be higher than the level reached with a lower dose. Since the dose rate in space is much lower than that of the Friebele experiment it could be expected that the attenuation reached during the mission would be a lot less than 12 decibels.
- Schott were unwilling to give the composition of the fibre optic taper which is the main component of the fibre optics. Thus, it is unknown as to whether the glass contains lead which increases the sensitivity of glass to radiation. However, it is quite possible that it does contain lead as this is common for high numerical aperture fibres such as these. Of the other fibre compositions tested by Friebele, the one with the next highest loss showed an input to output intensity ratio of 1.06 which would not present any problems.

If the ratio of 16 given above for the input to output intensities were correct then it would not be possible to increase the gain of the intensifier to compensate. However, it should be remembered that this figure was arrived at by assuming the very worst case conditions

- The maximum mission dose of 50 krads was assumed. The actual dose may well be lower than this but it depends on the orbit chosen for XMM.
- The worst possible glass composition was assumed. If the glass does not contain lead then there will not be any problem with radiation damage even if every other worst case condition holds
- Recovery of the radiation induced attenuation was ignored. The attenuation would undoubtedly be lower if this were taken into account.

Other factors of Friebele's experiment do not match those expected with XMM, for example, the transmitted radiation for MIC will be 490nm not 820nm and it is expected that the attenuation would be worse at shorter wavelengths. A full study of the correct fibres under the correct operating conditions would be necessary in order to determine accurately the likely effect of the XMM radiation environment. However, it is reasonable to say that if the fibres do not contain lead then there should be no problem with radiation induced damage of the fibre optics.

Chapter 5

The CCD Camera

5.1 Introduction

The charge coupled device (CCD) is a silicon semiconductor device which is capable of image sensing. It consists of a large rectangular array of picture elements, or pixels, which go to make up the image – incident photons are stored as charge within the pixels. The CCD is able to repeatedly transfer the charge from one pixel to the next so that it may be read out of the device into appropriate processing electronics. The process of the transfer of charge from pixel to pixel is called charge coupling.

In MIC, the CCD has a fibre faceplate cemented to its surface and this collects photons that emerge from the fibre taper. The purpose of the CCD is to store photon events from the incoming image and to deliver these to the image processing electronics. The CCD is used in a fast scan mode, that is, many frames per second are read out so that in this respect the CCD acts much like a TV camera. However, compared to the Plumbicon TV camera that was used in the IPCS, the CCD has several advantages:

- It is geometrically stable – the pixels are physically fixed whereas in the IPCS small drifts in the camera scan waveforms resulted in the misregistration of pixels.
- High frame rates are achievable with the CCD, typically 10ms per frame if the full CCD is read out and about 1.6ms per frame if only a small portion is read out. This is discussed more fully in section 5.3.2.
- The CCD has simple drive requirements which means it has a much lower power consumption than the Plumbicon. This is an important property for a space based

system.

- The CCD is physically much smaller than the plumbicon – again, this has obvious advantages for a space based system.

The CCD is a very versatile image sensor which has many desirable properties not just for MIC but for a wide variety of applications.

5.1.1 The Operation of CCDs

Charge is generated in the CCD when incident photons raise the energy of electrons from the valence to the conduction band resulting in the generation of an electron-hole pair. The electron is confined to the immediate vicinity of the point of impact of the photon by the application of a positive potential supplied by an electrode above the pixel. This drives the holes away from the electrode and the electrons become trapped beneath it in the potential well that results. In practical CCDs the electrode, or gate, is electrically insulated from the bulk silicon by a thin layer of silicon dioxide. Also, it is undesirable for the electrons to be stored at the surface of the bulk silicon because this causes problems during charge transfer – the surface layer contains many structural irregularities and defects which can trap electrons and degrade the charge transfer efficiency. Instead, the general structure

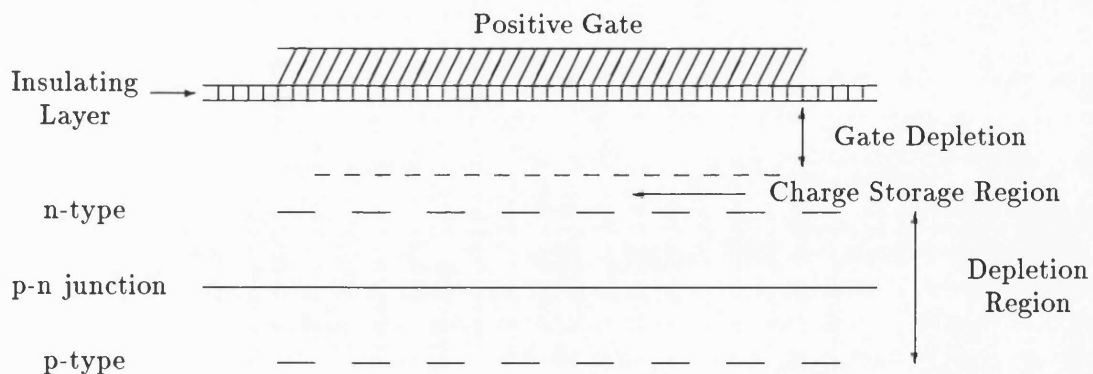


Figure 5.1: Generalised structure of a charge storage site of a buried channel CCD

shown in figure 5.1 is used to create a potential well which is buried inside the bulk silicon. Instead of being attracted just to the positive gate the electrons are also confined by the

positive potential created by the depletion region of the p-n junction. The result is a charge storage region which is buried within the bulk silicon. CCDs which have this construction are known as buried channel CCDs (BCCDs).

Charge is transferred in a CCD by means of a clocking voltage applied to the electrodes associated with each pixel. Take, for example, a pixel that consists of three electrodes, known as a 3-phase structure. Figure 5.2 shows how the clocking voltages applied to the

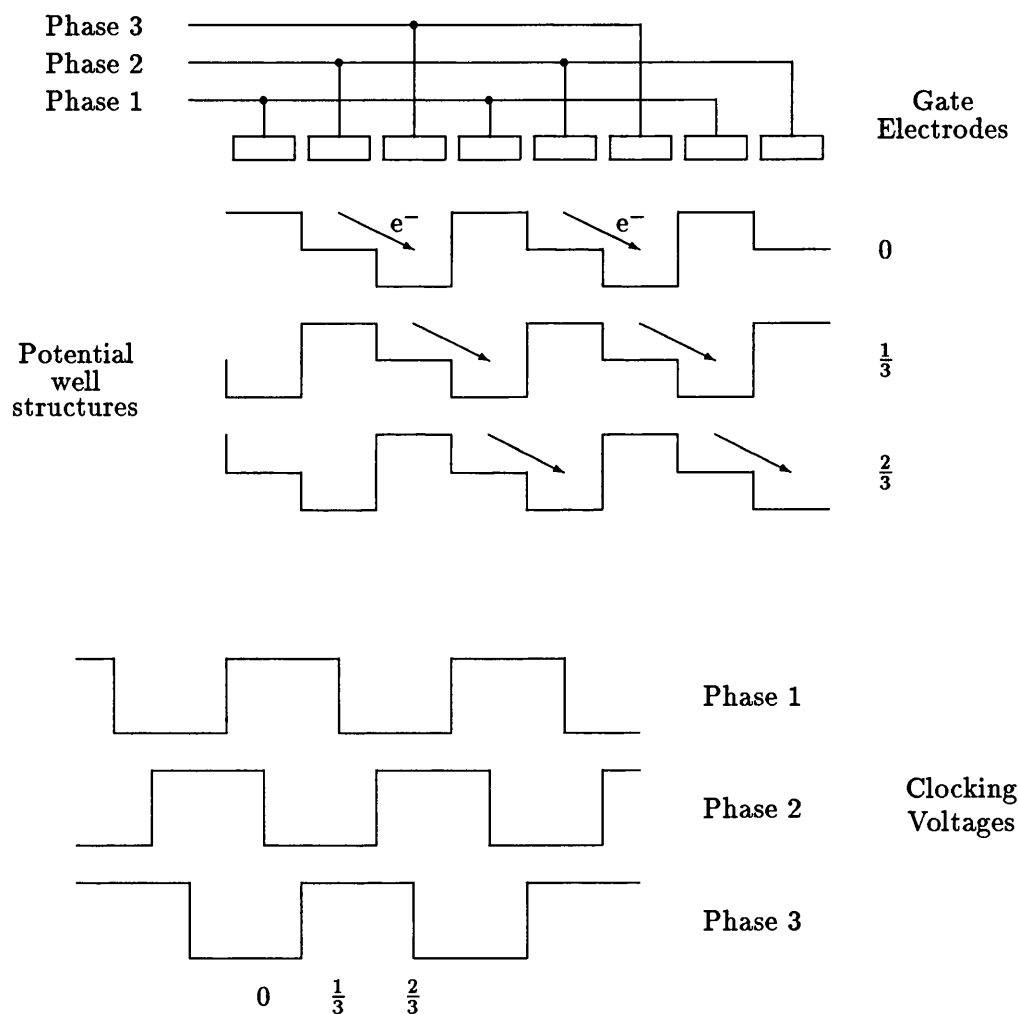


Figure 5.2: Clocking voltages and potential well structures that give rise to charge transfer. The text describes the diagram more fully.

three electrodes result in the transfer of charge from one pixel to the next. At the top the gate electrodes are represented. Each group of three electrodes constitutes a pixel. At the

bottom are the clocking voltages applied to the gate electrodes – they all have the same structure but are of different phase with respect to each other. Above the clocking voltages the potential well structures that result from the application of the clocking voltages are shown. The structure is shown after 0, 1/3 and 2/3 of a cycle. With reference to the same figures shown on the clocking voltages, it is easy to see how the three phases result in charge transfer; it is the change of profile of the potential within the bulk silicon that facilitates the transfer.

Transfer of charge may also be achieved using 4-phase, 2-phase and virtual phase structures. The 2-phase structure uses an implant beneath each electrode to alter the depth of the potential well beneath it and produce a staircase potential structure. With one of the two electrodes held at a constant potential and the other toggled between high and low, the staircase potential is altered in such a way as to transfer the charge from one site to the next much as in figure 5.2. The 4-phase structure achieves a similar staircase potential by means of electrodes whereas the virtual phase structure removes the constant d.c. electrode and achieves the same effect with different levels of doping.

Whilst the pixel boundaries between rows are formed by the clocking voltages, those between the columns are formed by additional thin columns of heavily doped material which are known as channel stops. These prevent any movement of charge between pixels in the same row.

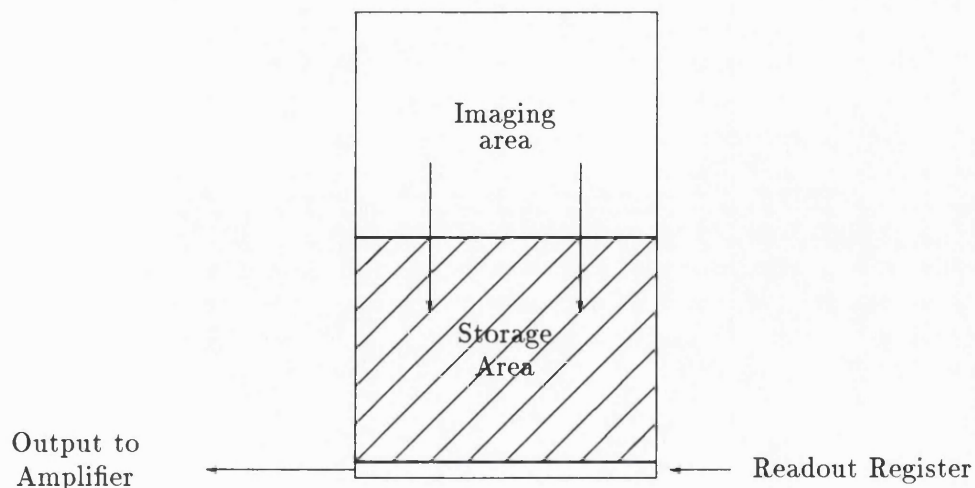


Figure 5.3: Schematic of the regions of a frame transfer CCD

The MIC CCD is a frame transfer CCD which is illustrated in figure 5.3. The device consists of an image area, a storage area and a readout register. There are three sets of clocks that control the frame transfer CCD

1. The vertical clocks for the image area
2. The vertical clocks for the storage area
3. The Horizontal clocks for the readout register

The image area collects a charge image of the field of view. With clocks 1 and 2 active, the whole image, or frame, is transferred to the storage area. The storage area is the same size as the image area and is masked from the source of photons. While the next frame is integrating on the image area the storage area is read out of the device as follows.

- With clocks 2 active, a single row of the storage area is transferred into the readout register, which consists of only one row of pixels.
- With clocks 3 active, this row is read out from the device one pixel at a time in a direction perpendicular to the direction in which it entered the readout register.

These two steps are repeated until the whole frame has been read out of the device pixel by pixel. Because it transfers charge in only a single row of pixels, the readout register is often called the serial or horizontal register whereas the storage area is known as the parallel or vertical register because it transfers charge in all the columns simultaneously and in a direction perpendicular to the horizontal register.

After all the pixels in a row have been read out the next row is transferred from the parallel register to the serial register and this is read out pixel by pixel and so on. In this way the entire image is read out of the CCD one pixel at a time. While the read out is taking place the next frame of data is integrating in the image area.

The XMM-MIC CCD is a Thomson CSF TH7863 which has 384 horizontal and 288 vertical pixels which are $23\mu\text{m}$ square. The choice of CCD was determined by the following

- It had undergone radiation testing at ESA. The effects of radiation on the CCD are discussed in section 5.4.
- It has a 2-phase horizontal and 4-phase vertical clock structure which permitted the simplest design of the control electronics.

Associated with the CCD are the CCD camera electronics which are not only required to process the pixel data but to control the operation of the CCD. The camera electronics are discussed in section 5.3.

5.2 CCD Performance

There are several quantities relating to CCD performance that affect the performance of the system as a whole.

Quantum Efficiency

The quantum efficiency of the CCD peaks at around 40% in the red and drops off towards the UV. At 490nm, which is the wavelength of the green light emitted by the phosphor, the quantum efficiency is still $\sim 25\%$. This quantity determines what proportion of the photons emitted by the phosphor contribute to the output signal of the CCD. For example, the number of photons from an event that reach the CCD is typically 6×10^5 and, with a quantum efficiency of 25%, this corresponds to 1.5×10^5 electrons per event. This signal is sufficient to make the event clearly discernible above any noise.

Charge Transfer Efficiency

The charge transfer efficiency (CTE) is the percentage of the signal in a pixel that is transferred during a single charge transfer to the next pixel. This depends on external clock electronics but is typically $\sim 99.9995\%$. If the device had poor CTE then it would easily be noticed as a ‘smearing’ of events. If a significant proportion of the charge in a pixel is left behind during charge transfer then, after several hundred transfers, the event shape would be obviously asymmetrical and there would be a small tail to it. This would also affect the centroiding procedure described in section 6.6.3. No effect of charge transfer inefficiency (CTI) has been noticed.

Noise

Thermal noise and readout noise contribute ~ 350 electrons to the signal. With the Analog-to-digital-converter (ADC) set so that 1 ADU is equivalent to 400 electrons, the noise on any data is less than 1 ADU.

Dark Current

The dark current is the thermally generated signal that exists even in the absence of incident photons. At 25°C, the expected operating temperature for XMM-MIC, the dark current is $\sim 2\text{--}3000$ electrons. As is discussed later, this level of dark current is beneficial for combating radiation damage effects. The dark current does not affect the photon event data as it is subtracted from the signal before it is processed.

Cosmetic Quality

The CCD may have a number of defects and blemishes. The manufacturers class blemishes into three types

- white defects – these depend on temperature like dark current and their level increases twofold every 8–10°C.
- black defects – these do not depend on temperature but their amplitude is proportional to the mean output voltage.
- trap defects – these give rise to a partial black column and hold a constant amount of charge.

The manufacturer's data say that if the blemish amplitude, α , is less than 20% of the video signal then it is not a blemish and if it is greater than 30% then the device is rejected. Thus, $20\% < \alpha < 30\%$. They go on to say that a device may have up to 10 black defects but no white or trap defects. The number of defects that may be present with amplitudes less than 20% could be quantified by exposing the CCD directly to a uniform flat field.

5.3 The CCD Camera

The camera electronics are required to operate the CCD and to process the pixel data for presentation to the image processing electronics. The camera was entirely designed and tested by Dr. D Bone at UCL.

There are a number of important requirements of the camera electronics which may be summarised as follows:

- The frame rate should be as fast as possible to maximise the system's dynamic range.

The read out register is run at 10MHz and the parallel register is run at 2 MHz.

- The power consumption should be as low as possible for a space based system. High speed CMOS devices of the 74HC series have been used wherever possible but also the choice of CCD and various features of the camera electronics facilitate lower power consumption
- The active area for CCD read out should be 256×256 pixels.
- There should be a windowing facility that allows up to 16 separate data acquisition windows to be selected within the 256×256 area. The windowing function is discussed in section 5.3.2

These requirements have been incorporated into the design of the camera electronics.

The CCD camera electronics may be split into two sections:

- A CCD support section that includes the sequencer and buffers for CCD clock voltage generation; a bit-map look-up table for controlling the format and windows and a computer interface
- A video signal processing and digitizing section that includes the analog-to-digital converter (ADC) as well as the video processor.

Figure 5.4 shows a photograph of the camera electronics as part of the detector head. The electronics are butted to the fibre taper which is not visible in the photograph, and this is butted to the intensifier which is also hidden from view. All the camera electronics are contained at the detector head on three printed circuit boards. This allows minimal power consumption by removing the need for power consumptive line drivers and receivers. For a space version of MIC the intention is to condense the electronics onto a single printed circuit board. The camera is powered by a +5V supply for the digital electronics and a +15V supply for the CCD and analog electronics.

A block diagram of the camera electronics is shown in figure 5.5. The two sections referred to above are indicated by dotted lines and the various parts within these are shown.

5.3.1 The Signal Processing and Digitizing Section

A block diagram of this section is shown in figure 5.6. Various clocks and signals are shown in figure 5.7 and these are referred to at various points in this section.

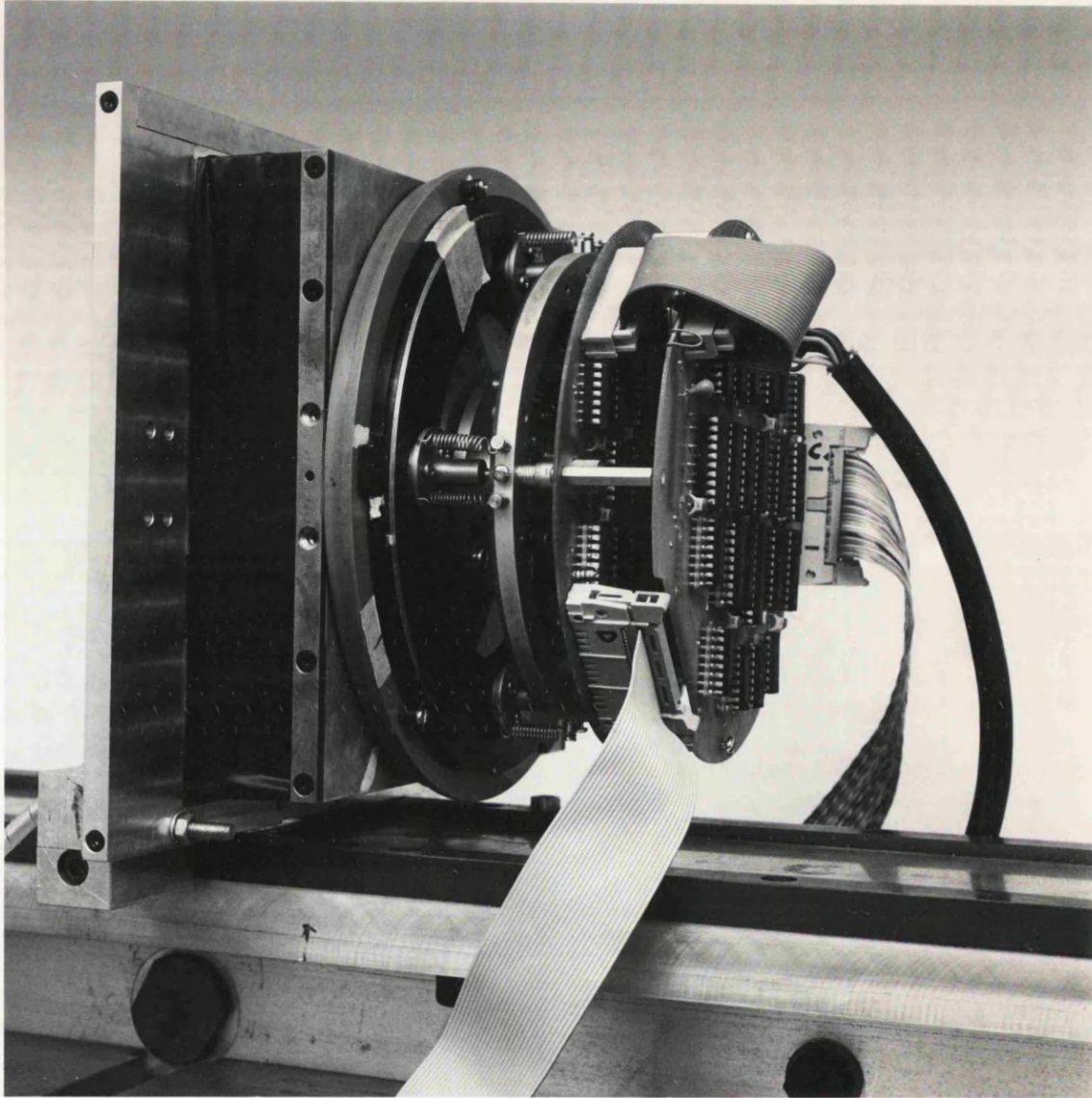


Figure 5.4: Photograph of the camera electronics as part of the detector head

A **pre-amplifier** with a gain of approximately 9 first receives the video output from the CCD. This gain value is convenient for matching the range of pulse heights to the range of the ADC. For example, for an event at the peak of the pulse height distribution with typically 40000 electrons in the peak pixel, and given that one electron represents $2.13\mu\text{V}$ on the CCD output, an amplification of 9 gives a value in ADU (analog-to-digital units) in the middle of the range of the ADC which is 2–2.5V.

The **sample-and-hold (S/H)** circuit removes reset noise and high frequency components in the signal. The signal appears as a series of spikes and noise with true signal data

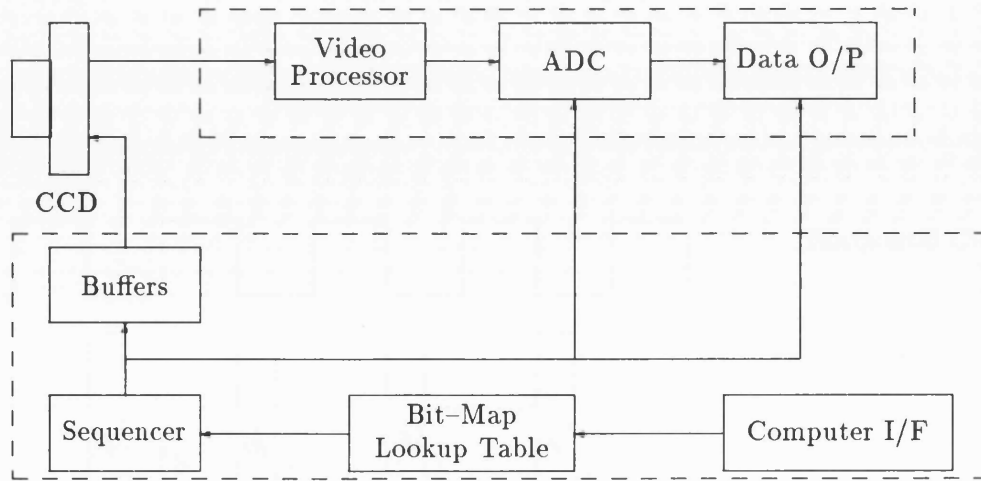


Figure 5.5: Block diagram of the CCD camera electronics

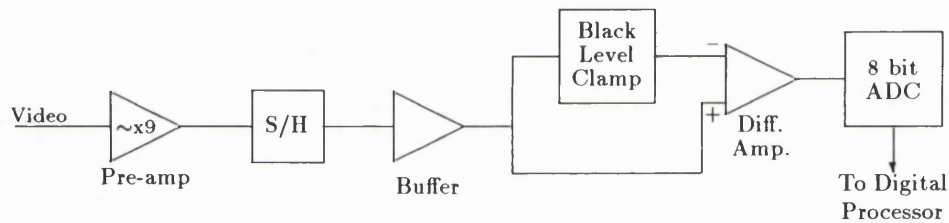


Figure 5.6: Block diagram of the video processor section

at regular intervals inbetween. The S/H circuit samples the signal every clock cycle at the point of the true data and then holds that level until the next sample. The resulting signal is flat at the level of the data for most of a clock cycle. Thus, the output of the S/H is essentially noise free.

The signal is then buffered before being passed to the **black-level clamp** circuit. At room temperature a lot of electrons are generated by random thermal processes. This dark current results in a d.c. bias upon which all other data sit. Moreover, for rows which are further away from the read out register, the dark current is higher since those rows are the last to be read out and so have a longer time in which to accumulate thermal electrons. Thus, each row has a different level of dark current and therefore a different

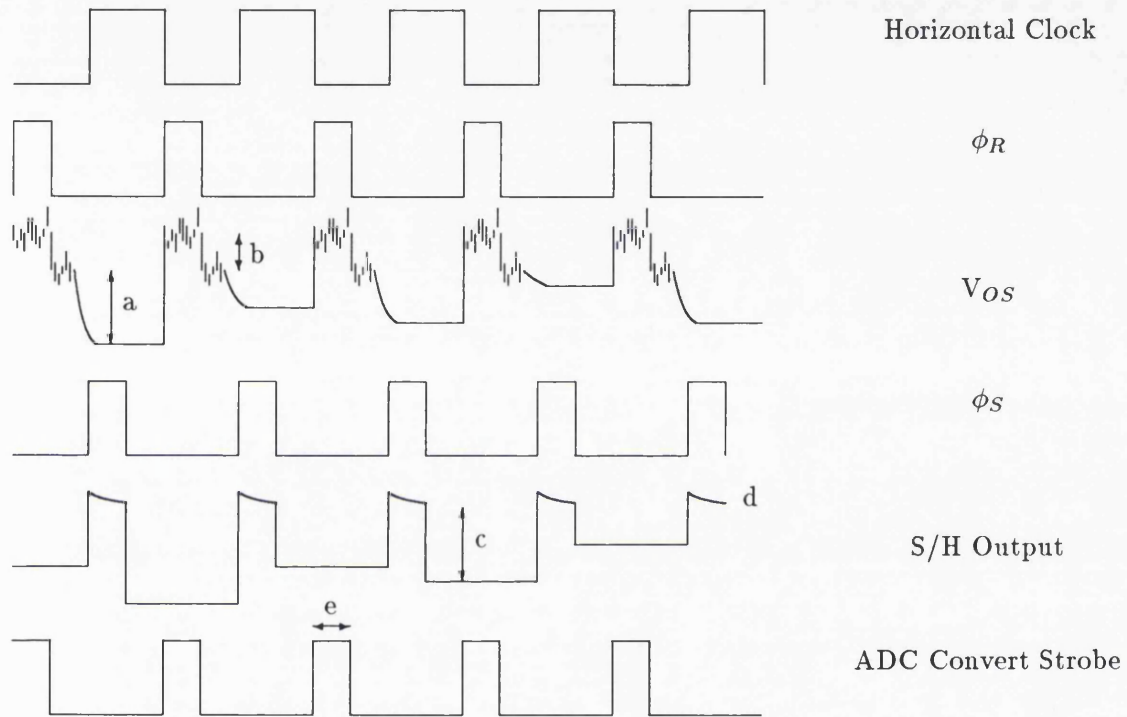


Figure 5.7: Clocks and signals associated with the signal processing and digitizing section. Four clocks are shown which have the same frequency but different phases: The horizontal clock of the CCD; the reset clock, ϕ_R ; the sample and hold clock, ϕ_S ; the ADC convert strobe. Also shown are the raw video output from the CCD and the output from the sample and hold. Five other quantities are indicated: (a) Raw signal, (b) reset clock feedthrough, (c) signal after sample and hold, (d) sample and hold clock feedthrough and (e) the ADC convert enable.

d.c. offset, or black level. With the Thomson chip the last eight pixels of each row are optically masked and these provide a reference black level clamp for the next row. This level is subtracted from the incoming video signal and additional gain is supplied.

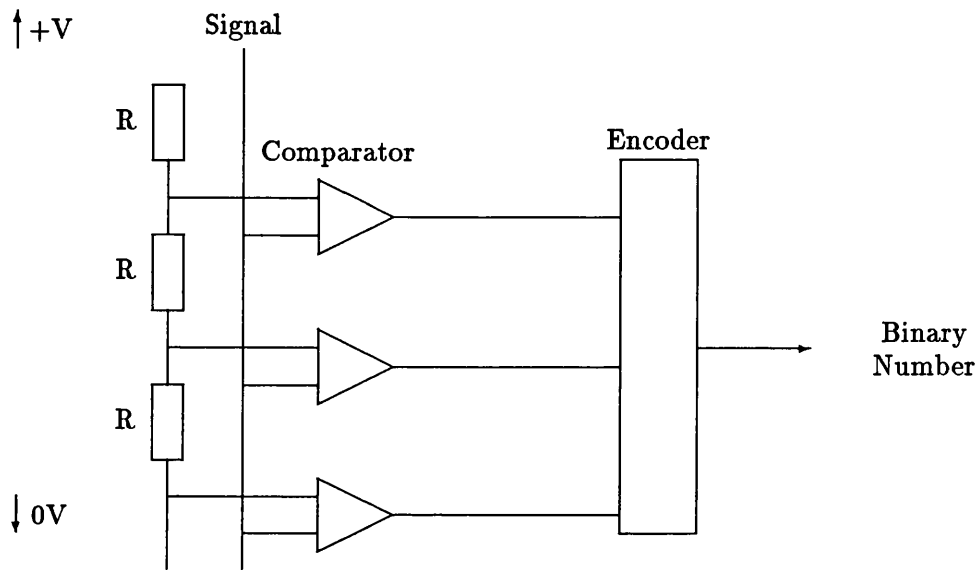


Figure 5.8: Schematic of a section of the 'flash' Analog-to-Digital Converter

The analog-to-digital converter (ADC) is a CMOS 'flash' converter which digitises the video signal into 8 bits at the 10MHz horizontal clocking frequency. A schematic of a small section of the converter is shown in figure 5.8. It consists of 256 resistors in series, each being of the same value to a high degree of precision. A voltage is applied across them so that at each successive point in the chain the voltage is an exact multiple of that across a single resistor. The output at each point of the chain is input to a comparator whose other input is the signal output from the sample and hold. These comparators output '1' if the signal is greater than the voltage at that point in the chain and '0' if it is smaller. Each voltage in the chain represents one step up in ADU, the whole range being 256 ADU. So, for example, if the signal output from the S/H was 150 ADU then the first 150 comparators would output '1' and the remaining 106 would output zero. The comparators continuously sample the data and the number of outputs whose value is 1

rises and falls according to the level of the signal – this is known as the thermometer effect. The outputs from the comparators are input to an encoder which outputs the correct binary number corresponding to the signal level. The convert strobe simply enables the output of the encoder and does so with the correct timing appropriate to the arrival of the true signal as shown in figure 5.7. Errors in conversion may arise from non-linearities in the resistor chain or from noise coupling through from the signal chain. The error on the ADC employed is $\sim \pm 1/2$ the least significant bit. The digitized signal is sent out of the camera head via the data output which consists largely of line drivers. These data are passed into the image processing electronics.

5.3.2 The CCD Support Section

This section generates the control signals for operating the CCD and for the timing of the video processor. It also performs the important windowing function that has been mentioned.

The sequencer

This section consists of a horizontal clock generator and a vertical clock generator.

The horizontal clock generator produces the following control signals:

- The horizontal clocks
- The reset clock for the CCD
- The sample and hold clocks
- The convert strobe for the ADC

All these clocks have the same frequency of 10MHz but have different phases appropriate to the timing required for the various components as shown in figure 5.7.

The vertical clock generator produces

- The clocks for the transfer of data from the image to storage areas of the CCD which run at 1.25MHz.
- The clocks for the transfer of data from the storage area to the read out register which are active once every row.

Again, for low power consumption, high speed CMOS is used to generate all these signals.

The Clock Buffer Circuit

Before the clocks generated by the sequencer can be used by the CCD, they have to be converted to the required levels. The levels are provided by +5V and +10V rails in the clock buffer circuit. Power consumption is kept to a minimum by the choice of integrated circuits. For the vertical clocks, which are mostly inactive, CMOS clock drivers are used to give minimum quiescent power consumption. The remaining clocks use bipolar drivers for level conversion in order to give minimum dynamic power consumption.

The Bit-Map Look-up Table and Windowing

Control of the clock generation is provided by an input from a bit-map look-up table which performs the windowing function.

The windowing facility allows up to 16 user defined windows to be placed within the 256×256 detector format. The facility is required for two reasons:

- Memory limitations forbid data acquisition on the full 2048×2048 , that is 256×256 with $\times 8$ centroiding resolution
- Up to ten of the windows will be used to acquire data on selected guide stars and these will be used to measure telescope tracking and roll errors. This function of windowing was discussed more fully in section 2.2. The remaining six windows can be used for scientific data acquisition.

An important property of windowing is that it can increase the dynamic range of the system considerably. This is described shortly.

Control of the windowing is provided by a $64k \times 4$ bit memory called the bit-map look-up table. Each memory location in the look-up table is associated with a 2×2 group of pixels. The reason for grouping the pixels into twos is simply to reduce the size of the memory, but it means that the window dimensions in pixels must be a multiple of two. The look-up table defines which pixels form part of an active window, the output of the look-up table being essentially a 'yes/no' in this respect. Pixels which do not fall within an active window fall into two categories in terms of how they are dealt with:

- If a whole row of pixels is not within a window then the bit-map look-up table instructs the sequencer that the row is not to be read out. The row is still shifted

into the read out register but this register is not clocked. This means that if there are several rows which are not in the window then these are 'dumped' on top of each other. Take the simple example of the windowing shown in figure 5.9. The first

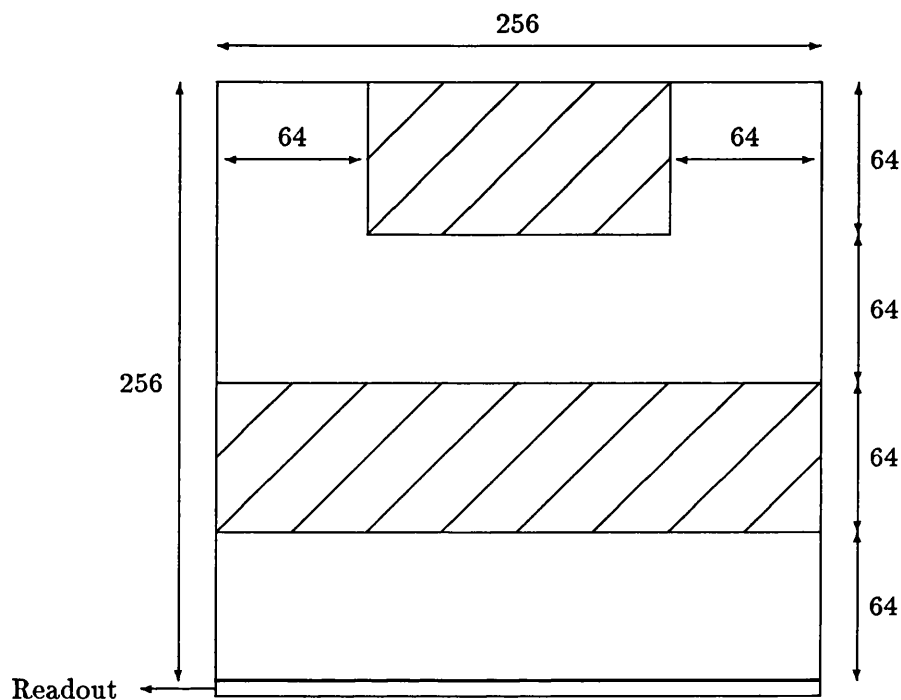


Figure 5.9: A simple example of CCD windowing

64 rows are dumped on top of each other in the read out register. Two rows before the window, the serial register is read out to clear it of the charge accumulated in it during the dumping. Then the next row, which is in the window, is read into the serial register and read out. This mechanism thus defines the horizontal boundaries of the data acquisition windows.

It also has one other important consequence – it increases considerably the frame rate of the CCD. The reading out of the serial register is the most time consuming part of a frame period because it is taking place almost constantly. By dumping a large number of unused rows and not clocking the serial register, time is saved which would otherwise have been taken to read out the dumped rows. Thus the frame time is reduced. For example, with only a 32 pixel strip, such as may be used

on a spectroscopic format, the frame time is reduced from 10ms on a full format to just 1.6ms. The effect of an increased frame rate is to considerably increase the high count rate end of the dynamic range characteristics because the probability of events being coincident within a frame period is reduced.

- For pixels that are part of a row in which there is a window but that are not actually within the window, the data output from the CCD are blanked, that is, set to zero. For example, take the windowing of figure 5.9. After the first window, A, the next 64 rows are dumped. Part of the next row forms a window so the row is read out. However, the bit-map look-up table has instructed the first 64 pixels of the row to be blanked along with the last 64 pixels. This blanking defines the vertical boundaries of the data acquisition windows but has no effect on the frame rate.

A different set of windows may be used for every separate integration and so the bit-map look-up table must be reloaded prior to every integration that has new window definitions. This is accomplished via the computer interface which consists of buffers and a decoder.

In summary, the CCD camera is a compact, low power consumption unit consisting of a CCD support section and a video signal processor that provides data for the image processing chassis. A specification of the CCD's most important characteristics is as follows.

Horizontal clock	10MHz
Vertical clock	2MHz
Full format	256×256
Pixel size	23 μ m
Full format frame rate	97Hz
Output	8 bits

For a space qualifiable version of MIC the vertical clock will need to be limited to 1.25MHz due to electronic reliability constraints, particularly associated with maintaining the correct clock overlaps for best operation of the CCD.

5.4 The Effect of Radiation on the CCD

The radiation environment encountered by a spacecraft orbiting the earth is particularly harsh, sources being from the Earth's own radiation belts, the sun and from cosmic rays. It is important that an estimate is made of the likely effect of radiation on the performance of the CCD, particularly since the CCD is such an important component of the system.

5.4.1 A Summary of Radiation Effects

Various studies have been carried out concerning the effects of radiation on CCD devices (Hopkinson, 1989; Officine Galileo, 1990; Holland et al., 1991). In particular, the damage incurred by the CCD depends not only on the total dose but more significantly on the type and energy of the radiation.

The various radiations may be split into two categories in terms of the way in which the energy is lost

- where there is ionising energy loss
- where there is non-ionising energy loss (NIEL)

Of the two, the second has the more permanent effect.

Ionising Energy Loss

This type of energy loss can be attributed mostly to electrons, gamma rays and X-rays. In general, the effects of ionising radiation are not permanent as they involve the creation of electron-hole pairs. There are three main effects of ionising radiation

- Flat band voltage shift. The creation of electron hole pairs in the oxide layer can result in trapped holes if the electrons migrate away. These holes modify the gate potential, usually to a more positive voltage, and affect the operation of the CCD. The effect is worse for CCDs that are irradiated whilst powered up or at low temperatures. The effect of the flat band voltage shift is generally to degrade the charge transfer efficiency (CTE) although if very severe it may halt charge transfer altogether.

- **Dark current generation.** Additional states at the oxide-silicon interface may be formed with energies in the forbidden gap. These assist electrons to hop to the conduction band and the result is an increase in dark current.
- **Charge transfer efficiency degradation.** Occasionally, the energy of an electron may be sufficiently high to displace the silicon atoms in the lattice resulting in interstitial silicon atoms and vacancies. The vacancies may act as carrier traps and the result is a degradation of the CTE.

Non Ionising Energy Loss

This form of damage results mostly from protons, neutrons and heavy ions. Most of the effects result from the displacement of silicon atoms from their position in the lattice. The resulting vacancies are mobile within the lattice and migrate, forming defect complexes with other sites in the lattice, for example, the phosphorous vacancy (P-V) complex or oxygen vacancy (O-V) complex. These complexes may act as carrier recombination or carrier formation centres or as carrier trapping sites. There are three main effects of displacement damage

- **Loss in sensitivity.** The presence of recombination sites affects the carrier diffusion length and lifetime and thus the number of carriers is reduced resulting in a loss in sensitivity.
- **CTE degradation.** The presence of trapping sites results in a degradation of the CTE because the release time constant of the trap may be long compared to the time taken to transfer charge to the next pixel – when the carrier is released it is in the wrong charge packet. CTE degradation is worse for protons than for very energetic electrons because the number of displacements produced per proton is far greater. If a proton is particularly destructive it may result in a defect cluster.
- **Dark current spikes.** The vacancy complexes form states with energies in the forbidden gap and this assists electrons to hop to the conduction band causing an increase in dark current. If the proton produces a defect cluster then the dark current in a certain pixel may be much larger than in its neighbours and this is known as a dark current spike.

5.4.2 Radiation Effects for the MIC CCD

When it is operating in space, MIC will be constantly generating heat and will attain a temperature of about 25°C. At this temperature the dark current will be high, typically being 2000–3000 electrons. This is an important property of the MIC CCD with respect to the effects of radiation. The presence of a large dark current will considerably reduce the effectiveness of the trapping site to affect the CCD's performance. Although displacement damage will still take place the resulting vacancies will be rendered inactive by the presence of the high dark current. The reason for this is that the trapping sites are saturated by the large numbers of thermal electrons, they cease to become efficient carrier traps and the CTE is largely preserved. The large dark current is not a problem; the black level clamp circuit removes the d.c. bias that arises as a result of the dark current. This circuit will also remove any additional dark current that is caused by incident electrons since the masked pixels will also be subject to the same level of electron bombardment. Dark current spikes will not be a problem either since they will be swamped by the large thermally generated dark current.

It is important, then, that MIC should have a large dark current to combat the effects of radiation. However, this does not mean that the CCD can be irradiated indefinitely without its performance being affected. The proposed lifetime of the XMM mission is ten years. This is a long enough time that the CCD could be subjected to a large total dose, especially if there is a large solar flare or if adequate precautions are not taken. The number of defects could build up to such a level that the large dark current would no longer be effective in preserving the CCD's performance characteristics.

In the space environment, electrons and protons are by far the most dominant forms of radiation. Electrons are likely to add to the system noise but not produce any long term effects whereas the effect of proton irradiation is likely to produce more permanent damage. High energy protons tend to pass straight through the silicon but the low energy protons may stop directly in the bulk silicon or the charge collection region. Thus, it is the low energy protons that are likely to cause more serious damage to the CCD. What dose of low energy protons can the CCD tolerate before its performance is affected?

Hopkinson (1989) reports the effect of radiation on EEV CCDs which are 3-phase devices. When operated in a fast scan mode at room temperature he reports that the CCD performance was essentially unimpaired after 3.4 krads of low energy protons. The

rad is a unit used to quantify the level of radiation to which an object is subjected and it stands for Radiation Absorbed Dose. The rad is equivalent to 6.25×10^7 MeV per gram. Since radiation interacts differently within different materials, the irradiated material must be specified when quoting a dose in rads. Also, it is not possible to convert a dose in rads into one of, for example, protons per cm^2 since the energy of the protons must be taken into account. Very approximately, says Holland, 1 rad is equivalent to 1.5×10^6 of 10 MeV protons per cm^2 .

Holland goes on to predict that EEV CCDs operated in TV mode at room temperature could withstand *at least* 10krads before their performance was degraded. The effect of radiation on a 4-phase structure is likely to be similar to that for the EEV 3-phase. The effect on a 2-phase structure is less predictable – the 2-phase structure has extra implants which could worsen the effect of irradiation on performance. However, in view of the stifling effect of a large dark current on trapping site efficiency, the dose that a 2-phase structure is able to tolerate is likely to be similar, i.e., about 10krads. As a general guideline, then, 10krads may be considered as the dose tolerable by the MIC CCD before its performance is affected. According to Holland, 10krads is equivalent to about 10^{10} protons/ cm^2 of 6.5 MeV, or low energy, protons. Therefore, the total dose of low energy protons, say up to 15 MeV, received by the MIC CCD over the entire ten year mission should be kept below about 10^{10} per cm^2 .

5.4.3 The XMM Radiation Environment

The level of radiation to which the CCD will be subjected depends very much upon the orbit of the XMM spacecraft. The original choice of orbit for the craft was a highly eccentric one which would take it through the heart of the Van Allen Belts. This orbit was thought to subject the craft to an unacceptable level of radiation and alternative orbits have been considered.

Daly (1991) has modelled the proton and electron spectra of the various orbit options and has also modelled the modified shielded spectra. His data suggest that for low energy protons in the 5-15 MeV range, with the worst case choice of orbit and the least effective shielding, the total flux of trapped protons over the entire mission lifetime would be about 10^8 per cm^2 , which is well below the suggested safe limit for the MIC CCD of 10^{10} . However, his data also suggest that the contribution from solar protons is much larger

and that, even in the best case, the contribution is twice that from trapped protons. This number is still well below the number indicated for the onset of the MIC CCD degradation so therefore, with appropriate shielding, it is unlikely that the CCD's performance will be significantly affected.

The 10^{10} figure set for the level tolerable by the CCD is an estimate based on data from other sources with different CCDs for different applications. If a reliable figure was wanted for a tolerable dose then an experimental study on the same setup would be necessary. It would be unwise to assume that the CCD will not be affected by irradiation – a large solar flare might produce a significant degradation of the CCD's performance. Two possible extra precautions are possible to keep the radiation effects to a minimum:

- The use of special CCDs. Devices that are made with multi-pinned phase (MPP) technology are known to be more radiation hard than standard CCDs. The volume of the potential well in these devices is reduced so that incident radiation is less likely to cause damage in the important charge storage region of the pixel. The increase in charge transfer inefficiency is reduced by a factor of about 3 in these devices. Even if an MPP device is not used for the XMM MIC, an EEV chip will probably be used as the Thomson chip is believed to be less radiation tolerant.
- High temperature annealing. Holland et al. (1991) found that around 80% of the lost CTE could be recovered by a high temperature anneal at 127°C for 45 hours. This could be used to recover most of the CCD's performance after a long period of irradiation or after a large solar flare.

In summary, due to its high dark current, the performance of the MIC CCD is unlikely to be affected by irradiation over its ten year lifetime.

Chapter 6

The Image Processing Electronics

6.1 Introduction

Before the processing electronics are described, a brief recap will be given.

A photon incident on the photocathode of the image intensifier releases an electron which is accelerated under the influence of an applied potential and enters a pore of the front channel plate. This initiates a cascade through three channel plates which produces a pulse of electrons striking the output phosphor. Around 10^7 photons per pulse are produced by the phosphor and these are coupled via a 6% efficient fibre optic taper to a fast scanning CCD. The CCD has a peak efficiency of 20% to the green light of the phosphor and is therefore able to detect around 1.3×10^5 photons per pulse which appear as a splash of charge, or event, on the CCD covering around 1.4 pixels FWHM. The CCD is read out to the CCD video processing electronics where the video data are amplified and black level clamped to remove the dc level. The video data are then digitized by an 8-bit flash analog to digital converter (ADC) and passed on, pixel by pixel, to the image processing electronics.

The primary functions of the image processing electronics can be summarised as follows:

- to 'recognise' events
- to centroid events to 1/8 CCD pixel
- to define an address for each event

- to transmit data on each event to the Direct Memory Access (DMA) interface within the computer for storage.

In addition there are a number of facilities which perform other important functions.

The processing electronics can be split up into a number of blocks that perform specific functions. Figure 6.1 is a block diagram of the electronics showing the relation between the various blocks.

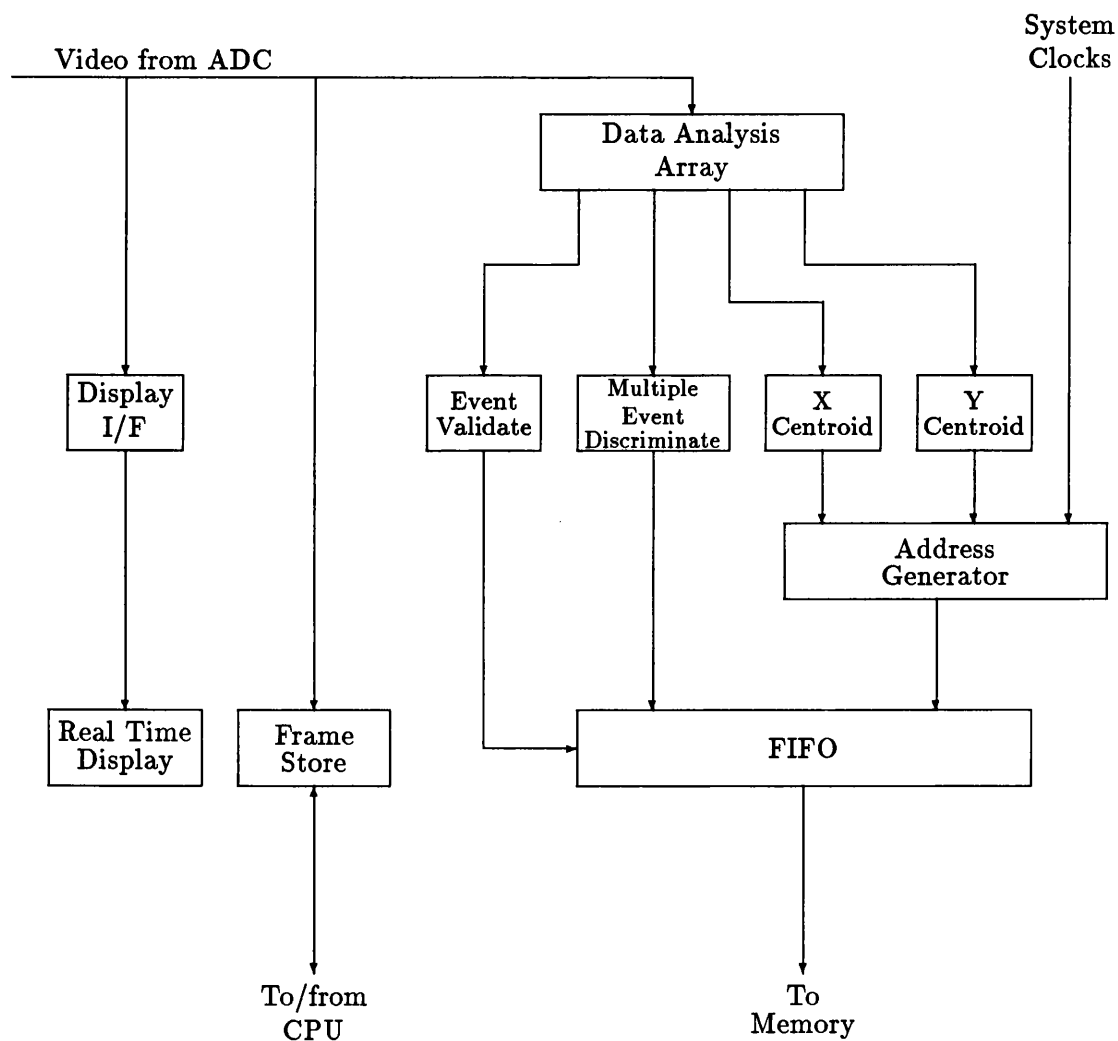


Figure 6.1: Block diagram of the image processing electronics

The *Data Analysis Array* (DAA) receives every pixel of data one after the other. It

centres each pixel of data in a 3×3 array with its nearest neighbours as it would have been on the CCD. The output of this array is used by the Event Validate, Centroid and the Multiple Event Discriminate circuits. *Event Validate* uses a number of criteria concerning the data contained in the 3×3 array to decide when an event is present and centred in the array. The *Multiple Event Discriminator* uses the array data to calculate the energy contained within the array and thereby decide whether there is one event present or more than one. If there are more than one then it sets a flag. The *Centroid* circuit uses a special centroiding technique to calculate the arrival position of an event to within $1/8$ of a CCD pixel in both X and Y and produces a 3-bit centroid position for both. The *Address Generator* uses the system clocks and the two 3-bit centroid positions to define an address at which the data for an event will be stored in the detector memory. The *First-in-first-out* (FIFO) memory is used to store the address and data of each event until the detector memory is ready to receive it. In addition to those blocks shown in figure 6.1 there is a *Memory Interface* which initiates and carries out transmission of an event from the FIFO to the memory. The *Display Interface* enables the raw video data to be viewed in real time on an electrostatic monitor which allows the immediate assessment of, for example, whether the camera is functioning properly or whether the input to the intensifier is too bright. The *Frame Store* is a very important test facility which operates in two modes

- It can grab frames of raw video which can then be analysed by the computer to study various properties of the data.
- It enables simulated data to be fed through the processing electronics in order to check that they are functioning correctly.

The CCD camera provides a number of signals as well as the data from the video processor. The sequencer within the camera provides the system clocks which control the timing of the image processing circuitry. There are four of these

- SYCLK – this is the main 10MHz clock of the CCD read-out register.
- LS*, line sync – this signal goes low after each row has been read out and it remains low until the start of the next row.
- FS*, frame sync – this signal goes low after each frame and it remains low until the start of the next

- WA, window active – used for the multiple windowing facility described in section 5.3.2, this signal is high when the CCD coordinates fall within a designated window.

The various circuits in the processing electronics are built on wire wrap boards which are housed in a chassis. Connections between the boards are made via a backplane which runs along the back of the chassis. A photograph of the image processing chassis is shown in figure 6.2. Two of the slot positions are empty. One is not occupied while the other has had the board removed to show the integrated circuits. This is the address generator and the FIFOs are clearly visible in the middle of the board. The wiring of the backplane is also clearly visible as are two other components, the power supply on the far right, which is a commercial item, and the display interface next to it which was designed by Dr. D. Bone at UCL.

Each board's circuit diagram is constructed in the form of a hierarchy. Large circuits which are too big to fit on one diagram are split into blocks. At the higher level of the hierarchy, the root level, the diagram shows the blocks and the connections between them which are made by wires and buses via module ports. These input and output ports are merely implied since on the boards themselves there is no physical separation between the blocks. The lower level shows the circuitry of each of the blocks including the module ports that in the root are shown to be connected to other blocks. In the root, connections to the backplane and to various cable headers are also shown. Connections between boards, which are made via the backplane, can be found by matching up the labels of the signals that go on or off the backplane on each diagram. The circuit diagrams were produced using the OrCAD schematic capture program running on a PC.

Low power consumption is important for a space based system and, wherever possible, high speed CMOS (Complementary Metal Oxide Semiconductor) devices have been used. These chips, of the 74HC series, have the advantage of low power consumption compared to TTL (Transistor Transistor Logic) chips. However, they are not as fast and they are more susceptible to damage by the build up of static charges at their inputs; unused inputs to CMOS devices are wired to ground and this should be assumed if not shown. Where TTL chips have been used, it is necessary that they drive TTL compatible CMOS chips of the 74HCT series which recognise the high and low levels associated with TTL chips.

Each chip on a particular board is assigned a number, prefixed by the letter 'U', for

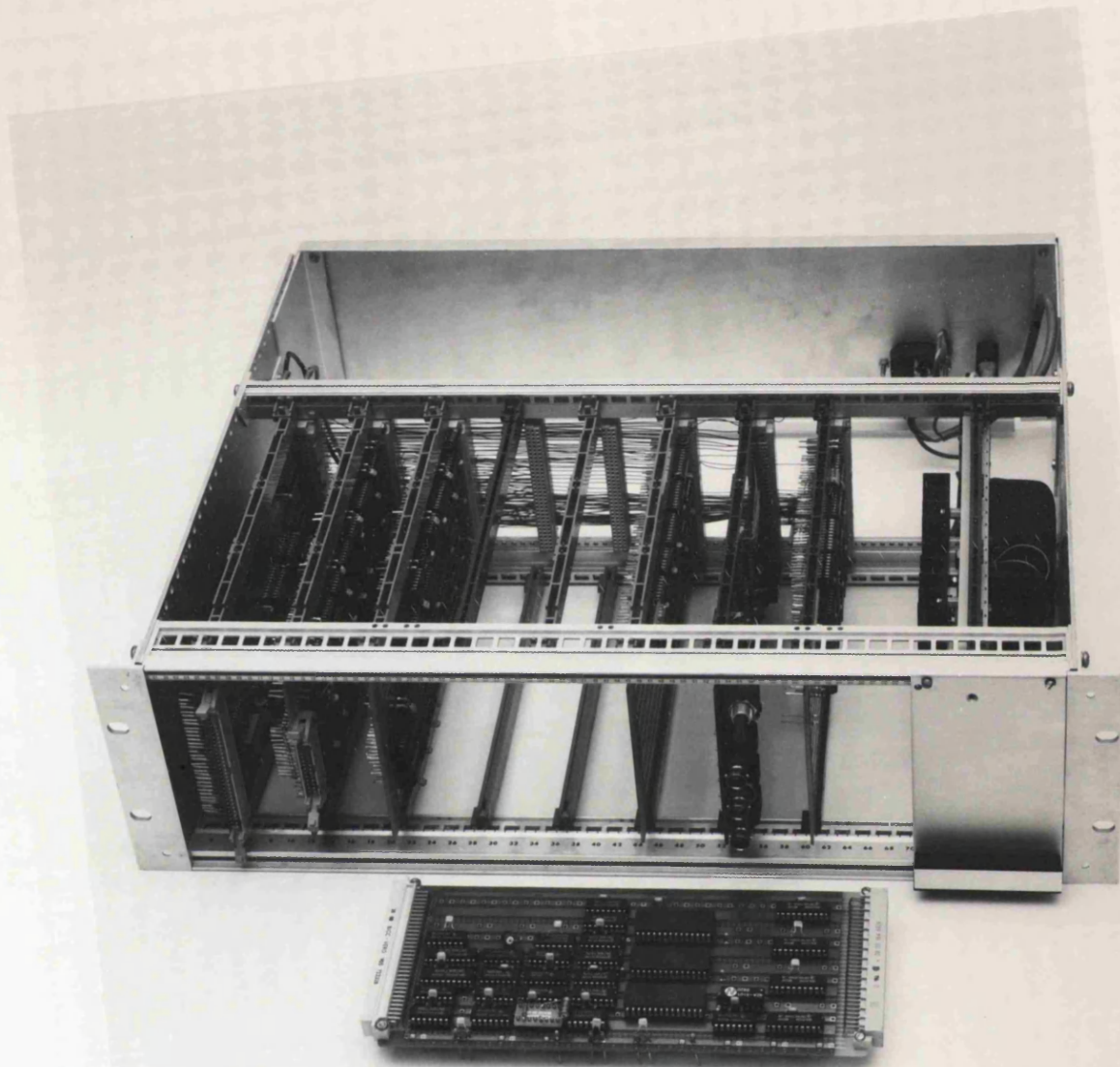


Figure 6.2: The image processing chassis

identification purposes. Other devices have different prefixes. Also shown next to the chip number is another identification in parenthesis and this refers to the chip's position on the board.

6.2 The Command Interface

This circuit allows the computer to write data to, or read data from certain locations within the image processing electronics. For example, the computer may need to read data from the frame store or it may need to load a look-up table or latch with data.

In write mode, input into the command interface are command lines and data lines. Output from the circuit are data and a pulse on a single line that determines the location into which the data are to be written. The pulse is known as an 'OC' command and the data are input at the terminal as a 'WD' command. So, for example, if one wanted to load the latch on the multiple event discriminator circuit with the number 153, one would issue the commands WD 153; OC 3. That particular latch is the only place that OC 3 is sent to, similarly for the other OCs. The command interface puts the data onto the backplane and sends the OC pulse to the correct location. OC commands are also used on their own to perform other functions apart from writes. A summary of all the OCs and their function is given in table 6.1

Read mode is only used for the frame store and so does not require an OC pulse to specify location. Data are automatically read into the computer via the command interface.

6.2.1 Circuit Description

The Command Interface consists of only one diagram shown in figure 6.3. WD data enter the circuit on the lines PD/0 to PD/15 via the 60 way header from a cable linked to the computer. The OC data come in on lines COM/0 to COM/7. Three other lines, PROC.CYCLE*, PROC.R/W* and PROC.BUSY control the transmission of the data to the correct location. All these lines have terminator resistors to reduce transmission line effects.

The first thing the computer does is tell the circuit whether a read or write is about to take place. It sets PROC.R/W* low for a write and high for a read. This appropriately

Table 6.1: A summary of OC commands and their function

Command	Function
OC 0	Start an integration
OC 1	Stop an integration
OC 2	Not used
OC 3	Load the multiple event threshold latch
OC 4	Write data to X centroid look-up table
OC 5	Write data to Y centroid look-up table
OC 6	Set Y centroid look-up table address
OC 7	Set X centroid look-up table address
OC 8	Select frame store operating mode
OC 9	Set address for frame store
OC 10	Write data to frame store
OC 11	Select centroid resolution
OC 12	Select multiple counting mode

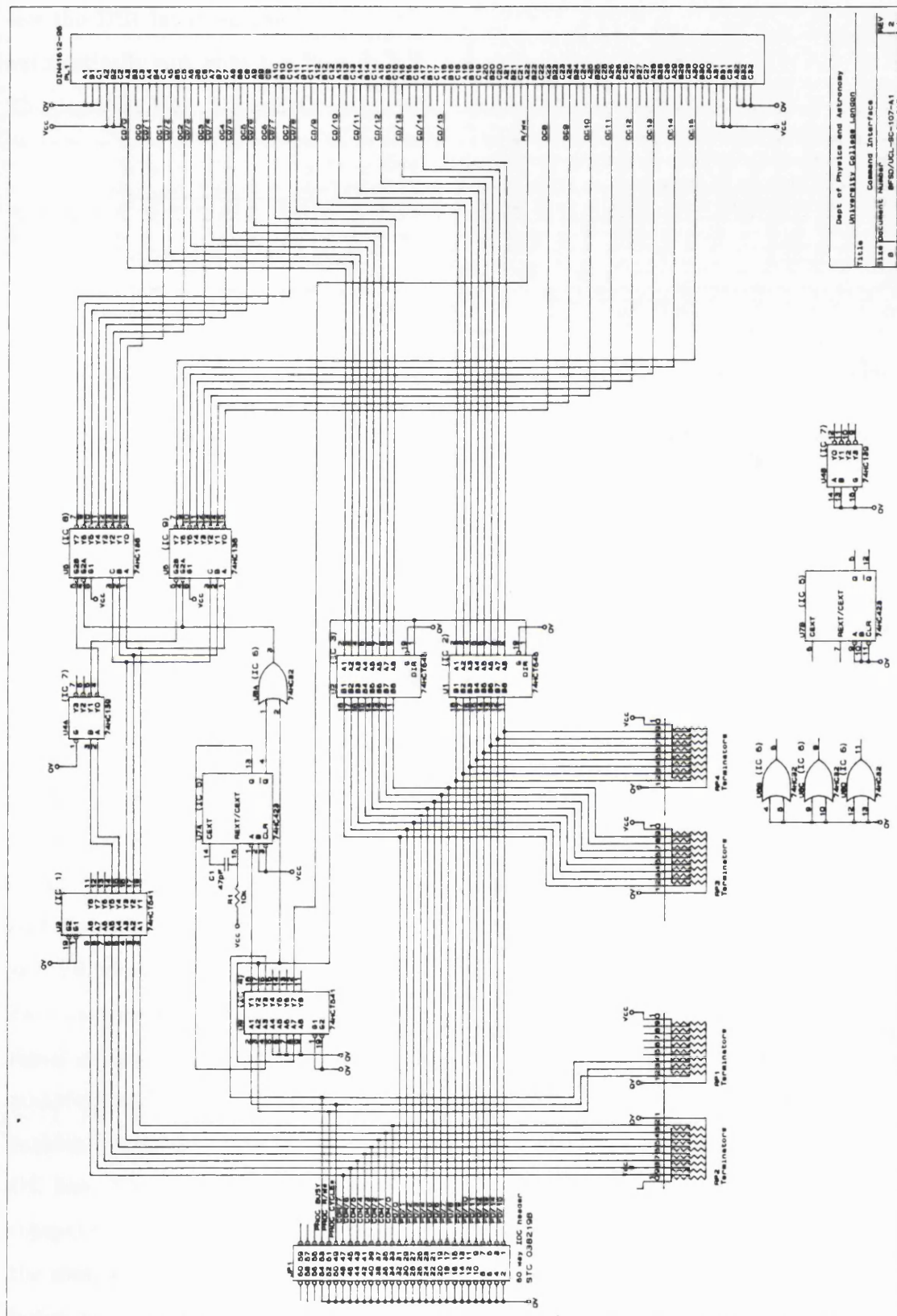


Figure 6.3: The command interface

sets the DIR input on the bus transceivers U1 and U2. If in read mode then data are automatically put onto the backplane and read into the computer via the transceivers. The decoders U4A, U5 and U6 are disabled in read mode and so no OC is sent.

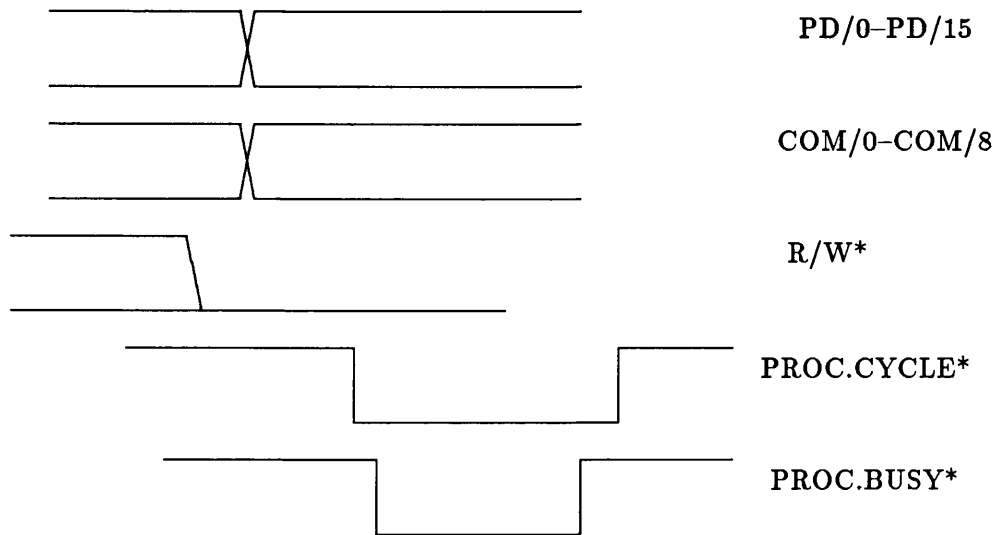


Figure 6.4: Typical timing for the write cycle

A typical timing diagram for the circuit in write mode is shown in figure 6.4. In this mode, once R/W* has been set low, the computer puts data onto the lines PD/0 to PD/15 with a WD command and COM/0 to COM/7 with an OC command. The PD data are sent out onto the backplane and the COM data are sent to the input of the decoders U5 and U6 which are disabled. The computer then waits a sufficiently long time that the data have settled before it initiates a write cycle by setting PROC.CYCLE* low. This signal is input into the monostable and produces a pulse of length 200ns according to the manufacturer's data for the given R_{ext} and C_{ext} . The pulse does two things. Firstly, it enables the decoders U5 and U6 and produces a pulse of the same length on the appropriate OC line. The pulse is long enough for any write to be completed. Secondly, it tells the computer, via PROC.BUSY, that the write is in progress. At the end of PROC.BUSY the computer can assume that the write is complete and it resets PROC.CYCLE* high indicating the end of the cycle.

6.3 Data Analysis Array

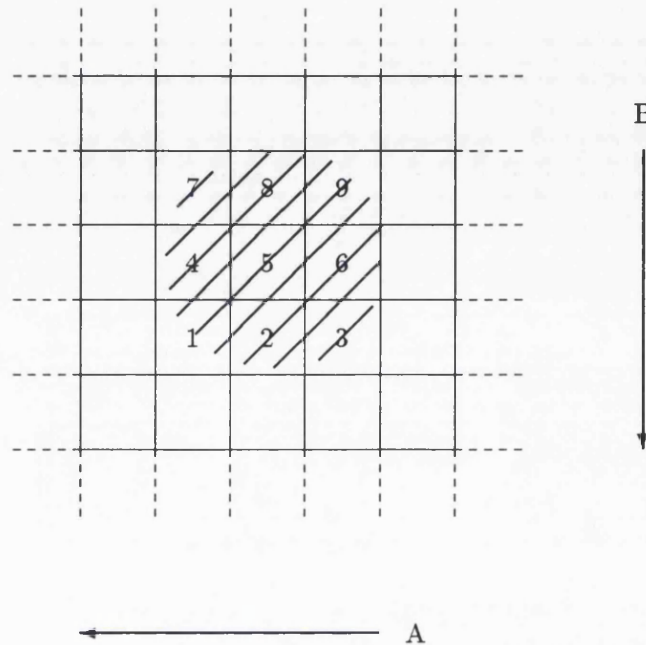


Figure 6.5: The way in which a photon event might appear on the CCD

Figure 6.5 shows how an event might appear on the CCD, where charge is present in the pixels labelled 1–9. As the CCD is read out serially, the data associated with each pixel of an event arrives in the processing electronics at a different time. However, to recognise each event, evaluate its energy and centroid it, it is necessary to form a 2D array through which each event is passed. The pixels of each row are read out one by one in the direction indicated by arrow A and, following the reading out of a whole row, the next row is shifted in the direction indicated by arrow B. This means that the data of the pixel labelled 1 arrives one clock pulse before that of 2 which in turn arrives one clock pulse before that of 3. Moreover, the data in 1 arrives a whole row before that in 4 which in turn arrives a whole row before that in 7 – similarly for 2,5,8 and 3,6,9. Therefore, to be able to perform the various processing functions, it is necessary to delay the data of each pixel in the first two numbered rows by an appropriate amount with respect to those in the last row, for example, data in 1 needs to be delayed by two rows and two pixels with respect to that in 9. The Data Analysis Array receives the data straight from the ADC in the CCD video processor and its job is to re-establish the 3×3 array shown in figure 6.5

by delaying the data in every pixel by an appropriate amount.

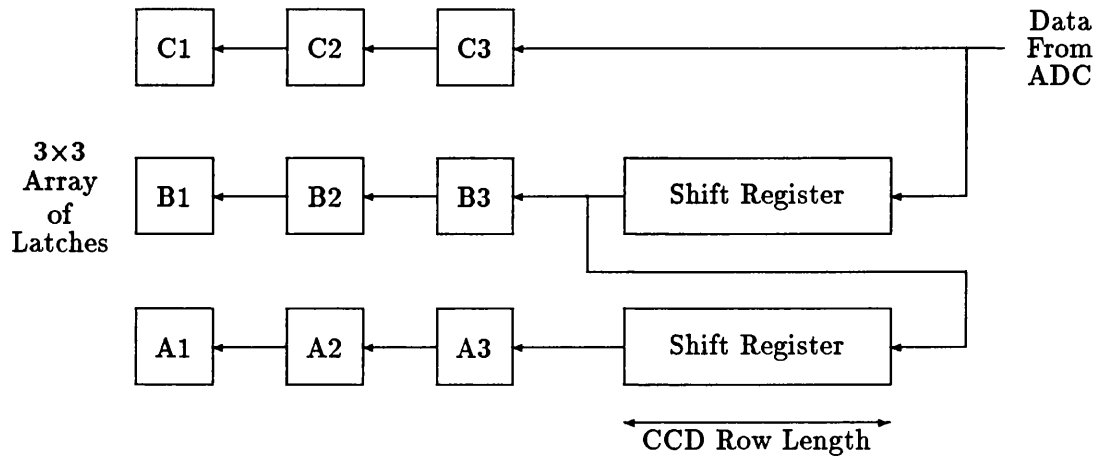


Figure 6.6: Schematic showing the idea behind the operation of the Data Analysis Array

The way in which the DAA delays the data has the same effect as if two shift registers were connected in series. Figure 6.6 shows a schematic of the way in which the DAA works. The component parts of the DAA are

- Two shift registers whose length is equal to a CCD row
- Three sets of three serially connected latches

In principle, the data of each pixel is shifted into the DAA by the 10Mhz system clock as it is read out from the CCD. The data of pixels 1,2 and 3 arrive in the DAA one after the other. They are passed through latches C3, C2 and C1 and also enter the first shift register where they are clocked a number of times equal to the number of pixels in a row. When the data emerge from the shift register they are passed through latches B3, B2 and B1 and also enter the second shift register at the same time as the data of pixels 4,5 and 6 are entering the first shift register. Both sets of three are shifted by the length of a CCD row and appear on the output of their respective shift registers at the same time. As this happens the data of pixels 7,8 and 9 are entering the DAA whereupon they are latched simultaneously with the outputs of the two shift registers. In this way the 3x3 array is re-formed at the outputs of the nine latches.

Every pixel on the CCD is passed through the DAA and so, at some time, every pixel will be central within the 3x3 array. This means that if there is an event present on the

CCD then, at some time, it will be central within the array and the data on the output of the nine latches may be used to perform the various processing functions.

In fact, the DAA does not use shift registers as they are far less practicable than the use of RAMs which produce exactly the same result.

6.3.1 Circuit Description

The Data Analysis Array is part of a larger board which also contains the Pulse Energy Discriminator circuit. The root diagram, which is shown in figure 6.7, shows how the three separate blocks are connected to each other and to the backplane and 26-way header that provides the input of signals and data from the CCD camera.

The Data Analysis Array itself may be split into two separate circuits.

- The Array. This is the main part of the circuit and is the block named 'Data Analysis Array'
- The timing circuit. This generates the signals which control the clocking of the various devices within the DAA and which are crucial to the correct operation of the circuit. This is the block named 'DAA timing circuit'

The details of the array are shown in figure 6.8 and the timing circuit is shown in figure 6.9.

An Overview of the Circuit Operation

With reference to figure 6.8, a summary of the operation of the data analysis array is as follows. A counter, formed by U43 and U45, generates the addresses for the two RAMs, U33 and U42. These are the addresses of the pixels in each row – the counter is reset after each row and counts from zero again at the start of the next. Assume that a number of rows have already passed through the DAA and that the RAMs contain data. Data from the next row enter the DAA via lines VDA/0–VDA/7 from the Frame Store or via VD/0–VD/7 from the CCD. The following sequence occurs

- The address input on the two RAMs is set and the data contained in that address appear on their outputs.
- Two things happen simultaneously

Figure 6.7: Root diagram of the data analysis array

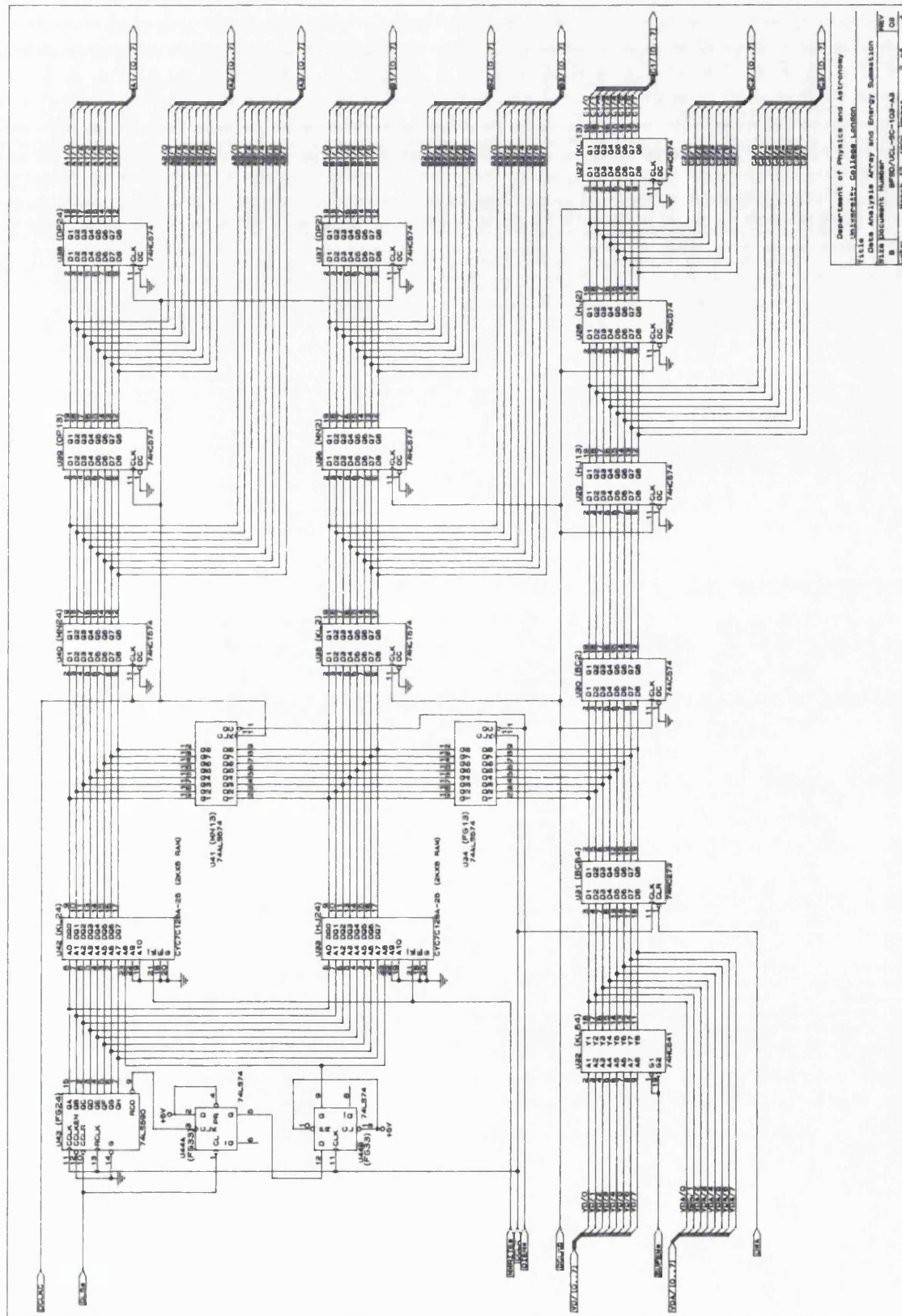


Figure 6.8: The array of the data analysis array

- The data appearing on the output of the RAMs are latched through U35 and U40 at the same time as the data coming into the DAA are latched through U29.
- The data appearing on the output of RAM U33 are latched through U41 at the same time as the data coming into the DAA are latched through U34.
- Before the address has changed the data on the outputs of U34 and U41 are written into that location, overwriting the data that were just read out.
- A new address is set and the process repeats.

In this way, the data from one row are passing down the column formed by U38, U39 and U40 while the data from the next row are passing down the column formed by U35, U36 and U37 and the data from the next row after that are passing down the column formed by U27, U28 and U29. Thus, every pixel on the CCD becomes central within the 3×3 array at some time during its passage through the DAA.

The Detailed Operation of the Data Analysis Array

Figure 6.10 shows a timing diagram for the data analysis array which is needed in order to understand the operation of the circuit. In this diagram the clocks that control the timing are shown as well as the data change at various gate outputs. A set of data is denoted by a letter and a number, for example C3, where the number represents the pixel number and the letter represents the row number – this is also the case on the DAA circuit diagram. High impedance states are represented by shaded areas.

The timing circuit receives a number of signals. The signal TEST* is generated by the frame store and comes in off the backplane via pin C11. This signal is buffered and used to generate BUFEN*. TEST* is low when the system is being tested with simulated data stored in the frame store and thus, when the system is in TEST mode, BUFEN* is high and this disables the outputs of the buffer U32 of the data analysis array that receives the data from the CCD camera. Otherwise the system is in NORMAL mode and receives data via this buffer.

The other four signals received by the the timing circuit are the system clocks described in section 6.1 which come in off the 26 way header. Window Active, Frame Sync and Line Sync are buffered and sent out onto the backplane to be used by other circuits. Singly

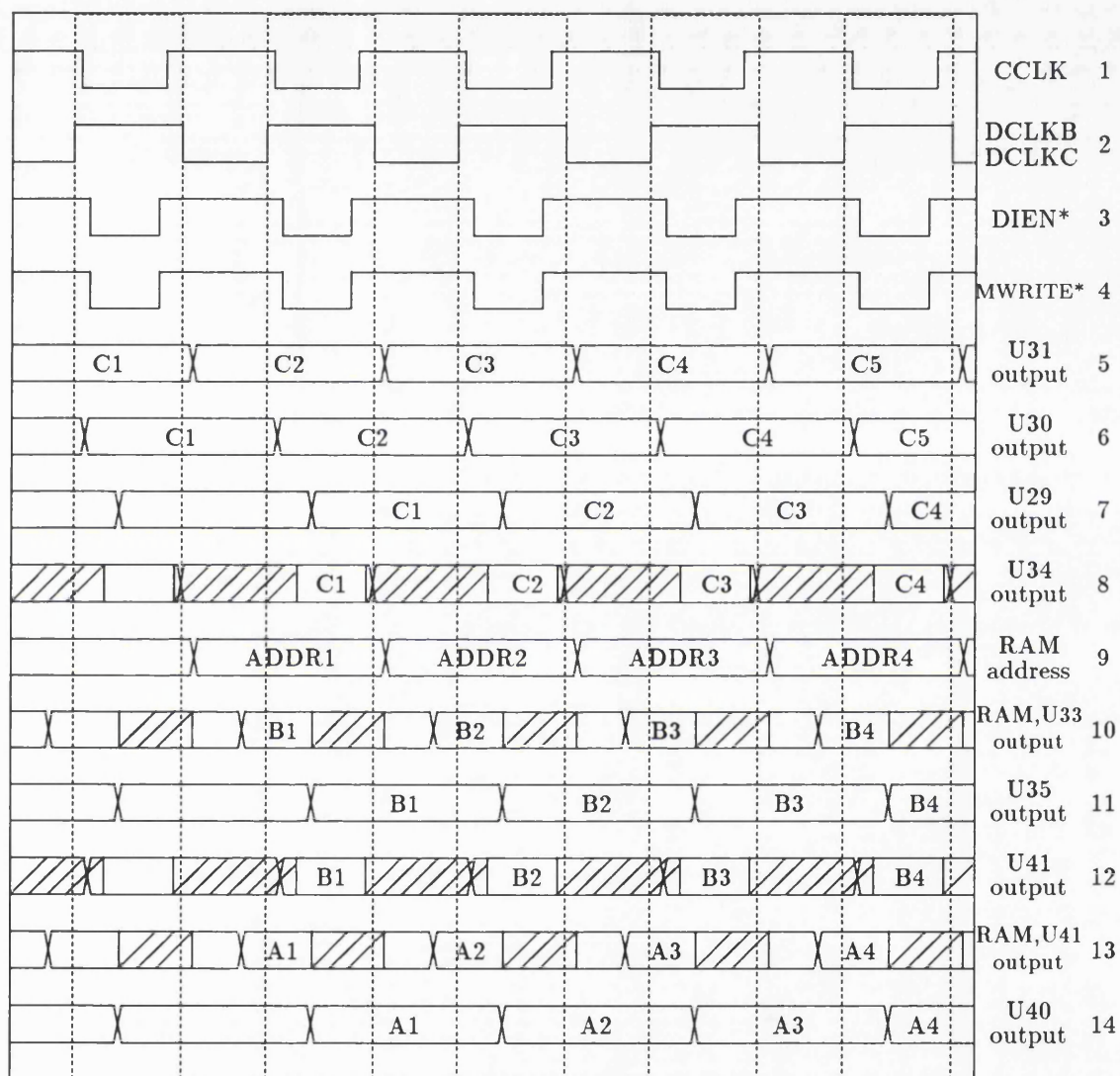


Figure 6.10: Timing diagram for the Data Analysis Array

buffered signals DWA and DLS* are used in the DAA. SYSCLK is the 10MHz system clock which comes in via pin 23 of the 26-way header and is buffered. This does not necessarily have an equal mark-space ratio – for example, although the rising edge will always occur every 100ns, the signal may be low for 80ns. To produce a known signal with an approximately equal mark-space ratio, the arrangement of DL1, U47A and U47B is used. The Q output of U47A is set by the rising edge of the buffered SYSCLK and is reset by the rising edge of the same signal delayed by 50ns. This generates CCLK, shown in line 1 of figure 6.10, which is also used to produce a number of other signals. CCLK is fed into a delay with 10ns per tap and, in combination with three NAND gates, this generates the signals DCLKA, DCLKB, DCLKC, DIEN* and MWRITE*. These signals are used for controlling the array and their timing is shown in lines 2–4 of figure 6.10. Three versions of the same signal, namely DCLKA, DCLKB and DCLKC, are generated to reduce the load that would otherwise be placed on a single signal. PCLK, which also has the same form, is buffered and sent out onto the backplane via pin C14 for use by other circuits.

A pixel of data coming in to the DAA from the CCD camera is clocked through U31 by CCLK as shown in line 5 of figure 6.10. This gate outputs zeros if DWA is low, that is, if the pixel data do not lie within an active window. This is to prevent invalid data from being stored in the RAMs. The output of U31 goes in two directions. It passes down the row of latches clocked by DCLKB and appears on the outputs of U30 and U29 as shown in lines 6 and 7. It is also clocked into latch U34 by the next rising edge of CCLK but the output of this gate is disabled by DIEN* high. While DIEN* is high, the counter formed by U43 and U44 has generated a new address input to the two RAMs, U33 and U42, as shown in line 9. The two sets of data stored in this address appear 25ns later on the outputs of their respective RAMs as shown in line 10. The output of U33 is latched through U35 by DCLKB and clocked into U41 by DCLKC whilst the output of U42 is latched through U40. The outputs of U29, U35 and U40 appear at the same time, as shown in lines 5,11 and 12. Meanwhile, DIEN* has gone low along with MWRITE* and, since the address input to the RAMs has not changed, the data on the outputs of U34 and U41 are written into the *same* location as the data that have just been latched through U35 and U40, overwriting that data. The next time that address is generated one line later, these data will be read out and latched through U35 and U40 before being

overwritten by the data of the same pixel of the next line. The sequence continues in the same way for the whole frame.

The sequence described above produces a 3×3 array of data appearing simultaneously on 9 latches, U27 to U29 and U35 to U40, which centres every pixel on the CCD within an array of its own nearest neighbours. This array can then be used for other functions within the processing electronics.

6.4 Event Validate

With every clock pulse, a new 3×3 array of pixel data is formed in the DAA. If an event is present on the CCD then, at some time, it will be centred within the array. Event Validate looks at the pixel data of every 3×3 array and, by using a set of criteria, it decides what is an event and what is not. If an event is present then a flag, called Event Centre Detection (ECD), is set and this is used by the FIFO to control the transmission of event data to the DMA interface.

6.4.1 Criteria for event determination

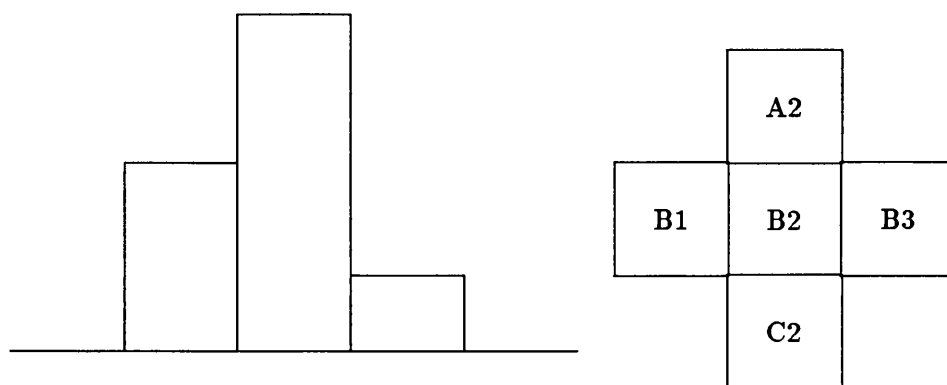


Figure 6.11: Cross hair used by Event Validate and a possible profile of the data in one direction

The profile of an event is approximately Gaussian in shape in both X and Y. When pixelated and digitized, the profile may look something like in figure 6.11. In the X

direction these pixels would be B1, B2 and B3 of the 3×3 array whilst in the Y direction they would be A2, B2 and C2, as indicated in this figure. If one takes the cross hair of the 3×3 array then clearly, when an event is present, the data in the centre pixel will be greater than those in the four pixels either side of it in the cross hair. A comparison of the data in the centre pixel with those in each of its four neighbours forms the first four criteria.

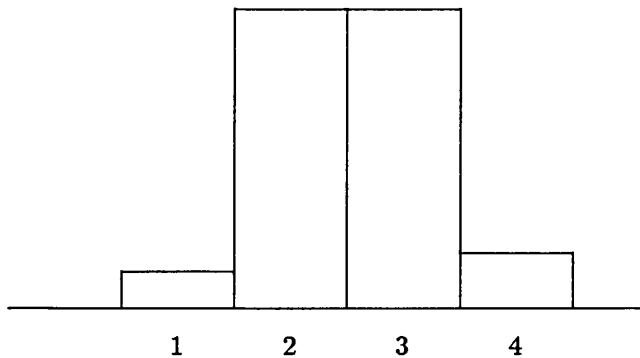


Figure 6.12: Profile of an event that has landed on the boundary between two pixels

However, there may be a case when there is an event but one or more of the above criteria break down. Consider the case when an event lands on the boundary between two pixels. The pixelated profile may look something like figure 6.12. One needs the additional requirement that the data in the centre pixel may be greater than those in the pixel on one side and *equal to* that in the pixel on the other side. One must be careful here. When pixel 2 in figure 6.12 is in the centre of the cross hair then the above requirement is satisfied and one can say that there is an event present. Now, on the next clock pulse, pixel 3 is in the centre of the cross hair and the requirement is once more satisfied so, again, one can say that there is an event present. To avoid counting this single event twice one must introduce a handedness to the requirement, that is, to require that the data in the centre pixel be greater than those immediately to its left (preceding it) and equal to that immediately to its right (after it), for example. In this way the requirement will only be met once for any event where two pixels have the same data value. This requirement is implemented in both X and Y as an alternative if one or more of the four above criteria is not satisfied.

The final criterion concerns the size of an event. All the criteria above may also be satisfied for noise produced by the image intensifier or the electronics. In the case of the intensifier, noise events have not originated from a photon incident on the photocathode of the image intensifier and, therefore, have undergone a smaller amplification. These events have a smaller pulse height and, when one looks at the pulse height distribution of events as in figure 3.7, one can clearly distinguish noise events at the lower values from photon events at the higher values. Similarly, electronic noise that satisfies all the other criteria is also distinguishable from true photon events. By requiring that the pulse height, and therefore the data in the centre pixel, be greater than a certain value, or Threshold, the majority of the noise events can be rejected. This forms the last criterion upon which an event is recognised.

With reference to figure 6.11, the criteria described may be summarised as follows. An event is present if

- $B2 > B3$ AND
- $(B2 > B1 \text{ OR } B2 = B1)$ AND
- $B2 > C2$ AND
- $(B2 > A2 \text{ OR } B2 = A2)$ AND
- $B2 > \text{Threshold}$

are all true simultaneously. An ECD is set up when this occurs.

6.4.2 Circuit Description

The Event Validate circuit is on the same board as the centroid circuit. The root diagram, showing the three blocks and the backplane connections is shown in figure 6.13. The event validate circuit itself is shown in figure 6.14.

The inputs to Event Validate are the pixel data of the five pixels that form the cross hair of the Data Analysis Array. Five magnitude comparators, U44–U48 are used to assess the five criteria itemised above. The data in the centre pixel, B2, are fed into all five comparators and this is compared with the threshold and with the data in the other four pixels which are each fed into one of the comparators. The threshold is set manually by means of hex switches.

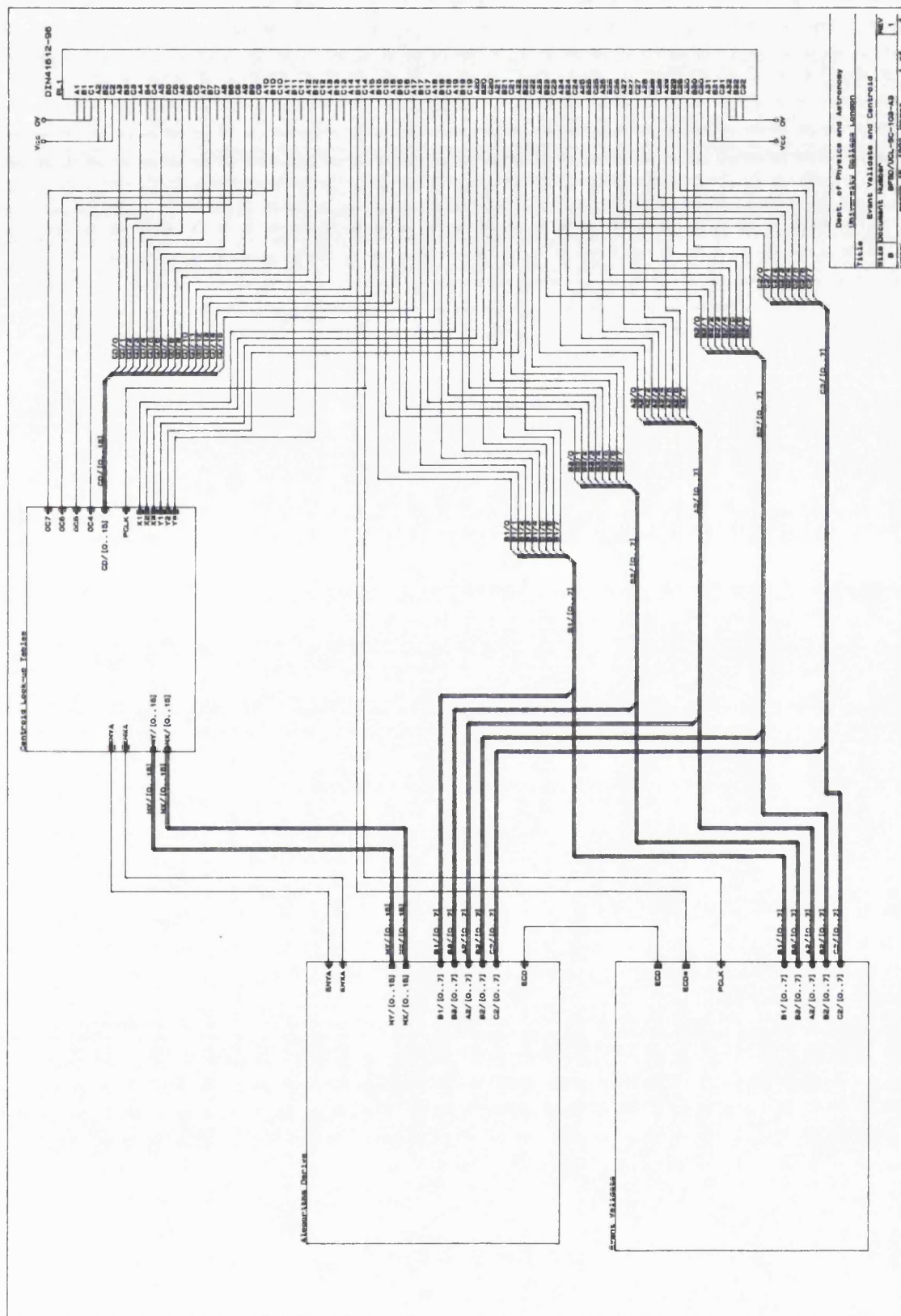


Figure 6.13: Root diagram of event validate and centroid

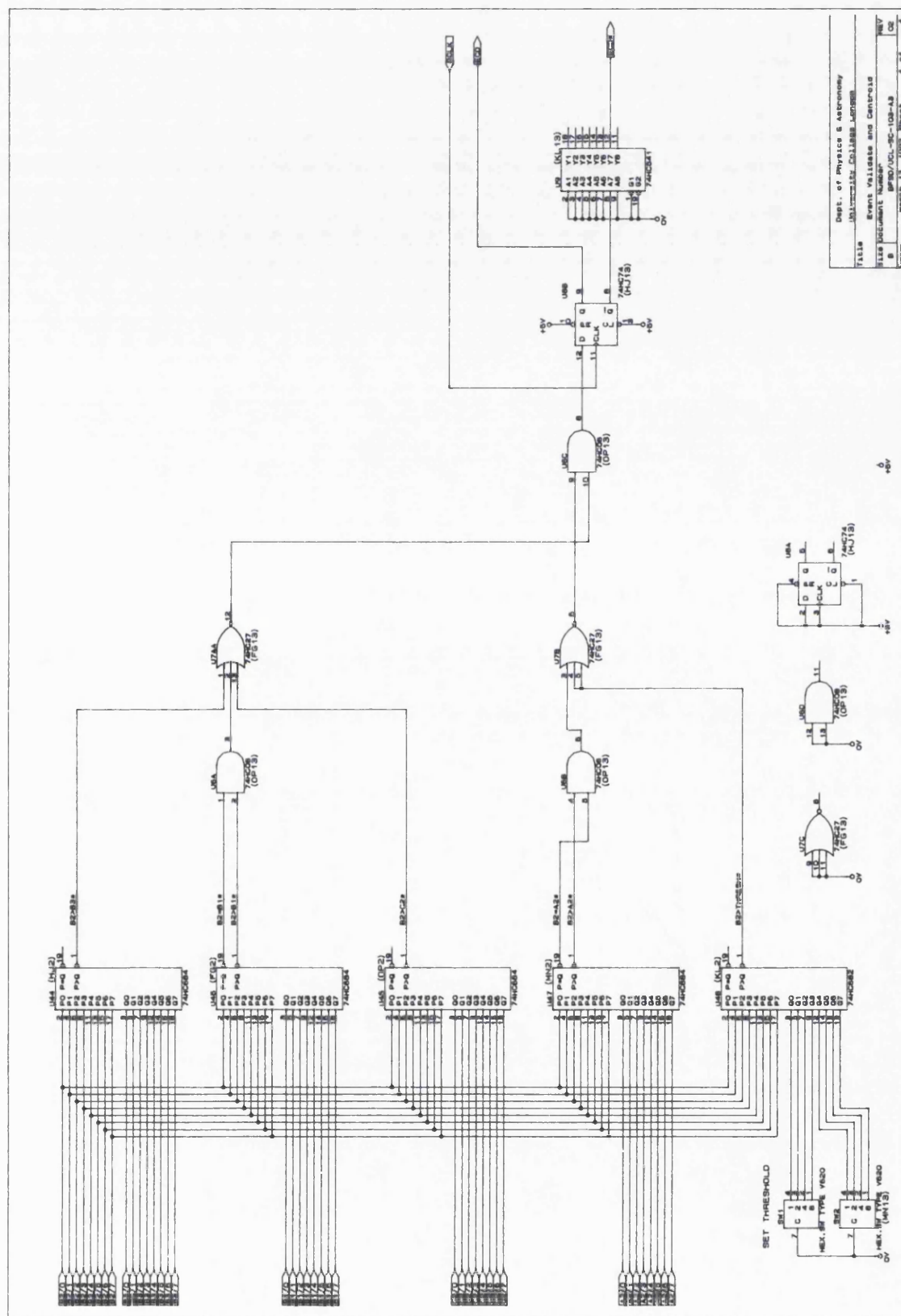


Figure 6.14: The event validate circuit

For a given comparator, if the data in B2 are greater than that of the data being compared then the output of pin 1 ($P > Q$) goes low. Note that two of the comparators, one for X and one for Y, have outputs for $P = Q$, as discussed in the previous section, and these are ORed with the $P > Q$, in U6A and U6B, to form the single outcome of that comparison.

The outcomes of the five comparisons are passed through two NOR gates and an AND gate, U7 and U6C, which constitutes an AND of all the comparisons. If all the criteria are satisfied then the D input to U8B becomes positive. Taking into account the gate delays and, given that the same clock as PCLK clocks the array latches of the DAA, then the result of the comparison should have settled to its correct level by the next rising edge of PCLK, pin 3 of U8B. If the D input is positive at the arrival of the rising edge of PCLK then ECD goes high and there is an event present. If the D input is low when the rising edge of PCLK arrives then ECD goes low and there is not an event present.

6.5 Multiple Event Discriminate

6.5.1 Introduction

Of all the performance requirements placed upon XMM MIC, the maximum point source count rate is perhaps the most difficult to achieve. The maximum achievable count rate with MIC is limited by the frame rate, that is, the speed at which the CCD is read out, and this depends upon the format used. The smaller the format used, the higher the frame rate and the better the dynamic range characteristics.

The reason why there is a limit to the brightness of an observable object is explained by coincidence losses. If two events arrive in the same place in the same frame then there will appear to be only one event present when, in fact, there are two. This means that only one event is detected and the other is lost. Thus, fewer events are detected than are actually input. This leads to a loss of linearity in the counts-in/counts-out curve. An example of a non-linear dynamic range curve for a point source is shown in figure 6.15 for two formats. Even on a very small format of 32 rows, the dynamic range curve departs from linearity at quite a low count rate. For flat fields or extended objects, the departure from linearity begins at a much smaller value of counts $s^{-1} \text{ pix}^{-1}$.

It does not matter that the dynamic range curve is not linear so long as it is possible to

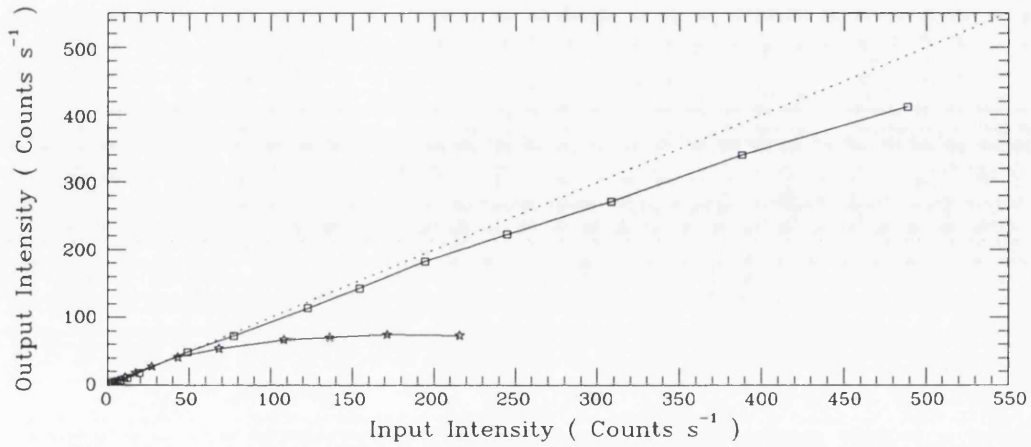


Figure 6.15: Dynamic range curve showing input intensity versus output intensity for a point source on full format (stars) and on a 32 row format (squares). The dotted line indicates linearity.

calibrate the brightness of the input. The further the departure from linearity, the harder it is to calibrate the source. For example, on the full format in figure 6.15 a detected count rate of 60 counts s⁻¹ pix⁻¹ could be calibrated as anything between 140 counts s⁻¹ pix⁻¹ and 220 counts s⁻¹ pix⁻¹. The requirement then, is not necessarily for linearity but for as small a departure from linearity as possible. Obviously, a fast frame rate improves the dynamic range curve but also the Multiple Event Discriminate circuit was implemented in order to further increase the linearity of this curve for any type of object.

6.5.2 Principle of Operation of the Multiple Event Discriminator

When two or more events arrive on top of each other on the CCD then, on average, a greater amount of charge will be stored on the CCD than would be the case for a single event. It should be possible to take account of this in order to improve the dynamic range characteristics of the detector. If all events had *exactly* the same height and width and landed in *exactly* the same place every time then it would be a simple matter to distinguish one event from two or three or more – the event height would be a multiple of a single event height.

However, there are two things to consider,

- Events are not *exactly* coincident. Events are considered coincident until they are

far enough apart that their two peaks can be resolved. Consider two events of

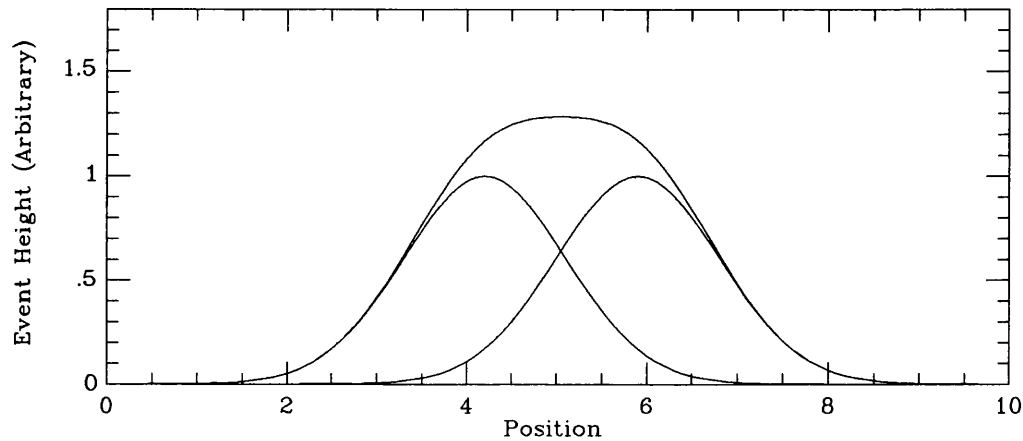


Figure 6.16: Two coincident events that are some distance apart. Both have the same height and width but their sum, the larger curve, has a height and width determined by the distance between the two events

the same height and width that are coincident but are some distance apart as in figure 6.16. Their combined height will not be twice the height of a single event and nor will their combined width be the same as a single event. In other words, the height and width of coincident events are not a simple function of the height and width of single events, but depend upon the distance between the events. It would be complicated to use height or width to distinguish single events from multiple events. However, a quantity which remains independent of the distance between the two events is the area under them, or the energy contained in them, and this is a simple sum of the energy of the two events separately. This suggests that when one is trying to discriminate between one or more events then it is the pulse energy that should be considered. If all events had the same height and width then finding out how many events were present would be a simple matter of determining how many multiples of a single event energy were contained in the coincident event energy, even for coincident events that were some distance apart.

- Events have height and width distributions. This means that they also have energy distributions which complicates the determination of the number of events present. Two small events on top of each other could have the same energy as one large event

and so it is not possible to tell how many events are present simply from the pulse energy

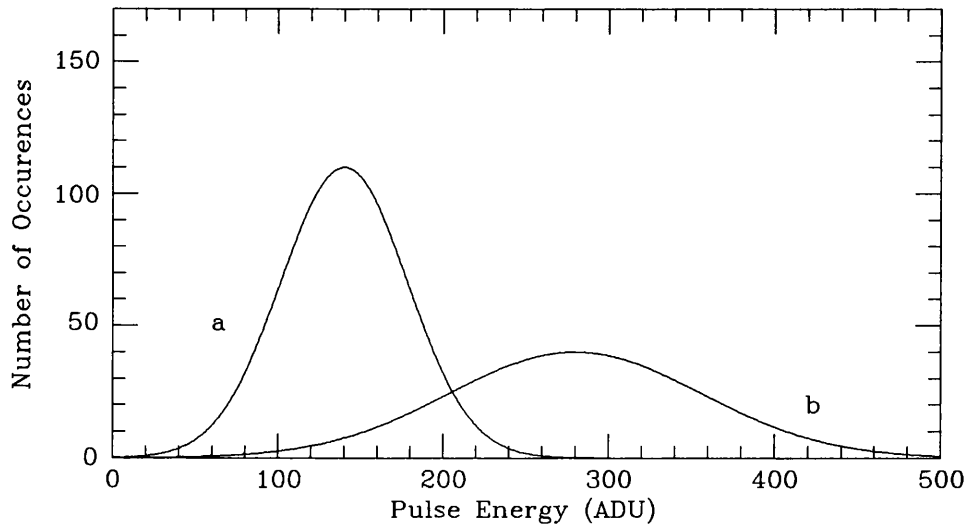


Figure 6.17: Pulse energy distributions for (a) single events and (b) double events

Figure 6.17 shows possible pulse energy distributions for single and double events. Although the two peaks are clearly separated, there is a region where the two distributions overlap. Thus, it is not possible to say that above a certain energy all the pulses consist of two events whilst below it they consist of one. However, what one can do is choose an energy threshold such that there are likely to be the same number of double events below the threshold as there are single events above it. If one takes everything above the threshold as two events and everything below it as one event then double events counted as single will be compensated for by single events counted as double. The situation is complicated by two things

- Firstly, the correct threshold setting depends upon the event rate. For example, if the rate was so small that there were almost entirely single events then one would set the threshold high in the distribution of possible single event energies so that almost everything was counted only once. On the other hand, if the rate was so high that almost every event was double then one would need the threshold lower so that almost everything was counted as double. One would need a different threshold for every count rate in order to achieve a linear response.

- Secondly, coincident events may be not just doubles, there may be 3, 4 or more events coincident with each other. If one were to take account of this then one would need not just a threshold for double counting but another for 3 and another for 4 and so on.

If one were to correctly compensate for the above two phenomena then the solution would be extremely complicated. Since the requirement is simply to straighten the dynamic range curve, it is sufficient to set a single threshold for every count rate and label everything below it as one event and everything above it as two. This threshold is best determined experimentally.

The Multiple Event Discriminator circuit calculates the energy of each pulse, be it single, double or more events. It does this by summing the data of all the pixels in the 3×3 array of the DAA. It compares this calculated energy with the user defined threshold. If the pulse energy is greater than the threshold then the circuit sends a flag indicating that there are two events present. These data are still centroided as if they were one event but the memory location corresponding to the position of the event is incremented by two instead of one. However, the centroiding accuracy is affected because the pulse profile of a multiple event is not a constant shape. Thus, when the Multiple Event Discriminator is used, it should only be in a high count rate, low resolution application.

6.5.3 Circuit Description

This circuit is on the same board as the Data Analysis Array and the root diagram was shown in figure 6.7.

The Pulse Energy Discriminator circuitry is shown in figure 6.18. In this circuit, every pixel of data in the 3×3 array of the DAA is added together to produce the pulse energy. The summation takes place in two steps. In the first step, pixels of the same column are added to form three separate additions, $A1+B1+B1$, $A2+B2+C2$ and $A3+B3+C3$. This first step is carried out in the adders U1 to U12, the data being input straight from the DAA. Only when the data in the B pixels are added are the carries used, as the sums should not exceed 255 before this. The three sums are synchronised again on the next rising edge of DCLKA and then they are added together in the adders U16 and U17 and U19–U22 to form the pulse energy on the lines PEN/0 to PEN/7. These lines form one set of inputs to the comparator U23.

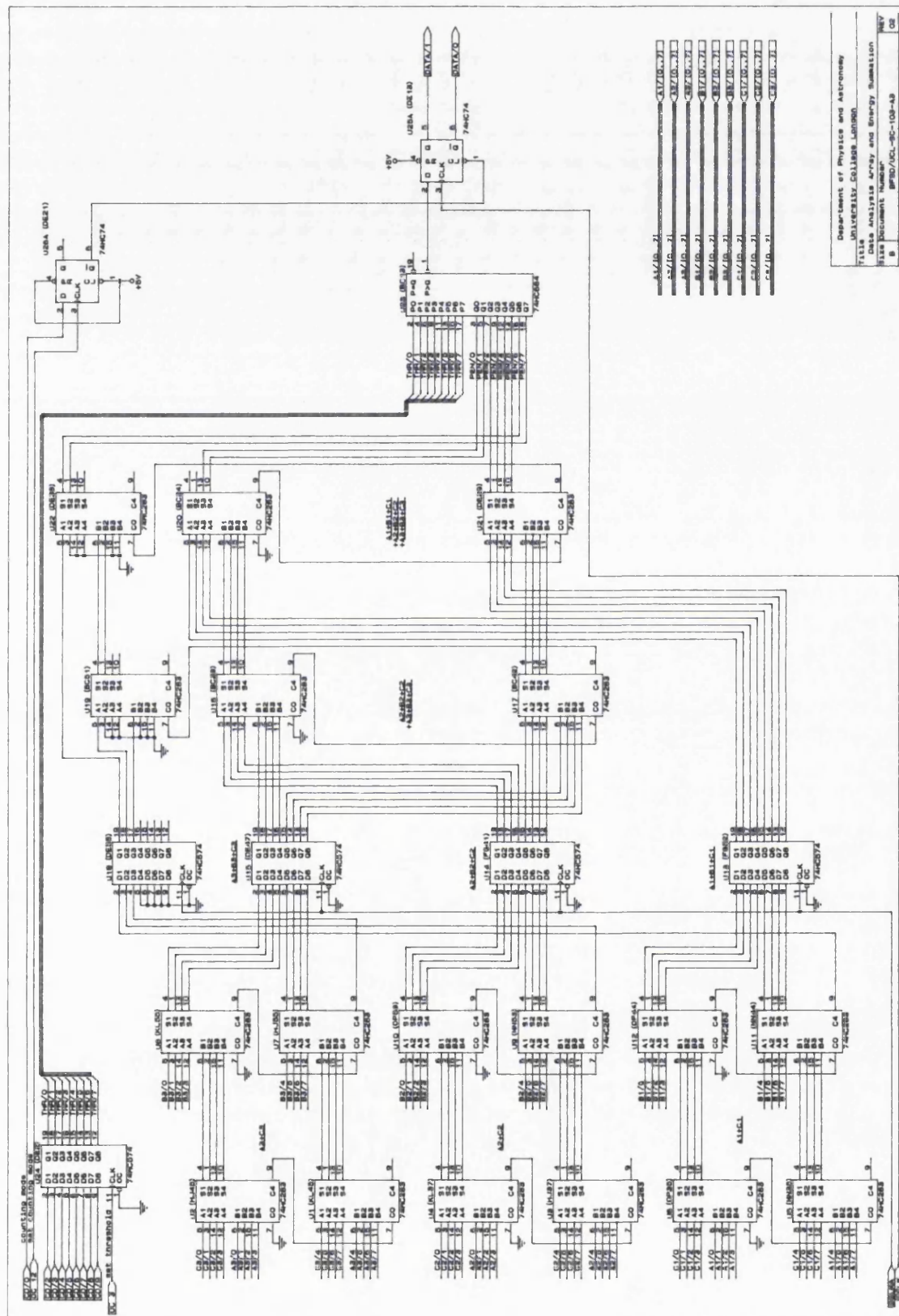


Figure 6.18: The pulse energy discriminator circuit

The other set of lines, which is the energy threshold, is provided on lines THR/0 to THR/7 by the output of the latch U24. This threshold is input to the latch on lines CD/2 to CD/9 by a WD command and is clocked in by OC 3. Notice that the two least significant bits of both the pulse energy and the threshold energy are missing. This is to allow energies up to 1024 ADU to be used but it still only requires 8 data lines. The restriction on the energy then is that it must be a multiple of four and this is sufficiently precise.

The result of the energy comparison is fed into the input of the flip-flop U25A, which is clocked on the next rising edge of CCLK. If the pulse energy is less than the threshold then pin 1 of the comparator goes low and this results in the lines AD/0 and AD/1 holding the number 01, or 1. If the energy is greater than the threshold then this results in the lines holding the number 10, or 2. The number on these lines is the number of events present and it is by this amount that the corresponding memory location is incremented. Thus, when the energy is greater than the threshold, the memory location is incremented by 2, whereas if it is smaller then it is incremented by 1.

There is an option for disabling the multiple event discriminate facility. This is provided by CD/0 and OC12. WD1, OC 12 disables the facility since it causes U25A to be cleared and only the data value 1 is passed on. WD 0, OC 12 enables the facility since the \overline{CLR} input of U25A is then high.

The results of the implementation of the multiple event discriminator circuit are discussed in section 7.3.2

6.6 Centroid

6.6.1 Introduction

Interpolative centroiding is the technique by which the resolution of the system can be increased to an accuracy as high as 1/8th CCD pixel in both X and Y. The technique is based upon finding the ‘centre of gravity’ of the event profile. Consider the event profile shown in figure 6.19. The centre of the event is obviously in pixel C, but it is not in the exact centre as can be seen from the relative sizes of the pixel data in the outer pixels. Imagine that the event has landed at a distance x from the centre of pixel C and that

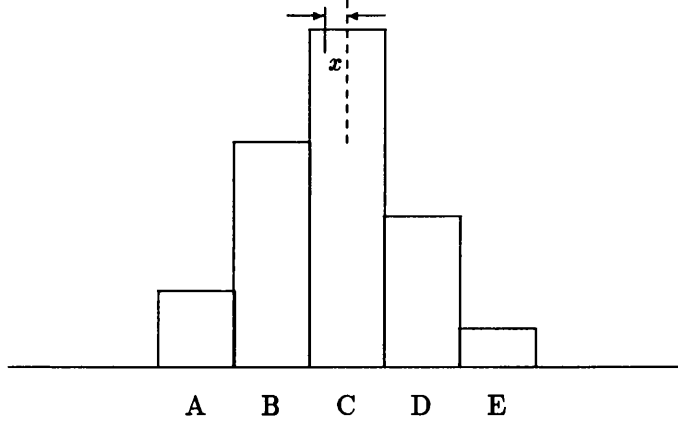


Figure 6.19: Profile of an event as seen on the CCD. This is useful for deriving the classic centroiding algorithm.

the centre of one pixel is unit distance from the centre of an adjacent pixel. The ‘centre of gravity’ of the event can be found by taking moments about the point x :

$$(2 - x)A + (1 - x)B = xC + (1 + x)D + (1 + 2x)E$$

or rearranging

$$2A + B - D - 2E = x(A + B + C + D + E)$$

which gives

$$x = \frac{2A + B - D - 2E}{A + B + C + D + E} = \frac{M}{N} \quad (6.1)$$

This is the classic 5-pixel algorithm (Boksenberg et al., 1985) and gives a centroid position in the range -0.5 to 0.5 with respect to the centre of pixel C. Each pixel may be split into 8 channels with ranges -0.5 to -0.375; -0.375 to -0.25 etc. For every event the result of equation 6.1 will lie in the range -0.5 to 0.5 and so one of the 8 channels may be assigned to it.

In MIC the centroiding algorithm is partially performed in hardware but, in order to keep power consumption to a minimum, a 3-pixel algorithm is used. In this case equation 6.1 reduces to

$$x = \frac{A - C}{A + B + C} = \frac{M}{N} \quad (6.2)$$

where B is the centre pixel.

However, a few problems are encountered with the implementation of centroiding algorithms and these are discussed in the next section.

6.6.2 The Problem of Pattern Noise and its Removal

A feature that is seen in all photon counting detectors that use interpolative centroiding is that of pattern noise. The effect is caused by events being placed in the wrong channel when they are centroided. That is, an event that truly landed, say, in the outside channel may have a value of M/N that places it in a channel one or two further towards the centre of the pixel. Events in any channel may be wrongly centroided but usually the effect is to place more events toward the centre of the pixel than towards the outside. When one takes a flat field, the effect described above manifests itself in the form of pattern noise as shown in figure 6.20. The effect obscures the real data, especially so when it is pronounced.

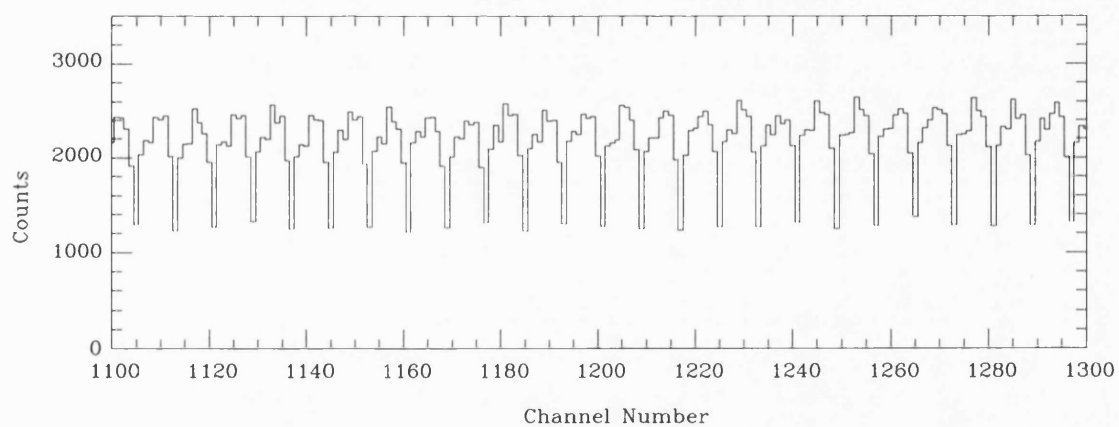


Figure 6.20: Pattern noise introduced into a flat field as a result of centroiding errors

The causes and parameters affecting the pattern are various. Dick et al. (1989) detail the different factors that determine the severity of the patterning seen. These are

1. Undersampling. If the event is not wide enough then, when pixelated, a lot of information about the shape of the event will be lost since most will be contained within one pixel.
2. Windowing. If the event is too broad then its wings will be lost outside the array

used in equation 6.2 and, because information is lost, errors will be introduced.

3. D.C. bias. If the event sits on a d.c. bias then obviously its pixel data will be altered and its centroid position calculated incorrectly. With MIC, the d.c. bias is removed by black-level clamping in the CCD camera.
4. Noise. The d.c. bias is noisy. Subtraction of the bias is made easier by setting any resulting negative values to zero. Positive noise, however, will contribute to the centroiding so that, in effect, the events are sitting on a small d.c. bias.

Points 3 and 4 above have a negligible effect with MIC. The first two points are both associated with the pulse width which, therefore, is by far the most important variable affecting the pattern. Now, even with an ideal width, which for MIC has been found to be 1.4 pixels for a 3-pixel algorithm, the patterning is still pronounced.

The fundamental reason why centroiding introduces a pattern noise is because the centroiding algorithm is not suited to the event shape; it is too simple. It assumes that all the charge contained in pixel A, for example, is concentrated at a single point exactly two pixels from the centre of pixel C. Of course, the profile of an event has a continuous distribution and is a rapidly varying function of the distance from its peak. Thus, the assumptions made in the derivation of equation 6.1 inevitably lead to errors. Furthermore,

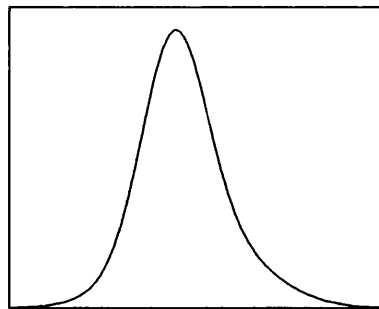


Figure 6.21: Profile of a real event seen with MIC that shows the asymmetry

the event profile is asymmetrical as can be seen from figure 6.21 which shows the profile of a real event seen with MIC and figure 6.22 which shows contour plots of two events. Even if an algorithm took into account the continuous nature of event profiles, it would

not cope with asymmetry.

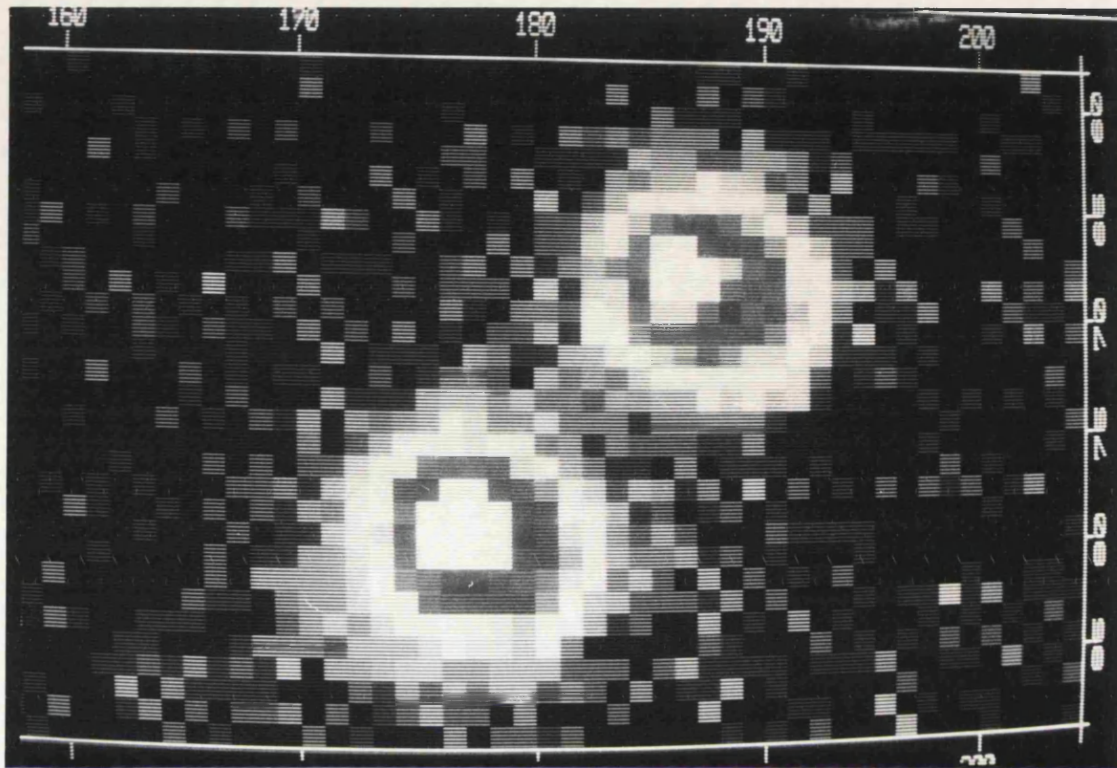


Figure 6.22: Two photon events showing their asymmetry

Patterning will always be present to some extent in a system that uses interpolative centroiding. It is essential that the patterning be removed in real time as otherwise it distorts the real data to such an extent as to make important, quick assessments extremely difficult. How then may the patterning be removed, bearing in mind the fundamental inadequacies of the centroiding algorithm outlined above?

Dividing one's data by a normalised flat field will remove any systematic error, whatever the cause. However, this cannot be done in real time, but, as discussed previously, it is necessary to be able to remove patterning in one's data as they comes in. Also, the pattern may change slowly during observing as will be discussed in section 7.6, so that quite a number of flat fields may have to be taken during the course of observing and valuable time is consumed. Flat fielding one's data, although it is the best way to remove systematic errors, is not the answer for removing patterning in real time.

A tried and tested method of removing patterning and any other systematic error in

real time is that of dithering (Shectman, 1981; Jorden and Fordham, 1986). It is used with the CCD-IPCS on the William Herschel Telescope and is particularly appropriate to the type of intensifier used there. The procedure for dithering has two stages:

- The input image is moved across and down by a discrete number of steps, that is, the primary electrons emitted from the photocathode are deflected in a controlled manner. Each step equals the size of a channel when subtended to the photocathode and the time at each step equals a number of CCD frames. The number of steps in each ‘dither cycle’ equals a multiple of the number of steps in a CCD pixel
- The centroid of each event is found. The number of dither steps already taken from the original, or base, position is subtracted from the event address. In this way, for a given input position, the event address is always the same even though its position on the CCD is not.

Each point on the input image is centroided in each of the 8 channels for an equal length of time. Thus, each position on the input image is subject to each of the 8 different errors associated with being centroided in the 8 different channels. The effect on the accumulated data is to average through the fixed pattern giving a distortion free image.

With MIC dithering has disadvantages. Dithering is not well suited to MCP intensifiers. With the CCD-IPCS, which uses a 4-stage magnetically focused EMI intensifier, the use of scan coils to perform the input image shifting added relatively little extra bulk to the system. With MIC there are two possibilities for dithering – that of using scan coils or that of mechanically dithering the intensifier using, for example, a piezo electric positioner. The first is impractical as it would require ~ 1 Tesla flux across the front gap which would be difficult to achieve. The mechanical dither method has the disadvantage of moving parts which are unacceptable for a space system.

However, another method which is capable of removing patterning has been developed for MIC and this is the subject of the next section.

6.6.3 The Centroiding Technique Used with MIC

This technique is very different from dithering. The technique does not remove patterning by averaging the effect of centroiding in each channel, it actually *corrects* the pattern so that one does not need good statistics to acquire pattern free data.

The technique has one major constraint – it requires that the event profile be the same shape over the whole field of view. In the CCD-IPCS the intensifier output is lens coupled to the CCD, and the distortion introduced on the event is not constant over the field but is worse at larger radial distances, as was discussed in section 4.3.1. This means that the event profile and consequently the pattern noise is different in different parts of the image. This does not matter with the CCD-IPCS as dithering is able to smooth through any pattern. As already mentioned, dithering is unsuitable for MIC. However, MIC uses a fibre optic taper to couple the output of the intensifier to the CCD and this does not produce the event profile distortions seen with the lens. Therefore, if localised shear distortions are ignored, the event profiles at any part of the CCD ought to be the same. This also assumes that the three channel plates and phosphor screen are also parallel and this is discussed in section 7.6.

Because the event profile is the same over the entire image area, the pattern noise is also constant in shape. This means that if one were able to construct a centroiding algorithm that was suitably matched to the event profile, there would not be any pattern at any point in the image. Such an algorithm would be very complex, impossible to implement in hardware and time consuming in software. Although this technique uses the standard algorithm, one can think of it as being refined by the technique to match the event profile.

Consider the standard algorithm of equation 6.1. This may be implemented in hardware using discrete integrated circuits. Alternatively, it may be implemented as a look-up whereby the event data are input as the address of a RAM and the centroid data are output. If the pixel data A–E, each of which has 8 bits, were input as the address then the memory would need to be enormous. By partially calculating the result of the algorithm to find M and N as in equation 6.1 and feeding these into the look-up, the size of the memory is greatly reduced. This is illustrated in figure 6.23. In fact, in the MIC planned for XMM, there are only three pixels of data used for centroiding in either X or Y but, even so, there is still a big saving on memory size if M and N are first calculated in hardware.

The result of M/N is always in the range -0.5 to 0.5 and, when the pixel is divided into 8 equal channels, the channel boundaries and corresponding centroid positions are as shown in table 6.2. Software is used to calculate the look-up table entries. Every possible value of M/N is calculated and a channel number is assigned to it. Each location defined

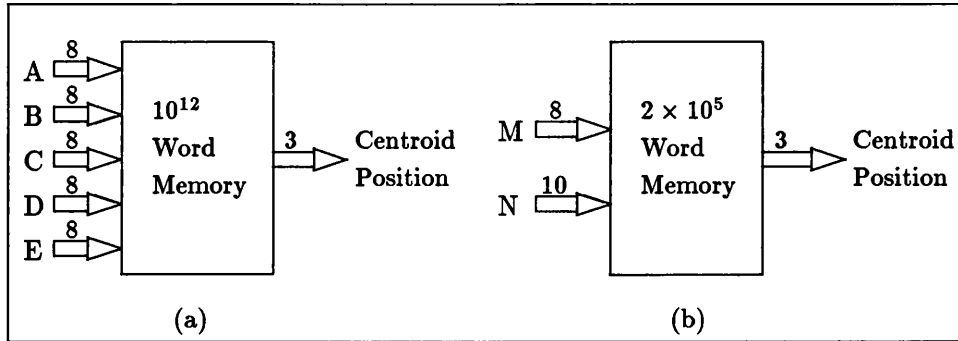


Figure 6.23: An illustration of how the size of memory needed for a look-up table is greatly reduced by partially calculating the centroid in hardware

Table 6.2: Boundary positions and centroid positions for equal channels

M/N	Channel Number	Centroid position
-0.5 → -0.375	0	000
-0.375 → -0.25	1	001
-0.25 → -0.125	2	010
-0.125 → 0	3	011
0 → 0.125	4	100
0.125 → 0.25	5	101
0.25 → 0.375	6	110
0.375 → 0.5	7	111

by a particular M and N has as its data the centroid position calculated from M/N. When the look-up table is loaded with these initial values the usual fixed pattern as in figure 6.20 is seen on a flat field. However, the use of a look-up table provides the flexibility to be able to correct the pattern.

One can think of the fixed pattern as being due to some channels being smaller than others. For example, imagine that channel 0 has far fewer counts in it compared to the other seven channels; one can say that this channel is too small because it is receiving too few counts. If one were to re-define the range occupied by channel 0 to be from -0.5 to -0.35, say, instead of -0.5 to -0.375, then it would automatically receive more counts. One

can re-define the range of any channel so that it receives more or fewer counts according to whether it has too few or too many. One should be able to alter the boundary values of all the channels simultaneously such that each receives the same number of counts. In fact, because the error distribution within a pixel is not linear, the refinement cannot be done in one go but must be converged upon by iteration.

The procedure for correcting the pattern, based on the concept described above, is depicted in figure 6.24 and is as follows.

1. Software uses equation 6.2 to calculate a channel number for every possible combination of M and N. Each combination of M and N is fed into the address of a hardware look-up table and for each the channel number is loaded as the 3-bit data of that location. All of these channels are defined by boundaries which make them equal in size.
2. An integration is taken on a flat field and, as events are detected, values of M and N derived from the event data are fed into the address of the look-up table. Corresponding 3-bit centroid positions are output from the lookup.
3. Software then takes a user defined area of the flat field image and adds up the total number of counts in each of the 8 channels. This enables good statistics to be achieved in a short integration time.
4. If the range of the 8 totals is within that expected of the random system noise then any fixed pattern in the flat field can be assumed to be negligible. The boundary values already loaded into the look-up tables can be used for all subsequent integrations. Otherwise,
5. Software calculates new channel boundaries by looking at the relative weighting of counts in the 8 channels. The look-up table is reloaded with new data such that the boundary values are altered. The procedure is then repeated from stage 2.

Circuit Description

The implementation of this centroiding technique in hardware is simple, consisting merely of circuitry to calculate M and N, look-up tables and circuitry to load them. The board also contains the event validate circuit and the root diagram was shown in figure 6.13

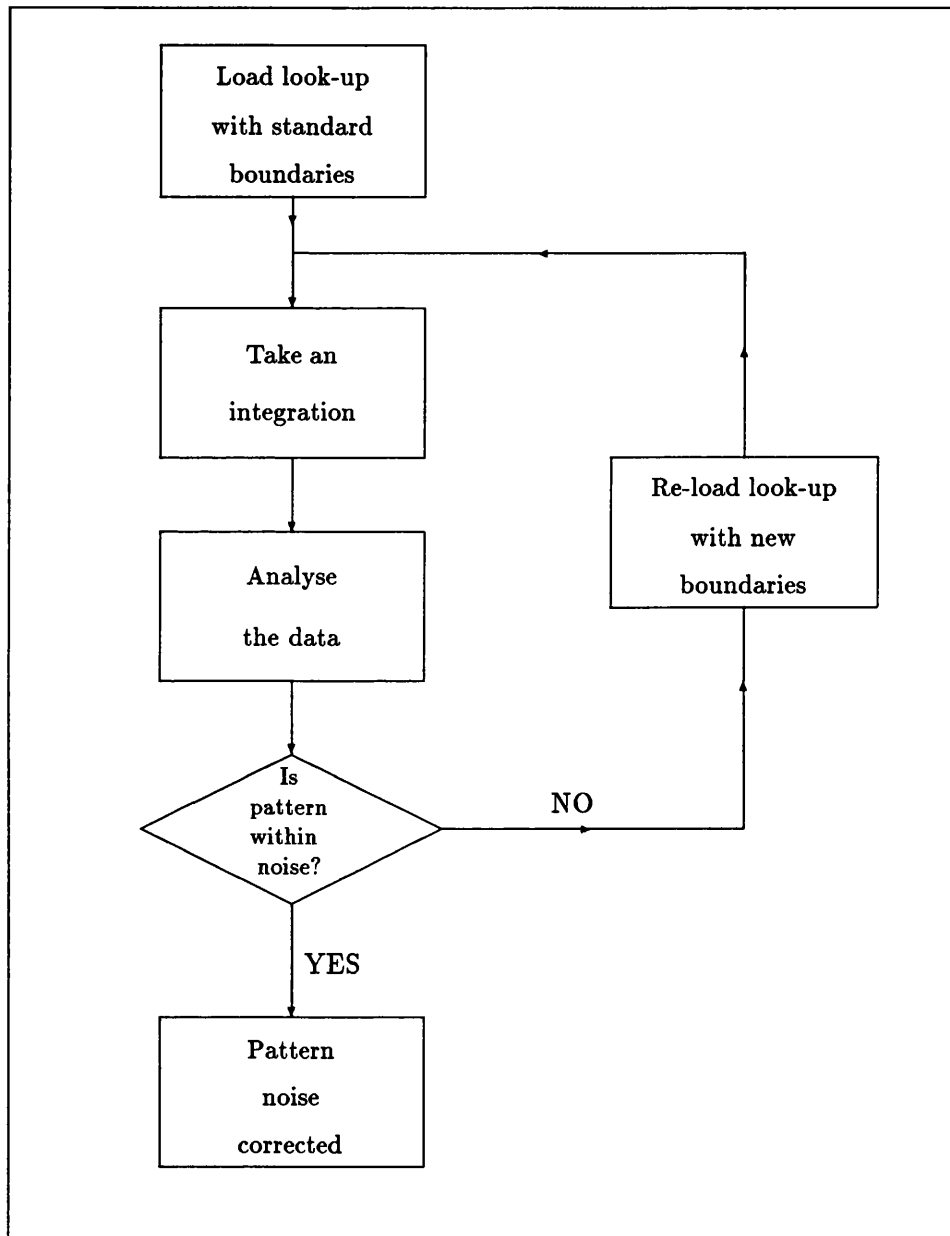


Figure 6.24: Flow diagram depicting the procedure for correcting the pattern noise

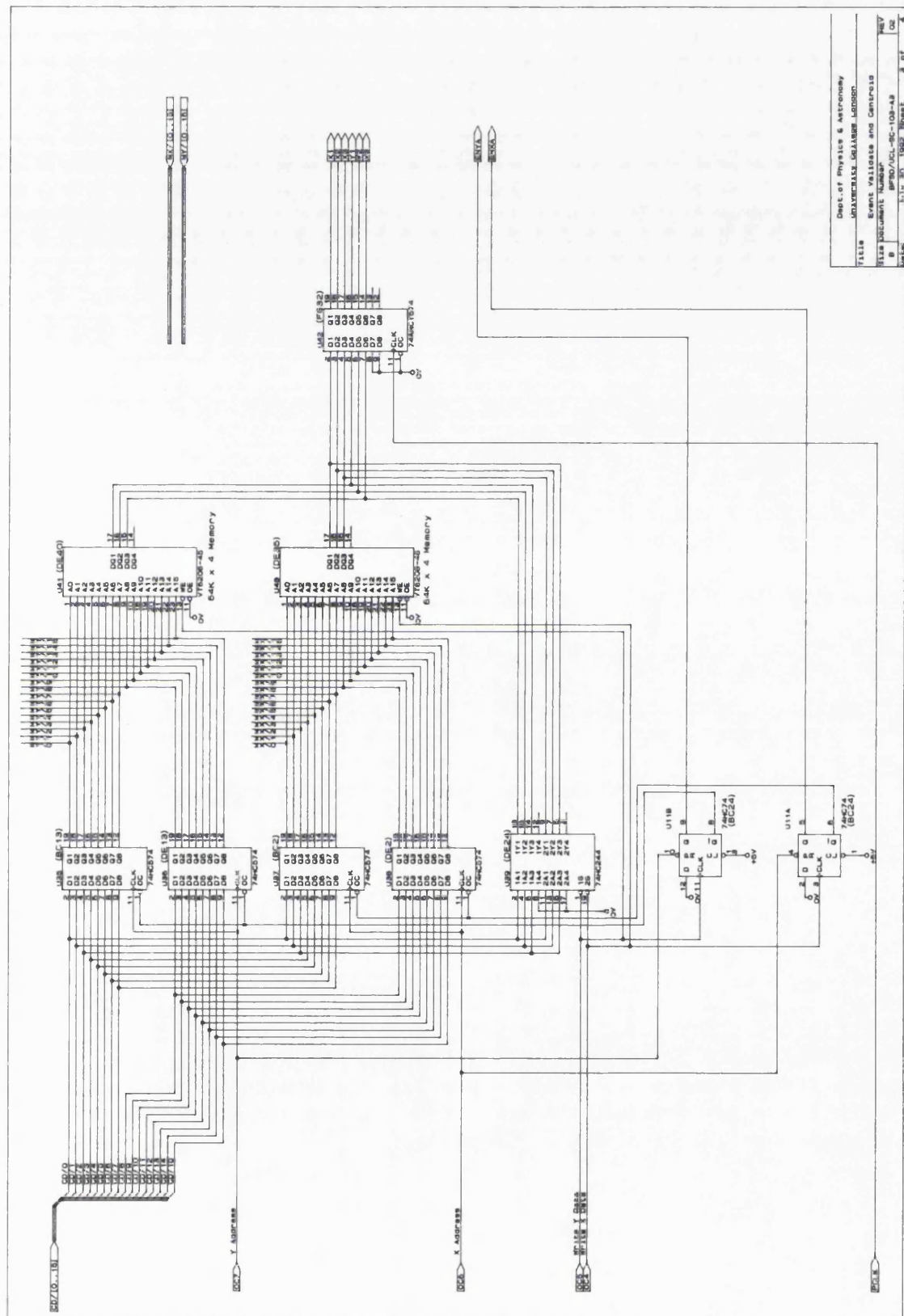


Figure 6.25: Centroid look-up tables circuitry

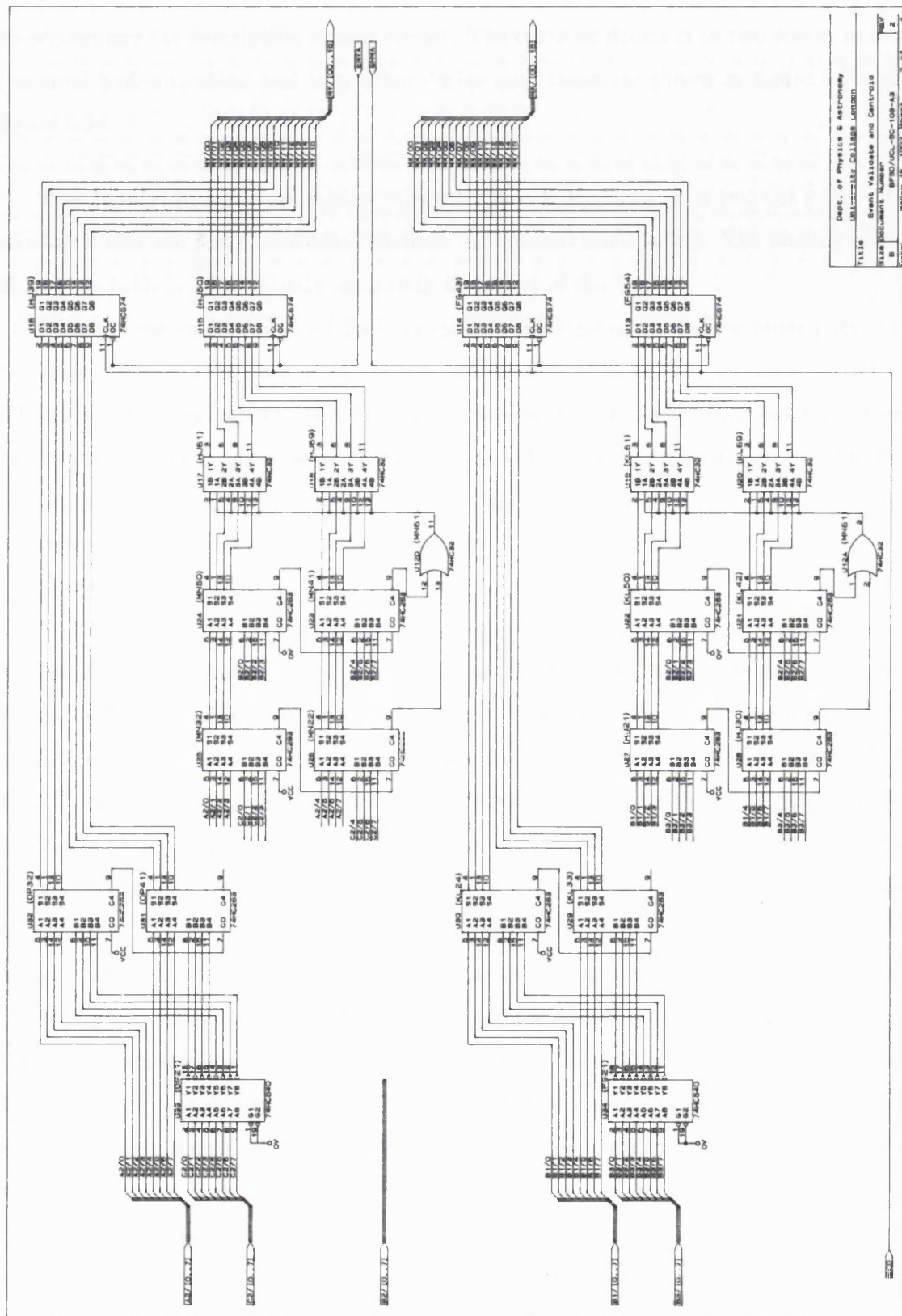


Figure 6.26: Circuitry that calculates M and N of the centroiding algorithm

to accompany the description of that circuit. The centroid circuit is in two blocks named 'centroid look-up tables' and 'algorithm derive' and these are shown in figure 6.25 and figure 6.26.

The 'centroid look-up tables' circuit essentially consists of two 64k×4 RAMs, one for X and one for Y, and some circuitry to control their loading. The loading of the X look-up table is done entirely separately from that of the Y.

Consider the loading of the X look-up table, U40. First of all the computer puts onto the lines CD/0–CD/15 its first calculated combination of M and N, M being on CD/8–CD/15 and N being on CD/0–CD/7. These are input to the latches U37 and U38 before OC 7 is issued, the rising edge of which clocks the M and N into the latches. OC 7 is also fed into the preset input of U11A which sends the output enables of the latches low thus outputting M and N to the RAM address inputs.

Now that the address is set up the data can be sent. The computer puts onto lines CD/0–CD/2 the 3-bit centroid position corresponding to the particular combination of M and N that has just been fed to the address inputs of the RAM. The data are input to the buffer U39 which acts as a data selector. When OC 4 is issued and input to 2G of U39, it selects the set of outputs that feed into the data inputs of the correct RAM, that is, the X look-up table. At the same time OC 4 also sends the write enable of the RAM low thus enabling the data to be written into the address which is still present at the address inputs. OC 4 also clocks the flip-flop U11A and disables the latches U37 and U38 so that the address is no longer present at the RAM inputs. The computer may now send its next combination of M and N and load the corresponding 3-bit centroid position. The computer cycles through every combination of M and N and the corresponding data are loaded into the location given by the combination. Exactly the same sequence is used for the Y look-up table except that OC 6 and OC 5 are used and different chips control the loading into RAM U41. The whole process of loading each look-up table takes two or three seconds

One other thing to notice is the lines MX/0–MX/15 and MY/0–MY/15. These are the RAM address inputs derived from the hardware calculation of M and N performed with real data during an integration. Before any integration, while the look-up table is being loaded, the inputs MX/0–MX/15 and MY/0–MY/15 must be disabled to prevent

the possible formation of spurious addresses. ENYA and ENXA disable the latches that hold these lines at the same time as the computer derived M and N are enabled onto the RAM address inputs. At all times other than look-up table loading, MX/0–MX/15 and MY/0–MY/15 are enabled and the combinations of M and N that are input during an integration lead to 3-bit centroid positions being output as X1 to X3 and Y1 to Y3 which are passed on to the address generator via the backplane.

The ‘algorithm derive’ circuit is just a straight calculation of M and N for both X and Y. The calculation for X is done separately but simultaneously to that of Y.

Take the X calculation. Three pixels of data, B1, B2 and B3 are input to the circuit. One part of the circuit performs $B1-B3$ to get M while the other part performs $B1+B2+B3$ to get N. $B1-B3$ is performed as follows. To take one number away from another one must add the negative of the first to the second. To find the negative of a number one must invert all the bits and add 1. Then when one adds the other number one must ignore any carry and treat the most significant bit as a sign bit, 0 being a positive number and 1 being a negative number. For example, five minus six: -6 is 1010 which when added to 0101 gives 1111. Take the most significant bit to mean a negative number then reverse the process of finding a negative number, that is, take 1 away and invert all the bits to get 001, so the answer is -1 . With five minus two, for example, one gets a carry. When this is ignored the result is 0011, that is 3. In the circuit, B3 is inverted by the inverting buffer U34 and 1 is added to it by tying the carry input of the adder U30 to 5 volts. U29 and U30 perform the addition of B1 and $-B3$ and their 8-bit output is input into the latch U14 to form M.

The addition of B1, B2 and B3 is straightforward. $B1+B3$ is first performed in U27 and U28 and the result of this is added to B2 in U21 and U22. Now, there are only 8 bits to hold the value of N. If N is greater than 255 then the extra most significant bit is set to 1. If the 8 bits that form N were sent straight to the latch to form N then, every time the addition exceeded 255, the result of M/N would be entirely wrong. In fact, what happens is that if the result is greater than 255 the resulting carry output is used to set all the 8 bits of N to 1 so that N remains at 255. N should not usually be much above 255 so the error in M/N incurred by setting all the bits to 1 would not be large. The bits are set to 1 using the OR gates U19 and U20. If either of the additions $B1+B3$ or $B2+(B1+B3)$

has a carry then this is fed into the latch U13 to form N, the other half of the address MX/0–MX/15.

Exactly the same calculation is performed in Y except that the pixel data input into the circuit is provided by A2, B2 and C2, and C2 is taken away from A2. The two addresses MX/0–MX/15 and MY/0–MY/15, formed by the respective M and N, are fed into the address inputs of the two look-up tables which output the 3-bit centroid position contained in that location.

Results of the Implementation of the Technique

On the whole, the technique has been very successful. Occasional problems have led to a better understanding of the formation of fixed pattern noise and its removal.

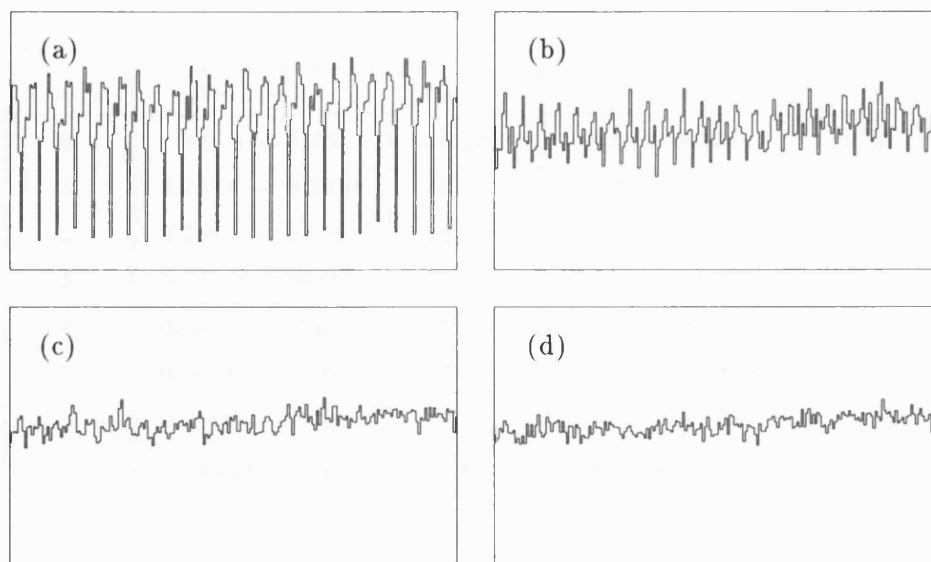


Figure 6.27: Four flat fields showing the gradual removal of the fixed pattern noise with each successive iteration

Figure 6.27 shows how the application of successive corrections gradually reduces the modulation until it is no longer discernible. Table 6.3 shows how the boundary values of the 8 channels and their respective number of counts changes during the procedure. Because the pattern has a periodic nature, that is, it repeats every 8 channels, the Fourier transform power spectrum of a flat field with pattern shows prominent spikes at 0.125 and

Table 6.3: Boundary positions and counts in each channel for the four successive flat fields shown above

Channel Number	Flat Field 1		Flat Field 2	
	Boundaries	Counts (%)	Boundaries	Counts (%)
0	-0.5 \rightarrow -0.375	7.32	-0.5 \rightarrow -0.3232	13.77
1	-0.375 \rightarrow -0.25	12.28	-0.3232 \rightarrow -0.1960	12.53
2	-0.25 \rightarrow -0.125	13.06	-0.1960 \rightarrow -0.0766	12.09
3	-0.125 \rightarrow 0	12.96	-0.0766 \rightarrow 0.0439	12.90
4	0 \rightarrow 0.125	14.57	0.0438 \rightarrow 0.1481	11.23
5	0.125 \rightarrow 0.25	14.18	0.1481 \rightarrow 0.2563	12.09
6	0.25 \rightarrow 0.375	13.92	0.2563 \rightarrow 0.3671	12.21
7	0.375 \rightarrow 0.5	11.71	0.3671 \rightarrow 0.5	13.20

Channel Number	Flat Field 3		Flat Field 4	
	Boundaries	Counts (%)	Boundaries	Counts (%)
0	-0.5 \rightarrow -0.3359	12.79	-0.5 \rightarrow -0.3388	12.51
1	-0.3359 \rightarrow -0.2090	12.42	-0.3388 \rightarrow -0.2111	12.41
2	-0.2089 \rightarrow -0.0854	12.20	-0.2111 \rightarrow -0.0844	12.55
3	-0.0854 \rightarrow 0.0311	12.34	-0.0844 \rightarrow 0.0336	12.50
4	0.0311 \rightarrow 0.1480	12.51	0.0336 \rightarrow 0.1505	12.48
5	0.1480 \rightarrow 0.2603	12.50	0.1505 \rightarrow 0.2628	12.47
6	0.2603 \rightarrow 0.3740	12.56	0.2628 \rightarrow 0.3760	12.55
7	0.3740 \rightarrow 0.5	12.69	0.3760 \rightarrow 0.5	12.54

at each harmonic of this frequency as is shown in figure 6.28. The power spectrum of the corrected flat field shows no such spikes and confirms the removal of the pattern.

A number of problems and effects have been seen while this technique has been used; some have been overcome and some have yet to be addressed.

Occasionally, the pattern possesses large positive spikes and has a shape inverse to that of figure 6.20. Initially, when a correction was attempted on this type of pattern, the technique broke down because the computer worked out boundaries that were nonsense. This was due to the iterative formula that was being used to calculate the new boundaries.

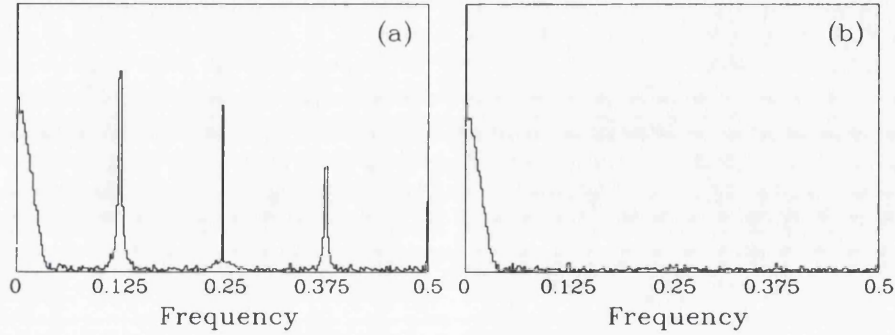


Figure 6.28: Fourier transform power spectra of the first and last flat fields above showing the removal of all harmonics.

The formula was

$$S_{i,n+1} = S_{i,n} + 0.125 \left(\frac{\mu_n - m_{i,n}}{\mu_n} \right) \quad (6.3)$$

where

$$\begin{aligned} S_{i,n+1} &= \text{New size of channel } i \\ S_{i,n} &= \text{Size of channel } i \text{ just used} \\ m_{i,n} &= \text{Number of counts in channel } i \\ \mu_n &= \text{Mean number of counts of } m_i, i = 1, 8 \end{aligned}$$

The computer would use this formula to work out the new size of each channel based on the discrepancy of its number of counts from the mean number in the 8 channels. It would then calculate the boundary positions of each channel given lower and upper boundaries to the pixel of -0.5 and 0.5 . This formula works fine unless, after the first flat field, any $m_i > 2\mu_n$ in which case the formula gives $S_{i,n+1} < 0$. This means that the formula is predicting that the channel should occupy a negative proportion of the channel, which is clearly nonsense. This suggests that, in order to avoid this, the iteration formula should not contain any plus or minus signs. Consider a formula that allocates a proportion of the pixel which is in inverse proportion to the number of counts it received

$$S_{i,n+1} \propto \frac{1}{m_{i,n}}$$

To be iterable it must take account of the old channel size and it must also be normalised such that $\sum_{i=1}^8 S_{i,n+1} = 1$. A formula which has these properties is

$$S_{i,n+1} = \frac{\left(\frac{S_{i,n}}{m_{i,n}}\right)}{\sum_{i=1}^8 \left(\frac{S_{i,n}}{m_{i,n}}\right)} \quad (6.4)$$

and this indeed can cope with any shape the pattern might take. The procedure converges slightly quicker using equation 6.3 and this is used except where there are positive spikes.

A problem that has yet to be resolved is that of the incomplete removal of the pattern towards the edge of the field. This must be due to a variation of the pulse profile, and hence the fixed pattern, towards the edge. There are a number of possible reasons for this variation

- It is possible that the third channel plate of the image intensifier is not parallel to the output phosphor or that any of the three channel plates are not parallel to the others. This would lead to a constant variation of the pattern across the field.
- In the prototype XMM-MIC there are three sets of fibre optics that are butted together – the intensifier output, the fibre taper and the CCD fibre input. If any of the butting surfaces were not parallel to the others then this would cause a similar variation in the event profile to that which would be caused by non-parallelism in the intensifier. Alternatively, it is possible that one of these fibre optic surfaces is curved so that it would be impossible to achieve perfect butting. This would also cause the pattern to vary over the field.
- Although the CCD is black-level clamped at the start of each row in order to remove the d.c. bias, it is possible that there are variations in the d.c. bias across a row which would lead to some events having artificially altered profiles and thus to a different pattern.

The fibre-optics are the most likely cause of the variation – some flat fields, where it was assumed that the butting has been accurate, have shown no variation in the pattern across the field. In the space qualifiable version of the detector, the CCD will be bonded directly to the fibre taper and this will form the output of the intensifier. This ought to eliminate any change in the event profile due to the imperfect butting of three fibre optic components.

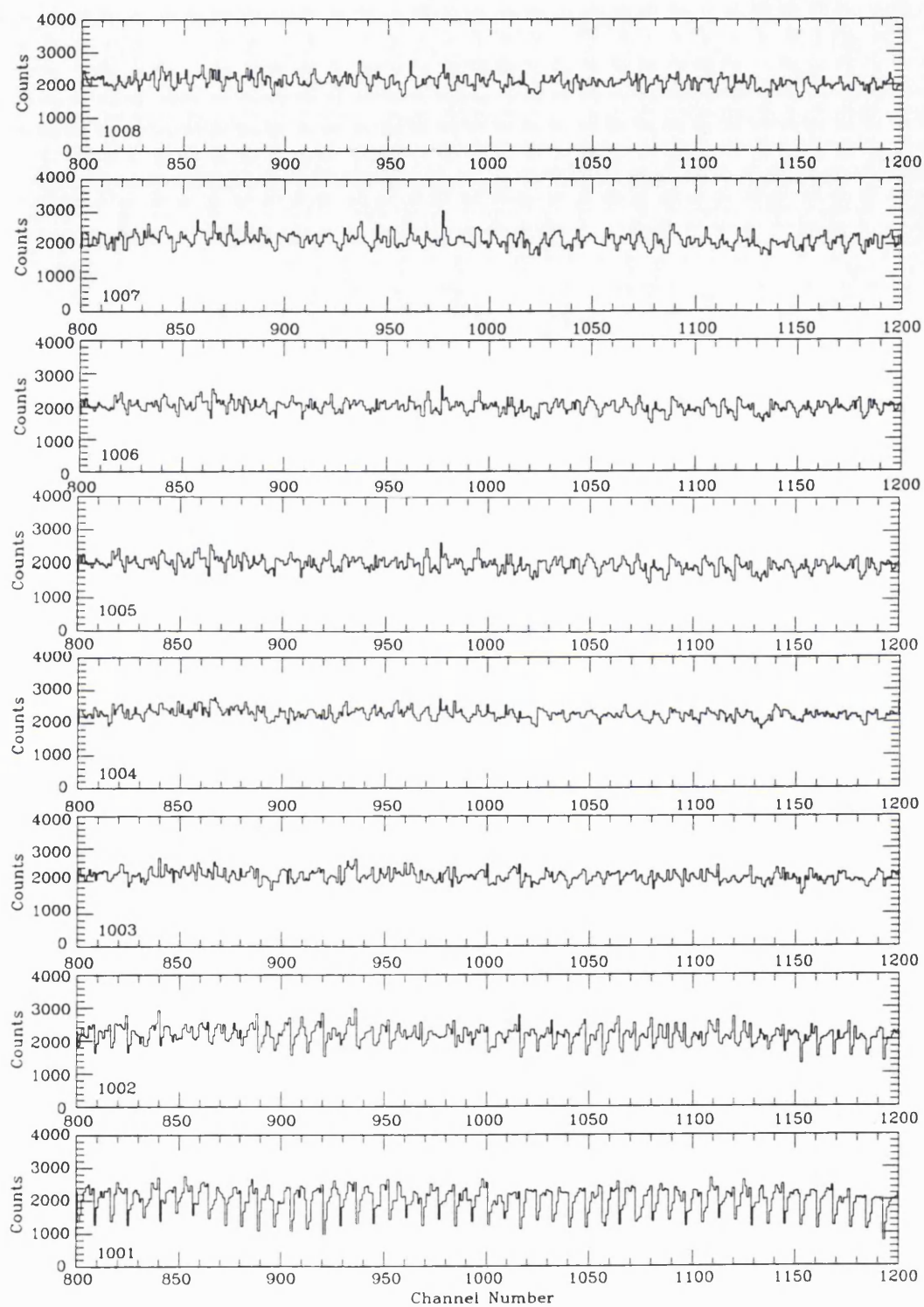


Figure 6.29: Fixed patterning in X associated with the eight spectra of a single pixel. Each spectrum is that of a channel in Y

A recently discovered phenomenon is shown in figure 6.29. This shows the fixed pattern in X of 8 spectra in the same pixel, each spectrum being that of a channel in Y. The fixed pattern is different for every channel of a pixel in Y but it repeats every 8 channels in Y. Previously it was thought legitimate to sum the counts in each channel of X over a large area of Y because it was assumed that within a pixel of Y the pattern was constant. Due to the asymmetrical nature of the event profiles, some centroid positions do not appear in the same pixel as the peak data. In the ground based system this is overcome by implementing an asymmetry correction and this needs to be implemented in the XMM system.

A further effect that has been seen arises from the discrete nature of M and N. Because M and N can only take certain integer values, the result of M/N also takes on discrete values. The modulus of M/N goes up from zero in a series of steps whose size gradually decreases. The two M/N either side of zero have the largest step. Consequently, because most errors arising from centroiding tend to place events towards the middle of the pixel, there is often a much larger number of counts in one of the two M/N around zero. The channel that contains this value of M/N , or spike, has a much larger number of counts in it. When the computer uses equation 6.3 to calculate new boundaries it will put the spike in another channel. However, this channel will now have too many counts in it. The computer will continue to calculate new boundaries, making the spike oscillate between two channels, but the pattern will never be removed.

The situation is improved when the events are asymmetrical because then a large number of counts do not accumulate about zero but rather about another value where the M/N values step more frequently and there is more precision available for allocating channel boundaries.

At the moment no long term solution to this problem can be seen, although a hardware fix has been implemented which randomly places events in one of the two channels between which the spike is oscillating.

There are three other effects which are known to alter the pulse profile and thus affect the shape of the pattern

- The shape of the pulse profile is very dependent on the four voltages applied across various gaps in the intensifier. These voltages are all derived from a single power supply using a resistor divider network and when switched on it takes many hours for the voltages to stabilise. If the fixed pattern is corrected before the voltages have stabilised then it will need to be corrected again some time later because, as the voltages drift so the pulse profile and pattern change and the entries in the look-up tables become inaccurate. By ensuring that the pattern correction is performed after the voltages have stabilised this problem can be eliminated.
- It has been observed that at higher count rates the fixed pattern in a flat field is a different shape. The reason for this is that, as the count rate goes up, the number of coincident and overlapping events per frame increases. These events have a completely different shape to single events and consequently they will be placed in the wrong channel. If the pattern is corrected at a low count rate then it will return at higher count rates and continue to get worse as the count rate goes up because the number of multiple events and, therefore, the number of incorrectly placed events, increases.

This is a serious problem because it means that on objects where there is a range of count rates, such as spectra with their various emission and absorption lines, the effect of pattern cannot be corrected for even by standard flat field calibration. This effect could be removed by dithering and this is discussed again in section 7.6.

- Local blemishes, such as fibre optic multifibre junction defects and low quantum efficiency CCD pixels, affect the pulse profile. Events are placed in the wrong location but the effect is only very local. The solution is to have better grade fibre optics and CCDs although it is anticipated that there will always be a certain number of these blemishes.

A General Summary of the Technique

The technique has been demonstrated to remove the fixed pattern associated with centroiding errors by using a hardware look-up table to redefine the channel boundary positions.

The technique has a number of advantages

1. It is quick to implement, typically requiring only three iterations of five minutes each to correct the pattern.
2. Unlike dithering, good statistics are not required on one's data since the pattern is already corrected prior to acquisition.
3. There are no moving parts and, in particular, there is no bulk associated with the implementation of the technique. This is important for a space-borne system.
4. The technique is applicable to both 5-pixel and 3-pixel centroiding and therefore in the case of MIC, to ground based or space based systems.
5. The system resolution ought to be improved by the technique because the centroiding accuracy is increased. At the moment the fundamental resolution of the intensifier is limiting the determination of the centroiding accuracy, which is believed to be $\sim 4\mu\text{m}$.

However, there are numerous disadvantages of the technique which were described in the previous section and which are mostly associated with the susceptibility of the pulse profile to alteration. If a novel, low power, lightweight method of dithering was designed then this would overcome the limitations of the technique.

6.7 Address Generator

So far the processing electronics have recognised an event, given it a value of one or two events and assigned to it a 3-bit centroid position. It is now necessary to give it an address for storage in the detector memory. The address generator gives each event its correct address and controls its transmission to the Direct Memory Access (DMA) interface which is used for controlling data storage.

Efficient use of detector memory is very important to save on power consumption. Also, in the prototype system extra memory is needed by the computer to perform its operations. The address generator forms an address in such a way that the most efficient use of memory is made.

Consider the following argument. Ideally, the most useful form in which to have an address is as in figure 6.30, with the X and Y positions separate and ready for use by, for example, graphics routines. There is no problem with memory space if the row length

Y Pixel Address	Y Centroid	X Pixel Address	X Centroid
--------------------	---------------	--------------------	---------------

Figure 6.30: Ideal form in which to have a memory address

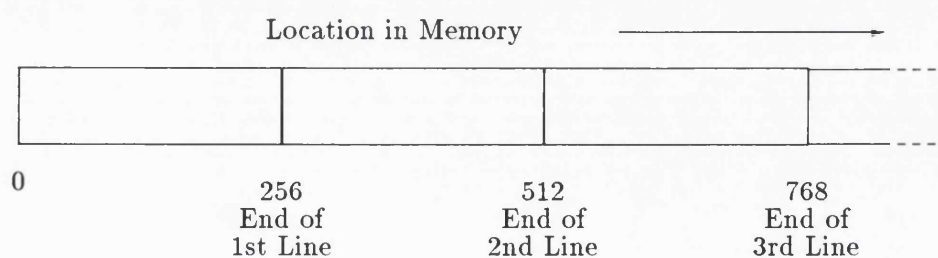


Figure 6.31: Memory allocation with a window length of 256

used is 256 – this is illustrated in figure 6.31. The address generator uses counters to generate addresses. With a row length of 256, the X counter counts to 256 and its carry increments the row counter by one and so the first pixel on the next row appears in a contiguous memory location to that of the last in the first row. In this case no memory is wasted.

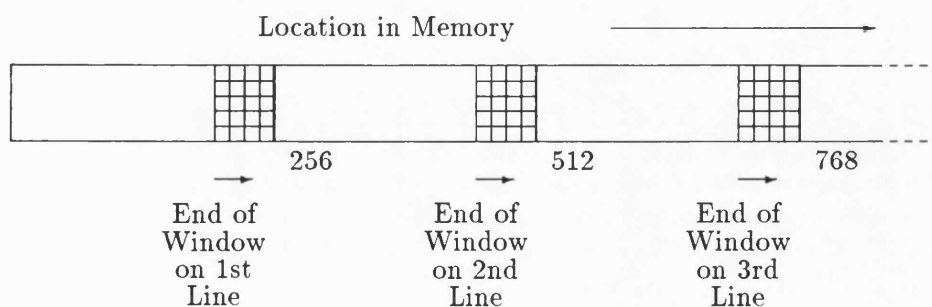


Figure 6.32: Waste of memory encountered when the window length is not 256

However, a requirement of the MIC detector for XMM is that the window may be of any length in X. Take, for example, a window of length 200. The X counter counts to 200

and then must be disabled. It is enabled again at the start of the next row and increments the row counter by one. The address of this first pixel of the second row is not contiguous with that of the last pixel in the window of the first row as shown in figure 6.32. There is a large block of memory (shaded) that is never accessed and thus, the most efficient use of memory is not made.

In fact the address generator does not produce addresses with the X and Y components separated. Its counters stop counting at the end of a window but then continue where they left off at the start of the window on the next line. The second counter is incremented only when the first counter has reached 256. In this way, no memory space is wasted but the X and Y information is lost and data from different windows may be mixed together. This is not a problem since the computer knows the start and finish of each window and so can unscramble the address to reproduce the correct X and Y position of each event. The advantage of this method of address generation is that not a single location of memory is wasted and it is a simple matter to unscramble the addresses.

Once the address has been generated it needs to be transmitted to memory. However, the rate at which the computer can store events in the memory differs from the rate at which events arrive in the processing electronics. If two events arrive in such quick succession that the computer is unable to store the first before the second arrives then an event will be lost. The events need to be temporarily stored until the computer is able to store them. A First-In-First-Out (FIFO) memory is used for this purpose. When an event is detected it is stored in the FIFO and the computer is informed that there are some data to be transferred. The computer then reads those data into the memory. If another event has arrived during this read then the computer is informed and will immediately read those data once it has finished the first read. In this way the computer stores the information of each event in its own time and none of the events are lost. The address generator controls the writing and reading of data into and out of the FIFO.

6.7.1 Circuit Description

A block diagram of the Address Generator is shown in figure 6.33. The output of the counters and the 3 centroid bits in X and Y are fed into 2-line to 1-line data selectors which give an output at either $\times 8$ or $\times 4$ depending on their select input. This address and the two data bits from the Multiple Event Discriminate circuit are stored in the FIFOs until

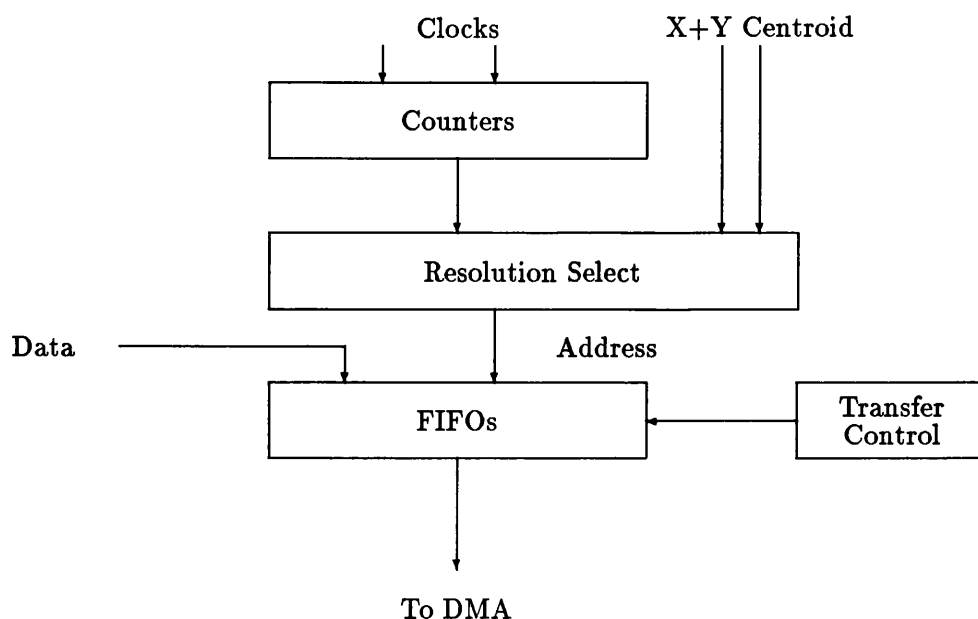


Figure 6.33: Block diagram of the address generator

the computer can store them in the memory. The Transfer Control circuitry controls the reading and writing of data into and out of the FIFOs.

The root circuit diagram is shown in figure 6.34 and the Address Generate and Transfer Control circuits, which are both part of the root, are shown in figure 6.35 and figure 6.36. The root shows the FIFOs U14 to U16 and the line drivers U10 to U13 whose outputs are passed onto a cable to the computer via the 60-way header. Various signals are also passed to and from the computer and transfer control.

The Address Generate Circuit

This part of the circuit is provided with only three signals to drive the counters U18 to U20. CCK, which is just a buffered PCLK, the system 10MHz clock, is used to increment the counter outputs. The carry output of one counter is used to clock the next so that the addresses of all the pixels are contiguous in the memory. This is the way in which the most efficient use is made of memory space. CCKEN* is essentially the inverse of Window Active, but delayed by an appropriate amount to account for the delay between pixel data entering the chassis and event data entering the address generator. This is used to disable the counter when there is not a window. It disables and enables all the counters at the

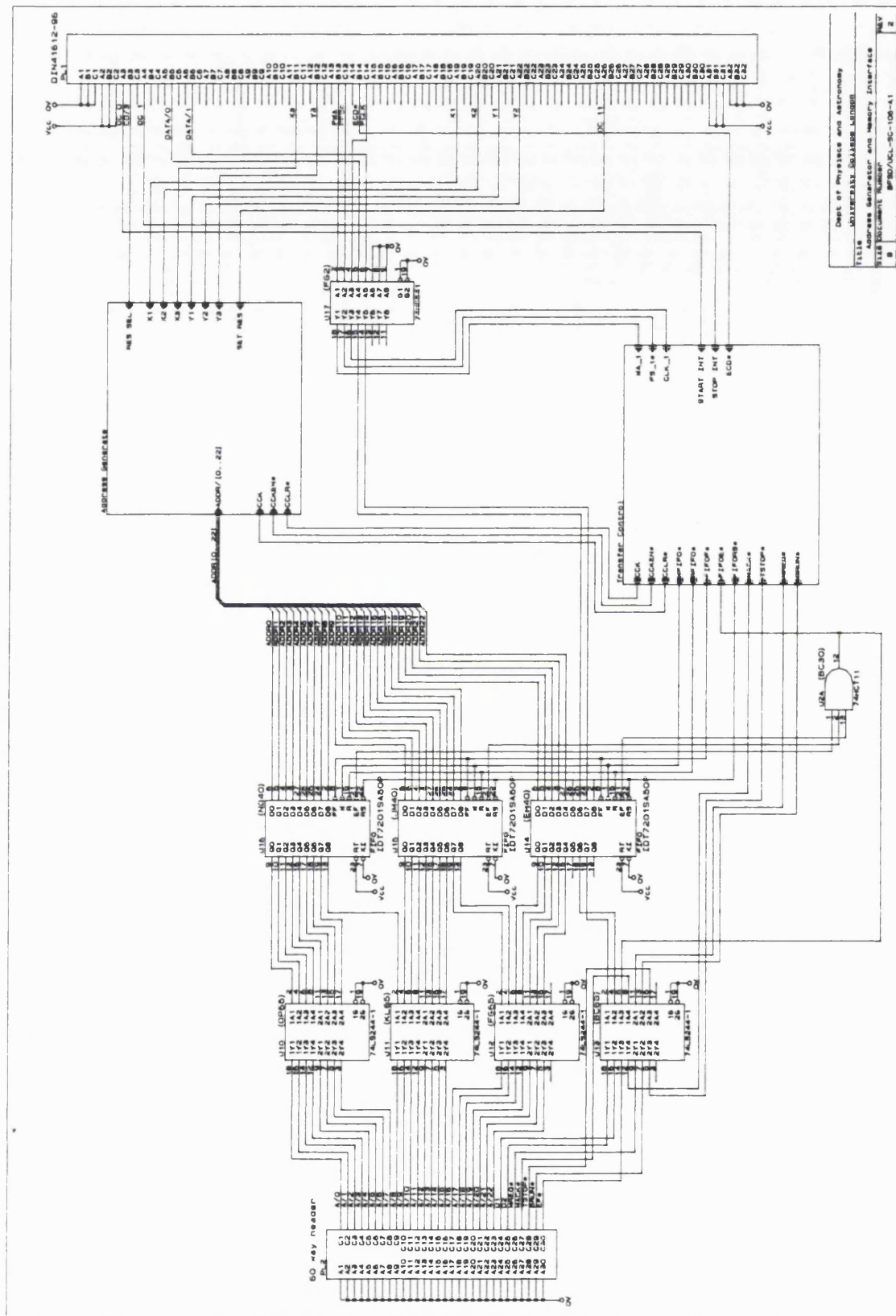


Figure 6.34: Root diagram of the address generator

Figure 6.35: Circuitry that produces the address for the address generator

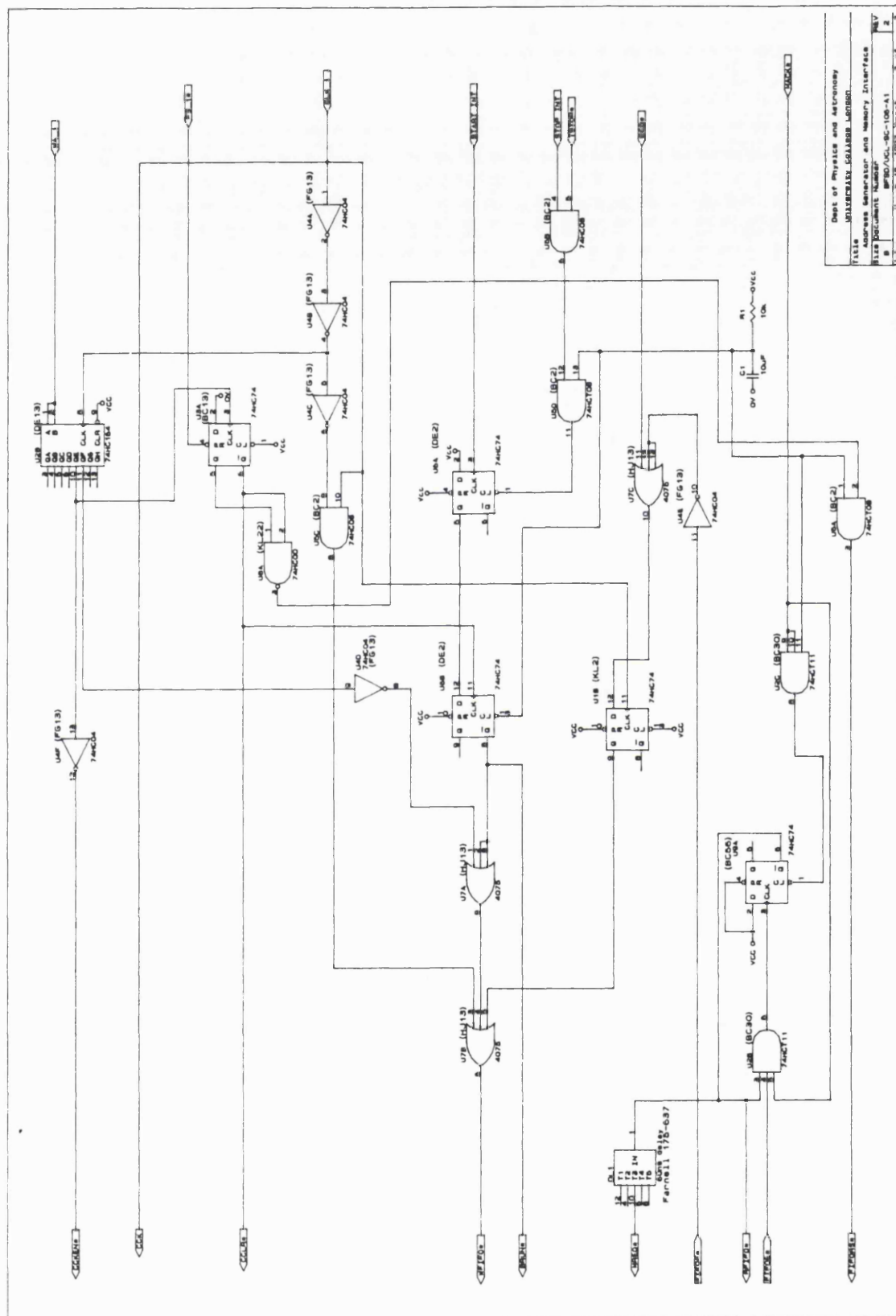


Figure 6.36: Control circuitry for the address generator

same time so that they start counting from where they left off. CCLR* is used to clear all the counters at the end of a frame.

The output of the counters is input into the data selectors U22 to U27, along with the 6 centroid bits X1 to X3 and Y1 to Y3. The select input is provided by the output of U1A which is determined by the level of CD/3 (RES SEL) on the arrival of OC 11 (SET RES). If the B input is high then all the centroid bits are passed through to form part of the address and the resolution is $\times 8$. Otherwise, X1 and Y1 are not passed through, the rest of the address is shifted by two bits and the resolution is $\times 4$. The address consists of a single number with the Y and X centroid bits tagged on the end. This is passed on to the FIFOs.

Transfer Control

The FIFO read and write cycles are independent. Essentially the two requirements are these: If an event is present then it needs to be stored in the FIFOs. If data are present in the FIFOs then it needs to be read from them into the detector memory. This is not the same as saying that if data are written in it must be read out; a FIFO can store up to 512 events and can write while it is reading. The control for read is independent to that of write.

Write Cycle. Typical timing for the write cycle is shown in figure 6.37. The first criterion for write is that there should be an event detected. This is provided by ECD* and synchronised by the flip-flop U1B. There are a number of other signals with which ECD* needs to be qualified.

- If the FIFO is full then there is no point in trying to write more data in. FIFOF* going low prevents WFIFO* going low and initiating a write cycle.
- The time taken to write data into the FIFO is *at least* 50ns. In order to make sure that the write pulse is long enough, the arrangement of the 3 inverters U4A to U4C and the AND gate U5C is used. This makes the space much longer than the mark and provides ample time to perform a write.
- In case junk data contrives to produce an ECD* outside a window then Window Active, which is derived from pin 10 of U28, is used so that a write may only take

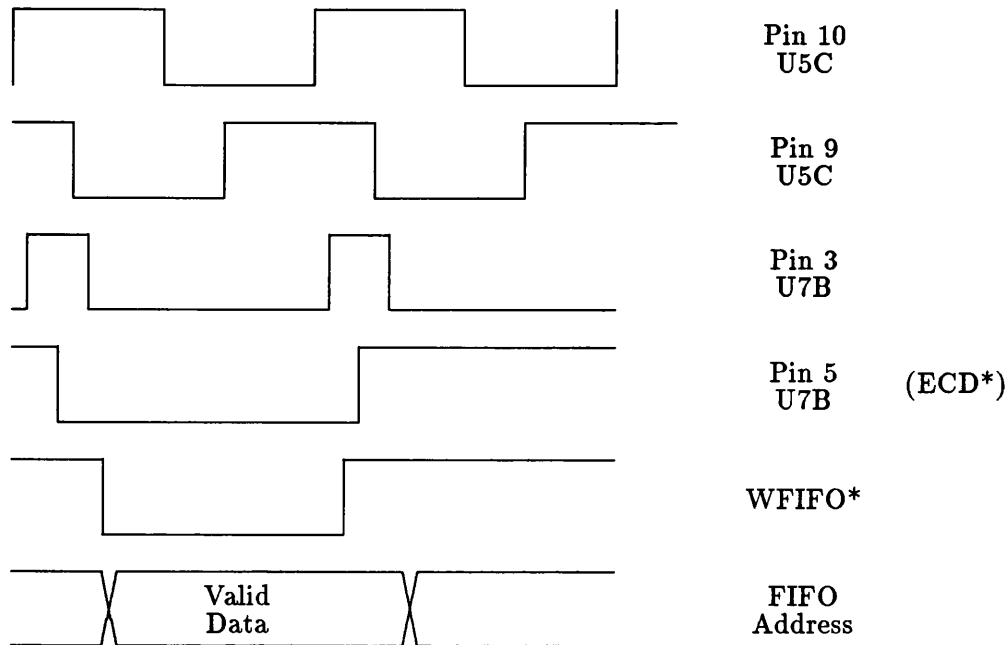


Figure 6.37: Timing diagram for the FIFO write cycle

place within a window.

- That an integration is in progress. A qualifying signal comes from START INT, STOP INT or TSTOP* via the \overline{Q} output of U6B. START INT and STOP INT are user controlled integration start and stop whilst TSTOP* is generated when the integration time has expired. The \overline{CLR} input of this chip is connected to the capacitor-resistance arrangement so that when the circuitry is switched on the chip does not enter an odd state. A number of other chips are also connected to this signal so that they are cleared when they are switched on.

The WFIFO* signal is generated by all the above conditions and is used to write data and addresses into the FIFOs.

Read Cycle. Typical timing for the FIFO read cycle is shown in figure 6.38. This is initiated by the FIFOs' empty flags, shown on FIFOE*, going high, indicating that there are data in the FIFO. All three EF outputs of the FIFOs are passed through U2A because they may go high at different times due to differing internal delays – they must

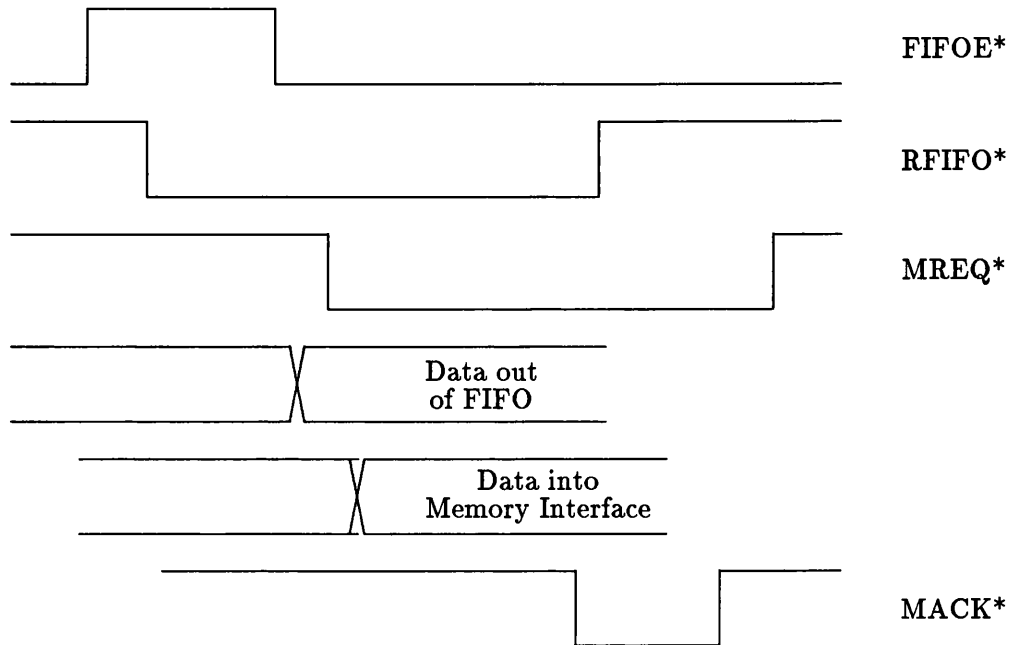


Figure 6.38: Timing diagram for the FIFO read cycle

all be high before the read is initiated. FIFOE* going high causes the FIFO read input RFIFO* to go low and start a read cycle. Data do not appear on the FIFO outputs for 50ns. RFIFO* is delayed by 60ns and sent out to the computer telling it that data are ready to be stored in the memory. This delay ensures that the data are present on the FIFO outputs before the computer is informed. The computer writes the data into the memory and sends back MACK* acknowledging that it has received the data. MACK* clears U9A and sends MREQ* high again which in turn resets MACK* high. That is the end of a read cycle when no more data are present in the FIFOs.

If there are more data present then the flip-flop will only be clocked again at the end of MACK*, even if FIFOE* has gone high again. If MACK* was not fed into U2B then the rising edge would occur during \overline{CLR} low and a read would be lost.

Thus, the computer reads data from the FIFOs at its own rate and independently of the rate at which events are detected.

Other signals derived from the transfer control electronics are BRUN* which tells the computer that a run is in progress and FIFORS* which resets the FIFO when the circuit

is switched on and before each window.

6.8 The Frame Store

The Frame Store is a very important test facility without which it would not be possible either to effectively test the rest of the processing circuitry or to analyse various properties of the rest of the detector.

The circuit operates in two modes.

- As a *frame grabber*. This function of the frame store allows us to understand more about the detector and to set it up for effective operation.

The circuit is able to grab a frame of raw video data while the detector is operating. This frame, which is a 'snapshot' showing individual photon events, can be read into the computer for analysis of various properties of the events. For example, if a large number of these snapshots are taken then the computer can determine the pulse height of each event in all the grabbed frames and build up a pulse height distribution which, for good statistics, takes only a few minutes. If the distribution is not ideal for photon counting then the voltages of the intensifier can be tweaked. Pulse width and pulse energy distributions are also determined in this way. Other application of the frame grabber are to study the asymmetry of the events in order to predict the effect on centroiding and to measure the readout noise of the CCD.

- As a *system test*. Without this function of the frame store it would be almost impossible to debug and modify the image processing electronics.

The computer is able to load the frame store with a frame of data that contains a simulated photon event. This frame of data can then be passed through the processing electronics again and again so that the same event is continually being processed. This allows the functioning of each circuit in the data processor to be assessed. For example, is the event being centred correctly in the data analysis array? Is it being recognised by event validate? Is it being given the correct address and centroid position? Does it have the correct pulse energy? Because the event is simulated, the computer knows all there is to know about the event and the answers to the above questions can be easily found. Also, since the same event, in the same

location, is passed through the electronics every frame it is easy to identify on the oscilloscope. A bug in the hardware is more easily found because the event can be tailored in order to eliminate suspected causes of the bug.

6.8.1 Circuit Description

The Frame Store has only one diagram and this is shown in figure 6.39. The most important features of the circuit at first glance are the two 64k×4 RAMs U15 and U16 which can store a frame of data. These two chips are used in both the functions of the chip. Although the circuit has two functions, it operates in three modes. The data on lines CD/0 to CD/2 determine, via the decoder U8, which mode will be entered when the OC 8 command is issued. For example, WD 0; OC 8 puts the circuit into normal mode whereas WD 1; OC 8 and WD 2; OC 8 put the circuit into computer mode and test mode respectively. These three modes determine and ensure the correct operation of the two functions of the circuit.

Use as a Frame Grabber

Imagine that the circuit is in normal mode. The system is taking in data as it would in normal operation and this is entering the frame store on lines VDA/0 to VDA/7 from the input to the Data Analysis Array. Now, in normal mode, the output of U4A enables the two counters. The counter U1 is able to count whenever the output of U5F is low, that is, when there is an active window, and it increments its output by one every clock pulse. The counter U2 is able to count every time there is a carry from U1 and so in this way the two counters provide a continuous set of addresses to the two RAMs U15 and U16. So, real data come into the frame store and are latched through U14 which is enabled by NORMAL*, and are written into the RAMs, which are write enabled by NORMAL*, at the appropriate address. Thus, as the counter increments, the appropriate data are written into every address of the RAMs. Frame after frame is written into the RAMs.

In order to grab a frame it is necessary to stop the writing in of frames. WD 1;OC 8 clocks the circuit into computer mode on the FS* pulse, that is, at the end of a frame. This disables the counters and RAM write enables which means that the last frame of data is stored in the RAMs. Now the frame needs to be read into the computer. In computer mode the two latches, U9 and U10, are enabled and addresses from the computer may be

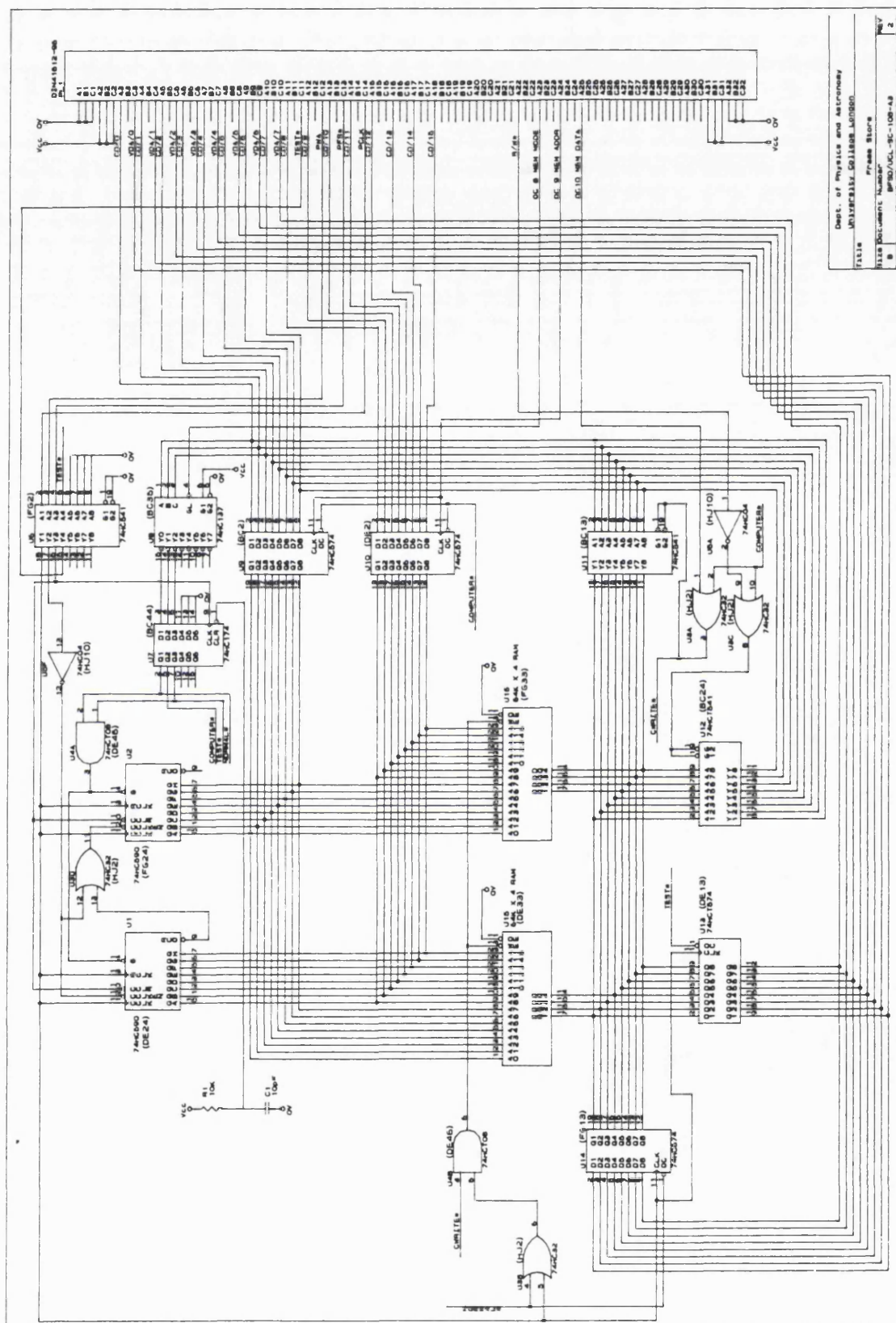


Figure 6.39: The frame store

input to the RAMs by the OC 9 pulse. So, for example, the first address is given by WD 0; OC 9, and this causes the data in address 0 to appear on the output of the RAMs. Then the computer sets R/W* high which enables U12 and the data are read into the computer via CD/0 to CD/7 and the command interface. The computer then send WD 1; OC 9 and reads the data contained in location 1. It continues to increment the address until it has the data for the whole frame. Thus, a whole frame of real data has been grabbed and may be analysed.

Use as a System Test

One wants to be able to put a simulated photon event in a given location within a frame and then allow this same simulated data to pass continually through the processing electronics.

Firstly, the circuit needs to be in computer mode so that the RAMs can be addressed and data can be written into them. To start with, WD 1; OC 8 puts the circuit into computer mode. Then WD 0; OC 9 clocks address 0 onto the input of the RAMs. Now one wants to be able to write simulated data into this address. This data enters via CD/0 to CD/7 and appears on the input of U11. Then an OC 10 command both enables this buffer and sends the write enable (\overline{WE}) inputs of the RAMs low, writing the data into this first location. The computer then issues WD 1; OC 9 for placing the next address onto the RAM inputs and then writes appropriate data into that second address, 1. It keeps incrementing the address and writing data until there is a whole frame of simulated data in the two RAMs. Generally, every location will contain zero, but for those that are part of a simulated photon event.

Now, in order that these data can be read out and passed through the processing electronics, the counters must be enabled. However, in order to do this one cannot use normal mode as might be expected as this would cause the simulated data to be overwritten. Instead, test mode, set up by WD 2; OC 8, is used. This enables the counters to increment the RAM addresses whilst also disabling their write enables. The data of each address is consecutively clocked through U13 which is enabled by TEST*. These data go out through VDA/0 to VDA/7 and into the input of the Data Analysis Array to be passed through the processing electronics. TEST* is also fed to the Data Analysis Array where it disables the buffer that receives real data from the CCD. Thus, this frame of simulated data is passed through the processing electronics again and again until frame

store is taken out of test mode and in this way the functioning of the electronics may be assessed.

6.9 The Memory Interface

6.9.1 Introduction

The memory interface supervises the transfer of data from the address generator in the processing chassis to the memory array.

The memory interface, memory array and CPU are housed in the computer along with other boards. Data are passed between boards via the VMEbus that runs along the back of the boards. The VMEbus includes a high speed data transfer bus (DTB) which is used by the memory interface to pass data to the memory array. The boards that sit on the bus may be classed as either masters or slaves. Masters control what goes on to the bus whereas slaves respond to commands issued by the masters. Both the memory interface and the CPU are masters. The memory array and the other boards are slaves. Only one master may have control of the bus at any given time and so bus contention arises. The memory interface needs the bus to transfer data to the memory array whereas the CPU needs it to perform its various functions. In order to use the bus the memory interface needs to acquire it from the CPU. The memory interface has a higher priority than the CPU so that if the interface wants the bus the CPU has to finish what it is doing and release it. By ensuring that the memory interface gets the bus quickly in this way, no data are lost due to the filling up of the FIFOs in the address generator.

The memory interface can operate in two modes

- As a master. Here, the memory interface has a higher priority than the CPU. It uses the bus to transfer data to and from the memory. In order to build up an image in the memory it is necessary to increment the data stored in the appropriate memory location every time a photon event occurs. Once it has acquired the bus the memory interface does this in three steps
 - The data are read from the specified memory location
 - New data are added to the data which have been read from the memory. If the multiple counting facility described in section 6.5.2 is enabled then this may be

2; otherwise the data will be 1.

- The summed data are written back into the same location.

The procedure outlined above constitutes a read-modify-write (RMW) cycle. If no more data are present in the FIFOs then the memory interface releases the bus.

- As a slave. Occasionally the CPU needs to read to or write from the interface circuit and when it does so the circuit is in slave mode. The interface contains an integration timer. Before the start of a run the CPU needs to clear the timer and then load a new integration time. The CPU may also read the time from the circuit at any time. The only other time the memory interface is in slave mode is when the CPU is loading the bias address. This is the address added to the address coming from the processing chassis that makes it correct for the memory array.

The following sections describe the operation of the circuit in these two modes.

6.9.2 The Read-Modify-Write Cycle

As was mentioned in the previous section, in order to build up an image in the memory it is necessary to increment the data contained in a specified memory location by an appropriate amount every time an event is stored in the FIFOs. This is done by means of a read-modify-write (RMW) cycle. The entire cycle has five steps

- The memory interface acquires the bus
- Data are read from the specified location
- The new data coming from the processing chassis are added to these data
- The summed data are written back in to the same location
- The memory interface releases the bus

A block diagram of the memory interface is shown in figure 6.40. There is also a timer, not shown, which is used to monitor the integration time and, as described in the next section, if the CPU wants to read the time the memory interface is put into slave mode. The diagram depicts the essential features of the circuit that take part in the RMW cycle. Control of the cycle is shared between two chips

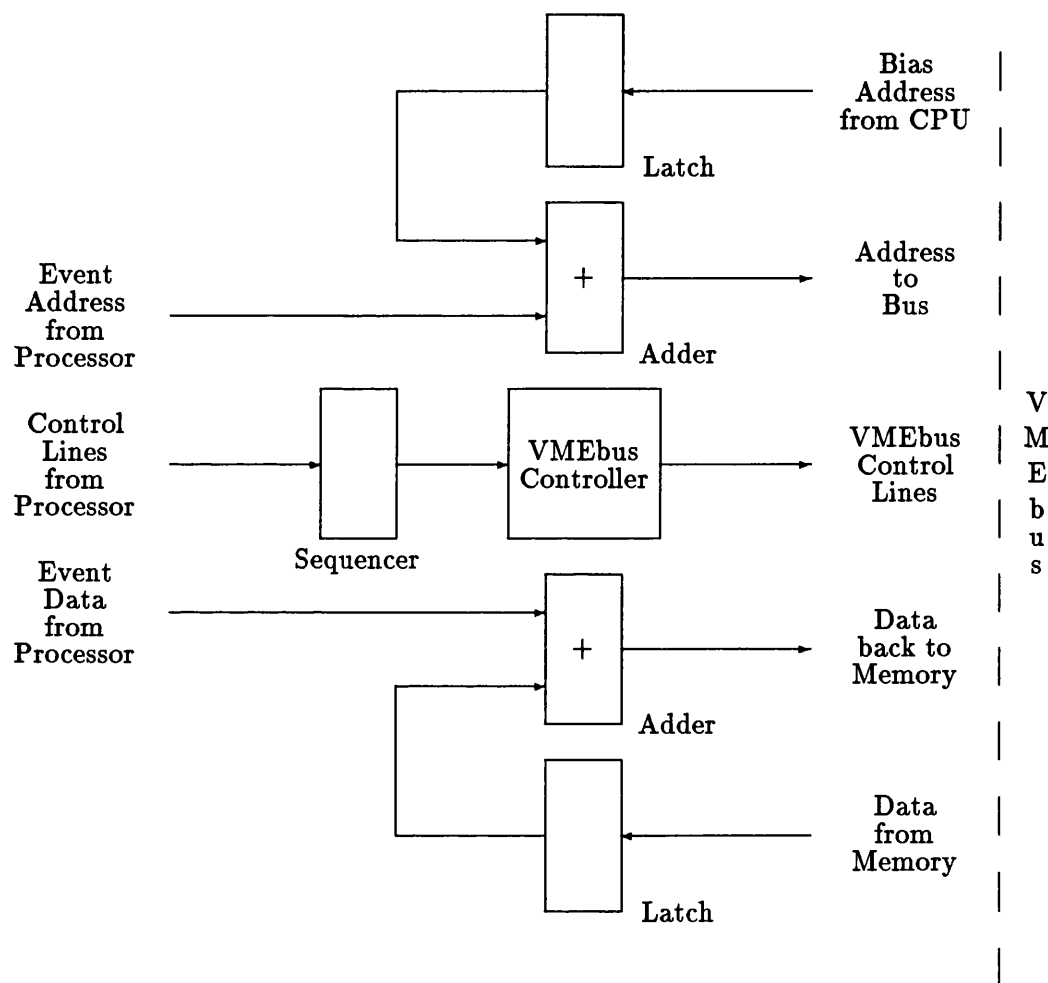


Figure 6.40: Block diagram of the memory interface showing the essential features of the circuit for read-modify-write

- The bus controller (BUSCON). This is a special interface device for the VMEbus. It handles the signals necessary to control the bus.
- The sequencer. This is a 256×8 bit read only memory (ROM). It outputs and receives signals to and from both the address generator in the processing chassis and the rest of the memory interface. At UCL it was loaded in such a way as to ensure that the RMW cycle takes place correctly.

Between them these two chips ensure that all the signals are supplied that are necessary for the correct functioning of the circuit.

Bus Acquisition

Before the memory interface can start a RMW cycle it has to acquire the bus from the CPU. It does this by issuing a bus request signal onto the VMEbus. An arbiter, which also sits on the bus, performs bus arbitration by assessing which of two masters has the highest priority. There are two levels to the arbitration

- There are four bus request lines, BR0 to BR3, and BR3 has the highest priority. So, if two masters want the bus but one requests on BR1 and the other requests on BR3, then the one requesting on BR3 would get the bus.
- There is priority according to physical slot position in the chassis – the higher the slot, the higher the priority. So, if two masters want the bus and are issuing requests on the same request line, the one in the higher slot position would get the bus

With MIC, the memory interface issues requests on BR3 while the CPU issues requests on BR1, so the memory interface has a higher priority. This is necessary to avoid loss of data caused by the filling up of the FIFOs. This would happen if the memory interface had to wait a long time before it got the bus.

Bus acquisition by the memory interface has a number of steps

- Initially the CPU has the bus and the ‘bus busy’ line, BBSY*, is set.
- When an event arrives in the FIFO the memory interface sends out a bus request signal BR3*.

- The arbiter sees that something else higher up wants the bus so it send out a 'bus clear' signal, BCLR*. The CPU sees this signal and releases the bus when it has finished what it is doing – this then resets BBSY*. The arbiter resets BCLR* ready for another master to take the bus.
- The arbiter then sends out a 'bus grant' signal, BG3IN*. This goes to every slot but is passed on if the board had not issued a request on BR3*. When the memory interface gets the bus grant it knows it has been granted the bus and BBSY* is set again. BR3* is reset because if the bus has been acquired it no longer needs to be requested.

This takes place every time the memory interface want the bus.

An Overview of Read-Modify-Write

The RMW cycle can be considered as a read followed by a write. The read and write cycles described below are the same for any master reading from a slave or writing back to it.

The read cycle can be considered to take place in a number of steps

- The master puts an address onto the bus. This defines which board and location within it the master wishes to access. At the same time the master puts the address modifier (AM) on to the bus. These are lines that allow the master to pass additional binary information to the slave; this information is associated with word length and as to whether it is for system or user access. In the case of the memory interface, an address arrives from the processing chassis and this is added to the bias address that ensures that the correct location is accessed. The summed address is passed out on to the bus.
- The master sends an address strobe (AS*) out on to the bus. This tells all other cards on the bus that a new address is present. When the memory receives this signal looks at the address on the bus to see if it is to be accessed and, once it knows that it is, then it is ready.
- The master sets the read/write line, R/W*, appropriately to let the slave know which cycle is about to take place. This line is set high for a read and low for a write.

- Once this has been set up then the master initiates the reading of the data by issuing data strobes DS0* and DS1*.
- The data contained in the location specified by the address appear on the bus.
- The slave sends an 'acknowledge' signal, DTACK*, informing the master that it has put the data on to the bus.
- When the master knows that the data are present it accepts them.

For the memory interface, the data taken from the memory are added to those coming in from the processing chassis.

The modified data formed by this addition are ready to be written back in to the memory. The write cycle for any master writing to a slave is as follows. As is discussed shortly, the cycle is slightly different in the RMW case.

- The address is put on to the bus as for the read cycle.
- The address strobe is sent and tells all cards that a new address is present
- The R/W* line is set low indicating that a write is about to take place.
- The master supplies the data for the write by putting it on the bus.
- The master then initiates the writing by issuing the data strobes, DS0* and DS1*.
- The slave writes the data into the location specified by the address
- The slave informs the master that the data have been written by sending out an acknowledgment, DTACK*

In the case of RMW, the write cycle is slightly different. The master is writing data back into the same location from which it has just read data. Thus, it is not necessary to issue a new address and another address strobe because the address is already present on the lines at the end of the read and the location specified by the address already knows it is to be accessed. It is the data stored in the sequencer that ensures that the RMW takes place as opposed to a read and then a write. Together with the bus controller it controls the entire process.

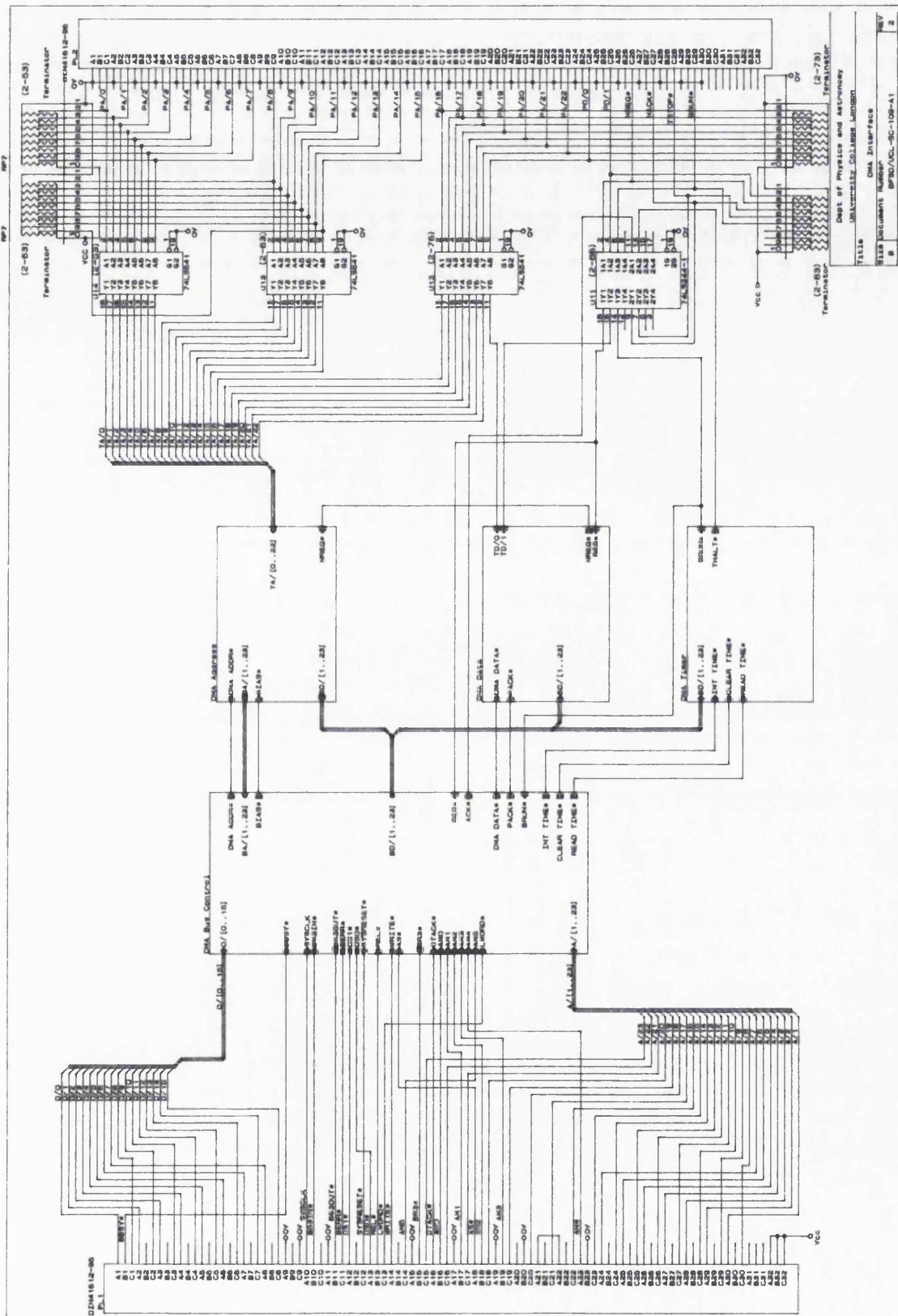


Figure 6.41: Root diagram of the memory interface

A Detailed Description of the Read-Modify-Write Cycle

The process of read-modify-write is more complicated than the outline given in the previous section might suggest. In order to understand the process it is necessary to study the memory interface circuit diagram and a timing diagram. The root circuit diagram is shown in figure 6.41. The circuit has been divided into four separate blocks. The DMA timer is described in the description of the circuit in slave mode in section 6.9.3.

The remaining three blocks are needed to understand the RMW process. 'DMA bus control' shows all the control circuitry including the sequencer and BUSCON and is shown in figure 6.42. The remaining two block, 'DMA address' and 'DMA data' are shown in figure 6.43 and figure 6.44. These handle the address and data for the memory array. An example of real timing is shown in figure 6.45 and this will be referred to in the text. Additionally, the information contained in table 6.4 will facilitate the understanding of the process. This table shows the sequencer states that control the RMW.

Table 6.4: Sequencer states for the control of read-modify-write. An x represents a 'don't care' situation. Key: A8=LDTACKN; A4=REQ*; A3=R/WN; A2=C2; A1=C1; Q7=ACK*; Q6=VMEN; Q5=DSI; Q4=MASN; Q3=R/WN; Q2=C2; Q1=C1.

A8	A7	A6	A5	A4	A3	A2	A1	Q8	Q7	Q6	Q5	Q4	Q3	Q2	Q1
1	0	x	x	1	1	0	0	x	1	1	1	1	1	0	0
1	0	x	x	0	1	0	0	x	1	0	1	0	1	0	1
1	0	x	x	0	1	0	1	x	1	0	0	0	1	0	1
0	0	x	x	0	1	0	1	x	1	0	1	0	1	1	0
0	0	x	x	0	1	1	0	x	1	0	1	0	1	1	0
1	0	x	x	0	1	1	0	x	1	0	1	0	0	1	0
1	0	x	x	0	0	1	0	x	1	0	0	0	0	1	0
0	0	x	x	0	0	1	0	x	0	0	1	0	0	1	1
0	0	x	x	x	0	1	1	x	0	0	1	0	0	1	1
1	0	x	x	1	0	1	1	x	1	1	1	1	1	0	0

Before any data are present in the FIFOs the circuit is idle and the sequencer states are as in the first line in the table. The whole process is triggered when data are present in

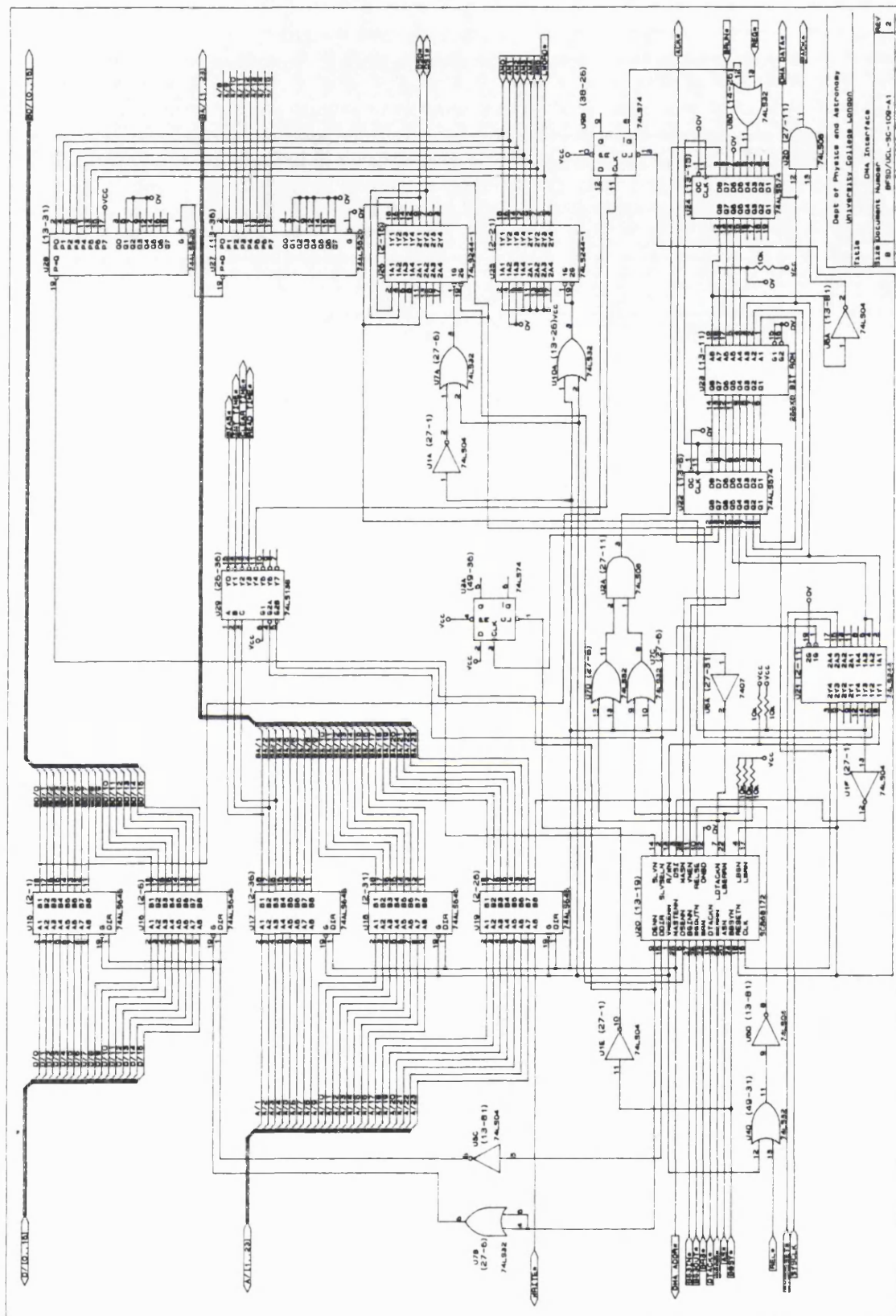


Figure 6.42: Memory interface control circuitry

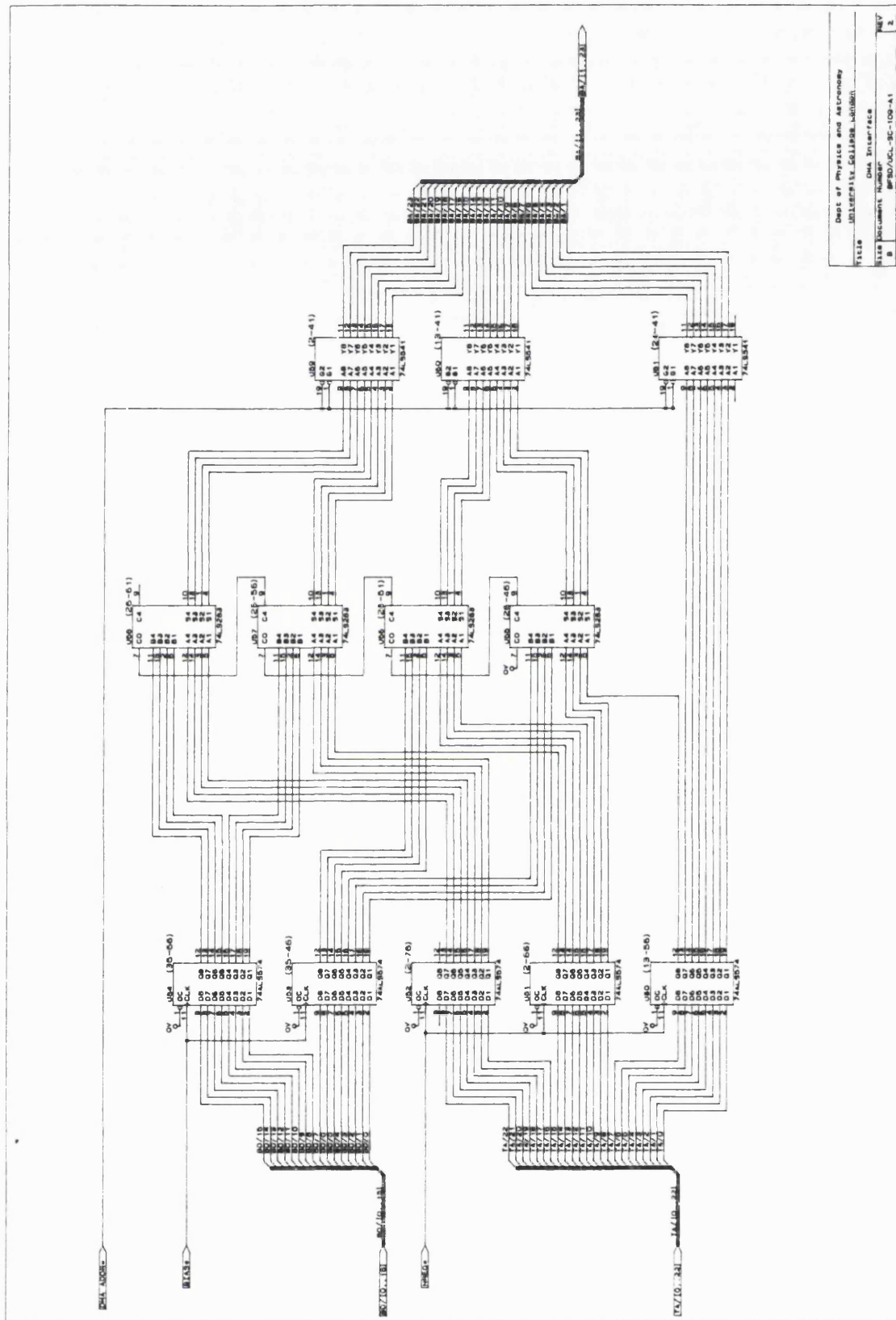
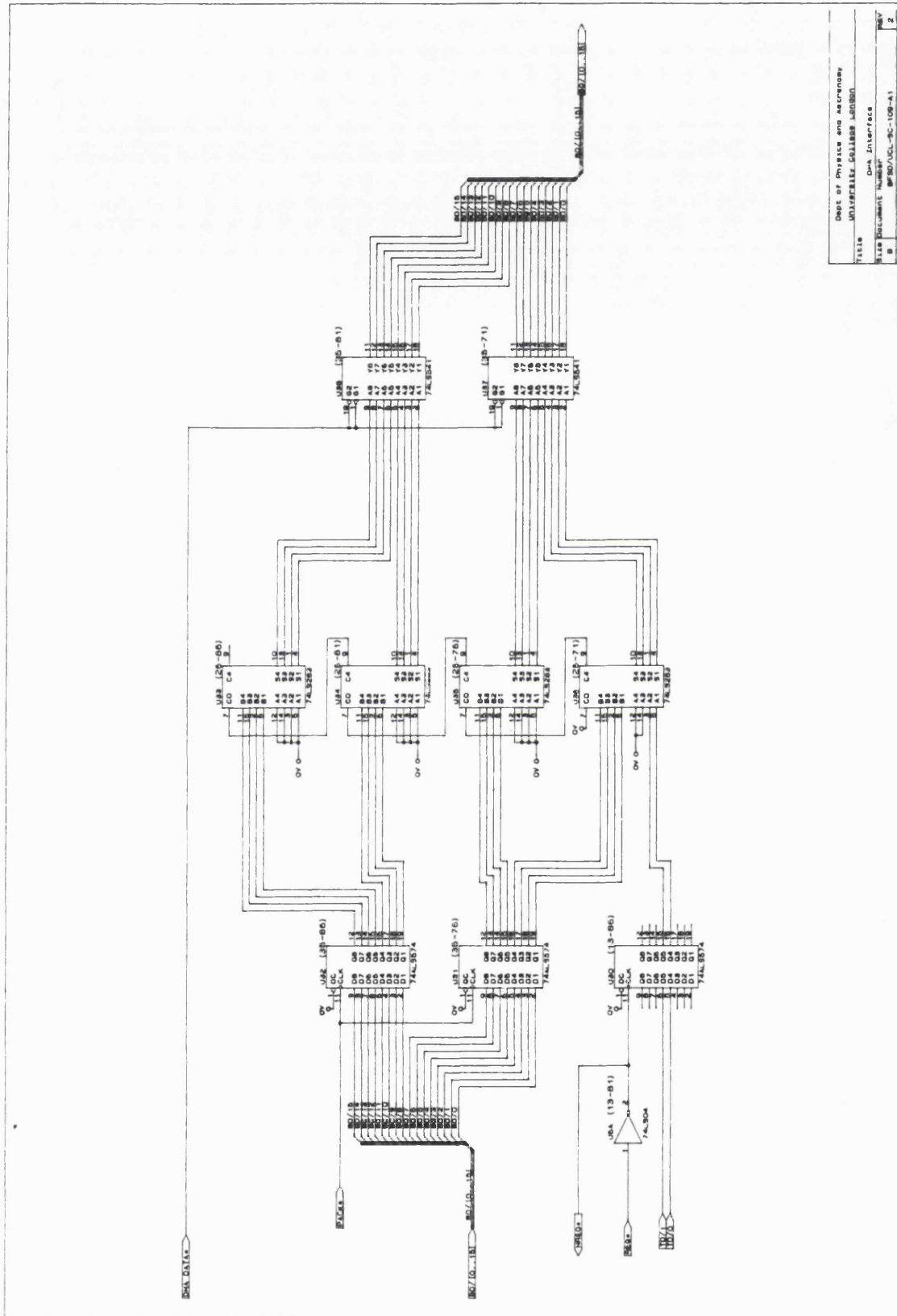


Figure 6.43: Address handling section of the memory interface



Dept of Physics and Astronomy	
UNIVERSITY COLLEGE LONDON	
Title	Data Interface
File Name	640/UC-109-A1
Page	2
Date	1992

Figure 6.44: Data handling section of the memory interface

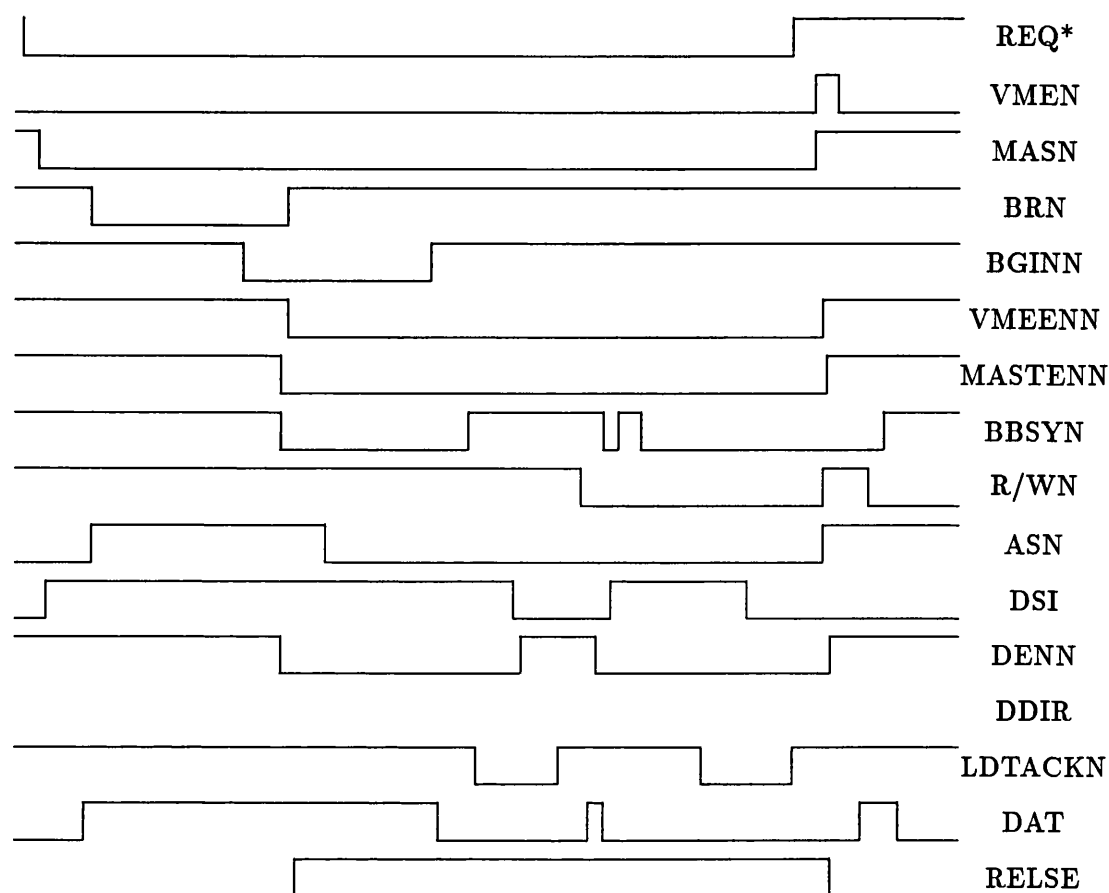


Figure 6.45: Real timing diagram for the signals that control the read-modify-write cycle of the memory interface

the FIFOs. The signal REQ* is sent from the address generator in the processing chassis to indicate that there are data in the FIFOs. This enters the sequencer U23 via a latch and produces the output of line 2 from the sequencer, that is VMEN and MASN both go low and these are input to the bus controller U20. VMEN indicates to the bus controller that a cycle is starting. The line 2 outputs are fed back into the sequencer and make DSI go low. This makes the DSI input to BUSCON go high and informs that there are data coming. Meanwhile, the computer is finishing what it is doing and so ASN and data both change.

Having received VMEN, MASN and DSI, BUSCON knows that there are data in the FIFOs and it initiates the cycle by issuing a bus request on BR3* which goes out onto the

bus for arbitration. Shortly after this BGINN goes low informing BUSCON that it has been granted the bus. Knowing this BUSCON sets BBSYN indicating that the bus is busy and also enables the data trceivers U15 and U16 via DENN going low so that the circuit is ready to receive data coming in off the bus from the memory – the direction for the data is set appropriately with DDIR being high. Since it now has the bus, BUSCON no longer needs to request it so that once it has set BBSYN it releases BRN. It then enables the address trceivers U17, U18 and U19 via VMEENN going low and the direction is set appropriately for a master with MASTENN also going low. The correct address, with bias added, is already present on the inputs of U59, U60 and U61. The bias had been previously loaded and the event address had been enabled when the request was issued from the address generator. When MASTENN and VMEENN go low the address is sent out onto the bus.

Meanwhile, the computer has requested the bus again by issuing a request on BR1* which comes in on REL*. As soon as VMEENN goes low the RELSE input to BUSCON goes high telling it that something else wants the bus and it should release it.

Now that the address has been put onto the bus BUSCON issues an address strobe on ASN telling the memory that a new address is present on the bus. The sequencer is sitting idle during this period. Meanwhile the arbiter has seen that the bus has been set busy and it releases BGINN. Shortly after the address strobe goes low the memory puts on to the bus the data contained in the address that is present on the bus. Shortly after the data appears on the bus, the memory sends an acknowledgement via DTACK* and this drives the LDTACK* low. This is fed into the sequencer at line 4 and this changes DSI to high. This disables the data strobes DS0* and DS1* and also makes BUSCON drive DENN high disabling the data trceivers U15 and U16 – the data has been caught by the signal PACK* which operated on LDTACK* going low. The data are added to that contained on the output of U30 which was clocked in by the original request coming from the address generator.

Once the data are secure and are added to the event data, LDTACK* is released by BUSCON and this causes the sequencer outputs to change. The sequencer drives R/W* low indicating to the memory that this is now a write cycle. This causes BUSCON to drive DDIR low and this, together with DENN going low again, enables the data trceivers in a direction appropriate for a write and the data are put onto the bus. The DSI input to

BUSCON is caused to go high and this tells the memory, via DS0* and DS1*, that new data is present on the bus. The data are written into the memory and another DTACK* is sent which again makes BUSCON drive LDTACKN low. This is fed in to the sequencer at line 8 and makes DSI go high and ACK* go low to tell the address generator that the cycle is complete. This initiates the end of the cycle, with LDTACKN and REQ* then VMEENN, VMEN, R/WN, ASN, DENN and DDIR all going high. The sequencer returns to line 1 of the table and awaits another request from the address generator.

6.9.3 Operation of the Memory Interface as a Slave

The memory interface may be put in a slave mode if the CPU wants to read from or write to locations within the circuit. There are only four operations that the CPU performs that requires the memory interface to be a slave.

- Loading the bias address to add to the event address coming from the processing chassis
- Clearing the timer ready for an integration. The timer keeps track of the integration time.
- Loading the timer with a new integration time
- Reading the time, that is, how long the integration has been in progress.

Once the CPU has acquired the bus it sends out a new address to all the boards. The memory interface has an address range defined for it as a slave and this is hard wired on the comparator U27 in figure 6.42. Only bits A/8 to A/15 are compared along with the address modifiers which are hard wired for short non-privileged access in comparator U28. If the address sent out by the computer is in the correct range then bits A/8 to A/15 and the address modifiers will be the same as those hard wired into the comparators and a flag on pin 19 of U28 will be produced. This then tells BUSCON that it is to be a slave. The three least significant bits of the address sent out by the CPU are used to define which location on the board is to be accessed. These three bits are input to the decoder U29.

The CPU starts its cycle by sending the data strobes DS0* and DS1* which are input to DSI on BUSCON. Knowing that it is a slave, BUSCON outputs a pulse on SLVSELN which activates the decoder. A pulse is produced on one of the four labelled outputs of

the decoder, according to the address appearing on the inputs A, B and C. This pulse writes data into or reads data from the location specified by the address.

The bias address is that address that is added onto an event address to give it the correct range for the memory. This is loaded prior to the start of a run into latches U53 and U54 in figure 6.43 using the pulse produced on BIAS*.

The Timer

The timer allows an integration time between 0 and 2^{16} with a temporal resolution of one second. The circuit diagram is shown in figure 6.46. The circuit uses an oscillator, U49, whose frequency is user defined by the hard wired pins P1 to P6. A frequency of 256 Hz is convenient because it gives a carry output from U48 every second. This is used to enable a second counter U47 whose carry output every 256 seconds is used to enable a third counter U46. Thus, the output from U47 and U46 goes from 1 to 2^{16} in steps of one second. Before the start of a run these counters are cleared using the pulse generated on CLEAR TIME*.

The user specified integration time is loaded prior to an integration by the computer. The pulse on INT TIME* loads the time into latches U44 and U45. The output of these latches then remains constant during the integration and, as the counters increment, the integration time is compared to that on the counter outputs. This is done in the comparators U42 and U43. When the two numbers are equal the required integration time has been reached and a pulse is produced on THALT* which tells the FIFOs to stop accepting data.

If the CPU wants to see how long the run has been in progress it may do so using READ TIME*. The counter outputs are input to the latches U40 and U41 and, when a pulse appears on READ TIME*, the current integration time appears on their outputs. To prevent the time being read as it is changing, the natural oscillator frequency and the delay through the counters are used to ensure that the counter outputs are steady on the rising edge of the clock input to the latches.

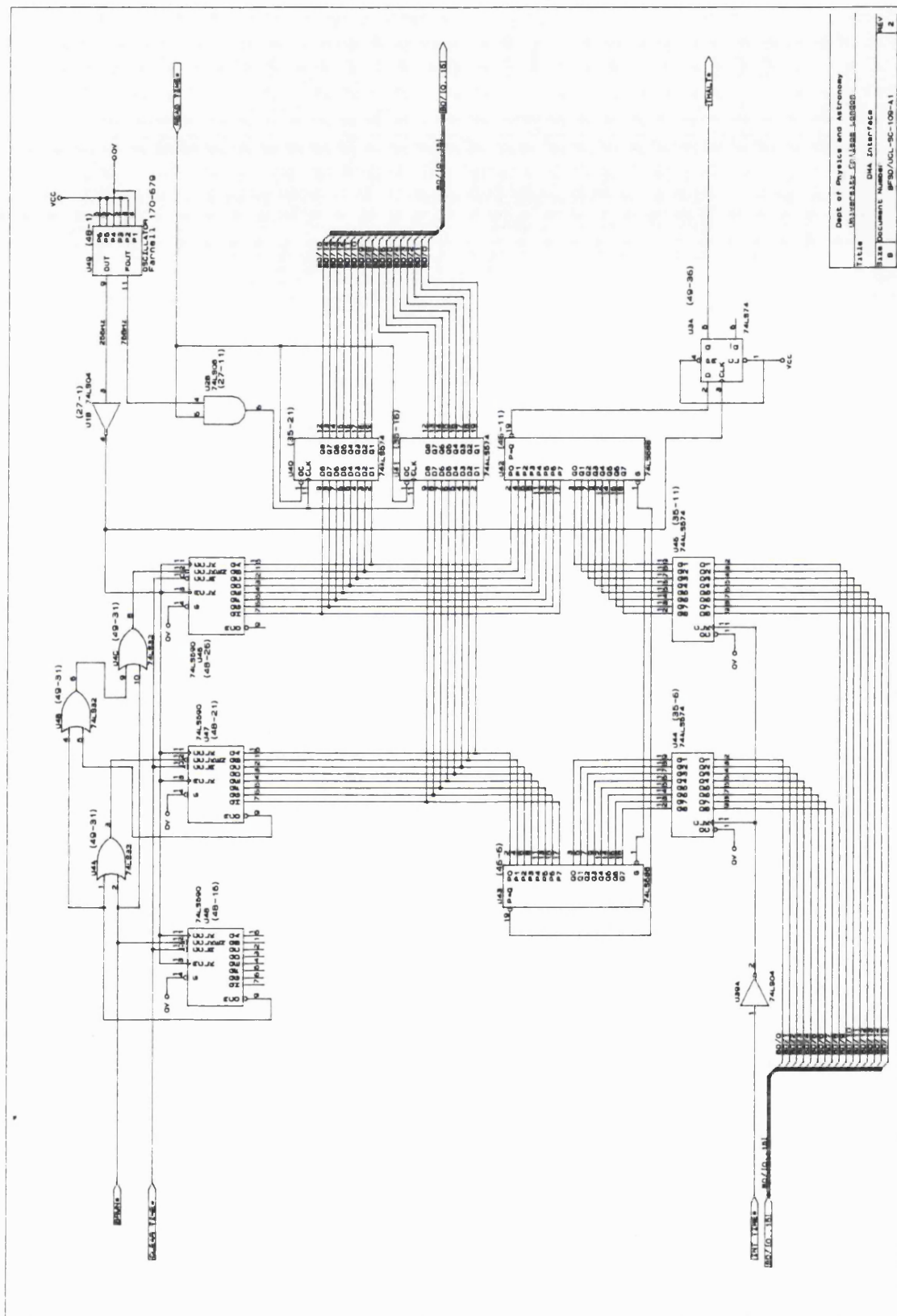


Figure 6.46: The timer of the memory interface

Chapter 7

System Performance

7.1 Introduction

The XMM-MIC has been designed to meet the requirements of the OM photon counting detector outlined in table 2.1. It is extremely important that the system should be tested, not just to assess its performance with respect to the given requirements, but to identify where improvements need to be made and to reveal faults or artefacts that may give cause for concern.

It is important that testing of a detector should be done both in the laboratory, to determine fundamental performance characteristics, and in an astronomical context to assess its general suitability for the purpose for which it was designed. Performance testing on the XMM-MIC has been carried out

- with a calibrated light source to measure photocathode sensitivity of the two intensifiers from ITL,
- on an optical bench with a slide projector to measure detector resolution, dynamic range and uniformity,
- on the 24 inch Radcliffe telescope at the University of London Observatory to measure dynamic range on star fields and test the detector in an astronomical environment.

The primary performance characteristics of the system, namely DQE, resolution and dynamic range, are determined ultimately by the image intensifier – it is important that

the intensifier should be of the highest quality in order to optimize these performance characteristics. After a brief analysis the two intensifiers received from ITL were thought to be of good quality and as a result a number of tests were carried out. Dynamic range tests were carried out both in the laboratory and in an astronomical environment as well as resolution and detector uniformity tests. At a late stage in the testing program it was found that the intensifiers had two problems associated with the events on the output phosphor. By replacing the 3.06:1 fibre taper by a 1:1 fibre block the event sizes were magnified and it was possible to examine in detail the size and shape of each event using the frame grabbing function of the frame store circuit described in section 6.8. Two properties of the events were found to be undesirable:

- The event widths were too narrow. The average event width was found to subtend to $65\mu\text{m}$ at the photocathode instead of the required $100\mu\text{m}$. With the 3.06:1 taper in place this is equivalent to 0.9 pixels FWHM instead of 1.4.

The reason why the events are so narrow is undoubtedly because the intensifiers were manufactured with a spacing between the back channel plate and the phosphor which is too small. In accordance with equation 3.7 which applies generally to proximity focussing, the FWHM associated with the spreading out of the electrons is reduced in proportion to the size of the gap across which they are being accelerated. This could be compensated for by reducing the voltage applied across the gap. However, since only the square root of the voltage contributes to the FWHM, the voltage would need to be reduced to an intolerably low level such that the energy of the electrons incident upon the phosphor would be insufficient to retain the required photon gain of the intensifier. Therefore, with these ITL intensifiers, it is not possible to achieve the required event width without degrading other properties associated with the events.

A suitable event width is needed in order to minimize the centroiding errors associated with the algorithm given by equation 6.1. As described in section 6.6.2, if the event width is too small then undersampling results because there is not enough information present in the digitized version of the photon event. A worsening of the pattern noise shown in figure 6.20 results from a reduction on the event width. The lack of information in the digitized events also led to an erroneous determination of the event widths when these intensifiers were first examined. The software used to

find the event widths gave a FWHM of 1.2 pixels which was close enough to the required width for the intensifiers to be useful. Only when the intensifier was coupled using the 1:1 block was this figure found to be in error.

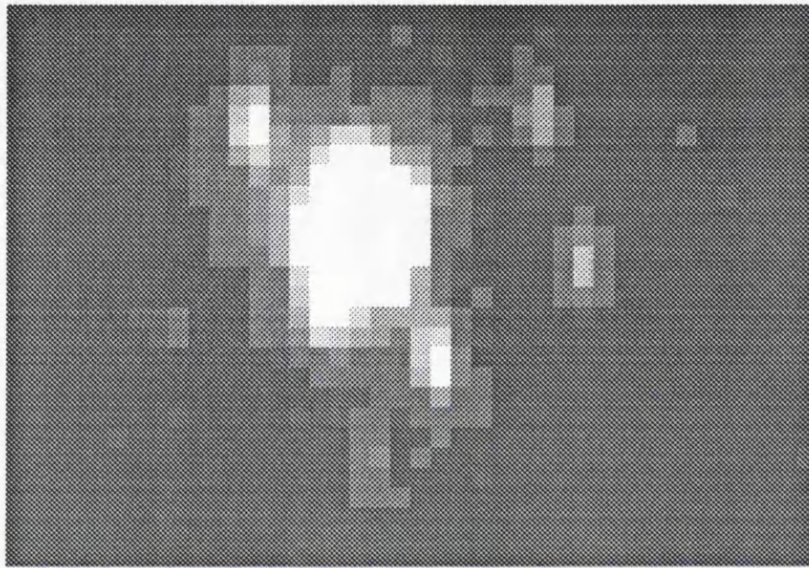


Figure 7.1: Signal induced background seen on a real event with the ITL intensifiers

- There is a large amount of signal induced background (SIB) associated with each event. This SIB, an example of which is shown in figure 7.1, takes the form of small splashes of photons closely associated with the primary photon events and distributed randomly around them. These ‘strawberries’ cannot be distinguished from the primary event with the usual 3.06:1 coupling because they are so close that they merge and appear as one event.

This SIB is caused by incomplete scrubbing of the microchannel plates during manufacture of the intensifiers. Gases that ought to be removed during scrubbing are desorbed from the surface of the channel plates and this leads to an increase in partial pressures of various gases. The presence of too many gas atoms and molecules leads to charge cloud fragmentation in the gap between the first and second chan-

nel plate. The fragments undergo electron multiplication leading to the presence of smaller 'events' closely associated with the primary event.

The effect of the SIB is that the event profile is not constant but has a random irregular shape. Because of this it is impossible ever to correct the pattern noise described in section 6.6.2 by fitting the algorithm to the event profile since this is always different. Thus, there would always be pattern noise present in data acquired with these ITL intensifiers. The event profiles seen with the 40mm intensifiers developed for the ground based MIC show no sign of SIB verifying that there is no fundamental design fault with the intensifiers.

Following the discovery of the two problems associated with the ITL intensifiers, it would be instructive to repeat all the tests carried out with the 25mm intensifier but to replace it with the 40mm intensifier developed for the ground based MIC which is known to be of high quality. A comparison of the results from the two sets of tests would give an indication of the degradation of performance brought about by the poor quality of the 25mm intensifiers. The tests with the 40mm tube would also give a estimate of the performance attainable with the XMM-MIC. For the tests that have been repeated with the 40mm tube the results are given alongside those for the 25mm tube. Those that have not been repeated required equipment which was not available.

The results for the two different intensifiers are not directly comparable since they are not identical. However, useful comparisons may be made when one takes into account the differences between the 40mm tube and the 25mm tube. The two intensifiers are the same except that

- The 40mm tube has $12\mu\text{m}$ pores on $15\mu\text{m}$ centres whereas the 25mm tubes have $10\mu\text{m}$ pores on $12\mu\text{m}$ centres.
- The 40mm tube has a front gap of $200\mu\text{m}$ whereas that of the 25mm tube is $300\mu\text{m}$.
- The 40mm tube has a quartz input window whereas the 25mm tube has a sapphire window.

7.2 Photocathode Sensitivity

Together with the transmission of the input window the RQE of the photocathode at various wavelengths determines the spectral response of the detector. The spectral response required of the photon counting detector is 1500–6500Å. The RQE also determines the ability of the system to detect faint objects and, as was mentioned in section 2.2, the requirement that the system must be able to detect a 24.5 magnitude star at the 3σ level means that the photocathode must have $> 20\%$ efficiency in the blue. Thus, the photocathode RQE is an important quantity that needs to be evaluated in order to determine its suitability with respect to the aforementioned requirements.

A calibrated light source at Imperial College of Science, Technology and Medicine (ICSTM) was used to determine the RQE of the two intensifiers supplied by ITL which had serial numbers 1910723 and 2910723. The RQE curve for the photocathode of intensifier

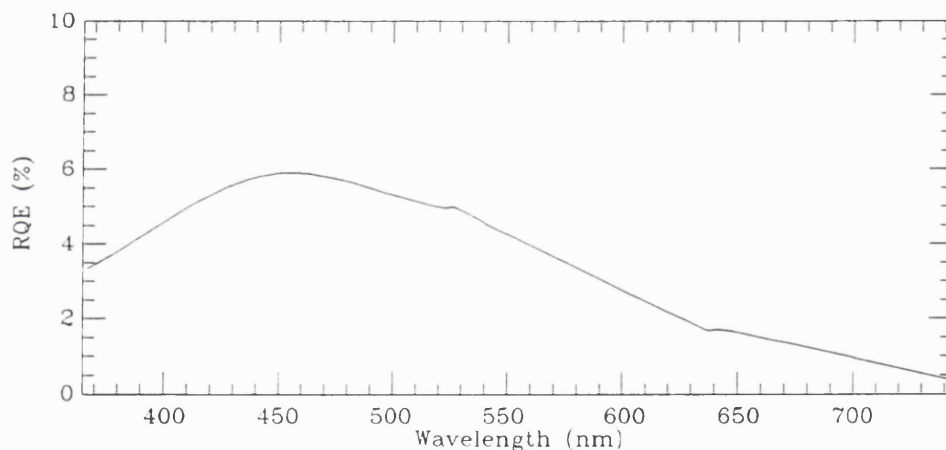


Figure 7.2: The RQE curve of intensifier 2910723 supplied by ITL

2910723 is shown in figure 7.2. This photocathode has a peak quantum efficiency of 6% in the blue. The sensitivity current of intensifier 1910723 was not measurable. This was due to a very high leakage current between the photocathode and the first channel plate which is most likely due to a sliver of indium solder. However, this intensifier did work well under normal operating conditions and it is expected that its photocathode has similar RQE characteristics to that of the other intensifier since it gives similar count rates under the same illumination conditions.

The RQE of these intensifiers is thought to have been degraded during seal off of the intensifiers. ITL suggest that too high a temperature was used in the 'hot seal' and that degradation of the photocathode response resulted. The ITL tubes were accepted despite their low RQE since resolution and dynamic range, which are important performance characteristics, are not affected by the RQE of the photocathode – useful tests may be carried out to determine these properties whatever the RQE of the photocathode.

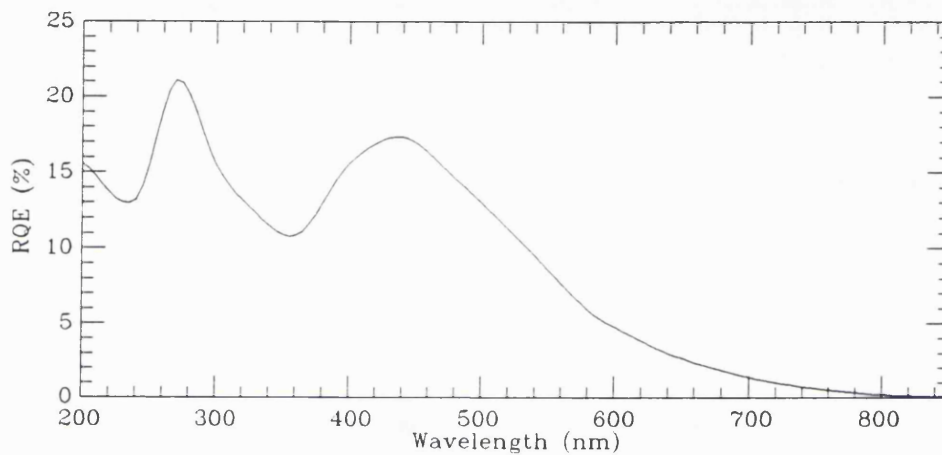


Figure 7.3: The RQE curve of a recently received DEP intensifier

DEP have manufactured a prototype 18mm intensifier to exactly the same design as the ITL intensifiers. This intensifier, which was recently received, shows a much more desirable RQE curve as in figure 7.3. This intensifier has a peak quantum efficiency of 21% in the UV and 18% in the blue. The double peak is believed to be due to a convolution of the window transmission characteristics and the photocathode response.

7.3 Dynamic Range

The required dynamic range characteristics of the detector were given in table 2.1. In particular, at the bright limit the detector is required to be able to cope with a count rate of 1000 counts s^{-1} on a point source and also a Zodiacal light background of 200k counts s^{-1} over the detector area.

7.3.1 The lower limit

The lower limit of the dynamic range characteristics of the detector is governed entirely by the ‘dark noise’ of the image intensifier since there is no ‘front end’ electronic noise associated with photon counting detectors. The electronics give rise to noise at a low level but this is effectively removed by the thresholding circuitry.

Dark noise is caused by thermally generated electrons emanating from the photocathode. These undergo the same electron multiplication as electrons resulting from photons and so are not distinguishable from real events. Therefore, these events contribute to the image as noise. However, the dark noise for an S-20 photocathode is low, being typically 50 counts $\text{cm}^{-2} \text{ s}^{-1}$ which corresponds to 0.04 counts $\text{pixel}^{-1} 1000\text{sec}^{-1}$ over the 2048×2048 format.

The dark noise of the ITL intensifiers is not measurable because it is dominated by scintillations arising from the sapphire input window. These scintillations are due to cosmic rays and the radioactive decay of window constituents. Typically, each scintillation adds 500 counts to the general background.

7.3.2 The Bright Limit

The high count rate end of the dynamic range requirements of the XMM-MIC outlined in table 2.1 are perhaps the most demanding of all the requirements placed upon the detector. The detector must be able to cope with a point source count rate of up to 1000 counts s^{-1} and this on top of a background count rate of up to 200k counts s^{-1} over the detector area. A number of factors affect the high count rate dynamic range characteristics of the detector and these are discussed in the following sections.

The Spatial Extent of the Object

In terms of counts $\text{s}^{-1} \text{ pixel}^{-1}$, the dynamic range is higher for point sources than for extended objects and is a consequence of coincidence losses. The effect is understood when one considers the meaning of coincidence. For a point source all the events arrive in a very localised area. When two events arrive in the same frame, one is lost but the coincidence is restricted essentially to events lying directly on top of each other. With an extended object such as a flat field events may arrive randomly in any pixel. Only when two events are separated by more than twice their FWHM may they be resolved,

otherwise their accumulated charge appears to have only one peak and is therefore seen as one event. This means that, for an event with a FWHM of 1.4 pixels, say, a large number of pixels around the event become ‘dead’ in that another event arriving in any of them will not be counted. Thus, in terms of counts per pixel, the count rate capability of MIC for extended objects is lower than for point sources.

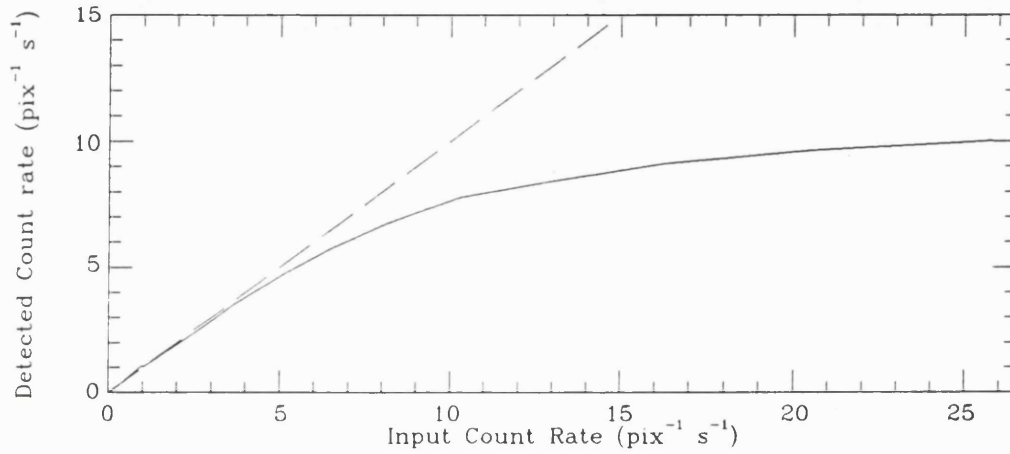


Figure 7.4: Flat field dynamic range curve on a format of 2048×2048. The dashed line represents a linear detector.

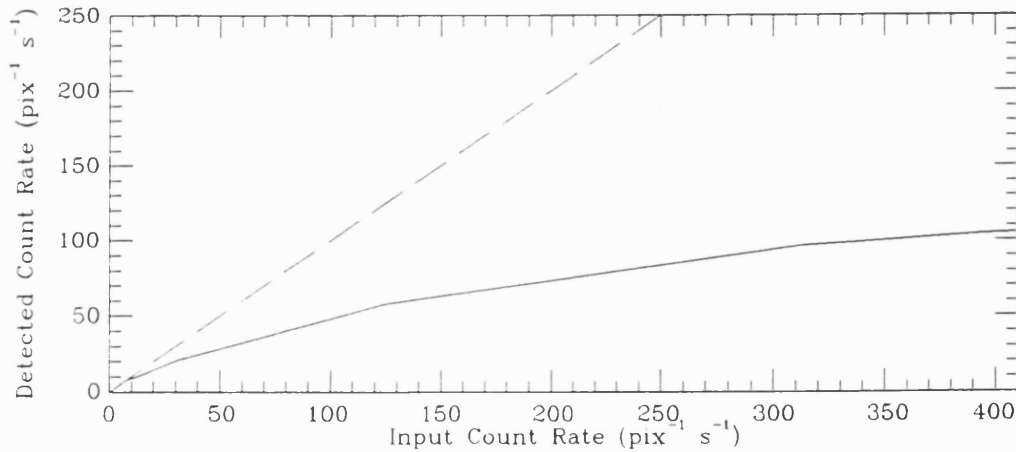


Figure 7.5: Point source dynamic range curve on a format of 2048×2048. The dashed line represents a linear detector.

Measurements of the XMM-MIC dynamic range characteristics were carried out on

an optical bench with a calibrated light source providing the illumination and a set of calibrated neutral density filters providing a means of varying the count rate. The dynamic range curve for a flat field on a 2048×2048 format is shown in figure 7.4. The point at which 10% of the incident events are lost due to coincidence is 5 counts s⁻¹ object⁻¹. This may be compared with the dynamic range characteristics for a 40μm point source shown in figure 7.5 where the 10% coincidence loss point is at 25 counts s⁻¹ object⁻¹. Although the size of this point source was much larger than those expected with XMM the dynamic range curve would be the same for both. The reason for this is that, even for events that are 40μm apart on the CCD, one will be lost because of the effect of the dead area described above. This implies that one should always quote figures for point source dynamic range in counts s⁻¹ object⁻¹ and not counts s⁻¹ pixel⁻¹ because the image of a point source may cover several pixels but exhibit the same dynamic range characteristics as if it covered only one.

The Frame Rate of the CCD Camera

Section 5.3.2 described how the frame rate may be varied by choosing the number of rows that are read out each frame. The fewer rows that are read out the faster the frame rate of the camera. Also, the faster the frame rate the smaller is the probability that, for a given count rate, there will be two events coincident within a single frame.

For a point source the effect of frame rate on coincidence losses can be derived by considering the Poissonian distribution of photon arrival times. Photon events arrive at the input of the detector with a mean rate σ per second and with a Poissonian time distribution

$$P(x) = \frac{\mu^x}{x!} e^{-\mu} , \quad (7.1)$$

where $P(x)$ is the probability that x events will occur in a frame period τ and μ is the mean number of events in τ , equal to $\sigma\tau$.

With a point source all events are assumed to arrive in close proximity so that if two events occur in the same frame then the detector sees it as one and one is lost. This assumes that the double counting circuit is not enabled. If three events arrive in the same frame then two are lost, and so on. That is, no matter how many events arrive in the same frame, only one is counted. Therefore, at the detector output the expected number

of events per frame, \bar{n} , is given by

$$\begin{aligned}\bar{n} &= 1.P(1) + 1.P(2) + 1.P(3) + 1.P(4) + \dots \\ &= 1 - P(0)\end{aligned}\quad (7.2)$$

the second step arises since

$$\sum_{x=0}^{\infty} P(x) = 1 \quad (7.3)$$

Now from equation 7.1,

$$P(0) = e^{-\sigma\tau} \quad (7.4)$$

so if τ is the frame time then

$$\bar{n} = 1 - e^{-\sigma\tau} \quad (7.5)$$

Thus, for a given input photon rate, σ , the output count rate, R_{σ} , is given by

$$R_{\sigma} = \frac{\bar{n}}{\tau} = \frac{1}{\tau} \left(1 - e^{-\sigma\tau} \right) \text{ events per second} \quad (7.6)$$

When only 32 CCD rows are read out instead of the full 256 the frame time is reduced

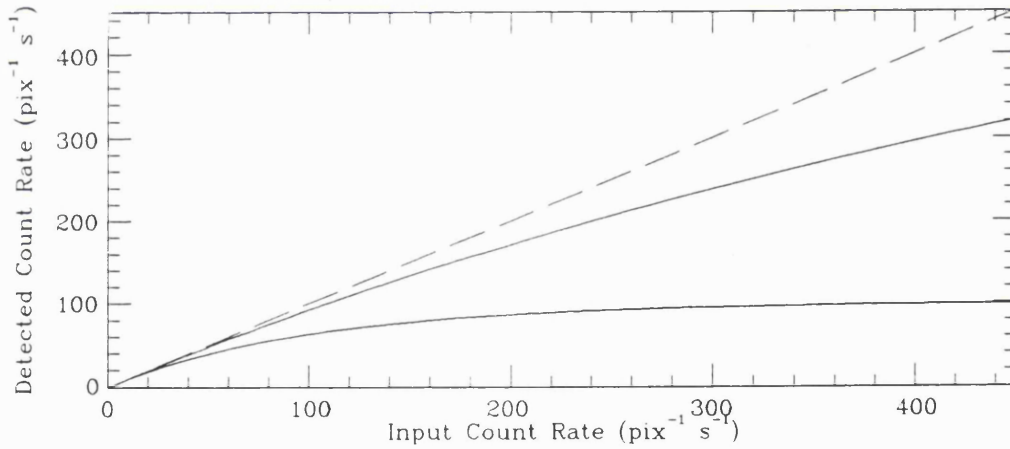


Figure 7.6: Theoretical point source dynamic range curves showing the effect of frame rate on coincidence losses. The upper curve is with a format of 256×2048 and a frame time of 1.6ms and the lower curve is with a format of 2048×2048 and a frame time of 10ms

from 10ms to 1.6ms. Inserting these values for frame time into equation 7.6 gives the two dynamic range curves shown in figure 7.6. One can calculate the percentage, L_{σ} , of events lost through coincidence with other events via

$$L_{\sigma} = \frac{\sigma - R_{\sigma}}{\sigma} \times 100 \quad (7.7)$$

or, using equation 7.6

$$L_{\sigma} = 100 - \frac{100}{\sigma\tau} \left(1 - e^{-\sigma\tau} \right) \quad (7.8)$$

The 10% coincidence loss point occurs at ~ 130 Hz for a frame time of 1.6ms and at ~ 20 Hz for a frame time of 10ms. These values agree exactly with simple simulations of the effect of frame time on dynamic range (Oldfield and Fordham, 1991). With the 32 row format, the frame sync period, that is, the time during which the CCD is being read out, is a significant percentage of the overall frame time and this serves to lower the 10% coincidence point to ~ 40 Hz when this is taken into account in simulations.

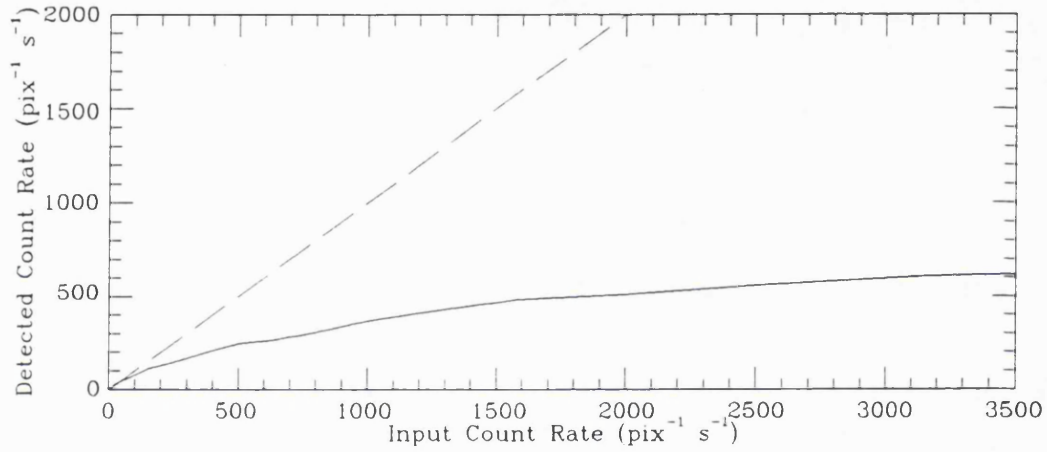


Figure 7.7: Point source dynamic range curve on a 256x2048 format.

Now, the actual XMM-MIC point source dynamic range characteristics do not agree well with what one expects from the above analysis, particularly at fast frame rates. The point source dynamic range curve for a full format and frame time of 10ms was shown in figure 7.5. Here, the 10% coincidence loss point occurs at 25 Hz which is slightly higher than predicted by the above analysis. The dynamic range curve for a 32 row format and frame time of 1.6ms is shown in figure 7.7. The 10% coincidence loss point occurs at 200 Hz in this case which is far higher than either the 40 Hz predicted by simulation or the 130 Hz predicted by the simple analysis above.

As will be discussed in section 7.3.2 the explanation for the discrepancy between the expected dynamic range curve and the observed dynamic range curve is due to the long secondary components of the phosphor decay. These components lead to increased linearity in the dynamic range curve.

The Multiple Event Recognition Circuit

The reasoning behind the implementation of the multiple event discriminator circuit was given in section 6.5.2. Briefly, by considering the energy contained within an event profile, the circuit is able to distinguish between one event and more than one event. The circuit is given an energy threshold which it uses to decide that all energies below it are due to one event and all those above it are due to two. The memory location associated with double events is incremented by two instead of the usual one and in this way the dynamic range curve is made to turn over at a higher count rate.

This procedure is a valid one, as is any effect that straightens the dynamic range curve. For any dynamic range curve, there will be a linear region and a non-linear region. The non-linear region may be used to acquire photometrically accurate data as long as the accumulated counts can be directly related to the photons input. For spectroscopy, where there are variable emission line widths, and ground based imaging, where there is variable seeing, the coincidence losses will be variable and so this would not be the case. However, theoretically, this will be a valid procedure for point source imaging applications in space, where the source is a constant size.

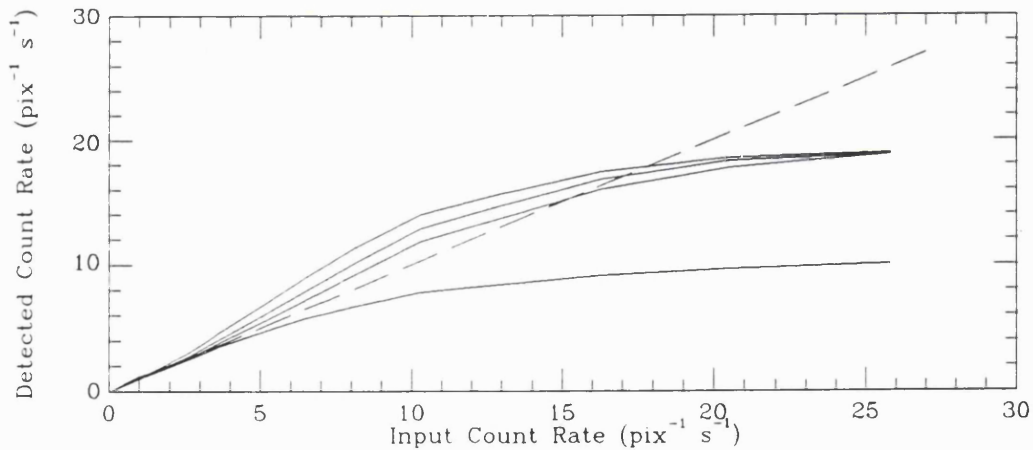


Figure 7.8: Flat field dynamic range curves for three multiple counting thresholds on a format of 2048x2048. From top to bottom, the curves are for thresholds of 375, 450 and 525 ADUs respectively. For comparison, the dynamic range curve with multiple counting disabled is shown as the lowest curve.

The multiple counting threshold may be set too low in which case the dynamic range

curve will exhibit overcounting. On the other hand the threshold may be set too high in which case the dynamic range curve may not straighten out as much as it could. In order to find the optimum setting for the multiple event discriminator threshold a series of tests were carried out on an optical bench with a constant intensity light source and a set of calibrated neutral density filters to vary the count rate. Figure 7.8 shows the results of these tests for a flat field on the full 2048×2048 format. Three settings were used and one can see that at too low a threshold there is overcounting which results in the dynamic range curve appearing above the linear region indicated by the dotted line. From these tests the optimum setting can be seen to be slightly greater than 525 ADUs. At this setting the 10% coincidence loss occurs at 16 counts s⁻¹ pixel⁻¹ which corresponds to 10⁶ counts s⁻¹ over the detector which is well above the 200k counts s⁻¹ set for the maximum background count rate achievable with the XMM-MIC. This figure compares with that of 320k counts s⁻¹ when there is no double counting threshold set.

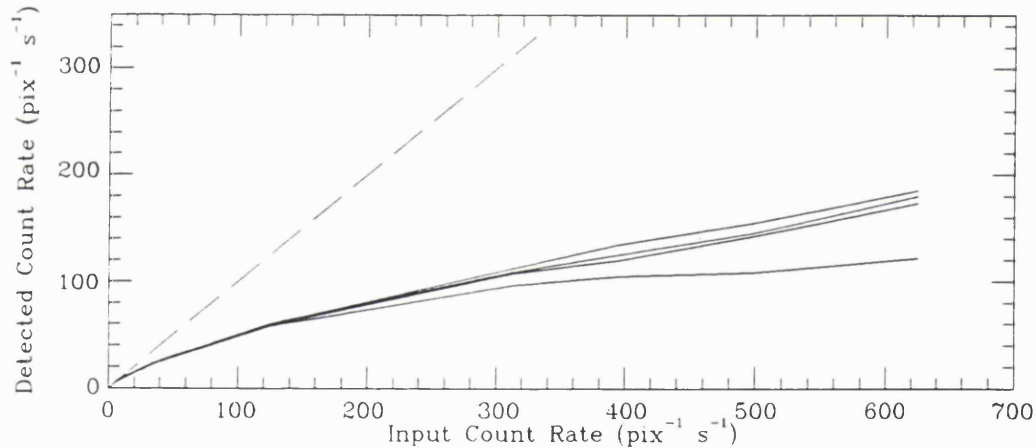


Figure 7.9: Point source dynamic range curves for three multiple counting thresholds on a format of 2048×2048. From top to bottom, the thresholds are 450, 500 and 550. For comparison, the dynamic range curve with multiple counting disabled is shown as the lowest curve.

Figure 7.9 and figure 7.10 show the effect of multiple counting thresholds of 450, 500 and 550 ADUs on the point source dynamic range curves for a full format and for a 32 CCD row format. The curves are slightly jagged due to badly calibrated ND filters. These curves were obtained with a 40μm pinhole which, as explained earlier, produces the same

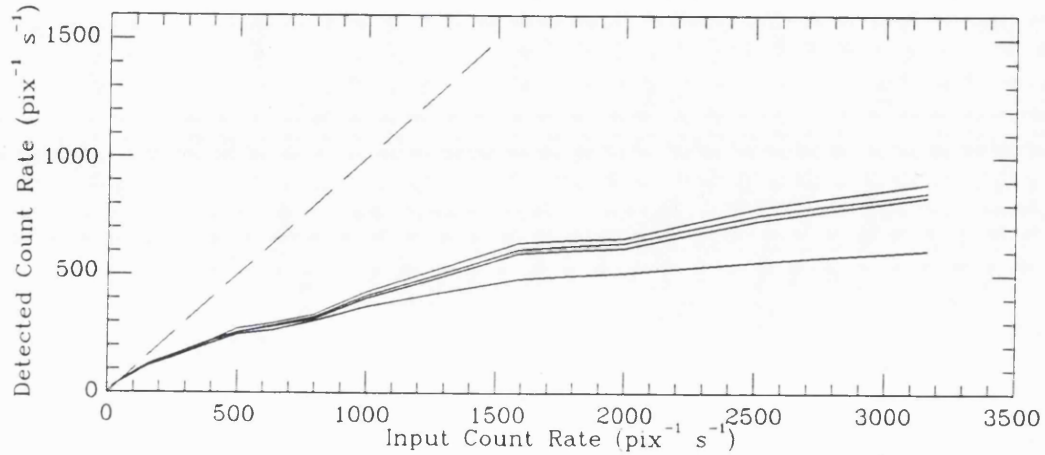


Figure 7.10: point source dynamic range curve on a format of 2048×2048. From top to bottom, the thresholds are 450, 500 and 550. For comparison, the dynamic range curve with multiple counting disabled is shown as the lowest curve.

dynamic range curve as a much smaller point source. The multiple counting circuit is not as effective as it is with a flat field. This is believed to be due to the fact that, with a pinhole, all the events arrive in the same place. With the ITL 25mm tubes, the pulse width is narrow so that most of the energy of an event is contained within the peak CCD pixel. When more than one event arrives in the same CCD pixel then the total in the peak would add up to greater than 255 ADUs but, because the ADC is only 8-bit, the peak pixel is saturated at 255. Thus, when the energy of a multiple event is summed the answer will be too low because the peak pixel value is too low at 255. This means that the energy of a double event may be placed below the multiple counting threshold and be counted as a single event when, in fact, it should be placed above the threshold and counted as double. Therefore, the multiple event discriminator circuit is not as effective as it should be and the dynamic range curve for multiple counting enabled is not very different to that when it is disabled.

The Decay of the Output Phosphor

As already mentioned, the actual XMM-MIC dynamic range curve does not agree well with that predicted by simulations. On a full format the real point source 10% coincidence loss point occurs at 25 Hz whereas that predicted by simulations gives 20 Hz. Similarly, with a

32 row format the real 10% loss point is at 200 Hz whereas simulations predict 40 Hz. The reason is that the linearity is being increased due to the phosphor decay characteristics discussed in section 3.3.4. There are two primary components associated. Firstly, events occurring in the CCD frame transfer period are being counted in the following frame period. Secondly, the charge build up on the output phosphor due to two coincident events in a frame period causes the double event to be counted twice – once in the arrival frame and once in the following frame.

This effect was first noticed with the ground based MIC which uses a 40mm intensifier with the same output phosphor. The real dynamic range curve did not match that predicted by detailed simulations. It was suspected that the phosphor decay was causing increased linearity and section 3.3.4 describes how the decay was characterised by experiment and subsequent analysis. The decay can be modelled by three decay components with time constants of $0.87\mu\text{s}$, $340\mu\text{s}$ and $7300\mu\text{s}$, the slower components giving rise to a long tail to the energy emitted by the phosphor as shown in figure 3.12. The long tail leads to some of the energy of an event being recorded in the following frame to the one in which it arrived. There will be increased linearity primarily when two events arrive in the same frame on top of each other. The intensity of the spot on the output phosphor will be sufficiently bright on the arrival of the second event that the secondary decay leads to a residual event in the next frame whose height is above the photon counting threshold. Thus, there will be extra counts which leads to increased linearity.

Once the decay constants and relative intensities of the secondary decay components had been determined it was possible to include the effect of the phosphor in simulations. The results of these simulations for a point source on a 32 row format are shown in figure 7.11. A simulation that does not include the effect of phosphor decay is also shown for comparison. One can see that the simulations agree well with the actual dynamic range curve of the ground based MIC suggesting that it is indeed the phosphor decay that is responsible for increasing the linearity of the dynamic range curve.

The effect of the phosphor is useful for increasing the dynamic range of the detector. The extra counts due to the phosphor decay compensate for losses due to coincidences. However, there are two provisos attached to this:

- That the short term phosphor decay characteristics do not vary after exposure to a bright source. If moving from one bright object to another that happens to sit

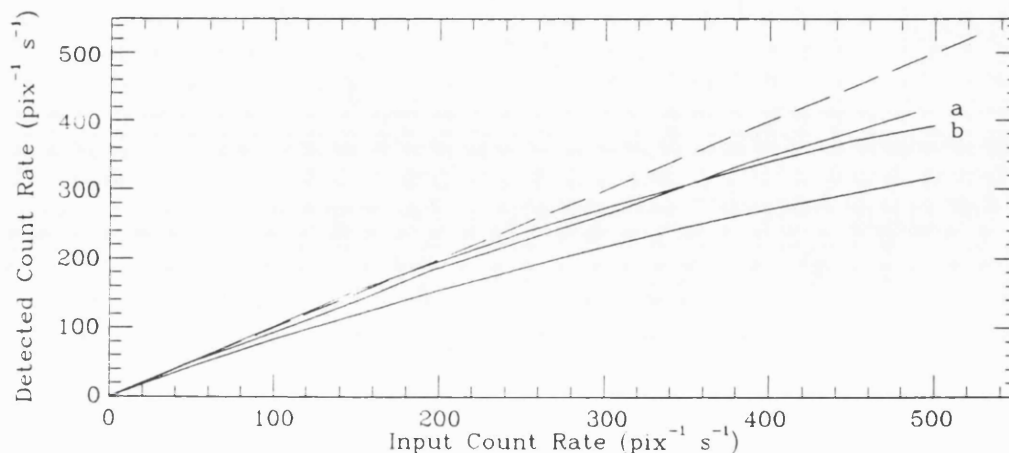


Figure 7.11: Real (a) and simulated (b) dynamic range curves for a point source on 32×388 format with the ground based MIC showing the effect of the long secondary decay components. For comparison, a simulated curve is shown for the same format but with phosphor decay not taken into account.

on the same area of the detector one needs to guarantee that the dynamic range is constant. This also applies during an integration on a single object if variable integration times are associated with the observing program. No such variation in the short term phosphor decay characteristics has been noticed.

- That the long term phosphor decay characteristics can be recalibrated. The phosphor characteristics will change with age and will thus affect the dynamic range curve. However, this can be overcome very easily during observations by utilizing 'standard stars' for recalibration.

Channel recovery in the Channel Plates

This effect was described in section 3.3.4. Basically, after the passage of an event, a channel or group of channels is left depleted of charge. It takes a finite time for the channel to recover this charge. If another photon event occurs in the same channel during this time then there will not be enough charge available for the subsequent electron charge to be of full size, that is, there is gain depression.

It is not believed that gain depression has a great effect on the dynamic range with XMM MIC. This is because simulations that do not include channel recovery effects seem

to fit the real data well. This implies that the high count rate end of the dynamic range characteristics are limited by the CCD frame period. Obtaining an accurate figure for channel recovery with MIC is not possible because of the limitations imposed by the CCD frame period.

7.4 Detector Resolution

The resolution of the detector is primarily governed by properties of the intensifier as was discussed in section 3.3.1. The FWHM of a point source is given by equation 3.5 and is the pythagorean convolution of

- a The resolution of the front gap between the photocathode and the first channel plate
- b The pore to pore spacing of the front channel plate
- c The inherent resolution of the centroiding electronics
- d The finite width of the point source

The resolution of the front gap was given in equation 3.7. An important point about the resolution of the front gap is that it is wavelength dependent because the transverse emission energy of the electrons emitted from the photocathode depends upon the energy of the incident photons. The values of ϵ vary from about 0.3 eV in the UV to 0.05 eV in the red (Eberhardt, 1977) although the actual values depend upon the composition of the photocathode. Thus, the resolution of the detector is generally better in the red.

Initial tests were performed with the ITL 25mm tubes. A luminescent panel with a constant intensity at 490nm was used as a light source. A $25\mu\text{m}$ pinhole was imaged via a 4.35:1 demagnifying lens onto the input window of the intensifier giving a spot size of $5.7\mu\text{m}$ on the photocathode. The spot was centroided to 1/8th of a CCD pixel, giving a pixel size of $8.80\mu\text{m}$. With the 25mm intensifiers, the best resolution obtainable with a front gap voltage of 300V was found to be $35\mu\text{m}$ FWHM as shown in figure 7.12. This figure is a lot higher than that predicted by equations 3.5 3.7 which give $25.8\mu\text{m}$. By varying the front gap voltage between 100V and 300V it was possible to model the observed variation in resolution by choosing appropriate values of the various parameters associated with equation 3.7. It was found that the resolution of the intensifier was $23\mu\text{m}$ which is a good match to the theoretical resolution based on the two equations mentioned

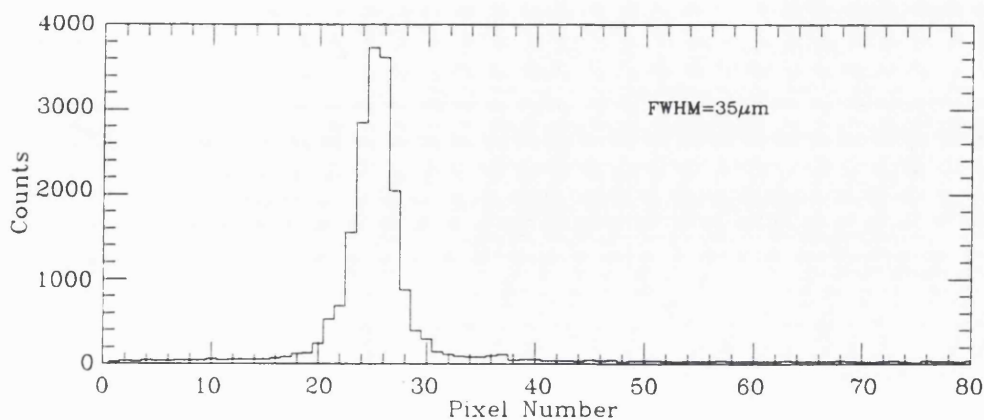


Figure 7.12: Cross section of a $5\mu\text{m}$ pin-hole acquired with the 25mm intensifier supplied by ITL.

above. However, the resolution of the centroiding electronics was found to be $22\mu\text{m}$ which is much higher than expected.

In order to try and deduce the reason for the poor resolution the 25mm tubes were replaced by the 40mm tubes used with the ground based MIC which are known to be of high quality. The tests were repeated with the $25\mu\text{m}$ pinhole and the results show that the system has very high resolution. In fact, the resolution is sufficiently high that the FWHM of the image is modified according to the position of the input spot with respect to the channel pores of the front channel plate. The best case condition corresponds to the pinhole being directly above a pore of the front channel plate and in this case the resolution is $13.88\mu\text{m}$ FWHM. Figure 7.13 shows this case and various lower resolutions corresponding to different positions of the input spot with respect to the pores. The worst case condition is shown in figure 7.14 and represents the case when the input spot is directly above the space between three channel pores as illustrated in figure 7.15. Electrons go down all three channels giving a 'top hat' image profile.

There are three points to note about the test results

1. The centroiding resolution of the system is inherently very good. Analysis of the data has shown that the centroiding resolution is $4.2\mu\text{m}$. The better resolution seen with the 40mm tube confirms that the poor resolution associated with the 25mm tube is due to the poor event profiles of that tube. The signal induced background

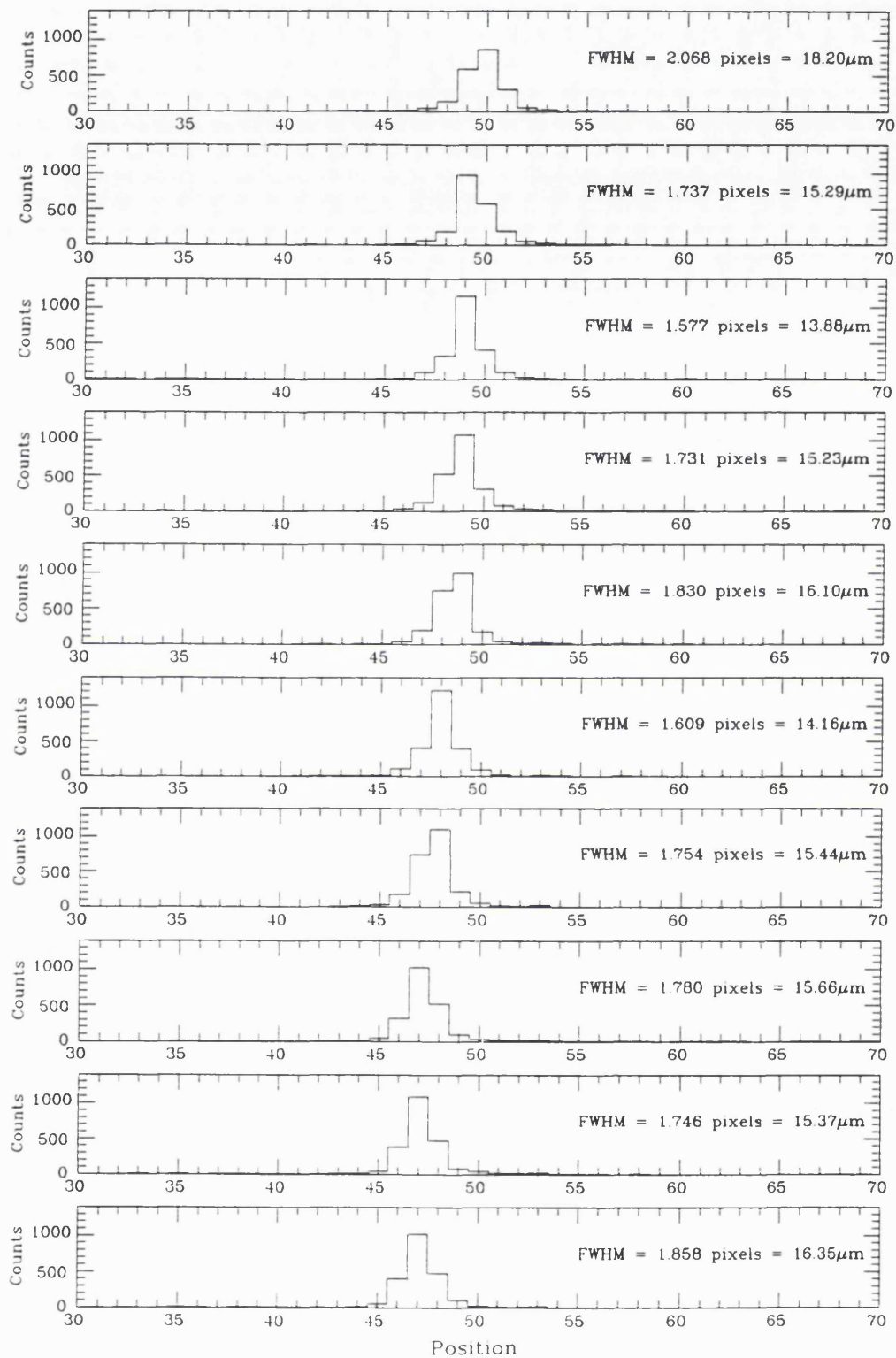


Figure 7.13: The effect of channel plate pore structure on detector resolution.

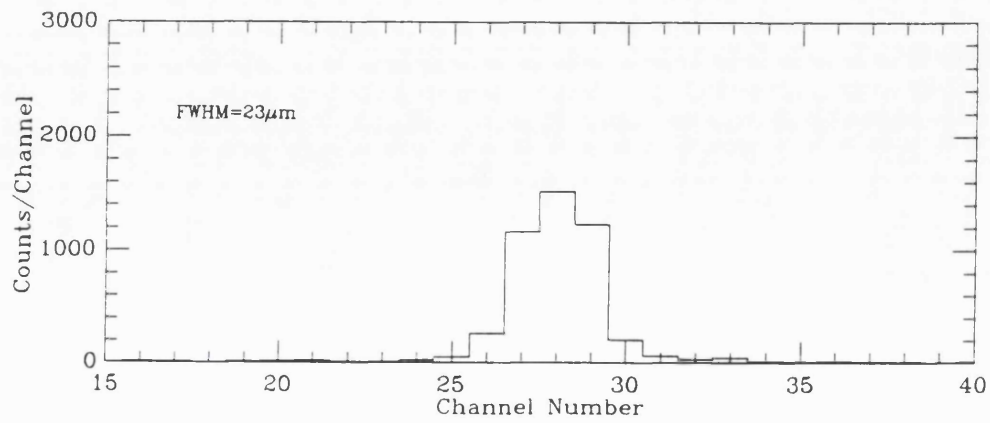


Figure 7.14: Worst case resolution of $5\mu\text{m}$ pin-hole where the input image straddles three channel plate pores.

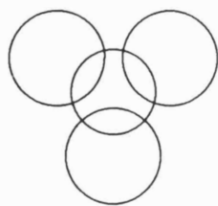


Figure 7.15: Input point source position giving rise to worst case resolution. The small circle represents the area covered by the point spread function of the front gap.

described in section 7.1 gives rise to a random, unpredictable event profile which in turn gives rise to centroiding errors that are not correctable using the iterative technique described in section 6.6.3.

2. Care must be taken in defining resolution. The FWHM of the image of a point source depends upon the position of the point source with respect to the pores of the front channel plate. Thus, when the FWHM is used as the definition of resolution, the resolution is variable. To avoid this the resolution should be defined in terms of the ability to resolve two closely spaced objects. From figure 7.14, the distance two objects have to be apart before they are clearly resolved is, in this worst case, 4 pixels, or $35.2\mu\text{m}$ when subtended back to the photocathode. Half this distance is the limiting resolution of the system, that is, $17.6\mu\text{m}$.

The theoretical resolution can be calculated from equations 3.5 and 3.7 given the following values for the various parameters

L	$200\mu\text{m}$
ϵ	0.1eV
V	300V
Pore spacing	$15\mu\text{m}$
Centroiding resolution	$4.2\mu\text{m}$
Image size	$5.7\mu\text{m}$

Eberhardt (1977) gives a value of ϵ at 500nm of 0.103 eV for a typical multialkali photocathode. Thus, for an S-20 photocathode, assigning a value of 0.1 eV to ϵ at the 490nm wavelength of the luminescent panel is a good approximation. All the other parameters above are known. Using these values gives a value of $20.5\mu\text{m}$ for the FWHM resolution.

There is a discrepancy between the theoretical resolution and the resolution actually obtained as detailed above. This is primarily due to the fact that the value of ϵ is an approximation and that the value of L has error bars associated with it.

3. There will be cases when the integrated image is undersampled by the detector because the pixel size is too small. This will happen mostly towards the red end of the spectrum where the emission energy is lower.

7.5 System Detective Quantum Efficiency

The detective quantum efficiency (DQE) of the system is the fraction of photons incident at the detector input that are detected and stored in the detector memory. It measures how efficient the detector is at detecting photons. The DQE of the detector is given by

$$\text{DQE} = \text{RQE} \times \text{Open area ratio of front channel plate} \times \text{Camera efficiency} \quad (7.9)$$

The RQE was discussed in section 7.2 – it needs to be better than 20% in the blue and there should be no problem with obtaining that figure. The open area ratio was given by equation 3.4 and, with $10\mu\text{m}$ pores on $12\mu\text{m}$ centres, this is 0.63. The camera efficiency could be as high as 100% but, as discussed in section 3.3.2, this depends on the quality of the pulse height distribution and on the setting of the photon counting threshold. With these figures the DQE could be around 13%, rising to 15% with funneled inputs to the channel plate pores.

As yet the DQE has not been measured as it requires the use of specialist equipment which is not yet available at UCL.

7.6 Detector Uniformity

Various forms of blemish, patterning or other artefacts may be present in images taken with the system. These features, which constitute detector non-uniformity, may not be apparent in the image because they may be obscured by the data themselves or may be at too low a level to be seen above the noise. It is important to identify such features so that they may be corrected during data reduction or removed in subsequent modifications of the system. The best way to reveal detector non-uniformity is to take a flat field with high signal to noise. Here, the only non-uniformity present in the data is the photon noise so that detector non-uniformity ought easily to be seen. High signal to noise ought to reveal low level features.

A 161,000 second flat field was taken with the XMM-MIC to produce a high signal to noise image. The exposure was the sum of two contiguous flat fields, the first, ‘A’, being an exposure of 78,000 seconds and the second, ‘B’, being an exposure of 83,000 second. The data rate for the flat field was $50,000 \text{ counts s}^{-1}$ over the detector area giving an average count per pixel of ~ 2000 in the final summed image. An area of 256×256 pixels

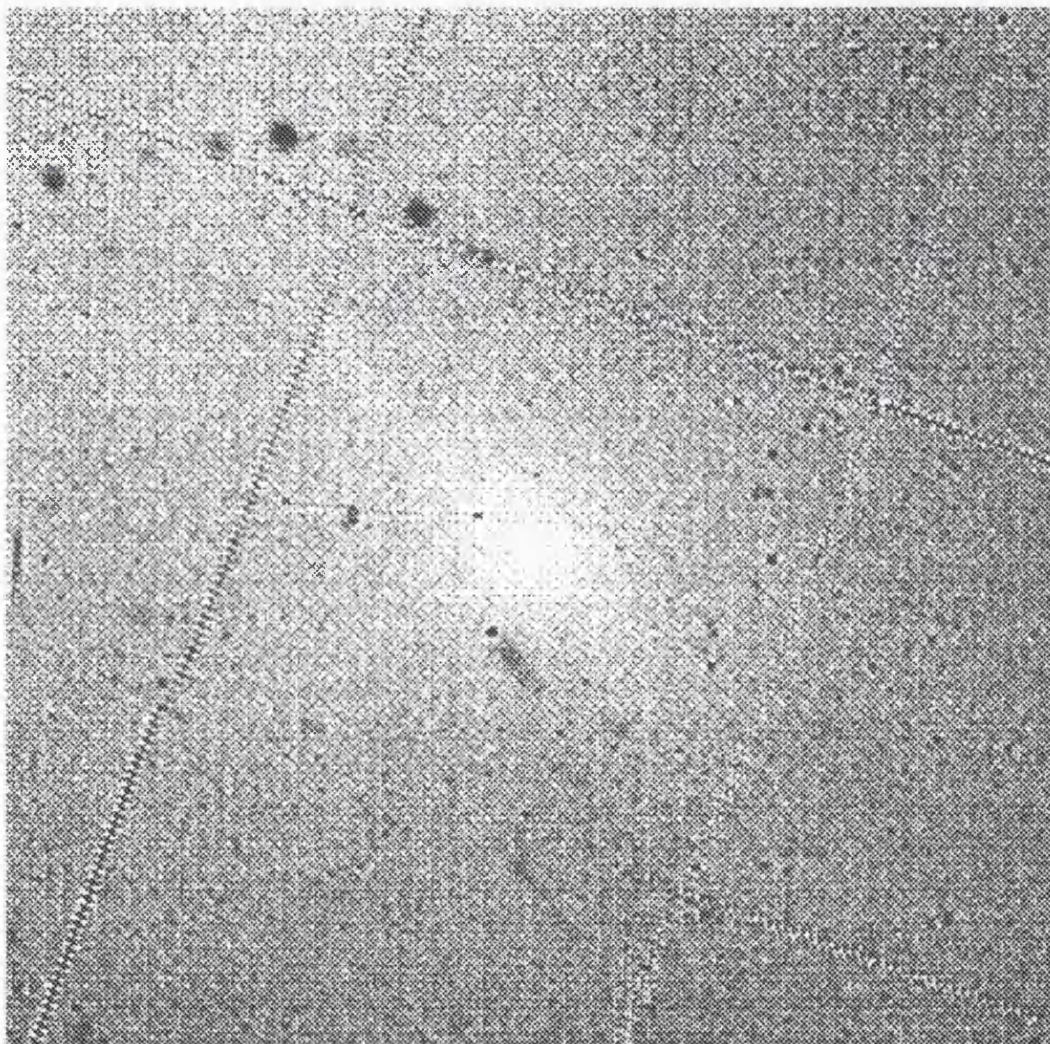


Figure 7.16: A high signal to noise flat field

was read out from the CCD and the data were centroided to 1/8th CCD pixel in both X and Y giving a detector format of 2048×2048 pixels. A high contrast image of the flat field is shown in figure 7.16 and a magnified part of it is shown in figure 7.17.

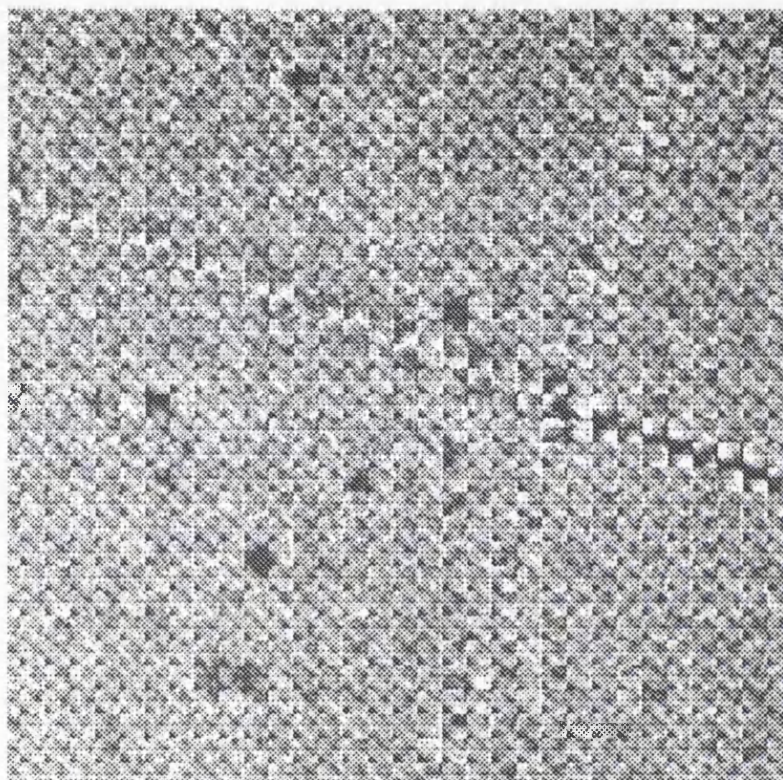


Figure 7.17: A magnified portion of the high signal to noise flat field

7.6.1 Fixed Pattern Noise

The various causes of fixed pattern noise were discussed in section 6.6.2. All of them bring about a change in the photon event profile that introduces centroiding errors. There is fixed pattern noise in the flat field that manifests itself as an apparent grid structure across the whole image. There are several causes.

Variation with Time

After switch on of the EHT supply that powers the intensifier there is a gradual drift of the voltages across the various gaps and this results in a change of the pulse profile with

time. If the pattern noise is corrected soon after switch on by the procedure described in section 6.6.3 then it will reappear as the voltage drifts.

This effect was known about and for this reason the voltages were allowed to stabilise for 16 hours before the pattern noise was corrected and the long flat fields were taken. Following this one of the two images that comprised the total flat field was divided by a normalised version of the other and it was found that the remnant fixed pattern due to other effects was removed. This meant that the pattern was the same shape in both flat fields showing that the pulse profile had not changed with time. Thus, the system stability was very high.

Variation from Spectrum to Spectrum

This effect was discussed in section 6.6.3. Figure 6.29 showed eight spectra associated with a single CCD pixel. The first two spectra have much higher fixed pattern noise compared to the remaining six, the first having $\sim 50\%$ modulation. The effect repeats every 8 pixels, that is, every CCD pixel. In other words, the next pixel in Y would show exactly the same effect, the same spectra having the highest modulation. This implies that the effect is associated with centroiding to $1/8$ th CCD pixel. This feature of pattern noise has only recently been noticed. Previously, when correcting pattern noise on shorter integrations, a large number of spectra were summed together to produce a spectrum of good signal.

This effect is believed to be due to the asymmetrical event profile. This leads to a situation where the event centre is not in the same pixel as the peak data. This is overcome by having an asymmetry correction circuit such as with the ground based MIC which does not show this effect.

Variation Across the Spectra

There is an increase in fixed pattern noise towards the edge of the spectra which must result from a variation in the pulse profile across the field. There are a number of possible causes but it is believed that the fibre optic coupling is the primary problem as discussed in section 6.6.3.

7.6.2 The Effect of Fibre Optic Multifibre Junction Defects

There is a faint square grid structure apparent in the images shown in figure 7.16 and figure 7.17. This is due to defects in the fibre optic packing structure originating in the manufacturing process. This 'stitching' pattern arises from defects in the boundaries between adjacent multifibres, as was described in section 4.2. It is the fibre block bonded to the CCD that is responsible for the stitching seen in these images. This was shown by rotating the intensifier and fibre taper with respect to the CCD and observing that the orientation of the stitching did not change.

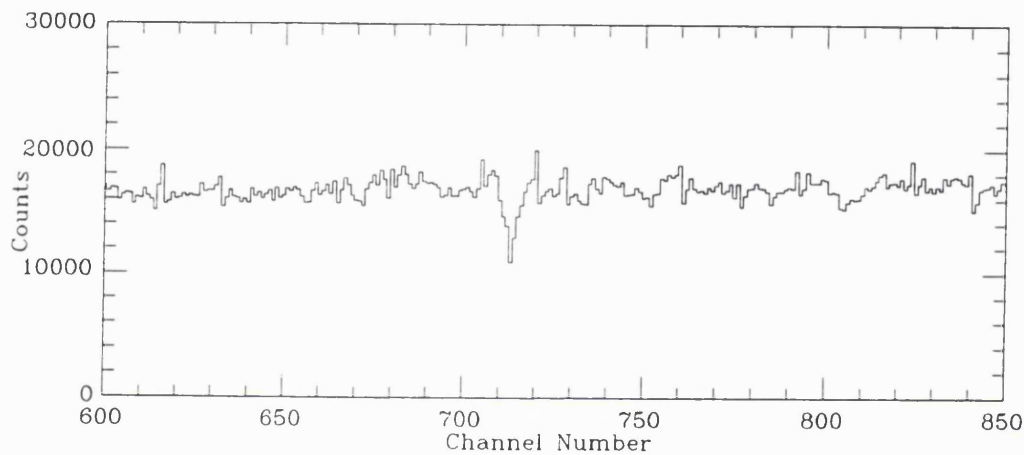


Figure 7.18: Profile through the stitching that results from multifibre junction defects present in the fibre optics.

Figure 7.18 shows a cross section through one of these lines. It is believed that no data are lost, merely that the event profile is changed and the centroiding accuracy is degraded. This causes events to be placed incorrectly resulting in two peaks either side of the defect as shown in the figure.

• For a space qualifiable version of the detector it is intended that the CCD be bonded directly to the fibre taper which will act as the output window of the intensifier. No stitching has been observed within the fibre taper and so this modification ought to eliminate this patterning. Additionally, higher quality fibre optics are now available. Galileo have developed fibre optics that use fractal (Cook and Burger, 1991) multifibres which pack together without introducing junction defects. CCD manufacturers are willing to use these fibre optics if requested to do so.

7.6.3 The Effect of low quantum efficiency CCD pixels

Figure 7.17 clearly shows a number of square areas of 8×8 pixels which have a lower number of counts. These are due to the effect of lower quantum efficiency CCD pixels. The lower QE CCD pixels alter the event profile as seen on the video output of the CCD camera and cause a loss in centroiding accuracy. This tends to shift events into adjacent CCD pixels so that events are not lost but merely positioned incorrectly.

The definition of a blemish was given in section 5.2. Typically, CCD manufacturers quote the highest grade CCDs as having fewer than 10 blemishes over the detector area. However, given the definition of a blemish it is likely that there are substantially more blemishes that would affect the event profile. Thus, as far as the XMM-MIC is concerned, it can be expected that there will be a lot more of these blemishes over the detector area, its effect depending upon its QE with respect to its neighbours.

7.6.4 Other Detector Non-Uniformities

Three other non-uniformities are apparent in the flat fields

- There is a brighter area in the centre of the image. This is caused by light scattered from the ring of solder seal that is used to make the intensifier vacuum tight. For a space qualifiable version of the detector, it will be necessary to shield this solder seal from any light source. It will be possible either to black off the solder ring or shield it from any source of light.
- There are a number of black spots over the image. These result from inadequate cleaning of the optics prior to carrying out the exposure.
- There are two defects shown in figure 7.16 which are approximately straight lines. They have not been apparent in previous flat fields taken with the XMM-MIC. It is possible that these lines originate from the intensifier and, if so, they are most likely to be due to scratches introduced during the photocathode manufacturing process.

Also, it was expected that aliasing effects would be apparent in the flat field as a periodic modulation, or ‘fringing’ in the data. This effect is caused by sampling the $12\mu\text{m}$ pore structure of the first channel plate with $8.80\mu\text{m}$ pixels. However, no such fringing is visible and this is undoubtedly due to the low detector resolution introduced by the image intensifier.

7.6.5 Variation of Pattern Noise with Count Rate

The effect was noticed during observing trials described in section 7.7 rather than with the long flat fields – these were of constant count rate. Nevertheless, this effect constitutes the most serious non-uniformity of the detector.

Section 6.6.3 describes the iterative procedure used to correct the pattern noise which requires a flat field to be carried out. This flat field is of a constant count rate and the procedure is carried out at this count rate. The observing trials revealed that the correction is only valid at that count rate and that at any other count rate the pattern reappears. At high count rates compared to the rate of the flat field used for the correction procedure the pattern produces $\sim 50\%$ modulation to the data.

The cause of this effect is that the average event profile is different at every count rate. At lower count rates there are fewer coincidences and so the *average* event profile becomes closer to that of a single event. At higher count rates there are more coincidences and the average event profile changes to one which involves one or more overlapping events. Thus, every count rate has a different average event profile and thus the shape of the pattern is different at every count rate.

It will be difficult to remove the pattern caused by the count rate dependent change in profile. Of course, coincident events could be removed in hardware using a discriminator circuit but this would lead to a very large loss in dynamic range. Therefore, it is likely that there will always be some level of fixed pattern noise with XMM-MIC. With a ground based MIC this problem could be overcome easily with the use of a dither circuit. Dithering, which was described in section 6.6.2, is routinely employed in a number of ground based detectors. However, additional constraints placed upon a space version of MIC mean that dithering is an impractical technique.

In practice, the effects of this count rate dependency on the fixed pattern may not be too serious. With XMM-MIC the Airy disc of < 1 arcsec means that any star image will subtend ~ 0.25 CCD pixels. With most photon events confined to such a small area, coincidences will have little effect on the event profile. This is illustrated in figure 7.19 which shows the profile of a point source at various count rates. However, this will only be the case with bright stars where the vast majority of coincidences will be between photon events from the star image. At lower count rates, where there will be a much greater proportion of coincidences between object events and background events, the event profile

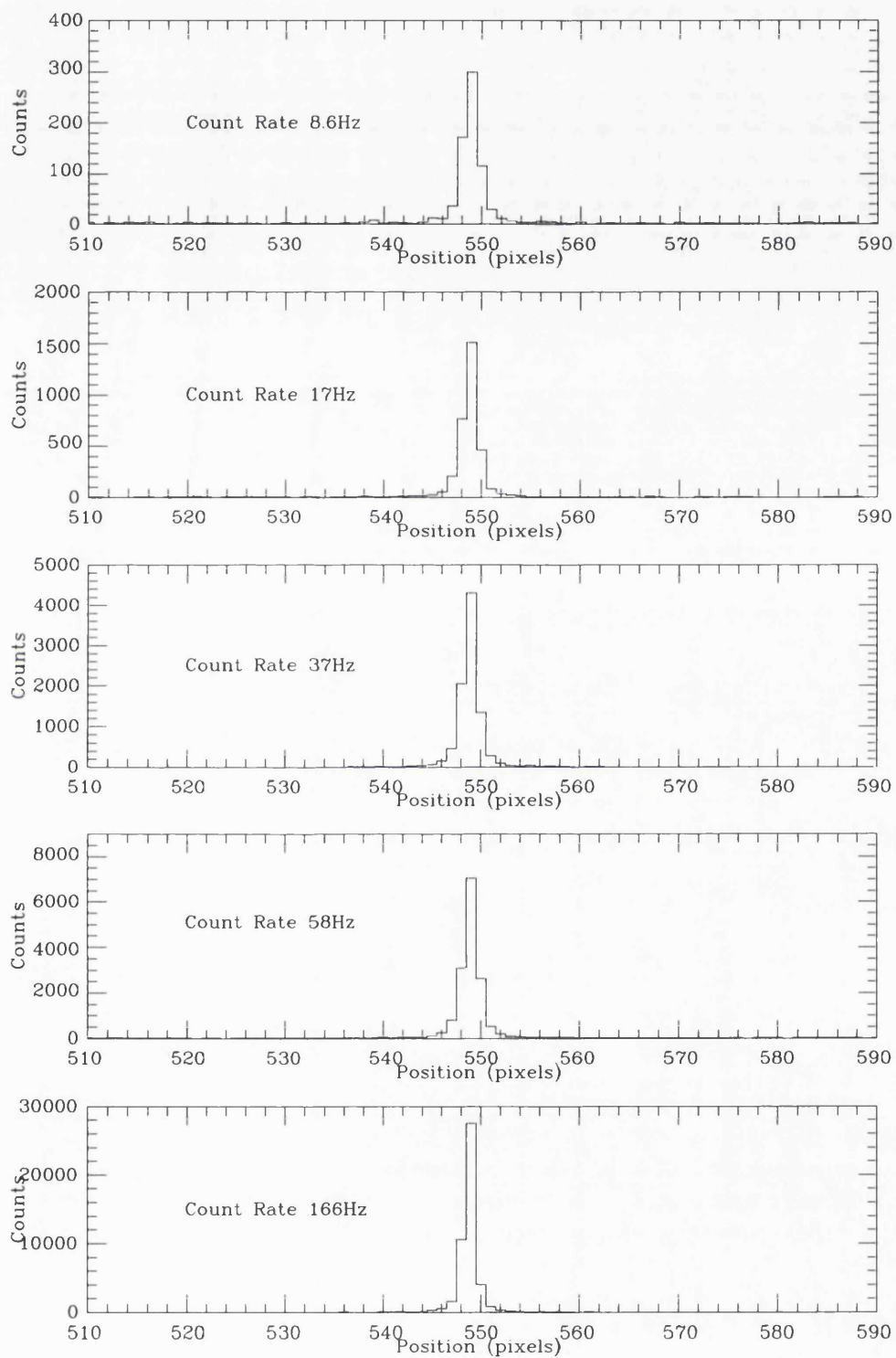


Figure 7.19: Point source profile at various count rates illustrating the negligible effect of count rate on the profile

will be altered and will thus introduce a visible level of fixed pattern. It would be possible to remove this patterning during data reduction using special software.

7.7 Observing Trials

Observing trials were carried out on the 24 inch Radcliffe telescope at the University of London Observatory (ULO) in January 1992. The observatory is situated adjacent to a busy main road which means that there is a high sky background almost entirely due to backscatter from sodium street lighting. This scattered light provides a background which is of a similar intensity to that expected for the XMM-OM. In this respect XMM-MIC was tested under similar conditions to those expected during the mission.

The aims of the observing trials were

- To test XMM-MIC in an astronomical environment,
- To obtain point source dynamic range results on astronomical objects

7.7.1 The Observing Programme

The programme was designed to evaluate the point source dynamic range of the detector by performing photometry on star fields containing stars of known relative magnitude. However, it was not possible to use previously published data on these stars because two quantities were unknown

- The wavelength response of the telescope optics
- The quantum efficiency variations across the detector area.

To avoid the necessity of knowing these two properties it was decided to perform the photometry using a narrow band filter and to assume that the variations of the two over the bandwidth of the filter were negligible. Also, using a filter centred around the two Na D lines enabled the relative intensity of the sky background with respect to the stars to be maximised.

This approach required accurate relative photometry on the same star fields using the same narrow band filter. This was performed with a direct, unintensified CCD which is known to be a linear device if saturation is avoided. These observations were made in

February 1991 with the commercial CCD camera situated on the 24 inch Allen telescope at the ULO. Ideally these observations would have been made on the same telescope as the MIC observations. However, at the time allocated for MIC observations, the Allen telescope was not available.

The choice of star fields was governed by two criteria

- the dynamic range on a single isolated star
- the effect of channel plate gain depression on dynamic range

The fields contained a range of separated objects, from well separated doubles to close binaries and multiples. The well separated doubles were far enough apart that the effect of gain depression could be neglected and they could be treated as isolated singles. The objects in close proximity were close enough so that any effect of gain depression would be clear.

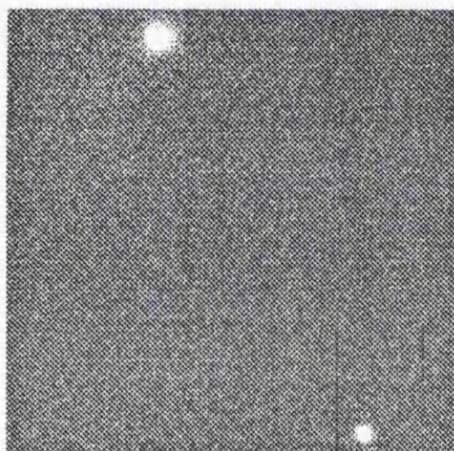
7.7.2 Observing

Observations with MIC were made using a 2048×2048 format and the windowing facility was used to collect data in a data acquisition area of 1024×1024 . This configuration represents the primary operating mode of XMM-MIC. A few observations were made with a 2048×2048 acquisition window in order to show that data could be acquired on any sized window. All exposures were carried out at $\times 8$ resolution which gave a pixel size of $8.80 \mu\text{m}$ when subtended back to the photocathode. The telescope plate scale was 30 arcsec per mm , or $1 \text{ arcsec per } 33 \mu\text{m}$. The multiple event recognition circuit was enabled for all observations and the threshold was set at 600 ADUs which is close to the optimum setting, as was discussed in section 7.3.2.

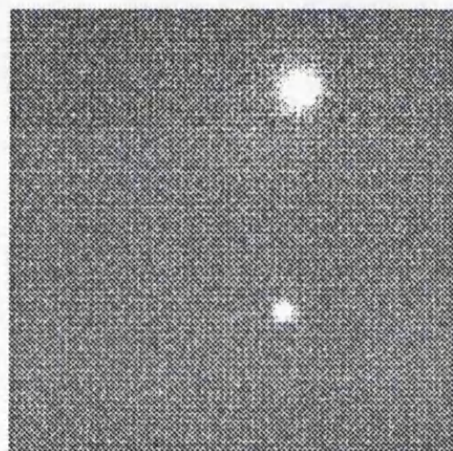
Table 7.1 shows a list of the objects in the star field observed and four of these fields are shown in figure 7.20. Data were taken on all these fields so that a comparison could be made and accurate relative magnitudes could be found. The seeing during the observations was $\sim 4 \text{ arcsec}$ on average. This means that the image size was around $130 \mu\text{m}$ FWHM and it meant that observations on the image scale of XMM was not possible. However, it did allow a dynamic range curve to be obtained on the equivalent of an extended point source such as, for example, a galaxy. The background count rate was variable and depended on the neutral density (ND) filter being used. For example, with ND 0.9 the background was

Table 7.1: Observing log for the XMM-MIC detector at the University of London Observatory.

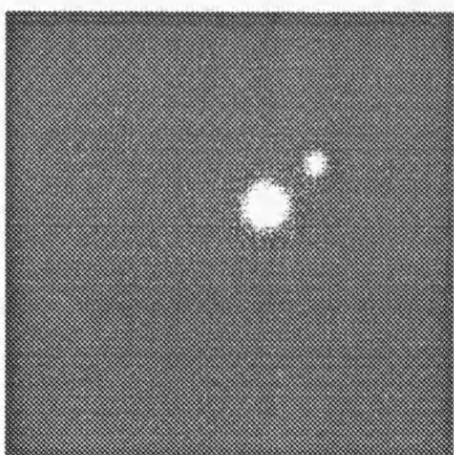
object	other	type	Mv approx	Separations	ND	time secs	format square
NGC1912	M38	Cluster	stars ≤ 8		0.9	2000	2048
HR1895	θ Ori	Group	5.1,7.9,6.7,6.4...	in 120"	1.5	1000	2048
					1.5	1000	1024
NGC2169		Cluster	6.9,7.0,8.6,7.5...	in 8'	0.9	2100	2048
HR2298	ϵ Mon	Triple	4.4,6.7,12.2	13",93"	2.0	772	1024
					2.0	2000	1024
HR2456	15 Mon	Group	4.7,9.0,8.3,7.6...		2.0	2000	2048
					2.0	2000	1024
HR3395		Double	6.0,7.2	10.3"	2.0	1000	1024
HR3427		Quad'	6.4,6.6,9.2,8.8	150",135"(2)	0.9	2000	2048
					0.9	600	1024
					1.5	1000	1024
HR3428		Quad'	6.4,7.7,9.4,10.4	63",83",21"	0.9	2000	1024
HR3429	ϵ Cnc	Double	6.3,7.4	135"	0.9	600	1024
					2.0	817	1024
HR3474	ι Cnc	Double	4.0,6.6	30"	2.6	2000	1024
					0.9	2000	1024
HR3759	τ Hya	Double	4.6,7.6	66"	2.0	1000	1024
HR3811		Triple	6.7,8.2,8.3	25",118"	0.9	1500	1024
HR4203	42 Lmi	Double	5.2,8.0	198"	2.0	1000	1024
HR4363		Double	6.5,8.2	12.7"	0.9	1015	1024
					1.5	2000	1024
HR4408	81 Leo	Double	5.6,9.2	56"	1.5	1000	1024
HR4414	83 Leo	Triple	6.5,7.6,9.9	28.5",90"	0.9	1000	1024
					2.0	1000	1024
HR4761	7 Cvn	Double	5.2,8.0	198"	0.9	500	1024
					1.5	700	1024
					2.0	2000	1024
HR4914	α Cvn	Double	2.9,5.6	19.4"	3.0	1900	1024



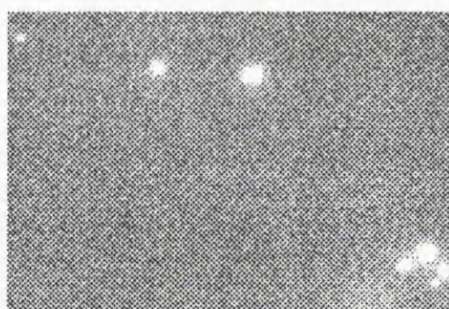
HR4761
Separation 198"



HR3759
Separation 66"



HR4914
Separation 19"



HR1895
Group including 'The trapezium'

Figure 7.20: Four star fields observed during the observing run. They are not all on the same scale

as high as $\sim 80\text{k counts s}^{-1}$ over the object whereas for ND 2.0 the background was as low as $\sim 5\text{k counts s}^{-1}$.

7.7.3 Data Analysis

All CCD and MIC data were analysed on the STARLINK facility at UCL. All CCD data had their CCD bias subtracted before the relative magnitudes of the stars in the field were determined

The ideal procedure for both the CCD and MIC data is to calibrate the data by removing the effect of detector non-uniformities such as those due to fibre junction defects and low quantum efficiency CCD pixels. This is done by dividing the data by a normalised flat field. A flat field is a uniform intensity distribution which is needed in order to reveal non-uniformities. A tungsten source cannot be used for this purpose as it does not give a uniform intensity distribution across the detector. Instead of a tungsten source the convention is to use sky fields and assume that the background is of uniform intensity. The principle behind this is as follows. It is necessary to know the background at the point of the star image but this is obscured by the star. Instead, one takes a field that does not have a star at the point at which the star appears in the image in question. The sky background from that field can then be used to correct for the sky background in the field in question.

The above procedure was not possible with the MIC data because of the way in which the data were acquired. For each star field a 1024×1024 data acquisition window was positioned within the 2048×2048 maximum detector format in order to collect data on as many stars as possible in a single integration. For each field this window was moved within the maximum format such that different areas of the photocathode were exposed each time, but a record was not kept of the position of the 1024×1024 area within the 2048×2048 . This meant that it was not possible to identify the area of one image that would give the sky background for a different image. Thus, the possibility of obtaining a uniform sky background flat field was lost.

Instead, the following procedure was adopted for MIC data reduction

- The average background was found in close proximity to a given star.
- This was then subtracted from the corresponding star image to form a ‘sky sub-

tracted' image.

- The total flux in each star image in the field was found
- The ratio was found of the flux of the brightest star in the field to that of the faintest star

There are two problems associated with the above procedure

- It assumes that the RQE of the photocathode is constant over the detector area
- It does not allow for any non-uniformities

So, although the detector non-uniformities could not be corrected using this procedure, the background level could be subtracted thus facilitating the analysis of the fluxes within the star images.

In principle, for a linear MIC detector the ratio of the star fluxes ought to be the same as those found for the CCD data. Any differences can be attributed to coincidence losses on the brighter of the two stars. The latter assumes that the count rate from the fainter star lies on the linear region of the dynamic range curve.

The most important star fields are those containing just doubles because the effect of gain depression can be easily assessed whereas, if there were other stars in the field, the gain depression due to many stars would be complicated to analyse. The distance between the various double stars ranges from 198" for HR4761 and HR4203 to 10.3" for HR3395. The 198" angular separation translates to 6.5mm on the detector input and this was considered far enough apart for the effects of gain depression to be negligible. Therefore, HR4761 and HR4203 may be considered as fields containing two isolated and stars the point source count rate can be found from the ratio of the two associated star magnitudes. A point source dynamic range curve can be constructed and, for HR4761, this was done by observing the field through different neutral density filters to provide points on the curve. Again, for all these observations, it was assumed that, for the fainter of the two stars, the count rate was situated on the linear region of the curve.

A plot of the results for the various bright stars is shown in figure 7.21. Here, the vertical axis is the detected count rate. This was found using the MIC data; for each of the bright stars in the fields the total flux contained in the star image was found. Dividing this by the integration time then gave the detected count rate. The horizontal axis is

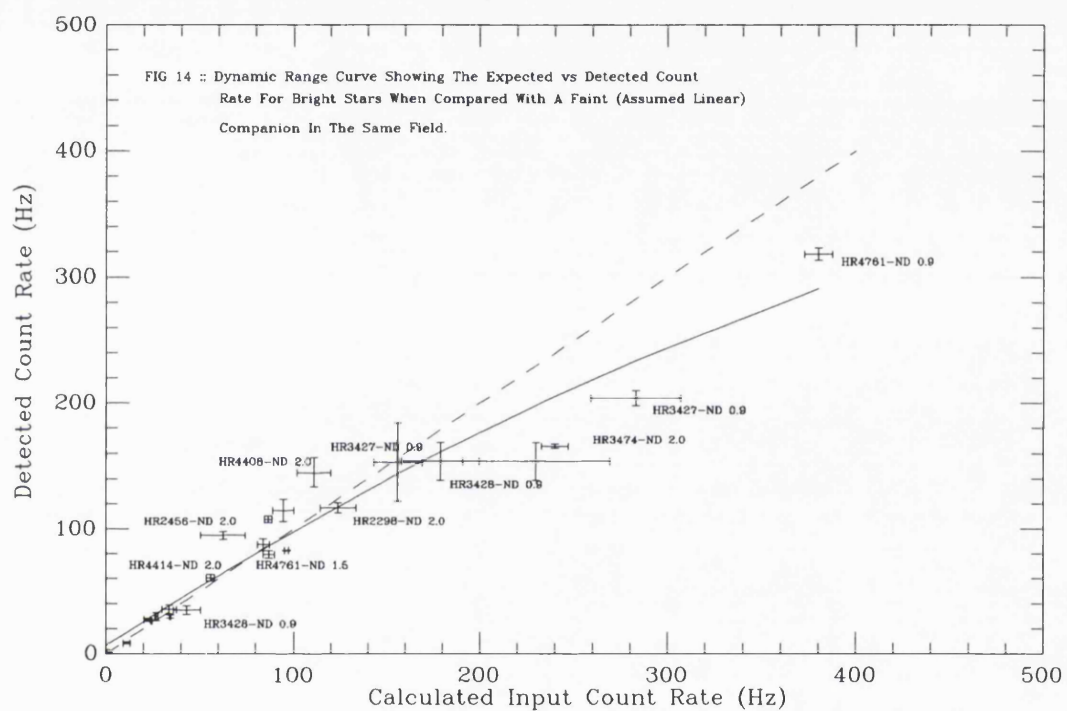


Figure 7.21: Dynamic range curve derived from astronomical trials

the calculated input count rate. This was found using both CCD data and MIC data as follows. The CCD is a linear device so that its detected count rate will be proportional to its input count rate. Therefore also, the ratio of the total fluxes in two stars in the field ought to be equal to the ratio of the respective input count rates in the two stars. Now, the ratio of the input count rates may be assumed to be a constant which means that the ratio of the input count rates for the CCD ought to be the same as the ratio of the input count rates for MIC. In other words

$$\frac{\text{Bright input rate (MIC)}}{\text{Faint input rate (MIC)}} = \frac{\text{Bright input rate (CCD)}}{\text{Faint input rate (CCD)}} \quad (7.10)$$

Now, by assuming that the faint MIC star lies on the linear region of the dynamic range curve the input rate in this faint star may be calculated. Knowing this and also knowing the correct ratio of the two count rates from the CCD data, the input count rate on the bright MIC star may be derived. Vertical error bars are derived from MIC data and horizontal error bars are derived from both MIC and CCD data.

Once the input count rate was deduced from the above procedure, this was used with the detected output count rate to plot a point on the graph shown in figure 7.21. This was done for all the bright stars in a field and a point placed on the plot as shown. A polynomial was fitted to the data and this is also shown in figure 7.21. The dashed line indicates the dynamic range curve for a linear detector. The polynomial fit shows that the 10% coincidence loss occurs at a count rate of $170 \text{ counts s}^{-1} \text{ object}^{-1}$ which is far higher than the 25 counts s^{-1} found from laboratory trials. This can be explained by the average object FWHM being $130\mu\text{m}$ as opposed to the $42\mu\text{m}$ in the laboratory trials. A larger FWHM would lead to fewer coincidence losses at higher count rates.

Two findings can be inferred from the results

- The effect of the background count rate does not appear to affect greatly the dynamic range curve of the star images. For example, it could be expected that the count rate associated with HR4761 at ND 0.9 is affected more than that at ND 1.5 where the count rate is lower. However, this does not seem to be the case.
- There does not seem to be any obvious effect from channel plate gain depression. For example, on HR2298 where two stars of magnitudes, M_v , 4.4 and 6.7 are $13''$ apart, there seems to be no dramatic loss in data from the brighter star.

The observing trials also provided valuable information concerning properties of the detector.

- The pattern noise is count rate dependent. This was discussed in section 7.6.5. A salient point about this effect is that it may never have been discovered if the detector had not been tested in an astronomical context. The discovery provides an illustration of how essential it is to test a detector in the environment for which it was intended because it introduces new test conditions that reveal deficiencies in the detector design.
- Bad weather meant that the observing trials took two weeks to complete. During this time the detector was switched on permanently and no electronic problems were experienced. This indicates that there are no major problems with detector reliability.

Chapter 8

Conclusions

8.1 Summary

Over twenty years of development in photon counting detectors at UCL has led to the design and construction of the microchannel plate intensified CCD image photon counting system, MIC-IPCS (MIC).

There are a number of major differences between MIC and the original IPCS developed by Boksenberg.

- MIC uses a highly compact proximity focussed microchannel plate (MCP) image intensifier whereas the IPCS uses an EMI 4-stage magnetically focussed intensifier. The benefits are small size, low weight, low power consumption, faster phosphor decay, lack of image distortion, choice of photocathodes and a better pulse height distribution.
- MIC uses a fast scanning CCD as a readout device whereas the IPCS uses a Plumbicon TV camera. The benefits are high frame rates, electronic stability and compactness.
- MIC has replaced the lens coupling between the intensifier and readout with fibre optic coupling. The fibre taper has a higher transmission efficiency and is more compact.

Additionally, these innovations have required substantial modifications to the processing electronics. In particular, MIC uses a look-up table based interpolative centroiding technique.

The MIC developed for space applications is an extremely compact, lightweight, low power consumption version of the ground based MIC. This detector incorporates a 25mm diameter MCP intensifier with an S-20 photocathode, three channel plates arranged in a Z configuration and a P-20 output phosphor. The output of the intensifier is coupled to a fast scanning CCD via a fibre optic taper giving a demagnification of 3.06. A custom built CCD camera processes the CCD pixel data and presents them to the data processing electronics. The processing electronics recognise events, centroid them to 1/8th pixel and define an address for them in the detector memory. A computer provides software control of the electronics and of data acquisition and display.

The detector has the following characteristics

Full format	2048×2048
Pixel size	8.80 μ m
Active area	18mm×18mm

An additional characteristic is a windowing facility that allows up to 16 user definable windows to be place anywhere within the 2048×2048 area. The windowing is required both to enable data acquisition on a number of guide stars and as a means of increasing the dynamic range of the system. Another feature of the space based MIC is a circuit that recognises when more than one event has landed in the same place on the CCD and this serves to improve the detectors dynamic range characteristics. Both the windowing facility and the multiple event circuit are unique to the space version of MIC.

The performance of the detector is greatly affected by the performance of the intensifier. Two intensifiers supplied by Instrument Technology Limited (ITL) showed a poor pulse width distribution and a large amount of signal induced background (SIB) and this affected the results of performance tests. Some tests carried out with the intensifier designed for the ground based MIC help to show what performance is possible. The space version of MIC has the following performance characteristics

- Responsive quantum efficiency (RQE). The RQE has been measured with a calibrated light source for the two intensifiers supplied by ITL. They show a peak efficiency of 6% in the blue compared with the XMM requirement of >20%. An intensifier supplied by Delft Electronische Producten (DEP) showed a peak of 21% in the UV.

- Resolution. With the ITL intensifiers the best resolution obtainable was 35/xm FWHM on a point source. With the ground based MIC tube it was found that the channel plate pore structure was being resolved so that the resolution varied according to the position of the point source. A limiting resolution of 17.6//m was derived.
- Detective quantum efficiency (DQE). It has not been possible to measure the DQE but it thought that it will be as high as 16%.
- Dynamic Range. The dynamic range is affected by the spatial extent of the object, the format used, channel recovery effects in the MCPs and the multiple counting circuit. The following figures have been found for the count rate at which 10% of counts are lost due to coincidence

Flat field, 2048x2048	5 counts s ⁻¹ pixel
Point source, 2048x2048	25 counts s ⁻¹ object ⁻¹
Flat field, 2048x256	35 counts s ⁻¹ pixel
Point source, 2048x256	200 counts s ⁻¹ object ⁻¹
Flat field, 2048x2048, multiple counting enabled	16 counts s ⁻¹ pixel

- Detector uniformity. The most serious detector non-uniformity is the fixed pattern noise arising from centroiding errors. When a long flat field was examined the fixed pattern was found to vary from spectrum to spectrum and across a spectrum. It can also be variable with time. More seriously, the pattern has been found to be count rate dependent. Other non-uniformities arise from low quantum efficiency CCD pixel, fibre optic bundle defects and from the reflections from the solder ring on the input to the intensifier.
- In an astronomical context. The detector was tested at the University of London Observatory for the purposes of assessing its performance in an astronomical context and to evaluate the effect of channel recovery on point source dynamic range characteristics. The results of the trials were not conclusive and did not show any channel recovery phenomena.

8.2 Future Developments

Future developments will consist largely of space qualification of the system and of modifications and updates in order to meet the scientific requirements of table 2.1.

Space Qualification

Up to now, the prototype version of XMM-MIC has been designed to have low power consumption, with the consideration of launch and the space environment having not been fully addressed. In terms of space qualification, several areas need to be considered

- Random and sinusoidal vibration and acoustic noise. Two components can be immediately identified as susceptible
 - The fibre optics – in the prototype system these have three components butted together which would not withstand high levels of vibration. In the space qualifiable version, as discussed in section 4.2, it is planned to have only a single fibre optic component that is both the intensifier output window and the taper and is also bonded to the CCD.
 - The intensifier – this has never been used in a space environment or undergone vibration testing. The channel plates are thought to be the only cause for concern although they ought not to be a problem since they are very well constrained by the intensifier housing.
- Electromagnetic Coupling (EMC). The primary source of EMC is likely to be the CCD drivers which have to drive a high capacitive load at high frequency. These will be housed at the camera head in a screened box. The cable that carries data from the ADC to the processing electronics may also be screened.
- Thermal environment. No problems are anticipated either for the detector or the electronics in meeting the operating temperatures specified for XMM.
- Radiation Environment. The dosage over the ten year lifetime is not expected to exceed 50 kRads. By using radiation hard components the electronic problems should be resolved. However, other components need careful consideration

- The input window of the intensifier. The choice of materials is between Magnesium Fluoride, Sapphire and Suprasil. All are known to suffer from some degree of radiation damage, in particular, a darkening of occurs at high dosages and future work will need to quantify this to determine whether it could be a problem. Additionally, Sapphire suffers from scintillations when subjected to radiation
- the effect of this on the performance of the detector in a space environment will need to be addressed in future work.
- The fibre optic taper. The effect of radiation on the taper was discussed in section 4.5. A browning of the glass gives rise to attenuation in the fibres but, unless this is particularly severe, any losses may be regained by increasing the intensifier gain. In future work it will be necessary to evaluate this effect to see if the latter is a valid assumption.
- The CCD. The effect of radiation on the CCD was discussed in section 5.4. It has been noted that Thomson CSF CCDs seem to be more prone to damage in a radiation environment and future work needs to investigate this. If a problem arises then future work will also need to investigate the possibility of using other CCDs, for example, from EEV. However, it should be remembered that the primary detectors on the XMM are cooled CCDs and the radiation environment has to be limited for their operation. As discussed in section 5.4, the effect of radiation on a fast scanning CCD running at room temperature will be far less severe.
- The electronics. Although radiation hard components may be used, there are important considerations that may require design changes such as freedom from latch up and single event upsets.

Improvements in Performance

There are several aspects of the detector's performance that need to be improved to meet the requirements of table 2.1

- Resolution. A resolution of better than $20\mu\text{m}$ FWHM on point source is required. At present a limiting resolution of $17.6\mu\text{m}$ has been achieved at a wavelength of 490nm
 - it will undoubtedly be worse at shorter wavelengths due to the greater energy

of the primary electrons emitted from the photocathode. The resolution can be improved by using smaller pore spacing on the front channel plate of the intensifier, for example, Galileo Electro-optics produce channel plates with $6\mu\text{m}$ pores on $7.5\mu\text{m}$ centres. It is anticipated that the resolution at 490nm would then be $14.8\mu\text{m}$.

- **Dynamic range.** The expected maximum count rate over the detector area is $200\text{ k counts s}^{-1}$. There should be no problem for MIC in achieving this as it has been demonstrated that the 10% coincidence loss point on full format for a flat field is at $10^6\text{ counts s}^{-1}$.

The maximum point source count rate of $1000\text{ counts s}^{-1}$ is unlikely to be achieved. MIC has 10% coincidence loss on a point source at 25 Hz on full format and 200 Hz on a 32 row format. However, the potential exists to detect at much higher count rates. It is possible to use the non-linear region of the dynamic range curve to calibrate the intensity of the input source. In space the seeing conditions are constant and so the dynamic range curve ought to be the same for all point sources. Thus the curve may be used to calibrate the intensity of the source. Care must be taken when applying this correction – the dynamic range curve may vary with time if, for example, the intensifier characteristics change or voltages drift. The curve will need to be recalibrated at intervals. Thus it will be possible to detect at higher count rates if

- windowing is used to increase the frame rate and thus, the dynamic range, on bright objects
- full use is made of the non-linear region of the dynamic range curve.

If these simple procedures are implemented then it is believed that point source count rate of $\sim 500\text{ Hz}$ are achievable. However, before their implementation two areas need to be investigated in future work

- Dynamic range tests will need to be carried out to test the validity of using the dynamic range curve for input source brightness calibration, especially if the multiple counting circuit is to be enabled
- Dynamic range tests will need to be carried out to try to understand the effect of pore paralysis. For example, how will the dynamic range curve be affected

by the presence of a nearby bright star?

- The detective quantum efficiency of the detector has yet to be evaluated and this is essential future work
- The lifetime of the detector is required to be ten years. The image intensifier is the life limiting component of the detector and it will be essential to carry out accelerated life tests on sample intensifiers.
- Detector non-uniformities. These come in two categories
 - Distortions and blemishes – These were discussed in section 7.6. The errors introduced by pin-cushion distortion, for example, can be completely removed during data reduction. Other non-uniformities can be minimized by careful consideration to design, for example, the butting between three fibre optics introduces non-uniformities but these may be removed by replacing the three by a single fibre optic component as already mentioned.
 - Fixed pattern noise – with the present prototype XMM-MIC there will always be some fixed pattern noise due to the count rate dependency discussed in section 7.6.5. Dithering was discussed in section 6.6.2 as a tried and tested method of removing fixed pattern noise at any count rate. It is used routinely with ground based systems but, as yet, it could not be implemented in space due to the mechanisms required to carry it out. In future work an investigation must be made as to whether a novel dithering mechanism can be invented that is usable in a space environment.

Another form of fixed pattern noise is the aliasing effects described in section 7.6. These were not seen in test done with the ITL intensifiers because of the poor centroiding resolution they produced. It is believed that the effect of these aliasing fringes can be substantially reduced by the use of intensifiers with $6\mu\text{m}$ pores on $7.5\mu\text{m}$ centres.

Although the development of the XMM-MIC is far from complete, it has been demonstrated that the system is capable of meeting all but one of the strict performance characteristics required of the blue camera for the XMM-OM. Furthermore, no major problems

are anticipated in the detector's performance in a space environment. Obviously, further work is needed before the detector meets all the requirements, scientific or otherwise, of a detector for space applications. This work ought to serve as a valuable reference manual and as a basis for any future developments.

References

- Airy, R. W., Norton, T. J., Morgan, B. L., Fordham, J. L. A., Bone, D. A., Powell, J. R., 1990. *Proc. SPIE*, **1235**, 338.
- Boksenberg, A., 1971. "Astronomical Use of Television-Type Image Sensors", Symposium held at Princeton University, Princeton, N. J., May 20–21, 1970, (NASA SP–256), **77**.
- Boksenberg, A., 1978. Proceedings of ESO Conference "Telescopes of the Future", Geneva, 1977 Dec 12–15, p.497.
- Boksenberg, A., Burgess, D. E., 1972. *Adv. E. E. P.*, **33B**, 835.
- Boksenberg, A., Coleman, C. I., Fordham, J. L. A., Shortridge, K., 1985. *Adv. E. E. P.*, **64A**, 33.
- Boskma, L., 1991. *Private Communication*, Delft Electronische Producten, Roden, Holland.
- Cho, D. J., Morris, G. M., 1988. *Proc. SPIE*, **976**, 172.
- Cook, L. M., Burger, R. J., 1991. *Proc. SPIE*, **1449**, 186.
- Csorba, I. P., 1985. "Image Tubes", Howard Sams, Indianapolis.
- Daly, E. J., 1991. "XMM Radiation Environment", Presented at an XMM-OM experimental engineering meeting, 28 November, 1991.
- Decker, R. W., 1969. *Adv. E. E. P.*, **28A**, 357.
- Dick, J., Jenkins, C., Ziabicki, J., 1989. *Pub. A. S. P.*, **101**, 684.
- Eberhardt, E. H., 1977. *Applied Optics*, **16**, 2127.
- Eberhardt, E. H., 1981. *IEEE Trans. Nucl. Sci.*, NS–28, 712.
- Eccles, M. J., Sim, E. M., Tritton, K. P., 1983. "Low Light Level Detectors in Astronomy", Cambridge University Press, Cambridge.
- Edgar, M. L., Lapington, J. S., Smith, A., 1991. "The Spatial Extent of Gain Depression for MCP Based Photon Detectors", Proc. 4th Int. Conf. Synchrotron Radiation Instrum., Chester, U.K., 1991.
- Flam, R. P., 1969. *Proc. IEEE*, Dec. 1969, 2152.
- Fordham, J. L. A., Bone, D. A., Jorden, A. R., 1986. *Proc. SPIE*, **627**, 206.
- Fordham, J. L. A., Bone, D. A., Norton, T. J., Read, P. D., 1990, *Proc. SPIE*, **1235**, 636.
- Fordham, J. L. A., Bellis, J. G., Bone, D. A., Norton, T. J., 1991. *Proc. SPIE*, **1449**, 87.

- Fraser, G. W., Pearson, J. F., Lees, J. E., 1987. Presented at IEEE Nuclear Science symposium, San Francisco, Ca., 21–23 October, 1987.
- Fraser, G. W., Pain, M. T., Less, J. E., Pearson, J. F., 1991. *Nucl. Instrum. Methods in Phys. Research*, **A306**, 247.
- Friebele, E. J., 1979. *Optical Engineering*, **18**, 552.
- Friebele, E.J., 1984. *Nucl. Instrum. Methods in Phys. Research*, **B1**, 355.
- Gatti, E., Oba, K., Rehak, P., 1983. *IEEE Trans. Nucl. Sci.*, **NS-30**, 461.
- Hobbs, T. I., Carden, D. A., Rodgers, A. W., Stapinski, T. E., Gorham, R. A., 1983. *Proc. SPIE*, **445**, 402.
- Holland, A., Holmes, A., Johlander, B., Adams, L., 1991. *IEEE Trans. Nucl. Sci.*, **bf 38**, 1663.
- Hopkinson, G. R., 1989. “*Radiation Damage Effects in EEV CCDs*”, Technical Note, Sira Ltd., Chislehurst, Kent, England.
- Jorden, A. R., Fordham, J. L. A., 1986. *Q. Jl. R. Astr. Soc.*, **27**, 166.
- Lampton, M., Carlson, C. W., 1979. *Rev. Sci. Instrum.*, **50**, 1093.
- McLean, I. S., 1989. “*Electronic and Computer Aided Astronomy – from Eyes to Electronic Sensors*”, Ellis Horwood, Chichester.
- Manara, A., Antonini, M., Campagni, P., Gibson, P. N., 1984. *Nucl. Instrum. Methods Phys. Research*, **B1**, 475.
- Martin, C., Jelinsky, P., Lampton, M., Malina, R. F., Anger, H. O., 1981. *Rev. Sci. Instrum.*, **52**, 1067.
- Mason, K. O., 1989. “*An Optical Monitor for XMM – Part One, Scientific and Technical Case*”, Principal Investigator in XMM Proposal, p. 24.
- Nartallo Garcia, R., 1990. M.Sc. Thesis, University of London.
- Norton, T. J., Airy, R. W., Morgan, B. L., Read, P. D., Powell, J. R., 1988. *Adv. E. E. P.*, **74**, 425.
- Norton, T. J., Airy, R. W., Morgan, B. L., Fordham, J. L. A., Bone, D. A., 1991. “*Photoelectronic Imaging Devices*”, Ed. B. L. Morgan, IOP Publishing, Bristol, p. 97.
- Norton, T. J., *Private Communication*.
- Officine Galileo Staff, 1990. Osservatorio Astronomico Di Brera, Merate, Italy. *XMM optical monitor technical report*, XMM-OM/OABM/TC/0003.01.
- Oldfield, M. K., 1991. *XMM optical monitor technical report*, “Background count rate

- contribution due to fluorescence in MCP sapphire windows.”
- Oldfield, M. K., Fordham, J. L. A., 1991. “Second generation PDA for HST – improvement in dynamic range and resolution of the MIC detector,” Report from UCL to British Aerospace.
- Papaliolios, C., Mertz, L., 1982. *Proc. SPIE*, **331**, 360.
- Pearson, J. F., Less, J. E., Fraser, G. W., 1988. *IEEE Trans. Nucl. Sci.*, **NS-35**, 520.
- Sandel, B. R., Lyle Broadfoot, A. L., Shemansky, D. E., 1977. *Applied Optics*, **16**, 1435.
- Sharma, A., Walker, J. G., 1989. *Quantum Optics*, bf 1, 11.
- Shectman, S. A., 1981. *Carnegie Institute of Washington Yearbook*, **80**, p586.
- Siegmund, O. H. W., Lampton, M. L., Raffanti, R., 1989. *Proc. SPIE*, **1159**, 476.
- Siegmund, W. P., 1991. “*Fiber optics in electronic imaging*”, Schott Fiber Optics Technical Report.
- Smith, S. R., Lowrance, J. L., 1972. *Pub. A. S. P.*, **84**, 154.
- Timothy, J. G., 1986. *Proc. SPIE*, **687**, 109.
- Timothy, J. G., 1991. *Photoelectronic Imaging Devices*”, Ed. B. L. Morgan, IOP Publishing, Bristol, p. 85.
- Williams, F. E., Eyring, H., 1947. *The Journal of Chemical Physics*, **15**, 289.
- Wiza, J. L., 1979. *Nucl. Instrum. Methods*, **162**, 587.
- Worswick, S. P., Wynne, C. G., 1985. *The Observatory*, **105**, 95.

List of Publications

- Fordham, J. L. A., Bellis, J. G., Oldfield, M. K., Bone, D. A., 1990. "*The effect of phosphor decay on dynamic range in the MIC detector*", XMM-OM technical report, XMM-OM/MSSL/TC/0009.01.
- Bellis, J. G., Bone, D. A., Fordham, J. L. A., 1991. *Pub. A. S. P.*, **103**, 253.
- Bellis, J. G., 1991. "*Fibre taper distortion associated with the MIC detector*", XMM-OM technical report, XMM-OM/MSSL/TC/0015.03.
- Fordham, J. L. A., Bellis, J. G., Bone, D. A., Norton, T. J., 1991. *Proc. SPIE*, **1449**, 87.
- Fordham, J. L. A., Bone, D. A., Oldfield, M. K., Bellis, J. G., 1991. "*Photoelectronic image devices*", Ed. B. L. Morgan, IOP Publishing, Bristol, p. 105.
- Bellis, J. G., 1992. "*The transmission efficiency of the fibre taper used in the MIC detector*", XMM-OM technical report, XMM-OM/MSSL/TC/0019.01.